Doctorate Dissertation

博士論文

Size-Controlled Metal Nanoparticles on SBA-15 with Immobilized Ionic Liquid: Synthesis, Structural Properties and Catalytic Performances

（イオン液体を固定化したSBA-15上のサイズ制御された金属ナノ粒子：合成、構造及び触媒活性に関する研究）

A Dissertation Submitted for Degree of Doctor of Philosophy
July 2018

平成30年7月博士（理学）申請
Department of Chemistry, Graduate School of Science,
The University of Tokyo
東京大学大学院理学系研究科化学専攻

KUSUMAWATI, Etty Nurlia
クスマワティ．エッティ　ヌルリィア

Abstract

Size-controlled synthesis of metal nanoparticles on SBA-15 in the presence of immobilized ionic liquid was developed to obtain highly dispersed small nanoparticles inside porous channels and minimize the pore-blocking effect caused by large particles. The resulting materials were characterized to study their structural properties and the catalytic performances were examined to investigate their activity and reusability. Size- and shape-controlled synthesis of nanoparticles on mesoporous silica SBA-15 was investigated for gold nanoparticles (AuNPs) in the presence of immobilized ionic liquid by varying the concentration and feed rate of sodium borohydride ($NaBH_4$). In this study, it was found that the size distribution and the shape of AuNPs strongly depend on the concentration and the feed rate of the reductant and the physical mechanism was discussed. The size-dependence of AuNPs on catalytic reaction was studied and the smallest nanoparticles with the average size 1.6 nm showed the best catalytic performance in the reduction of *p*-nitrophenol. Various other metal nanoparticles such as Pd, Cu, Ru and Pt were also successfully synthesized and the prepared catalysts were found active and reusable for *p*-nitrophenol reduction. The activity of different metals was compared and discussed. Moreover, palladium nanoparticle catalyst was found active and reusable for Suzuki-Miyaura coupling reaction between aryl halides and phenylboronic acid at room temperature. Characterization of the catalysts revealed that the metal atom was coordinated by chloride atoms forming metal chloride complex anion before reduction, whereas the ionic liquid was strongly bonded on the siliceous SBA-15 and the well-ordered mesoporous silica was kept unchanged after the formation of metal nanoparticles.

Table of contents

Chapter 1 Introduction

Chapter 2 Size-controlled gold nanoparticles prepared from immobilized gold ion-containing ionic liquid on SBA-15

Chapter 3 Size-dependence of gold nanoparticles in the reduction of *p*-nitrophenol

3.3.1. Effect of nanoparticle size
3.3.2. Effect of $NaBH_4$ concentration
3.3.3. Recycle study

Chapter 4 Immobilization of various metal nanoparticles on ionic liquids functionalized SBA-15 as active and reusable catalysts

4.2.1. Synthesis of SBA-15
4.2.2. Preparation of ionic liquid
4.2.3. Immobilization of metal ion-containing ionic liquid on SBA-15
4.2.4. Syntheses of MNPs_me-Im@SBA-15

Chapter 5 Room temperature Suzuki-Miyaura coupling reaction catalyzed by palladium nanoparticle

Chapter 1

Introduction

Abstract

This chapter presents the rationale which motivates the present study in the development of heterogeneous catalyst based on immobilization of various metal nanoparticles on mesoporous silica SBA-15 in the presence of ionic liquid. Section 1 describes general overview of the fundamental knowledge towards the main concepts of this study, which covers basic understanding of the nanoparticles, mesoporous silica, the growth principles of metal nanoparticles in colloidal and supported systems. Syntheses of size-controlled growth of nanoparticles by various techniques are also presented in this section. Section 2 of this chapter contains a brief review of the research progress on the development of metal nanoparticles on porous materials and preparation methods for the immobilization of metal nanoparticles containing ionic liquids catalysts on supports. Finally, scope and objectives of this study are presented in the last section.

1.1. Overview

1.1.1. Nanoparticles

Nanoparticles (NPs) are very important in developing sustainable technologies for the future and viewed as fundamental building blocks of nanotechnology. They are the starting points for many ‘bottom-up’ approaches to prepare nanostructured materials and devices. With respect to this, their syntheses are important components of rapidly growing research efforts in nanoscale science and engineering.[1] Moreover, due to large concentration of coordinatively unsaturated sites on surfaces, high dispersion and the presence of quantum confinement effects can drastically alter their activity in the field of catalysis.[2]

In various areas of science and technology, nanoparticles are also referred to as nanophase clusters, nanocrystals or colloids. Here I will mainly use the term nanoparticles for simplicity. Clusters or nanoparticles are aggregates comprised of a few to many millions of atoms or molecules. They may consist of identical atoms, or molecules, or two or more different species and have been studied in a number of media, such as molecular beams, the vapor phase, colloidal suspensions, and isolated states in inert matrices or on surfaces.[3–5] The physical and chemical properties, such as thermal and electrical conductivities, of metal nanoparticles (MNPs) are different from those of bulk metals which are manifested by delocalization of free electrons.[6] Since the high surface-area-to-volume ratio of MNPs provides a large number of active sites, the size and shape control of MNPs is the key to achieve enhanced reactivity.[7] The smaller the nanoparticle is, the larger the fraction of exposed surface atoms. However, as a consequence of the high surface energy and large surface area of MNPs, their thermodynamic stability is severely decreased, which obstructs the control of size and shape with high uniformity.[8]

The large surface-to-volume ratio of MNPs allows them naturally to act either as supports or active parts for organic transformations. Chemical and physical techniques have been developed to prepare MNPs, including chemical reduction using a reducing agent, electrochemical reduction, photochemical reduction and heat evaporation *etc.*[9] In chemical reduction technique, MNPs are usually synthesized in a "bottom-up" strategy by *in situ* reducing metal salt in the presence of molecular stabilizer. The nature of stabilizers used can be electrostatic (using surfactants or ionic liquids), steric (using polymers or dendrimers), electro-steric (using polyelectrolyte, a combination of electrostatic and steric) or complexible (through the use of small molecular ligands).[10]

1.1.2. Growth principles of colloidal metal nanoparticles

In colloid science, several theories to explain aggregation of sub-micrometer spherical particles have been developed and experimentally studied for decades. The pioneer works on metal colloid science were investigated by Michael Faraday in the 19th century with his ground-breaking experiments on gold sols.[11] In his work, the red color of a solution was attributed to the presence of colloidal gold, obtained by reduction of dissolved chloroaurate using white phosphorus.[12] The important progress in the description of NP behaviour then was achieved in the end of 19th century by Wilhelm Ostwald, in particular by his theory of particle growth via Ostwald ripening.[13] Since then, numerous experimental methods for the synthesis of metal, metal oxide and semiconductor NPs have been developed. However, only few studies deal with particle formation mechanisms and in a consequence, theoretical concepts describing the particle growth processes are very rare and the few existing models hardly able to explain how synthesis parameters influence the final particle size distribution.[14]

Nucleation is a thermodynamic model which describes the first step in a first order phase transition.[14] The theoretical work on nucleation applying equilibrium thermodynamics is based on the classical nucleation theory developed by Becker and Döring.[15] The theory applies that a thermodynamic system tends to minimize its Gibbs free energy (i.e. to maximize the entropy of the whole system). This theory only describes the nucleation, whereas the particle growth is separated as a subsequent process. The further growth can be explained such as by diffusion limited growth, aggregation or Oswald ripening. In this theory it is very important to distinguish between homogeneous and heterogeneous nucleation. Heterogeneous nucleation occurs at the surface of NPs in solution providing nucleation sites, used in seeded-growth synthesis, whereas homogeneous nucleation occurs spontaneously and randomly but requires a supercritical state such as a supersaturation.

LaMer *et al.* proposed the concept of burst nucleation which derived from the classical nucleation theory.[16,17] In this process, nuclei are generated at the same time due to homogeneous nucleation and subsequently grow without additional nucleation. The basic idea of this NP formation concept is to separate the nucleation and growth. The concentration of monomers is increasing (due to reduction) and reaches, at a certain critical supersaturation. The saturation increases and reaches a level at which the energy barrier for nucleation can be overcome leading to a rapid self-nucleation – the burst nucleation. Due to the burst nucleation, the supersaturation level lowers immediately below the self-nucleation level which ends the nucleation period. The growth then occurs by diffusion of further monomers in solution towards particle surfaces which can be interpreted as heterogeneous nucleation/growth.[14,16,17] The LaMer model only describes the nucleation process followed by the growth of stable nuclei but unable to characterize the evolution of NP size distribution.

Reiss then developed a growth model known as “growth by diffusion” in which the growth rate of spherical particles depends solely on the monomer flux supplied to the particles.[18] He deduced that if the diffusional growth is only dependent on the monomer flux, smaller particles will grow faster in the presence of larger particles, leading to a size focusing (narrow size distribution). However, this simplified mechanism does not include other effects such as aggregation, coalescence or dissolution (Ostwald ripening). Reiss's model then was extended qualitatively by Sugimoto *et al.* by including dissolution effects to obtain a size dependent growth rate by considering the Gibbs–Thomson equation.[19] As a consequence, broadening the size distribution due to nanoparticle dissolution is also possible which depends on the monomer concentration.

Further approaches to characterize particle growth are modelled by Privman *et al*. This model consists of two steps: a burst nucleation step, followed by an aggregation of the primary particles into micron-sized colloidal agglomerates.[20] The model incorporated the classical nucleation theory for the first step and rate equations for the second step.

Polte *et al.* proposed the growth mechanisms of colloidal MNPs from their research on AuNP and AgNP syntheses with sodium borohydride and sodium citrate as the reducing agent, by two categories of synthesis: (1) monomer-supplying chemical reaction faster than the actual particle growth and (2) kinetics of monomer-supplying reaction determines growth kinetics.[14,21–23] The first category is mainly covered by syntheses with BH_4^- as a reducing agent. It is deduced that the growth mechanism is only due to aggregation and coalescence (Fig. 1.1) and therefore governed by colloidal stability (the relation of the attractive and repulsive forces between nanoparticles), which is in contrast with LaMer model.

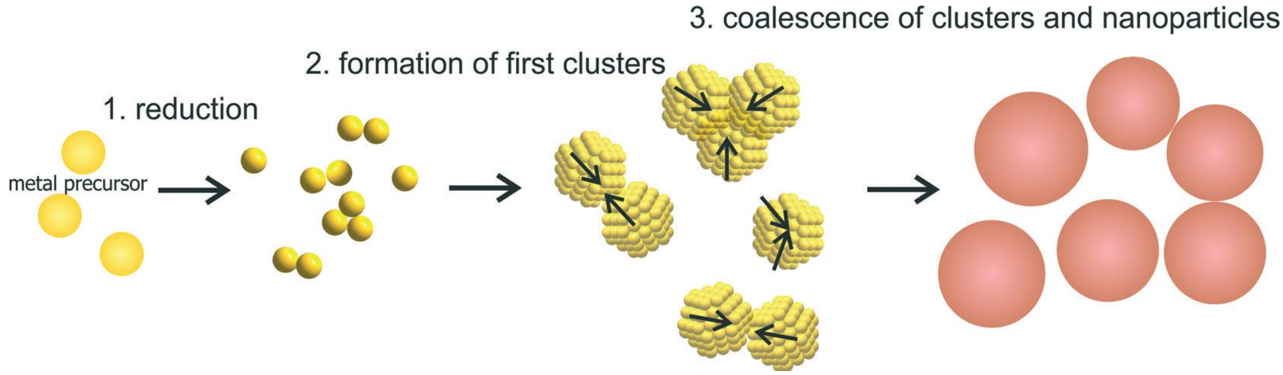

Fig. 1.1. Schematic mechanism of nanoparticle growth due to coalescence. This figure is reprinted with permission from ref. 14. Copyright 2015 The Royal Society of Chemistry.

The second category was discussed and explained by using the Turkevich method.[22,24,25] In this category the seed particles are formed in the beginning of the synthesis with a subsequent seeded growth which is most likely driven by a surface reduction. The seeded growth mechanism with the resulting final monodisperse gold NPs is caused by two factors: a change in the reduction chemistry and the colloidal stability. The first process is the reduction of gold salt which the metal atoms then subsequently form small clusters (second process) and undergo coalescence processes to form first NPs (third process). As a consequence, gold ions are attached near the surface in the electric double layer (EDL) as co-ions (fourth process), get reduced (fifth process) and grow onto the existing NPs (sixth process).[14]

1.1.3. Ionic liquids for the synthesis of nanoparticles

Ionic liquids (ILs) are liquid (molten) salts of weakly coordinating cations and anions that melt at or below 100 °C. ILs that are free-flowing liquids at room temperature are termed RT-ILs.

These have real advantages over higher melting salts in terms of the practicalities of handling. The cations are generally bulk, organic with low symmetry, such as ammonium, imidazolium, pyridinium, phosphonium, etc.[26–28] Whereas the anions can be classified as mono- or poly-nuclear anions, e.g. BF_4^-, PF_6^-, SbF_6^-, $Al_2Cl_7^-$, $Fe_2Cl_7^-$, $Sb_2F_{11}^-$. There are several advantages of ILs in respect of their properties, such as excellent and variable Lewis/ Brönsted acidity and negligible vapor pressure.[28] The liquid state is favored by small lattice enthalpies and large entropy changes, due to the large size and conformational flexibility of the weakly coordinating ions.[29] ILs have decisively different physical properties than other organic solvents, including high charge density, high polarity, high dielectric constant and supramolecular network formation.[30]

As previously mentioned, small NPs are only kinetically stable and will aggregate to thermodynamically more stable larger particles. Therefore, small metal nanoparticles require stabilization through additives which build up a protective layer to shield the particles from each other. Bilayers of surfactant ions lead to an electrostatic stabilization. Surface-capping ligands or polymers give a protective layer which provides steric coverage to prevent agglomeration.[31–35] In ionic liquids, MNPs can be synthesized and stored for some time without any additional stabilizers. The electrostatic and steric properties of ILs can stabilize MNPs without the need of surfactants, polymers or capping ligands. ILs may be regarded as a “nano-synthetic template”[36] that stabilizes MNPs on the basis of their ionic nature[37], high polarity, high dielectric constant and supramolecular network, without the need of additional protective ligands.

1.1.4. Size-controlled growth of nanoparticles

Bare MNPs are unstable and tend to agglomerate because they are attracted to each other by van der Waals, electrostatic or magnetic forces at short inter-particle distances. Without any counteractive repulsive forces NPs aggregate, agglomerate or undergo coalescent processes and such repulsive forces can be achieved by electrostatic, steric stabilization or electrosteric stabilization.[14] Many approaches for controlling NP size have been adopted by controlling the concentration of the ratio between reducing agent and the metal precursor, pH of solution, temperature of synthesis, and by the presence of a stabilizing agent, such as polymer PVP (polyvinylpyrrolidone), PVA (polyvinyl alcohol), ionic liquids, surfactants and dendrimers.[38–42]

Ji *et al.* reproduced the size variation of gold nanocrystals through citrate reduction in boiling water from Frens's work in 1973[43] by varying the molar ratio between sodium citrate (Na_3Ct) and auric acid ($HAuCl_4$).[44] They found that further increase of Na_3Ct/ $HAuCl_4$ from 3.5/1 in traditional Frens's method to 28/1 violated the increasing trend of the average size predicted by the nucleation growth mechanism. They concluded that pH solution (3.7 – 7.4) determined the size, size/shape distribution and size/shape evolution pattern of the resulting gold nanocrystal with the size 20 – 40 nm. Shervani and Yamamoto were successfully synthesized Au NPs with 5.3 nm in size by adjusting the amount of $NaBH_4$ and pH of solution by adding NaOH in the mixture.[45] They found that the smallest NPs can be obtained by adding 4 equiv. of $NaBH_4$ and an excess $NaBH_4$ or high pH caused the NPs to aggregate into wire or mesh-like structures. Soon after, Deraedt *et al.* studied the effect of $HAuCl_4$/ $NaBH_4$ ratio by various amount of $NaBH_4$ 2, 10, 50 or 100 equiv. per Au atom.[46] The average size of AuNPs in 2 equiv. of $NaBH_4$ was 5.5 ± 0.2 nm whereas long-term stable 3.2 ± 0.8 nm AuNPs was found in 10 equiv. of $NaBH_4$.

Introduction

Li and Gu investigated the effects of mass ratio, pH, temperature and reaction time on the fabrication of partially purified pomegranate ellagitannin (PPE)-gelatin nanoparticles.[47] They found that PPE-gelatin NPs fabricated using PPE/gelatin ratio below 7/5; pH 4.0, temperature 25–40 °C, and the reaction time 1.5 days had smaller particle sizes, higher zeta-potentials, and good loading efficiency. Maidul islam and Mukherjee investigated the effect of temperature on the formation and stabilization of silver NPs in aqueous poly(ethylene oxide)–poly(propylene oxide)–poly(ethylene oxide) (PEO–PPO–PEO).[48] They concluded that at lower temperature, change of polymer morphology mainly controls the particle size and their distribution whereas at higher temperature, the chemical change of the polymer plays a major role and at an intermediate temperature, the balance between the two effects provide the formation of AgNPs with small size with narrow distribution (2–5 nm).

Zhang and Sham studied the electronic behaviour of AuNPs capped with dendrimer and thiol molecules in which d electron (or hole) distribution of ~2 nm AuNPs can be turned by selective capping.[49] Few years later, López-Cartes *et al.* investigated the surface, size effects and the role of microstructure of AuNPs prepared with three different capping system using a tetralkylammonium salt (NR_4Br), an alkanethiol (SR), and a thiol-derived neoglyco-conjugate (SRmaltose) by XAS analysis.[50] The strong Au-S interaction resulted in a d-charge transfer from Au to S atoms and gave the average size 1.4 nm and 1.8 nm for Au-SR and Au-SRmaltose, respectively. Whereas a weak interaction between protective molecules (NR_4Br) and Au surface atoms gave 1.5 – 5.0 nm particle size for Au-NR_4Br. Tsukuda *et al.* investigated the cluster size effect on the aerobic oxidation of benzyl alcohol by gold and palladium nanoclusters (NCS) stabilized by PVP.[38] The smaller Au:PVP NCs with the size 1.3 nm showed the best catalytic performance compared to that of larger NCs of Au:PVP with the size 9.5 nm and Pd:PVP NCs

(1.5 and 2.2 nm). On the other hand, Deng *et al.* prepared gold protected ionic-surfactant (CTAB: hexadecyltrimethylammonium bromide) and AgNPs by the reduction using $NaBH_4$.[51] The catalytic activity of AuNPs without protective surface with size of 4.4 nm showed better catalytic performance than that of smaller CTAB-protected AuNPs with the size of 3.3 nm towards anthracene hydrogenation.

The decrease in activity was also observed in some cases due to the presence of capping agents on the metal surface due to the diffusion limitation and/or blocking of active sites.[52,53] Much effort has therefore focused on stabilizing the MNPs to avoid sintering (the loss of active catalyst surface area due to crystallite growth of either the support or the supported metals) via alloying, modifying the metal-support interface through the construction of unique interfacial structures and support modification via appropriate nanostructuring.[2] For example, Park and Choi successfully controlled the size, amount, and crystal-line structures of various metal NPs including Au, Pt, Pd, Ru and RuO_2 NPs deposited on IL functionalized reduced graphene oxides (RGOs) to enhance the reactivity towards methanol oxidation and pseudo-capacitance.[54] The average particle size of Au/IL-RGO, Pd/IL-RGO, and Ru/IL-RGO was found to be 4.3±0.42, 2.3±0.26, and 1.9±0.21 nm respectively. In addition, Pt/IL-RGO showed narrow size distribution with the size 2.1±0.17 nm whereas broad distribution of PtNPs with the size of 4.4±0.6 nm prepared without surface modification. They deduced that the sizes and morphologies of NPs were dependent on the type of NPs, the interaction between NPs and IL-RGOs and the growth kinetics of NPs.

1.1.5. Mesoporous Silica SBA-15

Mesoporous silica materials can be defined as porous silica materials with diameters between 2 and 50 nm, such as MCM (Mobil Crystalline Materials) family, SBA (Santa Barbara Amorphous) family, HMS (Hybrid Mesoporous Silicas), etc. which have been synthesized by using different templating agents. MCM-41 and SBA-15 are most well-known among mesoporous silica materials since they have well-defined and designable mesopores which possess a narrow pore distribution, hexagonal arrangement of uniformly sized cylindrical pores and large surface area.

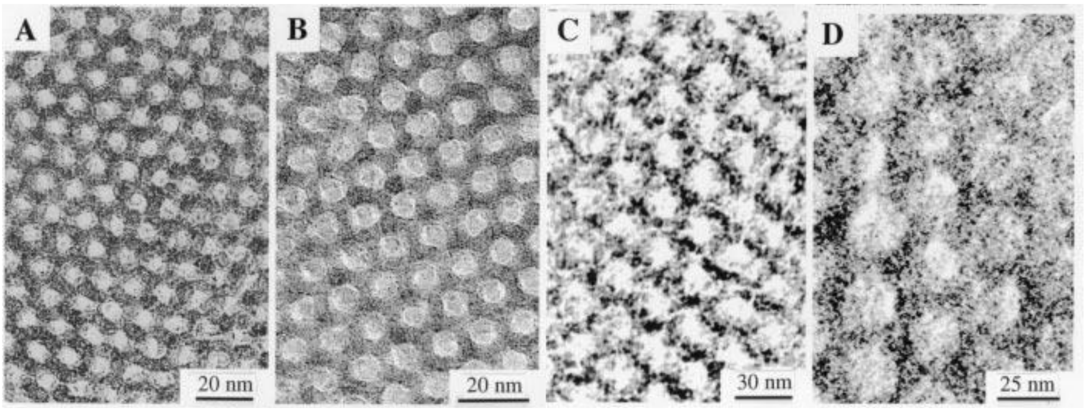

Fig. 1.2. TEM images of SBA-15 with different average pore sizes: (A) 60 Å, (B) 89 Å, (C) 200 Å, and (D) 260 Å. Reprinted with permission from ref. 55. Copyright 1998 Science.

SBA-15 was introduced by Stucky *et al.* in 1998 which was synthesized using amphiphilic block copolymers as the organic structure-directing agents.[55] Nonionic diblock copolymers ((poly(butylene oxide)-poly(ethylene oxide)) and star diblock poly(ethyleneoxide)-poly(propylene oxide) copolymers were also used to synthesize cubic mesoporous silica and various mesoporous oxides.[56] SBA-15 has attracted much attention in the field of catalysis due to many desirable features including tailored pore size, high degree of structural ordering, ease of synthesis, availability of economically facile synthesis pathways, hydrothermally/ thermally stable and so forth.[57] SBA-15 was initially considered as an extra-large-pore MCM-41 with a hexagonal structure of disconnected channel-like pores.[58] The existence of microporosity in numerous SBA-15 samples were reported, but some claimed that some SBA-15 samples are non-microporous and the evidence of the microporosity was questioned by the authors who first suggested the presence of micropores in SBA-15.[59–65] Inagaki and Miyazawa observed the microporosity within the pore walls of SBA-15 from nitrogen adsorption-desorption isotherm analysis and this microporosity can be controlled via the synthesis conditions.[63] Ryoo *et al.* deduced that the microporosity in SBA-15 and its evolution during the synthesis are consequences of the fact that poly(ethylene oxide) blocks of the poly(ethylene oxide)–poly(propylene oxide)–poly(ethylene oxide) template penetrate the silicate walls of SBA-15.[57,66,67]

1.2. Background

1.2.1. Metal nanoparticles on porous materials

Compared to bulk particles, MNPs when dispersed on the surface of support materials can be much more active and selective catalysts.[68,69] The role of supports appears to be an importance point in determining the optimum size for activity since it affects the reaction mechanisms. Numerous studies on the synthesis of supported MNPs on supports materials either active or inert supports are both popular subjects to investigate. There are numerous publication regarding the use of active metal oxides as the supports for metal nanoparticles which showed high activity in organic transformations.[70–75] In particular, for inert or inactive supports such as silica, carbon or porous silica, the activity seems to solely depend on the nanoparticle size. Among the inert supports, SBA-15 offers many advantages from its physical properties such as uniform pore size distribution, large pore size and surface area, and easy surface modification. This section therefore will mainly focus on the use of SBA-15 as support materials for MNPs.

The supported metal nanoparticles can be prepared conventionally by impregnation, co-precipitation, or deposition-precipitation methods. These methods however are not appropriate to obtain the required highly dispersed MNPs since they usually yield large particles which weakly bind to the support.[76,77] To avoid the aggregation and minimizing the formation of large nanoparticles, supported MNPs are usually prepared by reduction using H_2 gas or reducing agent ($NaBH_4$) and by modifying the support surface with various organic molecules to obtain high dispersion of MNPs.[78–82]

Supported gold nanoparticles usually prepared from $HAuCl_4$ as metal source in aqueous solution and further reduced by reducing agent (e.g. $NaBH_4$) or by the reduction using H_2 gas. Yang *et al.* prepared highly dispersed metal NPs (Pt, Au, Pt-Pt and Pt-Au) on TPTAC $(CH_3O)_3Si(CH_2)_3N(CH_3)_3Cl$) functionalized SBA-15.[78] Disk-shaped PtNPs and AuNPs as well as bimetallic Pt-Au NPs were found inside porous channels SBA-15 with controlled morphology and composition. The size of the prepared monometallic and bimetallic NPs was found to be 2.3 nm, 4.0 nm, ~5 nm for Pt/SBA-15, Pt-Pt/SBA-15, Au/SBA-15 and two distinct sizes of ~5 nm and ~0.6–1 nm for Pt-Au/SBA-15. They suggested that the morphology of the metal NPs was affected by the loading amount as well as the intrinsic properties of the metals. Liu and coworkers also prepared AuNPs on SBA-15 modified with TPTAC in both alcoholic and aqueous solutions to generate positively charged functional groups on SBA-15 pore surfaces.[83] Large NPs with the size 15–43 nm were obtained when prepared in aqueous solution, whereas well-dispersed 5 nm particles were obtained inside porous channels prepared in ethanolic solution. However, large aggregates with 10–15 nm NPs were detected as the main components after reduction by $NaBH_4$ and even larger when reduced by H_2, resulting in average size 7–25 nm. On the other hand, Petkov *et al.* successfully prepared gold nanowires inside porous channels of thiol-modified SBA-15 by electroless reduction with 5 nm thick and 100–1000 nm to more than 3 μm long.[42]

Beck *et al.* studied the formation and structure of Au/TiO_2 and Au/CeO_2 nanostructures in SBA-15 by various methods (i) deposition-precipitation, (ii) adsorption of Au colloid stabilized by PVA (polyvinylalcohol) prepared by $NaBH_4$ reduction and (iii) reduction of $HAuCl_4$ precursor by $NaBH_4$ in the presence of PDDA (poly(diallyldimethylammonium) chloride).[84] It was found that AuNPs prepared by the method (ii) (AuTiSBA_PVA) showed most stable with the size 2.7 nm and after the catalytic test the size was 2.9 nm compared to AuNPs prepared by (i) and (iii) method with the size of 5.1 nm and 5.7 nm, respectively. However the catalytic performance towards CO oxidation was lower than that of $AuTiO_2$_PVA which has similar size (2.7 nm) prepared on TiO_2 (non-porous support). They suggested that the activity is strongly affected not only by the particle size, but also the length of Au/TiO_2 or Au/CeO_2 perimeter that is in good correlation with the surface charges of the components in different preparations.

Highly dispersed coinage MNPs (Au, Ag and Cu) prepared on 3-aminopropyl-triethoxysilane (APTES) modified SBA-15 for highly selective nitroaromatics reduction was reported by Sareen *et al.*[79] Gold NPs with the size of ~5 nm exhibited the best catalytic performance for m-dinitrobenzene reduction compared to that of larger AgNPs (~11 nm) and CuNPs (~13 nm). Veisi *et al.* reported that supported PdNPs with the size of 10 nm prepared on 1,3-dicyclohexylguanidine functionalized SBA-15 was found highly active and reusable for

Suzuki-Miyaura coupling reaction.[82]

Besides polymers or other organic molecules, ionic liquids are also used to modify the support SBA-15 in order to obtain highly dispersed metal NPs. Ma *et al.* successfully prepared supported PdNPs on ionic liquid 1,1,3,3-tetramethylguanidinium (TMG)-modified SBA-15 reduced by H_2 at 180 °C.[85] PdNPs were mainly observed inside porous channels with the size 3–6 nm which showed more stable and better performance towards solvent-free Heck reaction than that of PdNPs prepared in the absence of ionic liquid (TMG) which exhibited large particle in the range of 9–12 nm. Meanwhile, Han *et al.* prepared immobilized Pd(II) on imidazolium ionic liquid (*N*-3-(3-triethoxysilyl propyl)-3-methyl imidazolium chloride) functionalized SBA-15 for room temperature Suzuki coupling reaction.[86] The activity of the material gradually decreased during the recycle process. They suggested that Pd(II) complexes were reduced to PdNPs during the reaction and at the end of reaction PdNPs was re-deposited on the pore walls and did not simply agglomerate due to the pore-containing effect of SBA-15 and stabilized imidazolium on inner walls. As comparison, this catalyst showed better performance than that of Pd(II) on SBA-15 in the absence of ionic liquid.

In 2012, Fattori and coworkers employed imidazolium-grafted on SBA-15 to immobilized AuNPs inside porous channel.[87] The amount of $AuCl_4^-$ loaded on the modified SBA-15 was varied from 1.8, 9.0 and 14.2% denoted as SBA-15/R^+Cl^-/Au1, SBA-15/R^+Cl^-/Au2, and SBA-15/R^+Cl^-/Au3 respectively. The AuNPs were observed mainly inside pore channel with the average size 1.5, 2.35, and 4.7 nm for SBA-15/R^+Cl^-/Au1, SBA-15/R^+Cl^-/Au2, and SBA-15/R^+Cl^-/Au3 respectively with highly dispersed and stable after thermal treatment at 973 K. The ion-exchange properties of the prepared sample were thoroughly studied by ion-exchange isotherm, however their local structure information and catalytic activities were not investigated.

Recently, Mazali *et al.* reported the preparation of supported AuPd nanoalloys on imidazolium-functionalized SBA-15 and investigated the structural correlations toward 4-nitrophenol hydrogenation reaction.[88] Small NPs between 1-5 nm have non-passivated surfaces and are highly dispersed on SBA-15, however AuNPs contain some large NPs outside pores. It was found that PdNPs showed the best catalytic performance than that of the PdAu nanoalloys.

1.2.2. Preparation of immobilized metal ions containing ionic liquid on solid support

Valkenberg *et al.* reported the immobilization of ionic liquids on various solid supports, including silica, alumina, zeolite and MCM-41 based on $FeCl_3$, $SnCl_2$, and $AlCl_3$ for Friedel–Crafts processes.[89–91] Their works explained different possibilities for the preparation of heterogeneous, acidic catalysts, either prepared from or based on the example of Lewis-acidic ionic liquids. They introduced the term of novel Lewis acid catalysts (NLACs). The immobilization of ionic liquids can be carried out via the anion (NLAC I), cation (NLAC II and NLAC III).[91] Since then, the immobilization of ionic liquids on solid supports were investigated numerously especially for support modifications.

Sasaki research group reported successful immobilization of various metal ions containing ionic liquids on silica for various organic transformations, such as Kharash reaction, Suzuki cross-coupling reaction, alkoxylation, carbonylation, hydrogenation reaction, etc.[92–99] A series of metals ion-containing ILs on silica Aerosil 300 were prepared by firstly immobilization of imidazolium ionic molecules on silanol groups of silica surfaces followed by addition of metal chloride as the metal precursor ($MnCl_2$, $FeCl_2$, $CoCl_2$, $NiCl_2$, $CuCl_2$, $PdCl_2$ and $PtCl_2$) and the local structures around metal atoms were analyzed by EXAFS analysis.[92,94] These catalysts were proven highly active and reusable. Moreover, syntheses of metal ion-containing dialkyl-imidazolium ionic liquids salts as well as their structures and properties were investigated by single crystalline X-ray analysis and TGA analysis.[100] And more recently, this group reported the immobilization of palladium ion-containing ionic liquid on mesoporous SBA-15 as active and reusable for the synthesis of oxamate and urea by oxidative single and double carbonylation of amines, also for polyester amide synthesis via carbonylation-polycondensation reaction.[101,102]

1.3. Scope and purposes of this study

As it has been stated in the previous section, metal nanoparticles hold great promise for heterogeneous catalysis due to their properties such as high reactivity and the presence of quantum confinement effects. However, for this reason it is a great challenge to design effective heterogeneous catalyst based on supported metal nanoparticle which is not only active and selective but also stable and reusable. Moreover, catalytically active nanoparticles are subject to sintering especially at high temperature, unstable and tend to agglomerate without any counteractive repulsive forces. On the other hand, the size and morphology of the nanoparticles affect greatly to its catalytic performances. As it was discussed before, the use of stabilizers or capping agents is the most efficient way to control the nucleation and growth of the nanoparticle to prevent it from agglomeration. However, in some cases the presence of stabilizing agents on the surface of metal nanoparticles decreases the activity of the catalyst due to the diffusion limitation and/or blocking of active sites and that requires extra steps to remove such molecules before the catalyst can be used.

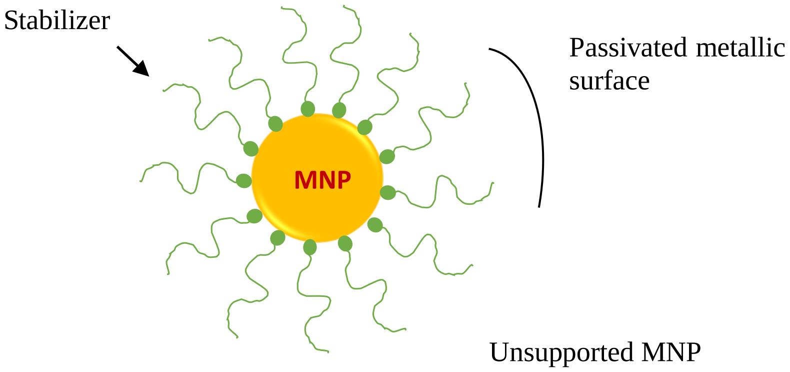

Fig. 1.3. Metal nanoparticle (MNP) with passivated metallic surface.

On the other hand, in many cases when metal nanoparticles are dispersed on the surface of support, they can be much more active and selective catalysts. For this, mesoporous silica SBA-15 offers many advantages as support material due to its unique properties such as uniform pore size distribution and large surface area. However, large particles formed on such porous material can be disadvantageous due to the pore size limitation which further cause pore-blocking effect. Large nanoparticles block the reactants or substrates to reach active sites which may be available inside porous channels resulting in the decrease in catalytic activity. Therefore, it is very important to develop effective methods for size- and shape-controlled syntheses of metal nanoparticle on porous material, since it can result in modulating their physical and chemical properties, and further affecting the catalytic performance of the catalyst.

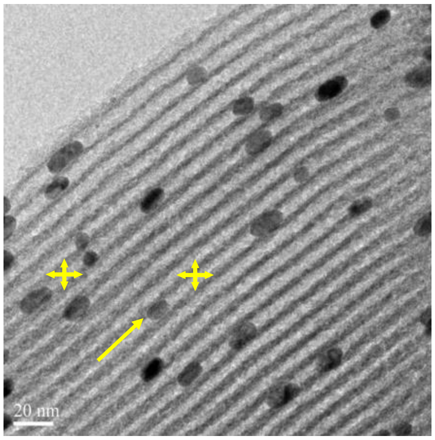

Fig. 1.4. Pore-blocking effect caused by large NPs inside mesoporous SBA-15.

In consideration of the present cases regarding MNPs in heterogeneous catalysis, (a) effective heterogeneous catalyst should be developed based on supported metal nanoparticles that can be efficiently used in various organic transformation, (b) methods for size- and shape-controlled syntheses of MNPs on porous material should be also developed in order to obtain particles with small and uniform size distribution, and minimize the pore-blocking effects, (c) the catalyst properties must be studied and investigated to better understand the characteristics and features of the catalysts, and (d) the activity and reusability of the catalyst should also be investigated to study their catalytic performance and in regard to the ease in handling and separation. In response to these demands, the main purposes of this thesis are:

1. Design heterogeneous catalysts based on supported MNPs (Au, Pd, Cu, Ru and Pt) on mesoporous silica SBA-15 by employing immobilized ionic liquids.
2. Control the particles size and shape by varying the concentration and feed rate of the reducing agent ($NaBH_4$).

3. Study the catalyst properties mainly based on TEM, XAFS, XPS, FTIR and XRD.
4. Investigate the activity and reusability of the catalysts in the reduction of *p*-nitrophenol and Suzuki-Miyaura coupling reaction.

In **Chapter 2**, the size-controlled nanoparticles on porous material were studied for AuNPs on mesoporus silica SBA-15 in the presence of immobilized ionic liquids. In order to control the nanoparticle size and shape, the concentration and feed rate of sodium borohydride were varied at room temperature (20 °C) under nitrogen flow. The resulting materials were characterized by TEM, XAFS, XPS, FTIR and XRD.

In **Chapter 3**, size-dependence of AuNPs was investigated for *p*-nitrophenol hydrogenation reaction. Various AuNPs with different size and morphology were compared and the reusability of the catalyst was tested. Moreover, the effect of recycle process in the size of Au nanoparticle was also investigated.

In **Chapter 4**, the synthetic approach studied in Chapter 2 was applied to prepare various supported MNPs (Pd, Au, Cu, Ru and Pt) on SBA-15. Two different ionic liquids were immobilized on SBA-15 for the synthesis of palladium nanoparticles (PdNPs_me-Im@SBA-15 and PdNPs_bu-Im@SBA-15). The resulting materials were characterized by TEM, XAFS, FTIR, XPS, solid state NMR, and N_2 adsorption-desorption isotherm. Moreover, the catalytic performance and reusability were investigated in the reduction of *p*-nitrophenol.

In **Chapter 5**, room temperature Suzuki-Miyaura coupling reaction catalysed PdNPs(2.4 nm) was investigated. The coupling reaction between aryl halides and phenylboronic acid in aqueous solution was studied and the reusability of the catalyst was investigated.

Finally in **Chapter 6**, all the results obtained in this thesis are summarized and the outlook is presented.

The originality of this work is the development of synthetic strategy in controlling the size and shape of supported MNPs on porous support. Size-controlled syntheses and growth mechanism of MNPs have been studied and most of the approaches are limited in colloidal system and only few have been reported on solid supports. On the other hand, supported MNPs on porous materials have been developed in the presence of immobilized stabilizer such as IL, polymer or any other organic molecule for heterogeneous catalysis, however none have attempted to study the size-controlled growth and discuss how the growth kinetics affects the size/shape evolution. In this work, the development of size-controlled synthetic method of supported MNPs on porous material was studied for AuNPs on mesoporous silica SBA-5 in the presence of immobilized IL by varying the concentration and feed rate of the reducing agent ($NaBH_4$) in order to obtain small particles with uniform size distribution inside pores. The morphology and structural property were studied and the catalytic performances were examined.

1.4. References

(1) Swihart, M. T. Vapor-Phase Synthesis of Nanoparticles. *Curr. Opin. Colloid. interface Sci.* **2003**, *8*, 127–133.

(2) Cao, A.; Lu, R.; Veser, G. Stabilizing Metal Nanoparticles for Heterogeneous Catalysis. *Phys. Chem. Chem. Phys.* **2010**, *12* (41), 13499.

(3) Ferrando, R.; Jellinek, J.; Johnston, R. L. Nanoalloys: From Theory to Applications of Alloy Clusters and Nanoparticles. *Chem. Rev.* **2008**, *108* (3), 845–910.

(4) Baletto, F.; Ferrando, R. Structural Properties of Nanoclusters: Energetic, Thermodynamic, and Kinetic Effects. *Rev. Mod. Phys.* **2005**, *77* (1), 371–423.

(5) Johnston, R. L. Atomic and Molecular Clusters. *Physics (College. Park. Md).* **2002**, 256.

(6) Lue, J. T. A Review of Characterization and Physical Property Studies of Metallic Nanoparticles. *J. Phys. Chem. Solids* **2001**, *62* (9–10), 1599–1612.

(7) Tao, A. R.; Habas, S.; Yang, P. Shape Control of Colloidal Metal Nanocrystals. *Small* **2008**, *4* (3), 310–325.

(8) Moon, H. R.; Lim, D.-W.; Suh, M. P. Fabrication of Metal Nanoparticles in Metal–organic Frameworks. *Chem. Soc. Rev.* **2013**, *42* (4), 1807–1824.

(9) Roucoux, A.; Schulz, J.; Patin, H. Reduced Transition Metal Colloids: A Novel Family of Reusable Catalysts? *Chem. Rev.* **2002**, *102* (10), 3757–3778.

(10) Wu, L.; Zhang, Y.; Ji, Y. Homogeneous Recyclable Catalysts Based on Metal Nanoparticles for Organic Synthesis. **2013**, 1288–1302.

(11) Park, J.; Joo, J.; Soon, G. K.; Jang, Y.; Hyeon, T. Synthesis of Monodisperse Spherical Nanocrystals. *Angew. Chem. Int. Ed.* **2007**, *46* (25), 4630–4660.

(12) Faraday, M. The Bakerian Lecture: Experimental Relations of Gold (and Other Metals) to

Light. *Philos. Trans. R. Soc. London* **1857**, *147*, 145–181.

(13) Ostwald, W. On the Assumed Isomerism of Red and Yellow Mercury Oxide and the Surface-Tension of Solid Bodies. *Zeitschrift Fur Phys. Chemie--Stochiometrie Und Verwandtschaftslehre* **1900**, *34* (4), 495–503.

(14) Polte, J. Fundamental Growth Principles of Colloidal Metal Nanoparticles - a New Perspective. *CrystEngComm* **2015**, *17* (36), 6809–6830.

(15) Becker, D.; Doring, W. Kinetic Treatment of the Nucleation in Supersaturated Vapors. *Ann. Phys.* **1935**, *24*, 719–752.

(16) La Mer, V. K.; Dinegar, R. H. Theory, Production, and Mechanism of Formation of Monodispersed Hydrosols. *J. Am. Chem. Soc.* **1950**, *72*, 4847–4854.

(17) LaMer, V. K. Kinetics in Phase Transitions. *J. Ind. Eng. Chem.* **1952**, *44*, 1270–1277.

(18) Reiss, H. The Growth of Uniform Colloidal Dispersions. *J. Chem. Phys.* **1951**, *19* (4), 482–487.

(19) Sugimoto, T. Preparation of Monodispersed Colloidal Particles. *Adv. Colloid Interface Sci.* **1987**, *28*, 65–108.

(20) Privman, V. Mechanisms of Diffusional Nucleation of Nanocrystals and Their Self-Assembly into Uniform Colloids. *Ann. N. Y. Acad. Sci.* **2009**, *1161*, 508–525.

(21) Polte, J.; Erler, R.; Thünemann, A. F.; Sokolov, S.; Ahner, T. T.; Rademann, K.; Emmerling, F.; Kraehnert, R. Nucleation and Growth of Gold Nanoparticles Studied via in Situ Small Angle X-Ray Scattering at Millisecond Time Resolution. *ACS Nano* **2010**, *4* (2), 1076–1082.

(22) Polte, J.; Ahner, T. T.; Delissen, F.; Sokolov, S.; Emmerling, F.; Thünemann, A. F.; Kraehnert, R. Mechanism of Gold Nanoparticle Formation in the Classical Citrate

Synthesis Method Derived from Coupled in Situ XANES and SAXS Evaluation. *J. Am. Chem. Soc.* **2010**, *132* (4), 1296–1301.

(23) Wuithschick, M.; Witte, S.; Kettemann, F.; Rademann, K.; Polte, J. Illustrating the Formation of Metal Nanoparticles with a Growth Concept Based on Colloidal Stability. *Phys. Chem. Chem. Phys.* **2015**, *17*, 19895–19900.

(24) Turkevich, J.; Stevenson, P. C.; Hillier, J. A Study of the Nucleation and Growth Processes in the Synthesis of Colloidal Gold. *Discuss. Faraday Soc.* **1951**, *11* (c), 55–75.

(25) Kimling, J.; Maier, M.; Okenve, B.; Kotaidis, V.; Ballot, H.; Plech, A. Turkevich Method for Gold Nanoparticle Synthesis Revisited. *J. Phys. Chem. B* **2006**, *110* (32), 15700–15707.

(26) Welton, T. Ionic Liquids in Catalysis. *Coord. Chem. Rev.* **2004**, *248* (21–24), 2459–2477.

(27) Zhao, D.; Wu, M.; Kou, Y.; Min, E. Ionic Liquids: Applications in Catalysis. *Catal. Today* **2002**, *74* (1–2), 157–189.

(28) Olivier-Bourbigou, H.; Magna, L. Ionic Liquids: Perspectives for Organic and Catalytic Reactions. *J. Mol. Catal. A Chem.* **2002**, *182–183*, 419–437.

(29) Krossing, I.; Slattery, J. M.; Daguenet, C.; Dyson, P. J.; Oleinikova, A.; Weingärtner, H. Why Are Ionic Liquids Liquid? A Simple Explanation Based on Lattice and Solvation Energies. *J. Am. Chem. Soc.* **2006**, *128* (41), 13427–13434.

(30) Consorti, C. S.; Suarez, P. A. Z.; De Souza, R. F.; Burrow, R. A.; Farrar, D. H.; Lough, A. J.; Loh, W.; Da Suva, L. H. M.; Dupont, J. Identification of 1,3-DialkylimidazoIium Salt Supramolecular Aggregates in Solution. *J. Phys. Chem. B* **2005**, *109* (10), 4341–4349.

(31) Janiak, C. Ionic Liquids for the Synthesis and Stabilization of Metal Nanoparticles. *Zeitschrift fur Naturforsch. - Sect. B J. Chem. Sci.* **2013**, *68* (10), 1059–1089.

Introduction

(32) Bonnemann, H.; Richards, R. M. Nanoscopic Metal Particles - Synthetic Methods and Potential Applications. *Eur. J. Inorg. Chem.* **2001**, 2455–2480.

(33) Astruc, D.; Lu, F.; Aranzaes, J. R. Nanoparticles as Recyclable Catalysts: The Frontier between Homogeneous and Heterogeneous Catalysis. *Angew. Chem. Int. Ed.* **2005**, *44* (48), 7852–7872.

(34) Pan, C.; Pelzer, K.; Philippot, K.; Chaudret, B.; Dassenoy, F.; Lecante, P.; Casanove, M. J. Ligand-Stabilized Ruthenium Nanoparticles: Synthesis, Organization, and Dynamics. *J. Am. Chem. Soc.* **2001**, *123* (31), 7584–7593.

(35) Aiken, J. D.; Finke, R. G. Polyoxoanion- and Tetrabutylammonium-Stabilized Rh(0)(n) Nanoclusters: Unprecedented Nanocluster Catalytic Lifetime in Solution. *J. Am. Chem. Soc.* **1999**, *121* (38), 8803–8810.

(36) mer, J.; Redel, E.; Thomann, R.; Janiak, C. Use of Ionic Liquids for the Synthesis of Iron, Ruthenium, and Osmium Nanoparticles from Their Metal Carbonyl Precursors. *Organometallics* **2008**, *27* (9), 1976–1978.

(37) Editor, G.; Endres, F.; Lee, J. M.; Palgunadi, J.; Kim, J. H.; Jung, S.; Choi, Y.; Cheong, M.; Kim, H. S.; Abbott, A. P.; et al. Ionicity in Ionic Liquids: Correlation with Ionic Structure and Physicochemical Properties. *Phys. Chem. Chem. Phys.* **2010**, *12* (8), 1648.

(38) Tsunoyama, H.; Sakurai, H.; Negishi, Y.; Tsukuda, T. Size-Specific Catalytic Activity of Polymer-Stabilized Gold Nanoclusters for Aerobic Alcohol Oxidation in Water. *J. Am. Chem. Soc.* **2005**, *127* (26), 9374–9375.

(39) Lo, T.; Yu, C.; Liu, Y.; Yang, K.; Chen, Q. Size-Controllable Synthesis of Catalyst of Gold Nanoparticles Supported on TiO_2 by Using Sonoelectrochemical Methods. *Mater. Res. Bull.* **2013**, *48* (2), 920–922.

(40) Briñas, R. P.; Hu, M.; Qian, L.; Lymar, E. S.; Hainfeld, J. F. Gold Nanoparticle Size Controlled by Polymeric Au(I) Thiolate Precursor Size. *J. Am. Chem. Soc.* **2008**, *130* (3), 975–982.

(41) Zanella, R.; Sandoval, A.; Santiago, P.; Basiuk, V. A.; Saniger, J. M. New Preparation Method of Gold Nanoparticles on SiO_2. *J. Phys. Chem. B* **2006**, *110* (17), 8559–8565.

(42) Petkov, N.; Stock, N.; Bein, T. Gold Electroless Reduction in Nanosized Channels of Thiol-Modified SBA-15 Material. *J. Phys. Chem. B* **2005**, *109* (21), 10737–10743.

(43) Frens, G. Controlled Nucleation for the Regulation of the Particle Size in Monodisperse Gold Suspensions. *Nat. Phys. Sci.* **1973**, *241* (105), 20–22.

(44) Ji, X.; Song, X.; Li, J.; Bai, Y.; Yang, W. Size Control of Gold Nanocrystals in Citrate Reduction : The Third Role of Citrate. *J. Am. Chem. Soc.* **2007**, *129* (45), 1957–1962.

(45) Shervani, Z.; Yamamoto, Y. Carbohydrate-Directed Synthesis of Silver and Gold Nanoparticles: Effect of the Structure of Carbohydrates and Reducing Agents on the Size and Morphology of the Composites. *Carbohydr. Res.* **2011**, *346* (5), 651–658.

(46) Deraedt, C.; Salmon, L.; Gatard, S.; Ciganda, R.; Hernandez, R.; Ruiz, J.; Astruc, D. Sodium Borohydride Stabilizes Very Active Gold Nanoparticle Catalysts. *Chem. Commun.* **2014**, *50* (91), 14194–14196.

(47) Li, Z.; Gu, L. Effects of Mass Ratio, PH, Temperature, and Reaction Time on Fabrication of Partially Purified Pomegranate Ellagitannin-Gelatin Nanoparticles. *J. Agric. Food Chem.* **2011**, *59* (8), 4225–4231.

(48) Islam, A. K. M. M.; Mukherjee, M. Effect of Temperature in Synthesis of Silver Nanoparticles in Triblock Copolymer Micellar Solution. *J. Exp. Nanosci.* **2011**, *6* (6), 596–611.

(49) Zhang, P.; Sham, T. K. Tuning the Electronic Behavior of Au Nanoparticles with Capping Molecules. *Appl. Phys. Lett.* **2002**, *81* (4), 736–738.

(50) Lopez-Cartes, C.; Rojas, T. C.; Litran, R.; Fuente, J. M. De; Penads, S.; Fernndez, A.; Martinez-Martines, D. Gold Nanoparticles with Different Capping Systems: An Electronic and Structural XAS Analysis. *J. Phys. Chem. B* **2005**, *109,* 8761–8766.

(51) Deng, J. P.; Shih, W. C.; Mou, C. Y. Electron Transfer-Induced Hydrogenation of Anthracene Catalyzed by Gold and Silver Nanoparticles. *J. Phys. Chem. C* **2007**, *111* (27), 9723–9728.

(52) Kim, C.; Lee, H. Change in the Catalytic Reactivity of Pt Nanocubes in the Presence of Different Surface-Capping Agents. *Catal. Commun.* **2009**, *10* (9), 1305–1309.

(53) Park, J. Y.; Aliaga, C.; Renzas, J. R.; Lee, H.; Somorjai, G. A. The Role of Organic Capping Layers of Platinum Nanoparticles in Catalytic Activity of CO Oxidation. *Catal. Lett.* **2009**, *129* (1–2), 1–6.

(54) Choi, B. G.; Park, H. S. Controlling Size, Amount, and Crystalline Structure of Nanoparticles Deposited on Graphenes for Highly Efficient Energy Conversion and Storage. *ChemSusChem* **2012**, *5* (4), 709–715.

(55) Zhao, D.; Feng, J.; Huo, Q.; Melosh, N.; Fredrickson, G. H.; Chmelka, B. F.; Stucky, G. D. Triblock Copolymer Syntheses of Mesoporous Silica with Periodic 50 to 300 Angstrom Pores. *Science.* **1998**, *279* (5350), 548–552.

(56) Zhao, D.; Huo, Q.; Feng, J.; Chmelka, B. F.; Stucky, G. D. Tri-, Tetra-, and Octablock Copolymer and Nonionic Surfactant Syntheses of Highly Ordered, Hydrothermally Stable, Mesoporous Silica Structures. *J. Am. Chem. Soc.* **1998**, *120* (24), 6024–6036.

(57) Shin, H. J.; Ryoo, R.; Kruk, M.; Jaroniec, M. Modification of SBA-15 Pore Connectivity

by High-Temperature Calcination Investigated by Carbon Inverse Replication. *Chem. Commun.* **2001**, *1* (4), 349–350.

(58) Osada, Y.; Okuzaki, H.; Hori, H. Ordered Mesoporous Molecular Sieves Synthesized by a Liquid-Crystal Template Mechanism. *Nature* **1992**, *355* (6357), 242–244.

(59) Kruk, M.; Jaroniec, M.; Ko, C. H.; Ryoo, R. Characterization of the Porous Structure of SBA-15. *Chem. Mater.* **2000**, *12* (7), 1961–1968.

(60) Ryoo, R.; Ko, C. H.; Kruk, M.; Antochshuk, V.; Jaroniec, M. Block-Copolymer-Templated Ordered Mesoporous Silica: Array of Uniform Mesopores or Mesopore−Micropore Network? *J. Phys. Chem. B* **2000**, *104* (48), 11465–11471.

(61) Lukens, W. W.; Schmidt-Winkel, P.; Zhao, D.; Feng, J.; Stucky, G. D. Evaluating Pore Sizes in Mesoporous Materials: A Simplified Standard Adsorption Method and a Simplified Broekhoff-de Boer Method. *Langmuir* **1999**, *15* (16), 5403–5409.

(62) Yue, Y.-H.; Gédéon, A.; Bonardet, J.-L.; D'Espinose, J. B.; Melosh, N.; Fraissard, J. Direct Incorporation of Al in SBA Mesoporous Materials: Characterization, Stability and Catalytic Activity. *Stud. Surf. Sci. Catal.* **2000**, *129*, 209–218.

(63) Miyazawa, K.; Inagaki, S. Control of the Microporosity within the Pore Walls of Ordered Mesoporous Silica SBA-15. *Chem. Commun.* **2000**, *21*, 2121–2122.

(64) Imperor-Clerc, M.; Davidson, P.; Davidson, A. Existence of a Microporous Corona around the Mesopores of Silica-Based SBA-15 Materials Templated by Triblock Copolymers. *J. Am. Chem. Soc.* **2000**, *122* (48), 11925–11933.

(65) Morey, M. S.; O'Brien, S.; Schwarz, S.; Stucky, G. D. Hydrothermal and Postsynthesis Surface Modification of Cubic, MCM-48, and Ultralarge Pore SBA-15 Mesoporous Silica with Titanium. *Chem. Mater.* **2000**, *12* (4), 898–911.

(66) Galarneau, A.; Cambon, H.; Di Renzo, F.; Ryoo, R.; Choi, M.; Fajula, F. Microporosity and Connections between Pores in SBA-15 Mesostructured Silicas as a Function of the Temperature of Synthesis. *New J. Chem.* **2003**, *27* (1), 73–79.

(67) Choi, M.; Heo, W.; Kleitz, F.; Ryoo, R. Facile Synthesis of High Quality Mesoporous SBA-15 with Enhanced Control of the Porous Network Connectivity and Wall Thickness. *Chem. Commun. (Camb).* **2003**, *75* (12), 1340–1341.

(68) Cao, A.; Veser, G. Exceptional High-Temperature Stability through Distillation-like Self-Stabilization in Bimetallic Nanoparticles. *Nat. Mater.* **2010**, *9* (1), 75–81.

(69) Campbell, C. T.; Parker, S. C.; Starr, D. E. The Effect of Size-Dependent Nanoparticle Energetics on Catalyst Sintering. *Science* **2002**, *298* (5594), 811–814.

(70) Nafria, R.; Ramirez de la Piscina, P.; Homs, N.; Ramon Morante, J.; Cabot, A.; Diaz, U.; Corma, A. Embedding Catalytic Nanoparticles inside Mesoporous Structures with Controlled Porosity: Au@TiO_2. *J. Mater. Chem. A* **2013**, *1*, 14170–14176.

(71) Miah, A. T.; Malakar, B.; Saikia, P. Gold over Ceria-Titania Mixed Oxides: Solar Light Induced Catalytic Activity for Nitrophenol Reduction. *Catal. Lett.* **2016**, *146* (2), 291–303.

(72) Yang, H.; Deng, J.; Liu, Y.; Xie, S.; Wu, Z.; Dai, H. Preparation and Catalytic Performance of Ag, Au, Pd or Pt Nanoparticles Supported on 3DOM CeO_2-Al_2O_3 for Toluene Oxidation. *J. Mol. Catal. A Chem.* **2016**, *414*, 9–18.

(73) Jiang, K.; Zhang, H.-X.; Yang, Y.-Y.; Mothes, R.; Lang, H.; Cai, W.-B. Facile Synthesis of Ag@Pd Satellites–Fe_3O_4 Core Nanocomposites as Efficient and Reusable Hydrogenation Catalysts. *Chem. Commun.* **2011**, *47* (43), 11924.

(74) Nasrollahzadeh, M.; Sajadi, S. M.; Rostami-Vartooni, A.; Bagherzadeh, M. Green Synthesis of Pd/CuO Nanoparticles by Theobroma Cacao L. Seeds Extract and Their

Catalytic Performance for the Reduction of 4-Nitrophenol and Phosphine-Free Heck Coupling Reaction under Aerobic Conditions. *J. Colloid Interface Sci.* **2015**, *448*, 106–113.

(75) Jin, Z.; Liu, C.; Qi, K.; Cui, X. Photo-Reduced Cu/CuO Nanoclusters on TiO_2 Nanotube Arrays as Highly Efficient and Reusable Catalyst. *Nat. Sci. Reports* **2017**, *7* (39695), 1–9.

(76) Wu, H.; Pantaleo, G.; Venezia, A.; Liotta, L. Mesoporous Silica Based Gold Catalysts: Novel Synthesis and Application in Catalytic Oxidation of CO and Volatile Organic Compounds (VOCs). *Catalysts* **2013**, *3* (4), 774–793.

(77) Okumura, M.; Nakamura, S.; Tsubota, S.; Nakamura, T.; Azuma, M.; Haruta, M. Chemical Vapor Deposition of Gold on Al_2O_3, SiO_2, and TiO_2 for the Oxidation of CO and of H_2. *Chem. Lett.* **1998**, *51*, 53–58.

(78) Yang, C. M.; Liu, P. H.; Ho, Y. F.; Chiu, C. Y.; Chao, K. J. Highly Dispersed Metal Nanoparticles in Functionalized SBA-15. *Chem. Mater.* **2003**, *15* (1), 275–280.

(79) Sareen, S.; Mutreja, V.; Singh, S.; Pal, B. Highly Dispersed Au, Ag and Cu Nanoparticles in Mesoporous SBA-15 for Highly Selective Catalytic Reduction of Nitroaromatics. *RSC Adv.* **2015**, *5* (1), 184–190.

(80) El-Sheikh, S. M.; Ismail, A. A.; Al-Sharab, J. F. Catalytic Reduction of *p*-Nitrophenol over Precious Metals/Highly Ordered Mesoporous Silica. *New J. Chem.* **2013**, *37* (8), 2399–2407.

(81) Hao, Y.; Chong, Y.; Li, S.; Yang, H. Controlled Synthesis of Au Nanoparticles in the Nanocages of SBA-16: Improved Activity and Enhanced Recyclability for the Oxidative Esterification of Alcohols. *J. Phys. Chem. C* **2012**, *116* (11), 6512–6519.

(82) Veisi, H.; Amini Manesh, A.; Eivazi, N.; Faraji, A. R. Palladium Nanoparticles Supported

on 1,3-Dicyclohexylguanidine Functionalized Mesoporous Silica SBA-15 as Highly Active and Reusable Catalyst for the Suzuki–Miyaura Cross-Coupling Reaction. *RSC Adv.* **2015**, *5* (26), 20098–20107.

(83) Liu, P. H.; Chang, Y. P.; Phan, T. H.; Chao, K. J. The Morphology and Size of Nanostructured Au in Au/SBA-15 Affected by Preparation Conditions. *Mater. Sci. Eng. C* **2006**, *26* (5–7), 1017–1022.

(84) Beck, A.; Horváth, A.; Stefler, G.; Katona, R.; Geszti, O.; Tolnai, G.; Liotta, L. F.; Guczi, L. Formation and Structure of Au/TiO_2 and Au/CeO_2 Nanostructures in Mesoporous SBA-15. *Catal. Today* **2008**, *139* (3), 180–187.

(85) Ma, X.; Zhou, Y.; Zhang, J.; Zhu, A.; Jiang, T.; Han, B. Solvent-Free Heck Reaction Catalyzed by a Recyclable Pd Catalyst Supported on SBA-15 via an Ionic Liquid. *Green Chem.* **2008**, *10* (1), 59–66.

(86) Han, P.; Zhang, H.; Qiu, X.; Ji, X.; Gao, L. Palladium within Ionic Liquid Functionalized Mesoporous Silica SBA-15 and Its Catalytic Application in Room-Temperature Suzuki Coupling Reaction. *J. Mol. Catal. A Chem.* **2008**, *295* (1–2), 57–67.

(87) Fattori, N.; Maroneze, C. M.; Da Costa, L. P.; Strauss, M.; Sigoli, F. A.; Mazali, I. O.; Gushikem, Y. Ion-Exchange Properties of Imidazolium-Grafted SBA-15 toward $AuCl_4^-$ Anions and Their Conversion into Supported Gold Nanoparticles. *Langmuir* **2012**, *28* (27), 10281–10288.

(88) Damasceno, J. P. V.; Maroneze, C. M.; Strauss, M.; Sigoli, F. A.; Mazali, I. O. Preparation of Supported AuPd Nanoalloys Mediated by Ionic Liquid-like Functionalized SBA-15: Structural Correlations Concerning Its Catalytic Activity. *New J. Chem.* **2016**, *40* (8), 6636–6642.

(89) DeCastro, C.; Sauvage, E.; Valkenberg, M. H.; Hölderich, W. F. Immobilised Ionic Liquids as Lewis Acid Catalysts for the Alkylation of Aromatic Compounds with Dodecene. *J. Catal.* **2000**, *196* (1), 86–94.

(90) Valkenberg, M. H.; DeCastro, C.; Hölderich, W. F. Friedel-Crafts Acylation of Aromatics Catalysed by Supported Ionic Liquids. *Appl. Catal. A Gen.* **2001**, *215* (1–2), 185–190.

(91) Valkenberg, M. H.; deCastro, C.; Hölderich, W. F. Immobilisation of Ionic Liquids on Solid Supports. *Green Chem.* **2002**, *4* (2), 88–93.

(92) Sasaki, T.; Zhong, C.; Tada, M.; Iwasawa, Y. Immobilized Metal Ion-Containing Ionic Liquids: Preparation, Structure and Catalytic Performance in Kharasch Addition Reaction. *Chem. Commun.* **2005**, 2506–2508.

(93) Zhong, C.; Sasaki, T.; Tada, M.; Iwasawa, Y. Ni Ion-Containing Ionic Liquid Salt and Ni Ion-Containing Immobilized Ionic Liquid on Silica: Application to Suzuki Cross-Coupling Reactions between Chloroarenes and Arylboronic Acids. *J. Catal.* **2006**, *242* (2), 357–364.

(94) Sasaki, T.; Tada, M.; Zhong, C.; Kume, T.; Iwasawa, Y. Immobilized Metal Ion-Containing Ionic Liquids: Preparation, Structure and Catalytic Performances in Kharasch Addition Reaction and Suzuki Cross-Coupling Reactions. *J. Mol. Catal. A Chem.* **2008**, *279* (2), 200–209.

(95) Khedkar, M. V; Sasaki, T.; Bhanage, B. M. Efficient, Recyclable and Phosphine-Free Carbonylative Suzuki Coupling Reaction Using Immobilized Palladium Ion-Containing Ionic Liquid: Synthesis of Aryl Ketones and Heteroaryl Ketones. *RSC Adv.* **2013**, *3* (21), 7791–7797.

(96) Patil, N. M.; Sasaki, T.; Bhanage, B. M. Chemoselective Transfer Hydrogenation of Alpha, Beta-Unsaturated Carbonyls Using Palladium Immobilized Ionic Liquid Catalyst. *Catal.*

Lett. **2014**, *144* (11), 1803–1809.

(97) Khedkar, M. V.; Shinde, A. R.; Sasaki, T.; Bhanage, B. M. Immobilized Palladium Metal Containing Ionic Liquid Catalyzed One Step Synthesis of Isoindole-1,3-Diones by Carbonylative Cyclization Reaction. *J. Mol. Catal. A Chem.* **2014**, *385*, 91–97.

(98) Patil, N. M.; Sasaki, T.; Bhanage, B. M. Immobilized Iron Metal-Containing Ionic Liquid-Catalyzed Chemoselective Transfer Hydrogenation of Nitroarenes into Anilines. *ACS Sustain. Chem. Eng.* **2016**, *4* (2), 429–436.

(99) Patil, N. M.; Sasaki, T.; Bhanage, B. M. Immobilized Ruthenium Metal-Containing Ionic Liquid-Catalyzed Dehydrogenation of Dimethylamine Borane Complex for the Reduction of Olefins and Nitroarenes. *RSC Adv.* **2016**, *6* (57), 52347–52352.

(100) Zhong, C.; Sasaki, T.; Jimbo-Kobayashi, A.; Fujiwara, E.; Kobayashi, A.; Tada, M.; Iwasawa, Y. Syntheses, Structures, and Properties of a Series of Metal Ion-Containing Dialkylimidazolium Ionic Liquids. *Bull. Chem. Soc. Jpn.* **2007**, *80* (12), 2365–2374.

(101) Gadge, S. T.; Kusumawati, E. N.; Harada, K.; Sasaki, T.; Nishio-Hamane, D.; Bhanage, B. M. Synthesis of Oxamate and Urea by Oxidative Single and Double Carbonylation of Amines Using Immobilized Palladium Metal-Containing Ionic Liquid@SBA-15. *J. Mol. Catal. A Chem.* **2015**, *400*, 170–178.

(102) Satapathy, A.; Gadge, S. T.; Kusumawati, E. N.; Harada, K.; Sasaki, T.; Nishio-Hamane, D.; Bhanage, B. M. Synthesis of Polyester Amide by Carbonylation-Polycondensation Reaction Using Immobilized Palladium Metal Containing Ionic Liquid on SBA-15 as a Phosphine-Free Catalytic System. *Catal. Lett.* **2015**, *145* (3), 824–833.

Chapter 2

Size-Controlled Gold Nanoparticles Prepared from Gold Ion-Containing Ionic Liquid on SBA-15

Abstract

A series of gold nanoparticles (AuNPs) with controlled size were prepared from immobilized gold-containing ionic liquid on SBA-15 (AuCl_me-Im@SBA-15) at room temperature. The size and shape of AuNPs could be controlled inside porous SBA-15 in the presence of immobilized 1-methyl-3-(3-trimethoxysilyl-propyl)-imidazolium chloride by controlling a concentration and feed rate of a reducing agent $NaBH_4$. The NPs were mainly observed inside porous channel of SBA-15. The average size of AuNPs decrease as the concentration of $NaBH_4$ increase from 1 mM to 100 mM. The smallest AuNPs with the average size of 1.6 nm was obtained at a fixed feed rate of 0.2 ml/min with 4 mM $NaBH_4$. Large particles with capsule-like shape were obtained at low feed rate of 0.04 ml/min. The all prepared AuNPs catalysts were characterized by TEM, XAFS, XPS, FTIR, and XRD.

2.1. Introduction

Gold nanoparticles (AuNPs) are one of the most promising materials as catalyst for various organic reactions.[1–4] Moreover, supported AuNPs catalysts have recently attracted tremendous attention due to their unique catalysis in selective hydrogenation of nitro-compounds.[5–7] Their catalytic activities strongly depend on the particle size and shape, morphologies, metal additives, nature of the supports, and the preparation methods.[8–10] In this study, mesoporous silica SBA-15 was selected as a support. SBA-15 is the most well-known mesoporous silica with well-ordered hexagonal structure from its family, Santa Barbara Amorphous (SBA) materials.[11] Compared to metal oxides or other materials, SBA-15 offers many advantages as support due to its high surface area, large pore size and uniform pore distribution. These properties allow it to be designed with more flexibility to meet the requirements for various applications. On the other hand, ionic liquids (ILs) or molten salts which are composed solely of ions, have versatile functionalities and when they are immobilized on solid support it is expected that some effects induced in catalysis. Our research group has reported successful immobilization of metal ion-containing ionic liquids salt and metal ion-containing ILs on silica Aerosil 300 and SBA-15 frameworks for various catalytic reactions.[12–18] In this study, AuCl containing immobilized IL on SBA-15 was prepared as a precursor for AuNPs catalysts.

The size of NPs is an important issue. For example, large NPs on porous materials would be an obstacle for substrate to reach active sites deeper into porous channel by blocking the pores. Therefore, small particles on porous support might be more favorable to optimize the catalytic performance. Moreover, in many cases catalytic activities of metal nanoparticles depend on particle size and shape.[19,20] Therefore, it is important to control these parameters.

NPs synthesis process contains the reduction of metal precursor with a reducing agent, such as sodium borohydride. It was reported that in order to obtain very small NPs below 2 nm in aqueous solution, synthetic protocols almost always use $NaBH_4$ as reducing agent.[21] Many approaches for controlling NPs size have been adopted by controlling the concentration ratio between reducing agent and metal precursor, pH of mixture solution, temperature, and the presence of stabilizing agent, such as polymer PVP (polyvinyl-pyrrolidone), PVA (polyvinyl alcohol), ionic liquids, surfactants and dendrimers.[22–26]

To manipulate size, shape and structure of NPs, one should understand the particle growth process. Privman described the nucleation and growth of NPs as a model consisting of two-steps: a burst nucleation step, followed by an aggregation of primary particles into micron-sized colloidal agglomerates.[27] Meanwhile, Polte and co-workers studied the metal colloidal growth by the reduction of AuNPs using $NaBH_4$. In those systems, the reduction process is much faster than the actual growth, and the growth mechanisms are always governed by coalescence.[21,28]

In this study, AuNPs size and shape were controlled by varying the concentration of $NaBH_4$ at different rate on SBA-15 in the presence of immobilized ionic liquid. It was found that small NPs with narrow size distribution were obtained at the feed rate of $NaBH_4$ 0.2 ml/min, whereas at the slowest feed rates 0.04 ml/min capsule-like NPs was observed. The metal precursor AuCl was immobilized on SBA-15 to form $AuCl_2^-$ species by reacting with Cl^-. These gold chloride complexes were reduced by $NaBH_4$ to obtain AuNPs and the growth mechanism was also discussed.

2.2. Experimental

All chemicals were used without further purification. Tetraethyl orthosilicate (TEOS, 95%) was used as silica source and was purchased from WAKO. Gold (I) chloride (AuCl, 98.5%) and amphiphilic triblock copolymer poly(ethylene oxide)-poly(propylene oxide)–poly(ethylene oxide) Pluronic P123 ($EO_{20}PO_{70}EO_{20}$, $M_{av} = 5800$) was purchased from Sigma-Aldrich. 1-Methylimidazole ($CH_3C_3H_3N_2$), and 3-trimethoxysilyl-propyl chloride ($C_6H_{15}ClO_3Si$), hydrogen tetrachloroaurate ($HAuCl_4{\cdot}4H_2O$, 99%), sodium borohydride ($NaBH_4$, 95%), sodium hydroxide (NaOH, 96.0%), hydrochloride acid (HCl, 35.0 - 37.0%), acetone (C_3H_6O, 99.0%), dehydrated toluene (C_7H_8, 99.5%), dichloromethane (CH_2Cl_2, 99.5%), acetonitrile (C_2H_3N, 99.5%), were purchased from WAKO.

2.2.1. Synthesis of SBA-15

SBA-15 was synthesized according to the procedure reported by Zhao *et al.*,[29] using Pluronic 123 triblock copolymer (P123) as structure-directing amphiphilic agent and TEOS as silica source. In a 250 ml pp (polypropylene) bottle, 4 g of P123 was first dissolved in the hydrochloride acid solution until a solution became clear and then TEOS was added drop-wise under stirring at room temperature. The chemical composition of the reaction mixture was 4 g P123:0.041 mol TEOS:0.24 mol HCl:6.67 mol H_2O. The mixture was then stirred to react at 35°C for 20 h followed by heating at 100°C for 48 h under static condition in polypropylene bottle. The mixture was filtered, washed with distilled water and dried at room temperature. As-synthesized SBA-15 was obtained after calcination, in which it was heated to 500 °C at a ramping rate of 1 ºC/min and kept at 500 °C for 6 hours in air.

2.2.2. Preparation of ionic liquid

Immobilized ionic liquid on mesoporous silica SBA-15 were prepared using 1-methyl-3-(3-trimethoxysilylpropyl)-imidazolium chloride (MTI). The procedure based on our group[12] was optimized in this study. In a typical reaction, the ionic liquid was prepared from 1-methyl-imidazole and 3-trimethoxysilylpropyl chloride, and the mixture was refluxed at 70°C under N_2 atmosphere for 48 h. The obtained molten salt then was kept in the refrigerator under N_2 atmosphere.

2.2.3. Immobilization of gold ion-containing ionic liquid on SBA-15

In a typical synthesis, 1 g of SBA-15 was reacted with 1.3 g of MTI in a separable flask with dehydrated toluene. The mixture was refluxed at 111 °C for 48 h under N_2 atmosphere. After separation and fully washed with dichloromethane, the obtained solid product after drying under reduced pressure was denoted as Imm_me-Im@SBA-15.[16,17]

The next step was the immobilization of AuCl on the functionalized SBA-15, Imm_me-Im@SBA-15. 40 mg of AuCl and 2 g of Imm_me-Im@SBA-15 in 250 ml of acetonitrile were refluxed at 82 °C for 24 h under N_2 atmosphere in a separable flask. After filtration, fully washed with acetone, the solid was dried under reduced pressure. The white powder material was denoted as AuCl_me-Im@SBA-15.

2.2.4. Synthesis of AuNPs_me-Im@SBA-15

In a typical reduction process, 0.1 g of AuCl_me-Im@SBA-15 in 10 ml distilled water was reduced by 10 ml of $NaBH_4$ solution under stirring using an automatic syringe pump with a controlled feed rate. The effects of reducing agent concentration ($NaBH_4$) were studied by varying the molar concentration (x) of $NaBH_4$ solution from 1 mM to 100 mM at a constant feed rate of 1.6 ml/min. On the other hand, the concentration of $NaBH_4$ was fixed to 4 mM to study the effect of feed rate (y) which varied from 0.04 ml/min to 1.6 ml/min. The reduction was conducted at room temperature under N_2 flow. The pinkish solid was separated from the mixture by filtration and fully washed with distilled water. Finally, the solid product was then dried at reduced pressure overnight. The resulting materials were denoted according to their size, such as AuNPs(1.6 nm)_me-Im@SBA-15 as determined by TEM observations.

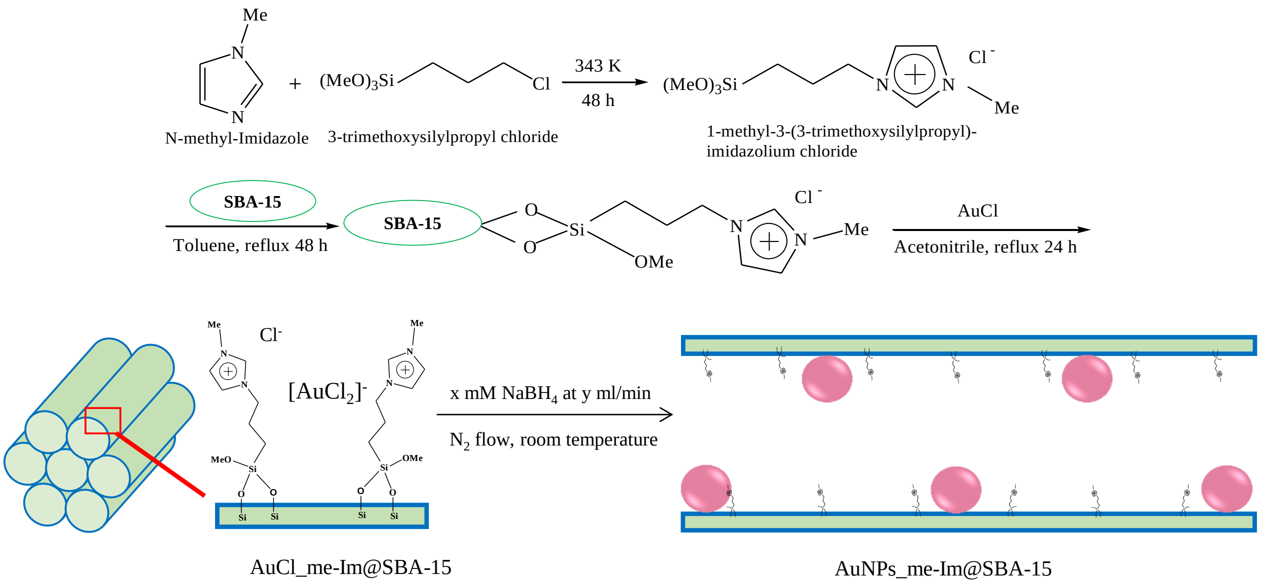

Scheme 2.1. Preparation steps for the syntheses of AuNPs_me-Im@SBA-15.

2.2.5. Synthesis of Au/SBA-15

Au supported on as-prepared SBA-15 denoted as Au/SBA-15 was synthesized as a reference catalyst according to C.Y. Ma *et al.*[30] via impregnation method with modification as described below. 4 mg of $HAuCl_4 \cdot 4H_2O$ was dissolved in 0.25 ml distilled water followed by the addition of 0.5 M NaOH to adjust the pH of solution. Then 0.2 g of SBA-15 was added into the solution and the mixture was kept under stirring for 12 h under N_2 atmosphere at room temperature. After drying at 70 °C for 5 h, the wet powder was calcined at 200 °C for 2 h.

2.2.6. Catalyst characterization

TEM images were observed on JEOL JEM-2100 operating at 200 kV, used to obtain bright field images for all catalysts, at The Institute for Solid State Physics (ISSP), The University of Tokyo. Low angle XRD patterns were recorded on Rigaku X-ray powder diffractometer (Smart Lab) with two Ge (220) crystals monochromator, at ISSP, using Cu Kα (λ = 1.54059 Å) as radiation source (40 kV, 30 mA) in the 2θ ranges from 0.5º to 8º. FTIR spectra of all samples in the frequency region (400-4000 cm^{-1}) were recorded at room temperature using JEOL SPX60 (KBr tablets) with a resolution of 4 cm^{-1}. X-ray photoelectron spectroscopy (XPS) measurements were conducted using PHI5000 Versa Probe with a monochromatic focused (100 μm ×100 μm) Al Kα X-ray radiation (15 kV, 30 mA) and dual beam neutralization using a combination of Argon ion gun and electron irradiation. The powder samples were placed on carbon tape with ~1 mm thickness on sample holder before transferred to the measuring chamber. The type of gold species is estimated by comparing the binding energy value obtained from experiment with data from NIST X-ray Photoelectron Spectroscopy Database. Measurements of X-ray absorption fine structure (XAFS) at the Au L_3-edge were carried out at the Photon Factory in the Institute of Materials Structure Science, High Energy Accelerator Research Organization (KEK-MSS-PF). The measurements were made in a fluorescence mode at BL-9C and BL-12C at room temperature. The XAFS raw data were analyzed by Athena and Artemis.

2.3. Results and discussion

2.3.1. Transmission electron microscopy (TEM)

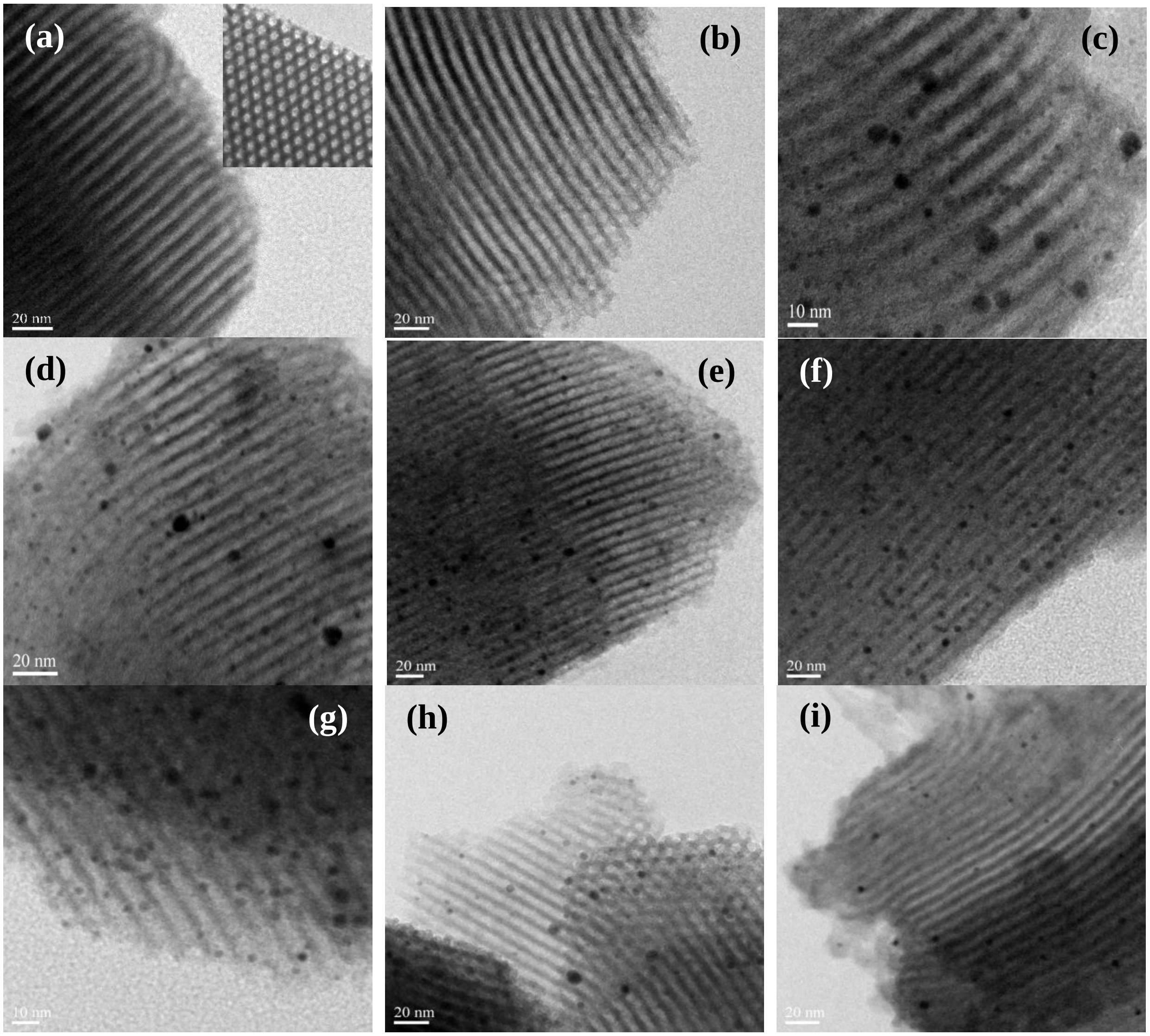

Fig. 2.1. TEM images of (a) SBA15, (b) AuCl_me-Im@SBA-15, (c-i) AuNPs_me-Im@SBA-15 reduced by different $NaBH_4$ concentration of 1, 4, 8, 10, 20, 50 and 100 mM at a constant feed rate of 1.6 ml/min.

TEM observations were used to study the effects of different concentration and feed rate of $NaBH_4$ solutions on the size distribution of AuNPs. Fig. 2.1a and b show TEM images for the as-prepared SBA-15 and AuCl_me-Im@SBA-15, respectively. Both images only show porous structures, indicating that no particles of $AuCl_x$ species were found on the internal or external surfaces of SBA-15. This suggested that $AuCl_x$ species were uniformly distributed in me-Im@SBA-15. However, after the reduction corresponding to Fig. 2.1 c-i, AuNPs were clearly observed mainly inside porous channels of SBA-15. The figures show different size of AuNPs inside porous SBA-15 by controlling the $NaBH_4$ concentration in the reduction process. It is noticed that large NPs were minimized by increasing the concentration of $NaBH_4$ resulting in the decrease of NPs size as shown from Fig. 2.1c to Fig. 2.1i.

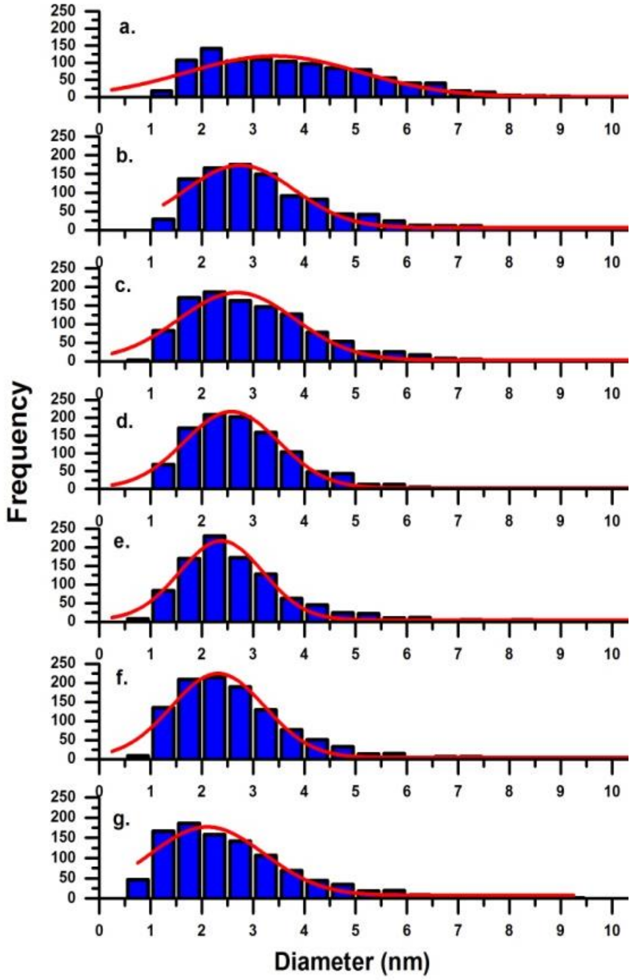

Fig.2.2. Size distribution histograms of AuNPs prepared by different $NaBH_4$ concentrations.

Table 2.1. Average size of AuNPs reduced by different concentration of $NaBH_4$ at 1.6 ml/min.

Sample	**$NaBH_4$ (mM)**	**NPs size (nm)**	**FWHM (nm)**
a.	1	3.4 ± 1.7	4.0
b.	4	2.7 ± 1.1	2.4
c.	8	2.6 ± 1.1	2.6
d.	10	2.6 ± 1.0	2.2
e.	20	2.4 ± 0.8	2.0
f.	50	2.3 ± 0.9	2.1
g.	100	2.1 ± 1.1	2.6

FWHM is full width at half maximum

Size-Controlled Gold Nanoparticles on SBA-15

AuNPs size distribution histograms and their average size distributions along with FWHM (full width at half maximum) are presented in Fig. 2.2 and Table 2.1. Each histogram was obtained by measuring particle size for more than 1000 particles from 45–50 TEM images taken for each condition. The diameter of NPs was analyzed by using imageJ developed by National Institute of Health (NIH). The diameter was manually measured for each NP to minimize the error caused by the background of the host material SBA-15. The number of large NPs decreased and that of small NPs increased as the concentration of $NaBH_4$ increased resulting in the decrease of average NPs size from 3.4 nm to 2.1 nm as shown in Fig. 5A. The pH value was monitored with different $NaBH_4$ concentrations. Increasing the concentration of $NaBH_4$ from 1 mM to 100 mM resulted in the increase of pH of mixture solution from 4.51 to 9.74.

At higher concentrations of $NaBH_4$ with increasing pH values, the Cl^- ions were replaced by OH^- ions to a larger extent. These results were confirmed from XPS analysis for Cl 2p region which shows the disappearances of both Cl $2p_{1/2}$ and Cl $2p_{3/2}$ peaks at higher $NaBH_4$ concentration (Fig. 2.10). Upon reducing $AuCl_x$ anions into AuNPs, OH^- anions became counter anions for the immobilized imidazolium cations. Excess OH^- anions may be adsorbed on AuNPs surfaces providing a protective layer. These adsorbed OH^- ions on the AuNPs surface prevent further agglomeration due to the electrostatic stabilization. Electrostatic stabilization is a process in which the particles are prevented from aggregating by adsorption of charged molecules (anionic) at the particle surface, providing a protective layer.[21,31] Moreover, high density of OH^- on the surface of AuNPs could increase the osmotic repulsive forces resulting in a narrow size distribution. The ionic liquid also has some important roles in the NPs growing process that will be discussed in the next section.

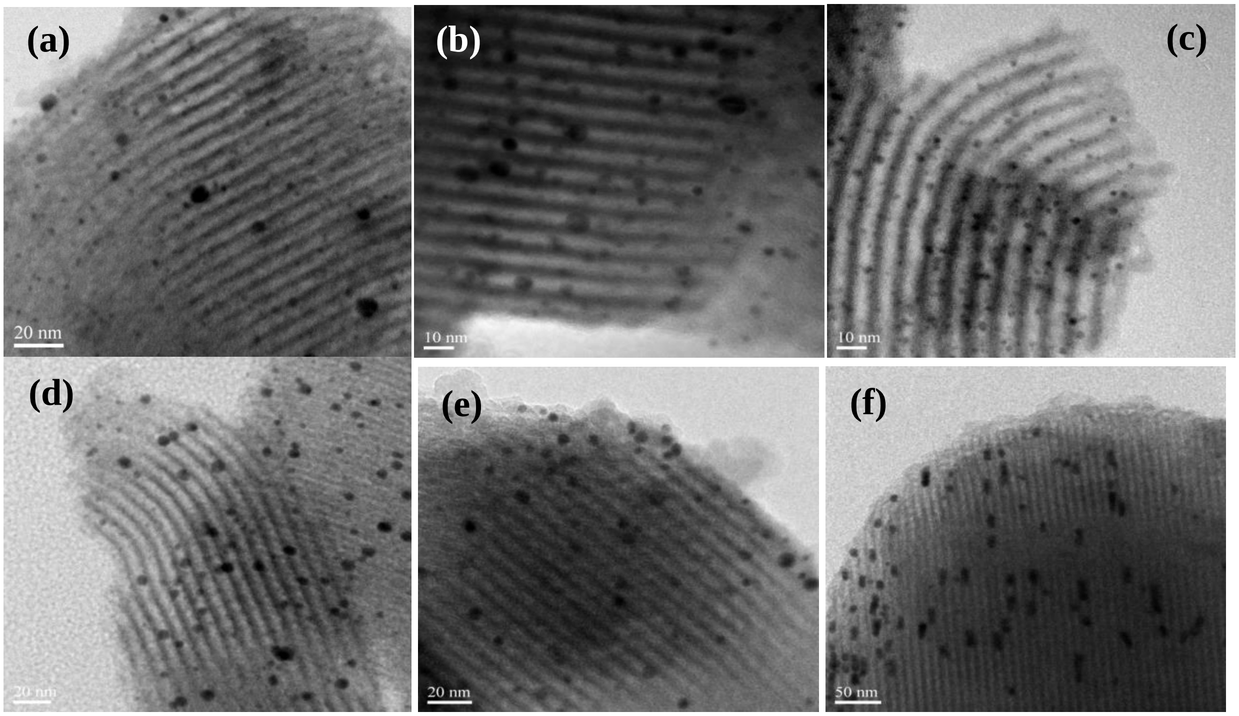

Fig. 2.3. TEM images of AuNPs_me-Im@SBA-15 reduced by 4 mM of $NaBH_4$ at different feed rate of (a) 1.6, (b) 0.4, (c) 0.2, (d) 0.1, (e) 0.06 and (f) 0.04 ml/min.

On the other hand, by slowing the feed rate from 1.6 into 0.2 ml/min with 4mM of $NaBH_4$, the average NPs size decreased from 2.7 nm to 1.6 nm (Fig. 2.5B). But further deceleration from 0.2 ml/min to 0.04 ml/min resulted in the increasing average NPs size from 1.6 nm to 2.7 nm. This trend might be due to the balance between the reduction and the growth rates of AuNPs in different conditions. The rate of the reduction process determines how fast the metal precursor ($AuCl_x$ anionic species) transformed to Au monomer and is proportional with the BH_4^- concentration in the system. The growth kinetics also includes the coalescence and agglomeration processes.

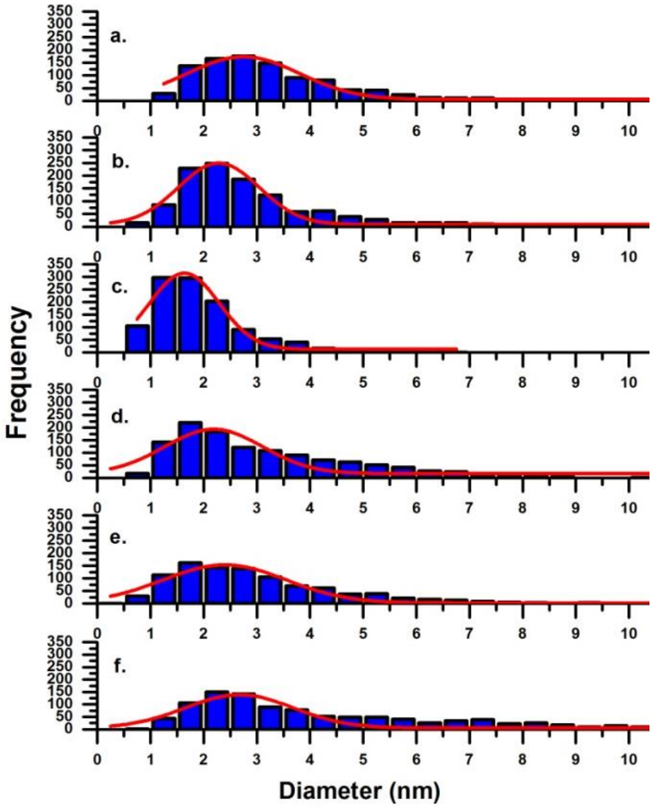

Fig. 2.4. Size distribution histograms of AuNPs prepared at different feed rate.

Table 2.2. Average size of AuNPs reduced by 4 mM of $NaBH_4$ at different feed rate.

Sample	Feed rate (ml/min)	NPs size (nm)	FWHM (nm)
a.	1.6	2.7 ± 1.1	2.4
b.	0.4	2.3 ± 0.8	1.8
c.	0.2	1.6 ± 0.6	1.5
d.	0.1	2.2 ± 0.9	2.2
e.	0.06	2.4 ± 1.2	2.7
f.	0.04	2.7 ± 1.0	2.4

FWHM is full width at half maximum

At fast feed rate of 1.6 ml/min, the reduction rate seems to be faster than the actual growth process. However, since the concentration of $NaBH_4$ in the system increased rapidly in short time, it caused higher diffusion rate of BH_4^- leading into higher nucleation rate. This causes higher monomer production rate, resulting in the existence of high amount of monomers in short time and hence faster coalescence and aggregation processes due to attractive interaction.

When the feed rate was adjusted to 0.2 ml/min, the size distribution was found to be the narrowest with the average size of 1.6 nm (Fig. 2.4 and Table 2.2). At this rate, the reduction rate seems to be proportional to the actual growth process. This suggests that electrostatic stabilization with a protective layer might be favorably operative, avoiding aggregation to larger NPs above 7 nm.

At slow feed rates of 0.06 and 0.04 ml/min, the reduction rate seems to be lower than the growth rate. As the concentration of $NaBH_4$ in the system increased very slowly, the monomer production rate became very low, whereas the coalescence and the aggregation processes took place as a function of time leading into the formation of larger NPs. In this region since the concentration of OH anion is low, the growth of a protective layer is also slow and the electrostatic stabilization is not favorably operative, thus the limitation of the NPs growth does not happen. Consequently, at very slow feed rate of 0.04 ml/min, large particles with capsule-like shape with the average size 2.7 nm could be observed from all observed NPs consisting of both spherical and capsule-like NPs as shown in Fig. 2.3f. These capsule-like NPs are the results of agglomeration of two or more spherical NPs and the aggregates size are limited by the pore size of SBA-15.

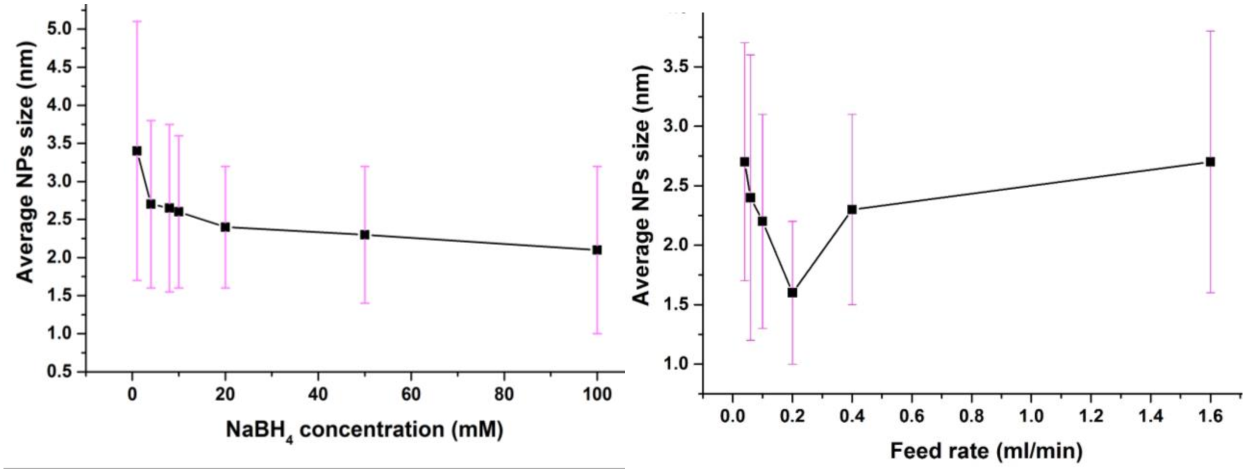

Fig. 2.5. Effects of (a) $NaBH_4$ concentration and (b) feed rate on AuNPs size.

2.3.2. X-ray absorption fine structure (XAFS)

2.3.2.1. X-ray absorption near edge structure (XANES)

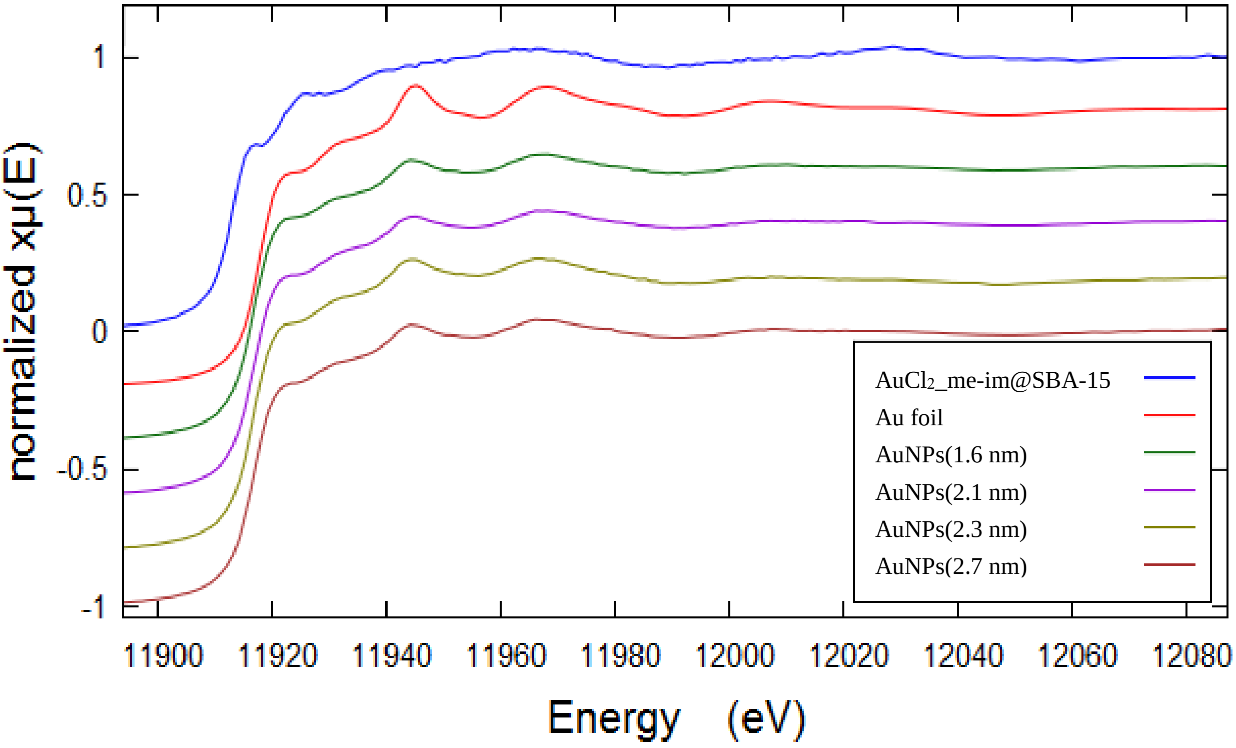

Fig. 2.6. Normalized Au L_3-edge XANES spectra of Au species in AuCl_me-Im@SBA-15, Au foil and AuNPs_me-Im@SBA-15 with different size.

The Au-L_3 XANES spectra were used to confirm the change in Au valence state before and after the reduction. Figure 2.6 provides a comparison between the XANES spectra of the standard Au foil and Au species before and after reduction. The presence of the characteristic Au^0 peaks at approximately 11,944 eV and 11,966 eV on all AuNPs samples and Au foil suggests that Au^+ species in AuCl_me-Im@SBA-15 was completely reduced to Au^0 after reduction by $NaBH_4$. In addition, the absence of white line at 11,920 eV indicates that the 5d-orbitals are filled and therefore, no cationic Au species are expected (AuClx and AuOx species) as in agreement with those of Au foil.[32–35]

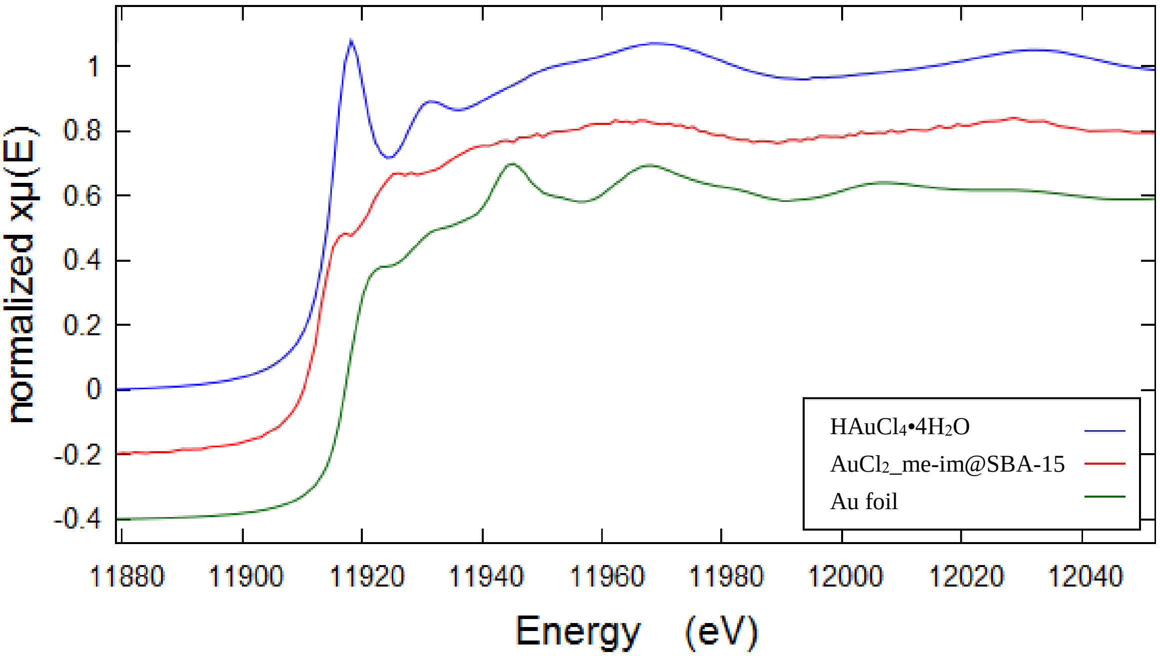

Fig. 2.7. Normalized Au L_3-edge XANES spectra of Au species in AuCl_me-Im@SBA-15, and in both reference compounds $HAuCl_4$•$4H_2O$ and Au foil.

On the other hands, a sharp peak observed at 11,918 eV on the reference compound $HAuCl_4 \cdot 4H_2O$ and the white line peak at 11,923 eV on the AuCl_me-Im@SBA-15 sample confirmed the presence of cationic Au species Au^{3+} and Au^{+} respectively as shown in Fig. 2.7.[35–37] The presence of these peaks correspond to the vacant 5d-orbitals which is due to dipole transitions from $2p_{3/2}$ to the $5d_{5/2,\ 3/2}$ at the L_3 edge.[38–42] Moreover, the difference in white line peak position and decrease in intensity of AuCl_me-Im@SBA-15 compared to those of the reference compound $HAuCl_4 \cdot 4H_2O$ are likely due to the fact that Au atom in AuCl_me-Im@SBA-15 sample has more electronic occupation in 5d-orbitals. And when the 5d state are fully occupied, no white line can be observed at this region and another peak appears at 11,945 eV, indicating that all the Au atoms are present as Au^0.

2.3.2.2. Extended x-ray absorption fine structure (EXAFS)

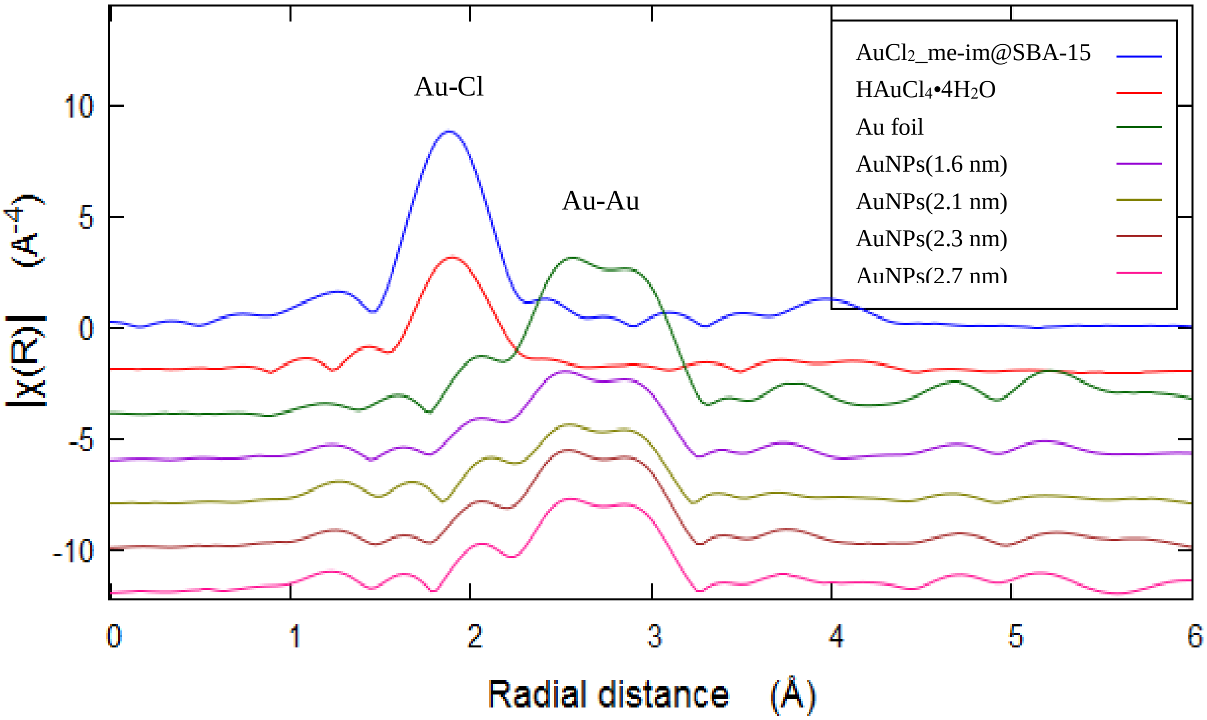

Fig. 2.8. k^3-weighted Fourier transform of Au L_3-edge EXAFS for AuCl_me-Im@SBA-15, AuNPs_me-Im@SBA-15 with different size and both reference compounds $HAuCl_4$•$4H_2O$ and Au foil.

The local atomic structure around Au atom was studied by EXAFS analysis. Figure 2.8 displays the Fourier-transformed EXAFS spectra (FT-EXAFS) for the prepared samples AuCl_me-Im@SBA-15 and AuNPs_me-Im@SBA-15 in comparison with the reference compounds $HAuCl_4$•$4H_2O$ and Au foil. The spectra of both $HAuCl_4$•$4H_2O$ and AuCl_me-Im@SBA-15 have similar features in *R*-space. This similarity was also observed for both the prepared AuNPs with different size and Au foil.

Table 2.3. EXAFS fitting results for the prepared Au catalysts.

Catalyst	**Shell**	**CN**	***R* (Å)**	**σ^2 (10^{-5} nm^2)**	**Δk (10 nm^{-1})**	**Δr (Å)**	**S_0^2**	**ΔE_0 (eV)**	**R_f (%)**
$HAuCl_4 \cdot 4H_2O$	Au-Cl	4.0	2.286 ± 0.002	2.1 ± 0.2	3–14	1.3 –2.5	0.26 ± 0.01	7.7 ± 0.6	0.2
AuCl_me-Im @SBA-15	Au-Cl	1.8 ± 0.2	2.270 ± 0.006	3.1 ± 0.7	3–12	1.2 – 2.6	0.26	10.2 ± 1.3	0.4
Au foil	Au-Au	12.0	2.856 ± 0.002	7.8 ± 0.2	3–15	1.4 – 3.4	0.80 ± 0.03	2.8 ± 0.5	0.3
AuNPs(1.6 nm)_me-Im@SBA-15	Au-Au	7.6 ± 0.5	2.841 ± 0.004	8.8 ± 0.5	3–12	1.6 – 3.4	0.80	3.1 ± 0.7	0.5
AuNPs(2.1 nm)_me-Im@SBA-15	Au-Au	7.8 ± 1.0	2.835 ± 0.006	10 ± 0.8	3–11	1.4 – 3.2	0.80	4.5 ± 1.0	0.9
AuNPs(2.3 nm)_me-Im@SBA-15	Au-Au	8.0 ± 0.7	2.845 ± 0.004	8.4 ± 0.5	3–12	1.6 – 3.2	0.80	3.6 ± 0.8	0.4
AuNPs(2.7 nm)_me-Im@SBA-15	Au-Au	8.2 ± 1.0	2.842 ± 0.006	9.2 ± 0.9	3–10.5	1.6 – 3.6	0.80	4.5 ± 1.0	0.6

Notes: CN is the coordination number, R is the bonding distance, σ^2 is the Debye-Waller factor, Δk and Δr refer to k- and R-range, S_0^2 is the amplitude reduction factor, ΔE_0 is the energy shift on the absorption edge, and R_f is the R-factor.

Table 2.3 summarizes the fitting results of EXAFS analysis, whereas the observed and fitted data for k^3-weighted oscillation and its Fourier transform of Au L_3-edge EXAFS are presented in Fig. S2.1 (see supporting information). In order to examine the coordination number (CN) around Au atom, the amplitude reduction factor S_0^2 was determined from the reference compounds. The S_0^2 values for AuCl_me-Im@SBA-15 and AuNPs_me-Im@SBA-15 were fixed to be 0.26 and 0.80 which were determined from the curve-fitting EXAFS data of $HAuCl_4 \cdot 4H_2O$ and Au foil. Neither Au-Au nor Au-O bonds can be observed from the FT-EXAFS fitting results before the reduction of AuCl_me-Im@SBA-15 suggesting that no AuOx or metallic Au species formed in the sample. The CN of Au-Cl in AuCl_me-Im@SBA-15 was found to be 2, indicating that Au atom is coordinated by two Cl atoms at the Au-Cl distance of 0.227 nm by forming an anionic complex $AuCl_2^-$. The schematic view drawn from these results is presented in Fig. 2.9. The figure shows that the gold chloride anion is held by imidazolium cation due to the charge balance on mesoporous silica SBA-15.

On the other hand, neither Au-Cl nor Au-O bonds could be observed after the formation of AuNPs for all samples with different size, meaning that $AuCl_2^-$ was completely reduced to Au^0 by $NaBH_4$ without any surface oxidation The CN of Au-Au in AuNPs_me-Im@SBA-15 was found to be 7.6, 7.8, 8.0, and 8.2 for AuNPs with the size of 1.6 nm, 2.1 nm, 2.3 nm, and 2.7 nm respectively at the Au-Au distance identical to Au foil which is 2.8 Å. These CNs were substantially lower than that for bulk Au (foil), as expected from the presence of small nanoparticles.

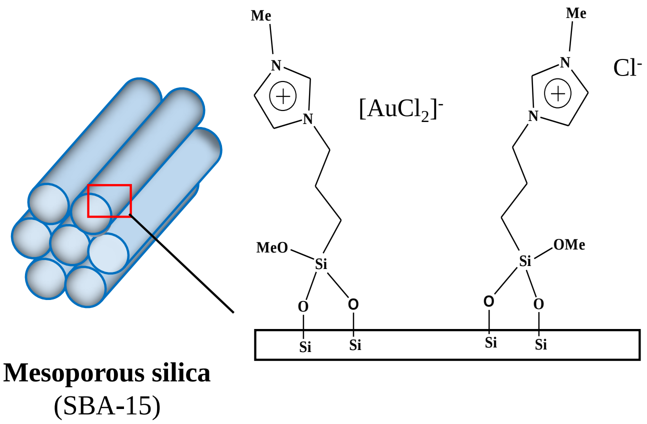

Fig. 2.9. A schematic view of immobilized $AuCl_2^-$ containing 1-methyl-3-(3-trimethoxysilyl-propyl)-imidazolium on mesoporous silica SBA-15.

2.3.3. X-ray photoelectron spectroscopy (XPS)

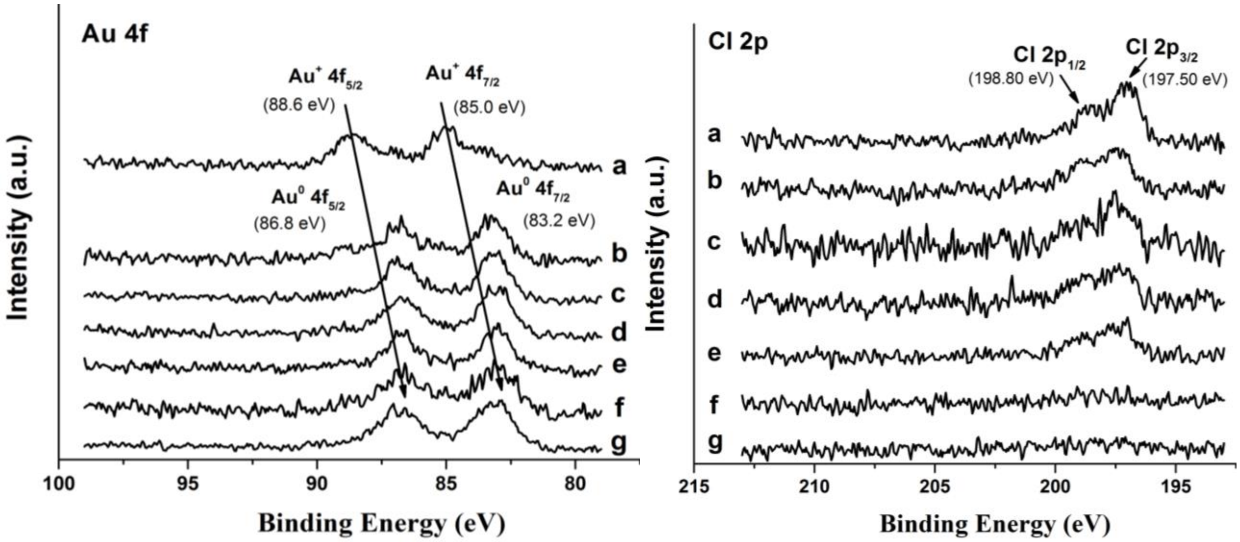

Fig. 2.10. XPS spectra of Au 4f and Cl 2p regions of AuCl_me-Im@SBA-15 before (a) and after reduction by 4 mM $NaBH_4$ at (b) 1.6, (c) 0.2, (d) 0.06, (e) 0.04 ml/min and at fixed feed rate of 1.6 ml/min by (f) 10 and (g) 100 mM $NaBH_4$.

While XAFS was measured for bulk technique that penetrates the entire sample volume, XPS is surface-sensitive with the sampling depth determined by the kinetic energy of the photoelectron.[43] The XPS depth profiling was not performed, however if the mean free path is in the range of 1–3.5 nm for Al Kα radiation and assuming that 95% of all photoelectrons are scattered by the time they reach the surface, the sampling depth can be estimated about 3–10 nm. The surface chemical composition for the specified samples determined by XPS is shown in Fig. 2.10. The transformation of Au ions into AuNPs located on the surface sample was confirmed from XPS spectra. Two peaks of Au 4f region ($4f_{5/2}$ and $4f_{7/2}$) shifted to the lower binding energy after the reduction from 88.6 and 85.0 eV to 86.8 and 83.2 eV, confirming the formation of metallic Au (Au^0) from Au^+ state in $AuCl_2^-$.

As discussed in the previous section, Cl^- ions were replaced by OH^- to a larger extent with increasing concentration of $NaBH_4$. The disappearance of peaks in Cl 2p region for both samples reduced by (f) 10 and (g) 100 mM $NaBH_4$ gave the evidence that Cl^- ions were completely replaced by OH^- at higher pH value. Whereas the reduction by 4 mM $NaBH_4$ at different feed rates (a–e), the Cl^- ions partially remained surrounding imidazolium cations.

It is worth mentioning that $NaBH_4$ was completely removed from the resulting materials after washing with distilled water. The disappearance of Na 1s and B 1s spectra at 1071–1072 eV and 187–189 eV is the evidence that $NaBH_4$ was washed out during the washing process. The XPS spectra of Na 1s and B 1s are presented in Fig. S2.2. The existence of imidazolium cation was also supported from N 1s spectra of Au catalyst after the reduction. The N 1s spectrum shows the quaternary ammonium ions at 401.4 eV and imine at 399.0 eV (Fig. S2.3).[44–48] This result agrees with the FTIR observation which will be discussed in the next section.

2.3.4. Fourier transform infrared Spectroscopy (FTIR)

The existence of ionic liquid on the surface of SBA-15 was examined by FTIR measurements. Figure 2.11 shows all the prepared materials, pure SBA-15 before immobilization processes (Fig. 7a), after immobilization of IL and AuCl (Fig. 2.11 b and c, respectively), and after the formation of AuNPs by different concentration of $NaBH_4$ at different feed rate (Fig. 2.11 d–h). Sharp bands at 1070, 792 (#) and 950 cm^{-1} (@) assigned to the stretching and bending vibrations of condensed Si-O-Si networks, and the stretching vibrations of uncondensed Si-OH groups were observed in all samples.[49,50] The broad bands at 3400 and 1630 cm^{-1} (θ) were attributed to the vibration of adsorbed water molecules.[50] The figures show all samples after immobilization of IL (Fig. 2.7 b–h) displayed several additional bands at 3138, 3090, 2940, 616 cm^{-1} (+), and 1561 and 1453 cm^{-1} (*) assigned respectively to the aliphatic C-H stretching and the ring stretching of imidazolium molecules.[49–51] The C-Si stretching vibrations between 1233 and 1200 cm^{-1} cannot be resolved due to the overlapping with broad bands of Si-O-Si stretching. These additional peaks indicate that the IL was successfully grafted onto the siliceous SBA-15. This observation also gives evidence that the bonding strength between the IL and the surface of SBA-15 is very strong, since increasing the concentration of $NaBH_4$ and controlling the feed rates on the reduction process do not affect the existence of IL. In other words, $NaBH_4$ only reduces the Au complex into AuNPs.

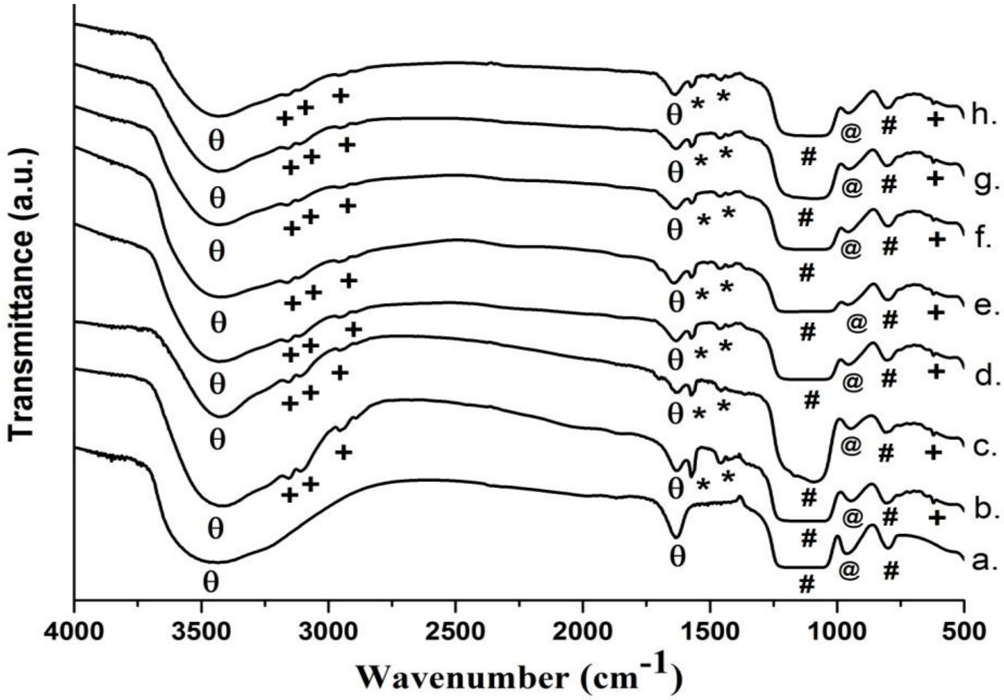

Fig. 2.11. FTIR spectra of (a) SBA-15 before immobilization, after immobilization (b) me-Im@SBA-15, (c) AuCl_me-Im@SBA-15, after reduction by (d) 4, (e) 50, and (f) 100 mM $NaBH_4$ at 1.6 ml/min and by 4 mM $NaBH_4$ at (g) 0.4 and (h) 0.04 ml/min.

Immobilized IL acted as a stabilizing agent and/or surfactant facilitating the uniform distribution of AuCl over SBA-15, forming $AuCl_2^-$ anionic species due to the electrostatic interactions. Moreover, the immobilized imidazolium cations serve as spacing functions to keep Au monomers separated due to the charge balance between the imidazolium cation and gold complex anion. These cations create a specific distance between monomers during the reduction process, effecting on the monomer diffusion rate. Moreover, it gives additional repulsive force that affects the agglomeration rate.

2.3.5. X-ray diffraction (XRD)

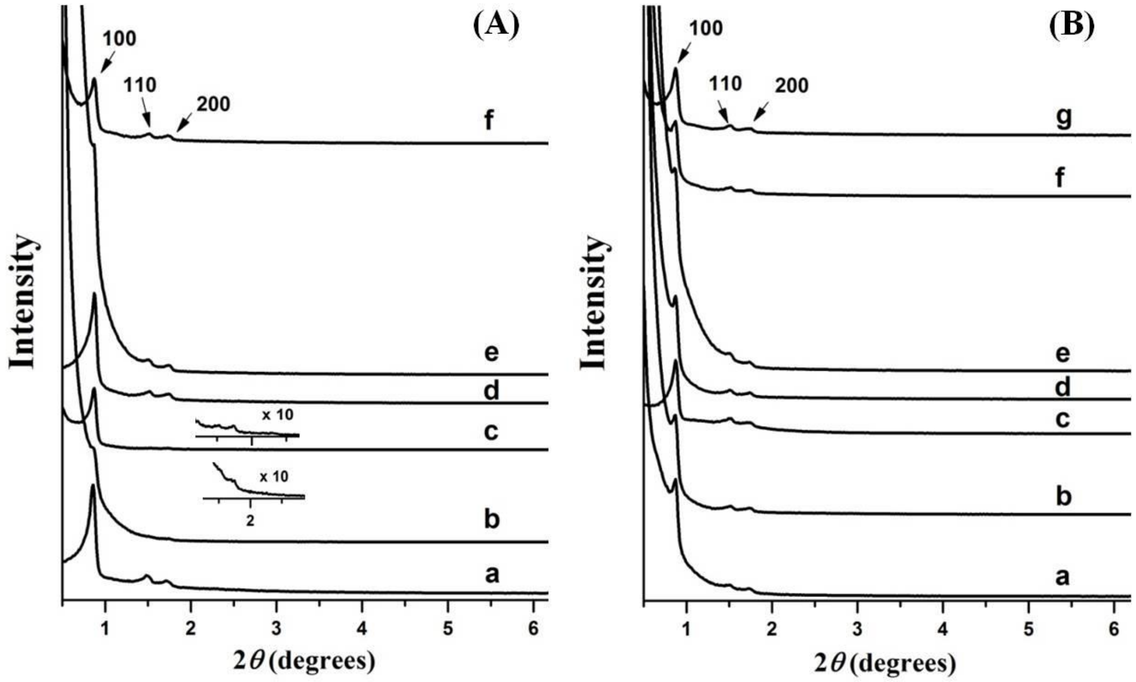

Fig. 2.12. Low angle XRD patterns of all the catalysts (A) before immobilization (a) SBA-15, after immobilization of ILs and AuCl (b) me-Im@SBA-15 (c) AuCl_me-Im@SBA-15, after the reduction by 4 mM $NaBH_4$ at (d) 0.2, (e) 0.06, and (f) 0.04 ml/min; and (B) by different concentration of $NaBH_4$ (a) 1, (b) 4, (c) 8, (d) 10, (e) 20, (f) 50 and (g) 100 mM.

Low angle XRD measurements are shown in Fig. 2.12. All prepared samples showed typical three reflection peaks corresponding to [100], [110] and [200], resulted from the quasi-regular arrangement of mesopores with *p6mm* hexagonal symmetry.[11,29] After immobilization processes, both peaks at [110] and [200] of me-Im@SBA-15 and AuCl_me-Im@SBA-15 showed weak intensities due to the successful immobilization of IL and AuCl on surface SBA-15. However, after the formation of AuNPs, these peaks appeared more eminently. The differences of intensity in each spectrum might be attributed to the disorder in the mesoporous structure after consecutive immobilization processes. Nevertheless, the three well resolved peaks attributed to highly ordered mesoporous material with hexagonal structure,[11,29,52] in addition to the TEM observation gave the evidence that the structure of SBA-15 could retain its structural integrity during the successive immobilization and reduction processes.

2.4. Conclusion

In the first study, AuNPs catalysts prepared from immobilized gold chloride containing ionic liquid on SBA-15 were successfully synthesized. Size and shape of AuNPs could be controlled inside porous SBA-15 by varying the concentration and feed rate of $NaBH_4$ solution. In this process, the size distribution and shape of AuNPs strongly depend on the concentration and feed rate of $NaBH_4$ solution as well as the immobilized ionic liquid, which affect the growth and agglomeration processes of the nanoparticles. The size of AuNPs decreased with increasing the $NaBH_4$ concentration. AuNPs with 1.6 nm was obtained by fixing the feed rate at 0.2 ml/min, whereas larger and capsule-like NPs were observed at slow feed rate of 0.04 ml/min reduced by 4 mM $NaBH_4$. This study gives good example of a successful synthesis of AuNPs from AuCl which is rarely used as the metal precursor. Moreover, the synthesis strategy described in this work can be a reference to control the NPs growth on porous support materials.

2.5. References

(1) Haruta, M.; Daté, M. Advances in the Catalysis of Au Nanoparticles. *Appl. Catal. A Gen.* **2001**, *222*, 427–437.

(2) Freakley, S. J.; He, Q.; Kiely, C. J.; Hutchings, G. J. Gold Catalysis : A Reflection on Where We Are Now. *Catal. Letters* **2015**, *145*, 71–79.

(3) Gulina, L. B.; Pchelkina, A. A.; Nikolaev, K. G.; Navolotskaya, D. V; Ermakov, S. S.; Tolstoy, V. P. A Brief Review on Immobilization of Gold Nanoparticles on Inorganic Surfaces and Successive Ionic Layer Deposition. *Rev. Adv. Mater. Sci.* **2016**, *44*, 46–53.

(4) Hutchings, G. J. Catalysis by Gold. *Catal. Today* **2005**, *100* (1–2), 55–61.

(5) Lou, X. B.; He, L.; Qian, Y.; Liu, Y. M.; Cao, Y.; Fan, K. N. Highly Chemo- and Regioselective Transfer Reduction of Aromatic Nitro Compounds Using Ammonium Formate Catalyzed by Supported Gold Nanoparticles. *Adv. Synth. Catal.* **2011**, *353* (2–3), 281–286.

(6) Guo, P.; Tang, L.; Tang, J.; Zeng, G.; Huang, B.; Dong, H.; Zhang, Y.; Zhou, Y.; Deng, Y.; Ma, L.; et al. Catalytic Reduction-Adsorption for Removal of *p*-Nitrophenol and Its Conversion *p*-Aminophenol from Water by Gold Nanoparticles Supported on Oxidized Mesoporous Carbon. *J. Colloid Interface Sci.* **2016**, *469*, 78–85.

(7) Zhu, Y.; Shen, J.; Zhou, K.; Chen, C.; Yang, X.; Li, C. Multifunctional Magnetic Composite Microspheres with in Situ Growth Au Nanoparticles : A Highly Efficient Catalyst System. *J. Phys. Chem. C* **2011**, *115*, 1614–1619.

(8) El-Sheikh, S. M.; Ismail, A. A.; Al-Sharab, J. F. Catalytic Reduction of *p*-Nitrophenol over Precious Metals/Highly Ordered Mesoporous Silica. *New J. Chem.* **2013**, *37* (8), 2399–2407.

(9) Gao, D.; Zhang, X.; Dai, X.; Qin, Y.; Duan, A.; Yu, Y.; Zhuo, H. Morphology-Selective Synthesis of Active and Durable Gold Catalysts with High Catalytic Performance in the Reduction of 4-Nitrophenol. *Nano Res.* **2016**, *9* (10), 3099–3115.

(10) Damasceno, J. P. V.; Maroneze, C. M.; Strauss, M.; Sigoli, F. A.; Mazali, I. O. Preparation of Supported AuPd Nanoalloys Mediated by Ionic Liquid-like Functionalized SBA-15: Structural Correlations Concerning Its Catalytic Activity. *New J. Chem.* **2016**, *40* (8), 6636–6642.

(11) Zhao, D.; Huo, Q.; Feng, J.; Chmelka, B. F.; Stucky, G. D. Tri-, Tetra-, and Octablock Copolymer and Nonionic Surfactant Syntheses of Highly Ordered, Hydrothermally Stable, Mesoporous Silica Structures. *J. Am. Chem. Soc.* **1998**, *120* (24), 6024–6036.

(12) Sasaki, T.; Zhong, C.; Tada, M.; Iwasawa, Y. Immobilized Metal Ion-Containing Ionic Liquids: Preparation, Structure and Catalytic Performance in Kharasch Addition Reaction. *Chem. Commun.* **2005**, 2506–2508.

(13) Sasaki, T.; Tada, M.; Zhong, C.; Kume, T.; Iwasawa, Y. Immobilized Metal Ion-Containing Ionic Liquids: Preparation, Structure and Catalytic Performances in Kharasch Addition Reaction and Suzuki Cross-Coupling Reactions. *J. Mol. Catal. A Chem.* **2008**, *279* (2), 200–209.

(14) Zhong, C.; Sasaki, T.; Tada, M.; Iwasawa, Y. Ni Ion-Containing Ionic Liquid Salt and Ni Ion-Containing Immobilized Ionic Liquid on Silica: Application to Suzuki Cross-Coupling Reactions between Chloroarenes and Arylboronic Acids. *J. Catal.* **2006**, *242* (2), 357–364.

(15) Khedkar, M. V.; Shinde, A. R.; Sasaki, T.; Bhanage, B. M. Immobilized Palladium Metal Containing Ionic Liquid Catalyzed One Step Synthesis of Isoindole-1,3-Diones by Carbonylative Cyclization Reaction. *J. Mol. Catal. A Chem.* **2014**, *385*, 91–97.

(16) Gadge, S. T.; Kusumawati, E. N.; Harada, K.; Sasaki, T.; Nishio-Hamane, D.; Bhanage, B. M. Synthesis of Oxamate and Urea by Oxidative Single and Double Carbonylation of Amines Using Immobilized Palladium Metal-Containing Ionic Liquid@SBA-15. *J. Mol. Catal. A Chem.* **2015**, *400*, 170–178.

(17) Satapathy, A.; Gadge, S. T.; Kusumawati, E. N.; Harada, K.; Sasaki, T.; Nishio-Hamane, D.; Bhanage, B. M. Synthesis of Polyester Amide by Carbonylation-Polycondensation Reaction Using Immobilized Palladium Metal Containing Ionic Liquid on SBA-15 as a Phosphine-Free Catalytic System. *Catal. Lett.* **2015**, *145* (3), 824–833.

(18) Patil, N. M.; Sasaki, T.; Bhanage, B. M. Immobilized Iron Metal-Containing Ionic Liquid-Catalyzed Chemoselective Transfer Hydrogenation of Nitroarenes into Anilines. *ACS Sustain. Chem. Eng.* **2016**, *4* (2), 429–436.

(19) Guczi, L.; Horváth, D.; Pászti, Z.; Petõ, G. Effect of Treatments on Gold Nanoparticles: Relation between Morphology, Electron Structure and Catalytic Activity in CO Oxidation. *Catal. Today* **2002**, *72* (1–2), 101–105.

(20) Tsunoyama, H.; Sakurai, H.; Negishi, Y.; Tsukuda, T. Size-Specific Catalytic Activity of Polymer-Stabilized Gold Nanoclusters for Aerobic Alcohol Oxidation in Water. *J. Am. Chem. Soc.* **2005**, *127* (26), 9374–9375.

(21) Polte, J. Fundamental Growth Principles of Colloidal Metal Nanoparticles - a New Perspective. *CrystEngComm* **2015**, *17* (36), 6809–6830.

(22) Lo, T.; Yu, C.; Liu, Y.; Yang, K.; Chen, Q. Size-Controllable Synthesis of Catalyst of Gold Nanoparticles Supported on TiO_2 by Using Sonoelectrochemical Methods. *Mater. Res. Bull.* **2013**, *48* (2), 920–922.

(23) Briñas, R. P.; Hu, M.; Qian, L.; Lymar, E. S.; Hainfeld, J. F. Gold Nanoparticle Size

Controlled by Polymeric Au(I) Thiolate Precursor Size. *J. Am. Chem. Soc.* **2008**, *130* (3), 975–982.

(24) Zanella, R.; Sandoval, A.; Santiago, P.; Basiuk, V. A.; Saniger, J. M. New Preparation Method of Gold Nanoparticles on SiO_2. *J. Phys. Chem. B* **2006**, *110* (17), 8559–8565.

(25) Petkov, N.; Stock, N.; Bein, T. Gold Electroless Reduction in Nanosized Channels of Thiol-Modified SBA-15 Material. *J. Phys. Chem. B* **2005**, *109* (21), 10737–10743.

(26) Vanecht, E.; Binnemans, K.; Seo, W. Growth of Sputter-Deposited Gold Nanoparticles in Ionic Liquids. *Phys. Chem. Chem. Phys.* **2011**, *13*, 13565–13571.

(27) Privman, V. Mechanisms of Diffusional Nucleation of Nanocrystals and Their Self-Assembly into Uniform Colloids. *Ann. N. Y. Acad. Sci.* **2009**, *1161*, 508–525.

(28) Wuithschick, M.; Witte, S.; Kettemann, F.; Rademann, K.; Polte, J. Illustrating the Formation of Metal Nanoparticles with a Growth Concept Based on Colloidal Stability. *Phys. Chem. Chem. Phys.* **2015**, *17*, 19895–19900.

(29) Zhao, D.; Feng, J.; Huo, Q.; Melosh, N.; Fredrickson, G. H.; Chmelka, B. F.; Stucky, G. D. Triblock Copolymer Syntheses of Mesoporous Silica with Periodic 50 to 300 Angstrom Pores. *Science* **1998**, *279* (5350), 548–552.

(30) Ma, C. Y.; Dou, B. J.; Li, J. J.; Cheng, J.; Hu, Q.; Hao, Z. P.; Qiao, S. Z. Catalytic Oxidation of Benzyl Alcohol on Au or Au-Pd Nanoparticles Confined in Mesoporous Silica. *Appl. Catal. B Environ.* **2009**, *92* (1–2), 202–208.

(31) Hotze, E. M.; Phenrat, T.; Lowry, G. V; Mellon, C. Nanoparticle Aggregation : Challenges to Understanding Transport and Reactivity in the Environment. *J. Environ. Qual.* **1909**, *39*, 1909–1924.

(32) Tanaka, T.; Ohyama, J.; Teramura, K.; Hitomi, Y. Formation Mechanism of Metal

Nanoparticles Studied by XAFS Spectroscopy and Effective Synthesis of Small Metal Nanoparticles. *Catal. Today* **2012**, *183* (1), 108–118.

(33) Nishimura, S.; Dao, A. T. N.; Mott, D.; Ebitani, K.; Maenosono, S. X-Ray Absorption Near-Edge Structure and X-Ray Photoelectron Spectroscopy Studies of Interfacial Charge Transfer in Gold–Silver–Gold Double-Shell Nanoparticles. *J. Phys. Chem. C* **2012**, *116* (7), 4511–4516.

(34) Ma, J.; Zou, Y.; Jiang, Z.; Huang, W.; Li, J.; Wu, G.; Huang, Y.; Xu, H. An in Situ XAFS Study—the Formation Mechanism of Gold Nanoparticles from X-Ray-Irradiated Ionic Liquid. *Phys. Chem. Chem. Phys.* **2013**, *15* (28), 11904.

(35) He, Y. X.; Fu, H. Y.; Li, C.; Ji, X.; Ge, X. W.; Zou, Y.; Jiang, Z.; Xu, H. J.; Wu, G. Z. Property Variation of Ionic Liquid [Bmim][$AuCl_4$] Immobilized on Carboxylated Polystyrene Submicrospheres with a Small Surface Area. *Chinese Sci. Bull.* **2013**, *58* (24), 2950–2955.

(36) Song, Z.; Kenney, J. P. L.; Fein, J. B.; Bunker, B. A. An X-Ray Absorption Fine Structure Study of Au Adsorbed onto the Non-Metabolizing Cells of Two Soil Bacterial Species. *Geochim. Cosmochim. Acta* **2012**, *86*, 103–117.

(37) Chang, S.-Y.; Uehara, A.; Booth, S. G.; Ignatyev, K.; Mosselmans, J. F. W.; Dryfe, R. A. W.; Schroeder, S. L. M. Structure and Bonding in Au(I) Chloride Species: A Critical Examination of X-Ray Absorption Spectroscopy (XAS) Data. *RSC Adv.* **2015**, *5* (9), 6912–6918.

(38) Zhang, P.; Sham, T. K. X-Ray Studies of the Structure and Electronic Behavior of Alkanethiolate-Capped Gold Nanoparticles: The Interplay of Size and Surface Effects. *Phys. Rev. Lett.* **2003**, *90* (24), 4.

(39) Benfield, R. E.; Grandjean, D.; Kröll, M.; Pugin, R.; Sawitowski, T.; Schmid, G. Structure and Bonding of Gold Metal Clusters, Colloids, and Nanowires Studied by EXAFS, XANES, and WAXS. *J. Phys. Chem. B* **2001**, *105* (10), 1961–1970.

(40) Mansour, A. N.; Cook, J. W.; Sayers, D. E. Quantitative Technique for the Determination of the Number of Unoccupied D-Electron States in a Platinum Catalyst Using the $L_{2,3}$ X-Ray Absorption Edge Spectra. *J. Phys. Chem.* **1984**, *88* (11), 2330–2334.

(41) Mattheis, L. F.; Dietz, R. E. Relativistic Tight-Binding Calculation of Core-Valence Transitions in Pt and Au. *Phys. Rev.* **1980**, *22* (4), 1663–1676.

(42) Zhang, P.; Sham, T. K. Tuning the Electronic Behavior of Au Nanoparticles with Capping Molecules. *Appl. Phys. Lett.* **2002**, *81* (4), 736–738.

(43) Peck, M. A.; Langell, M. A. Comparison of Nanoscaled and Bulk NiO Structural and Environmental Characteristics by XRD, XAFS, and XPS. *Chem. Mater.* **2012**, *24* (23), 4483–4490.

(44) Mun, J.; Jung, Y. S.; Yim, T.; Lee, H. Y.; Kim, H. J.; Kim, Y. G.; Oh, S. M. Electrochemical Stability of Bis(Trifluoromethanesulfonyl)Imide-Based Ionic Liquids at Elevated Temperature as a Solvent for a Titanium Oxide Bronze Electrode. *J. Power Sources* **2009**, *194* (2), 1068–1074.

(45) Rietzler, F.; Piermaier, M.; Deyko, A.; Steinrück, H.-P.; Maier, F. Liquid/Solid Interface of Ultrathin Ionic Liquid Films: $[C_1C_1Im][Tf_2N]$ and $[C_8C_1Im][Tf_2N]$ on Au(111). *Langmuir* **2014**, *30* (4), 1063–1071.

(46) Yao, M.; Fan, M.; Liang, Y.; Zhou, F.; Xia, Y. Imidazolium Hexafluorophosphate Ionic Liquids as High Temperature Lubricants for Steel-Steel Contacts. *Wear* **2010**, *268* (1), 67–71.

(47) Chang, J.-K.; Lee, M.-T.; Cheng, C.-W.; Tsai, W.-T.; Deng, M.-J.; Hsieh, Y.-C.; Sun, I.-W. Pseudocapacitive Behavior of Mn Oxide in Aprotic 1-Ethyl-3-Methylimidazolium–dicyanamide Ionic Liquid. *J. Mater. Chem.* **2009**, *19* (22), 3732.

(48) Jansen, R. J. J.; van Bekkum, H. XPS of Nitrogen-Containing Functional Groups on Activated Carbon. *Carbon N. Y.* **1995**, *33* (8), 1021.

(49) Udayakumar, S.; Raman, V.; Shim, H.; Park, D. Cycloaddition of Carbon Dioxide for Commercially-Imperative Cyclic Carbonates Using Ionic Liquid-Functionalized Porous Amorphous Silica. *Appl. Catal. A Gen.* **2009**, *368*, 97–104.

(50) Xu, J.; Wu, H.; Ma, C.; Xue, B.; Li, Y.; Cao, Y. Ionic Liquid Immobilized on Mesocellular Silica Foam as an Efficient Heterogeneous Catalyst for the Synthesis of Dimethyl Carbonate via Transesterification. *Appl. Catal. A, Gen.* **2013**, *464–465*, 357–363.

(51) Zhang, W.; Wang, H.; Han, J.; Song, Z. Multifunctional Mesoporous Materials with Acid-Base Frameworks and Ordered Channels Filled with Ionic Liquid: Synthesis, Characterization and Catalytic Performance of Ti-Zr-SBA-15-IL. *Appl. Surf. Sci.* **2012**, *258* (16), 6158–6168.

(52) Beck, J. S.; Schmitt, K. D.; Higgins, J. B.; Schlenkert, J. L. New Family of Mesoporous Molecular Sieves Prepared with Liquid Crystal Templates. *J. Am. Chem. Soc.* **1992**, *114* (27), 10843–10854.

2.6. Supporting information

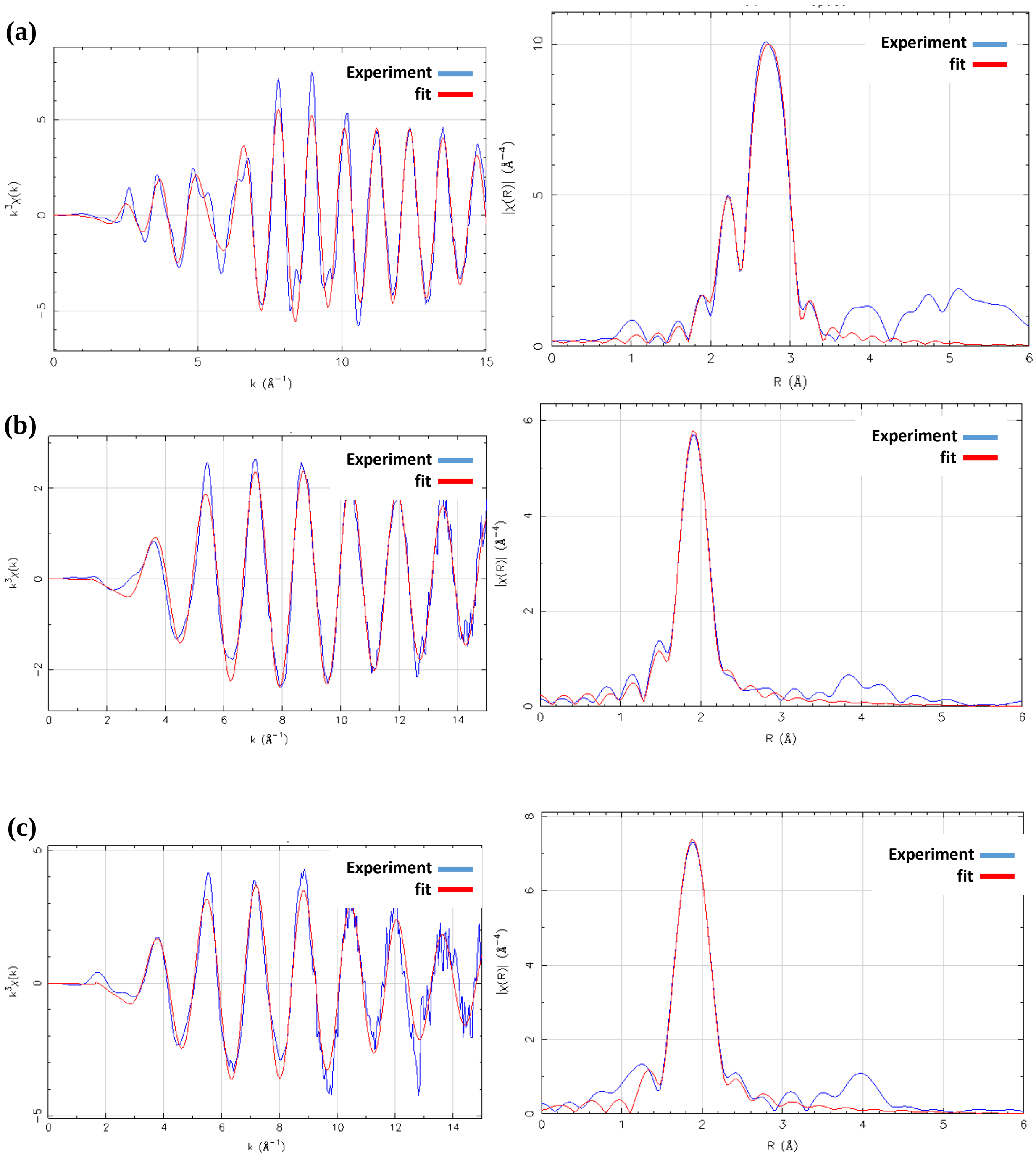

Fig. S2.1. Observed and fitted data for k^3-weighted oscillation and its Fourier transform of Au L_3-edge EXAFS for the reference compounds (a) Au foil and (b) $HAuCl_4$•$4H_2O$, as well as the prepared sample (c) AuCl_me-Im@SBA-15 and AuNPs_me-Im@SBA-15 with different size (d) 1.6, (e) 2.1, (f) 2.3, (g) 2.7 nm.

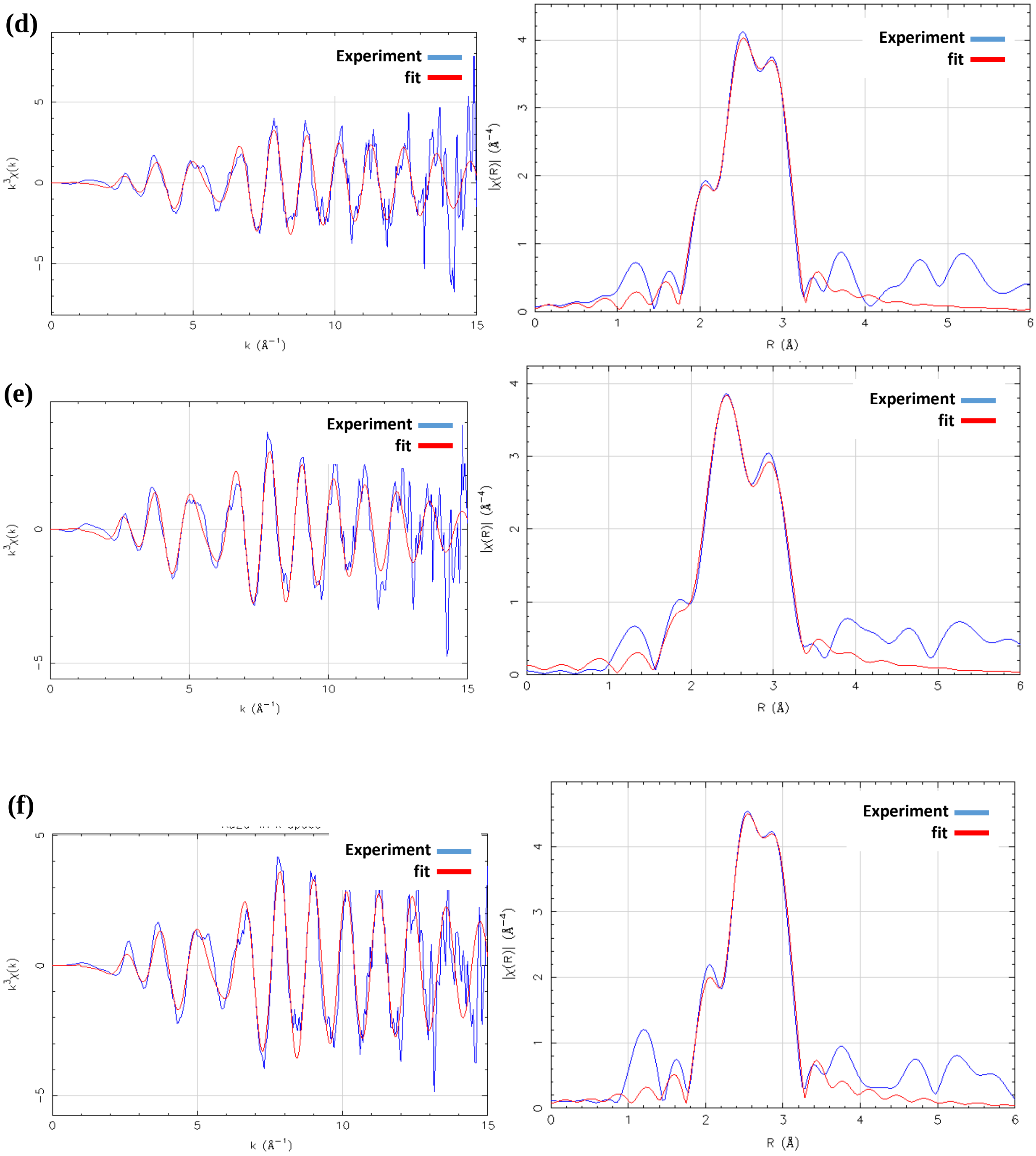

Fig. S2.1. Figure S2.1 continued.

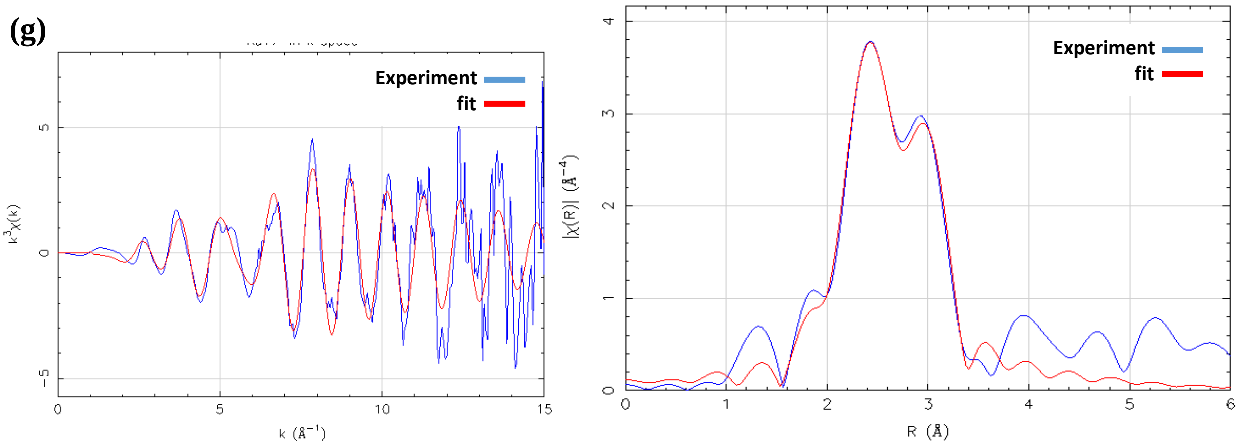

Fig. S2.1. Figure S2.1 continued.

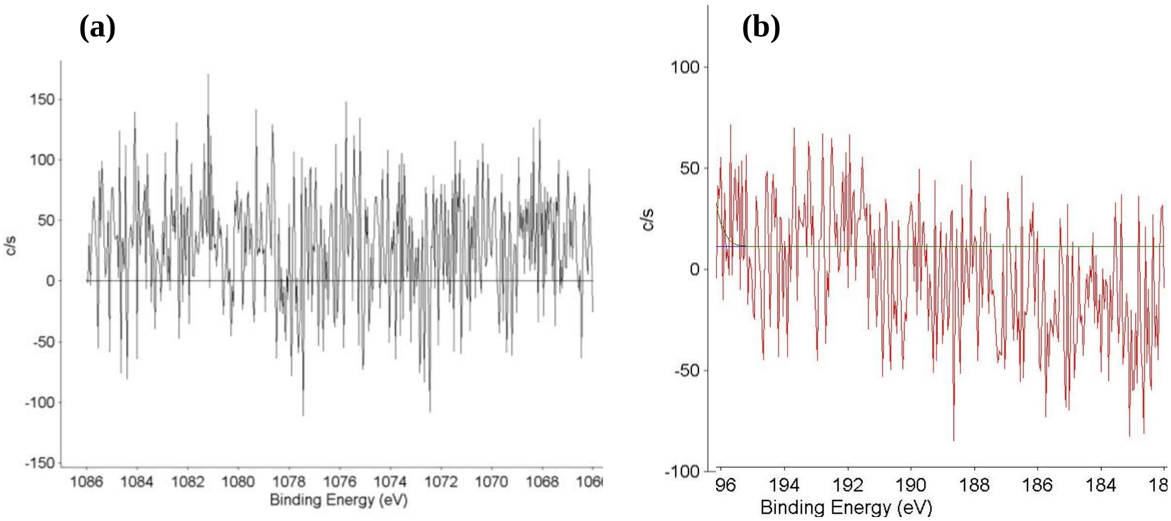

Fig. S2.2. XPS fitting spectra of (a) Na 1s and (b) B 1s of AuNPs_me-Im@SBA-15.

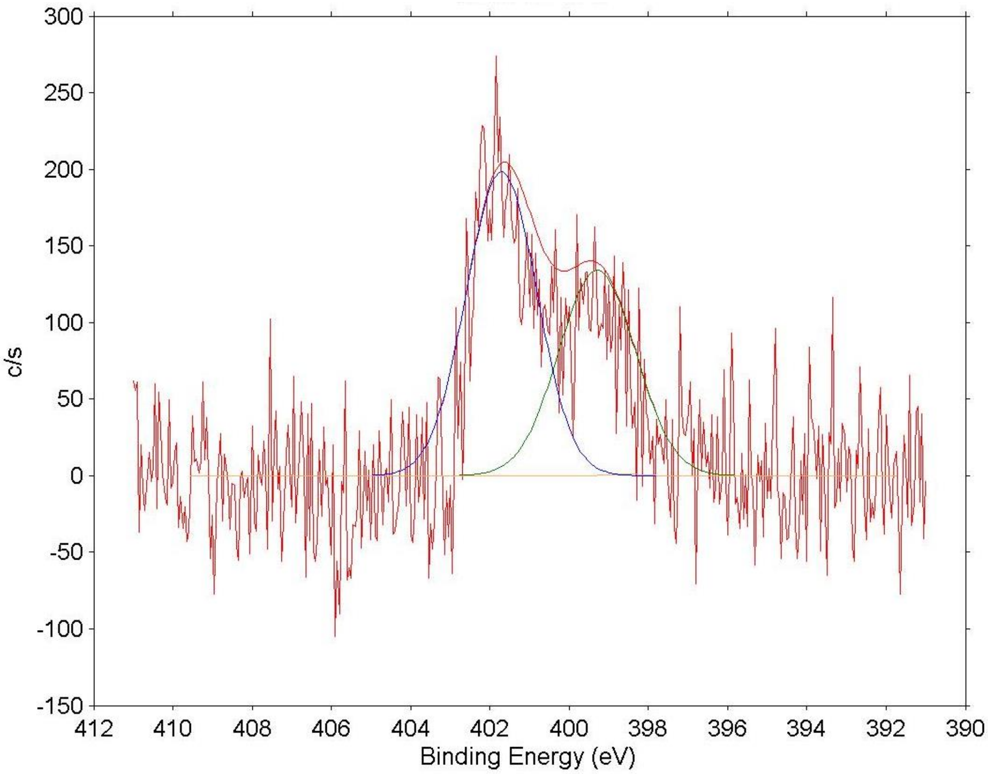

Fig. S2.3. XPS fitting spectrum of N 1s of AuNPs_me-Im@SBA-15.

Chapter 3

Size-Dependence of Gold Nanoparticles in the Reduction of *p*-Nitrophenol

Abstract

The size dependency of AuNPs_me-Im@SBA-15 prepared from the first study was investigated for hydrogenation of *p*-nitrophenol using $NaBH_4$. The catalyst with the smallest NPs, AuNPs(1.6 nm)_me-Im@SBA-15, exhibited the highest catalytic performance, whereas AuNPs(2.7 nm)_me-Im@SBA-15 showed lower catalytic activity. On the other hand, Au/SBA-15 with the size of 5.6 nm which was synthesized in the absence of ionic liquid, exhibited poor catalytic activity. In addition, the effects of $NaBH_4$ concentration and the amount of catalyst in the reduction of *p*-nitrophenol were also investigated. The catalyst was reusable for at least four recycle processes without a significant decrease in activity. Moreover, the effect of recycle process in the AuNP size as well as the absence of isosbestic point, and the presence of induction period on PNP reduction were discussed in detail.

3.1. Introduction

Catalytic reduction of *p*-ntrophenol (PNP) by $NaBH_4$ over metal catalyst has been widely used as a catalytic model to evaluate the catalytic activity of either mono- or bi-metallic nanoparticles.[1–9] In the catalytic reduction of PNP by metallic nanoparticles, the electron transfer takes place from borohydride ions (BH_4^-) to PNP through adsorption of molecules on the nanoparticle surface and this contributes to overcome the kinetic barrier of the reaction.[1,10] The catalytic activity is expressed by the rate constant (k) from the linear correlation of $\ln(C_t/C_0)$ versus reaction time (t) in the presence of an excess BH_4^- in which the strong UV-Vis absorption at 400 nm decreases and the reaction follows a pseudo-first-order reaction.

In general, the rate constant increases with the decrease in metal nanoparticle size which is proportional to the total surface area of metal nanoparticle. Panigrahi *et al.* reported the size dependence of AuNPs (8–55 nm) supported on ion-exchange resins and the rate constant of AuNPs with the size of 8 nm was estimated to be 2.75×10^{-4} s^{-1} which showed better catalytic activity than that of AuNPs with the size of 55 nm ($k = 0.33 \times 10^{-4}$ s^{-1}).[11] On the other hand, Gao *et al.* reported that Au/ZSBA-PL-350 with the size of 4 nm exhibited better catalytic performance with k value of 23.3×10^{-4} s^{-1} than that of Au/ZSBA-PL-100 with the size of 0.9 nm (5×10^{-4} s^{-1}).[8] They suggested that the poor performance of AuNPs size below 1 nm is due to the poor storage ability of electronic states for ultrafine AuNPs.

PNP is one of the most common organic pollutants in agricultural and industrial wastewater which shows excellent solubility and stability in water.[12–14] Due to its toxicity and hazard which cause harmful on living systems, many attempts had been made to remove it from the environment such as adsorption, electrochemical treatment and microbial degradation.[12,13,15] The catalytic reduction of PNP by solid catalysts is the most efficient and economical disposal method, and the product *p*-aminophenol (PAP) can be used in various chemical products such as dyes, pharmaceuticals, and anticorrosive lubricants.[2,16–18]

The purpose of this study is to investigate the catalytic activity and reusability of the prepared catalyst in order to design an efficient and reusable catalyst. The size dependence of AuNPs_me-Im@SBA-15 was investigated for PNP hydrogenation reaction by $NaBH_4$ at room temperature and under stirring. The effects of AuNPs size, $NaBH_4$ concentration and recycle process on the catalytic performance were also studied.

3.2. Experimental

All chemicals were used without further purification. *p*-Nitrophenol ($C_6H_5NO_3$, 98.0%), diethylene glycol dimethyl ether (diglyme, 98%) and sodium borohydride ($NaBH_4$, 95%) were purchased from WAKO.

The catalytic activities of the prepared AuNPs catalysts were investigated by the catalytic hydrogenation of *p*-nitrophenol (PNP) with $NaBH_4$ in a quartz cuvette with magnetic stirrer at room temperature using UV-vis spectroscopy (Jasco V-630 BIO). The catalyst suspension in water was sonicated for 20 min before the catalytic test. In a typical reaction, 0.3 mg/ml of catalyst in water was added to 1.0 mL of aqueous PNP solution (0.3 or 1 mM), and 1.0 mL of fresh $NaBH_4$ solution (15 or 50 mM) in a quartz cuvette. The cuvette with 3 ml mixture of Au:PNP:$NaBH_4$ = 1:10:500 was quickly inserted in UV-vis spectrometer and the reaction progress was monitored at 1 min interval under stirring at room temperature (20 °C). The initial absorbance (C_0) of the high concentration of PNP (1 mM) was determined by the extrapolation procedure due to the saturation in absorption.

3.3. Results and discussion

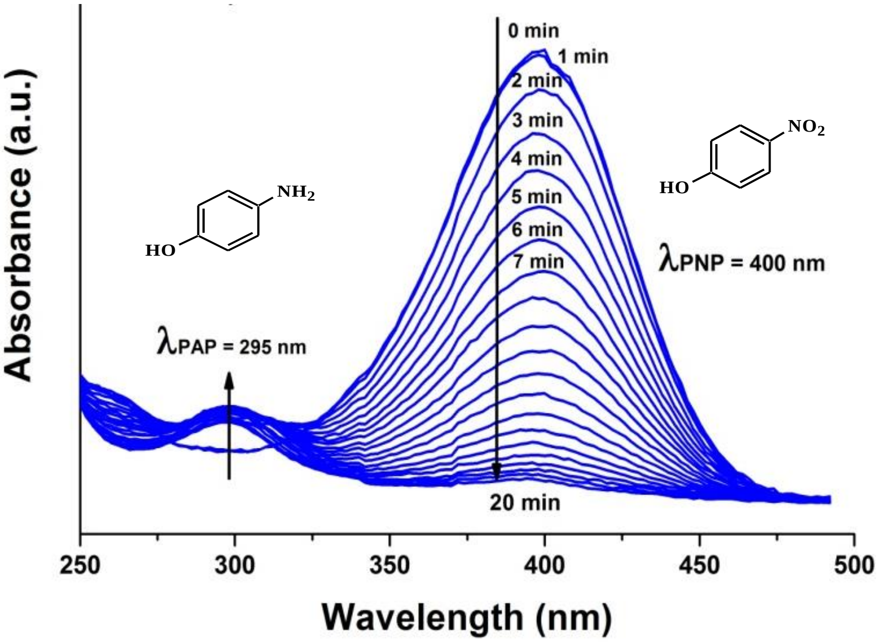

Fig. 3.1. UV-vis spectra of PNP reduction measured at 1 min interval catalyzed by AuNPs (1.6 nm)_me-Im@SBA-15 with molar ratio of Au:PNP:$NaBH_4$ =1:10:500.

The catalytic activity of the synthesized AuNPs catalysts studied in the previous chapter was investigated for transfer hydrogenation of *p*-nitrophenol (PNP) to *p*-aminophenol (PAP) by $NaBH_4$. Figure 3.1 shows typical changes of UV-vis absorption spectra during the reaction. The absorption band at 400 nm is characteristic for PNP solution in the presence of $NaBH_4$. Upon the addition of $NaBH_4$, the color of PNP solution changed from slight yellow to bright yellow due to the formation of *p*-nitrophenolate ion. The peaks at 400 nm gradually decreased and new peaks appeared at 295 nm after the addition of the catalyst, corresponding to the product PAP formation. The absence of well-defined isosbestic points at 280 and 313 nm in Fig. 3.1 is due to hydrogen gas bubbles formed during the reaction causing a minor degree of scattering. A separated experiment was conducted under static condition by using double amount of catalyst in order to investigate this matter. Two isosbestic points were clearly observed after the reaction which can be seen in the Fig. S3.1. The absence of isosbestic point also indicates that multiple intermediates are generated and showed at the same absorbance as PAP (near 300 nm) before being further reduced to PAP.[1,19–21] Figure 3.2 shows a multiple step reaction path of PNP before fully converted to PAP. GC measurement was performed to double check the final product after the reaction and compared it with the purchased PAP. The only observed peaks that appear at the same retention time as the purchased compounds are the internal standard (diglyme) and PAP. These results confirm that the reaction is highly selective to convert PNP to PAP without any byproducts.

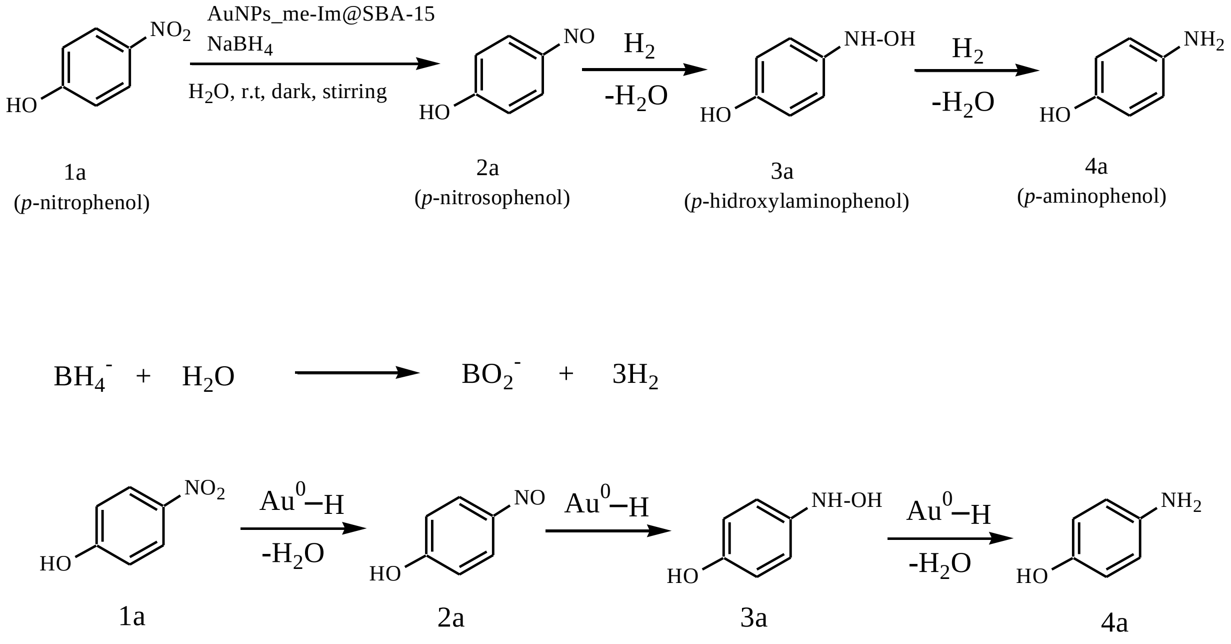

Fig. 3.2. Proposed mechanism for the reduction of *p*-nitrophenol and intermediates on Au nanoparticle surface.

Since the concentration of $NaBH_4$ is much higher than that of PNP (approximately 50 times), the $NaBH_4$ concentration remain essentially constant during the reaction and it could be reasonably assumed that the reaction follows a pseudo-first-order kinetics.[3,10,22–24] The average apparent reaction rate constant with error (k_{app} ± error value) was calculated by measuring the absorbance (A) of PNP at 400 nm and plotting $\ln(C_t/C_0)$ versus reaction time (t). The error value was given by repeated experiment in which each condition was repeated three times using fresh catalyst. The ratios of PNP concentrations (C_t) to the initial concentration (C_0) were given by the relative intensity of the respective absorbance (A_t/A_0) at 400 nm. The k_{app} was measured from the slope of the line along with the R^2 value for each catalyst after the induction period as shown in Fig. S3.2. The negative slope of the line of best fit in the plot gives the pseudo-first-order rate constant and the average k_{app} values are summarized in Table 3.1.

The induction period was observed at the beginning of reaction in each reaction using different size of AuNPs catalyst. Since the NPs are mainly located inside pores of SBA-15, it suggests that the reaction is limited by the diffusion of reactants to the active sites. Therefore, the induction period could be defined as the time required for hydrogen species and PNP to attach and react on the AuNP surface inside porous SBA-15 as described in Fig. 3.2. In addition, Ballauff *et al.* suggested that the delay time is caused by the reduction of oxygen present in the system which proceeds much faster than the reduction of PNP and as a result, the reaction could only initiate once all the dissolved oxygen was consumed.[25,26] Recently, Neretina *et al*. also claimed that dissolved oxygen is responsible for the induction period which is caused by the rapid conversion of PAP (or *p*-aminophenolate) back into *p*-nitrophenolate by a side reaction that terminates when the dissolved oxygen is consumed.[24] After an induction period where no reaction seemingly occurred, a pseudo-first-order reaction proceeds yielding PAP that rapidly desorbed from the AuNPs surfaces.

3.3.1. Effect of nanoparticle size

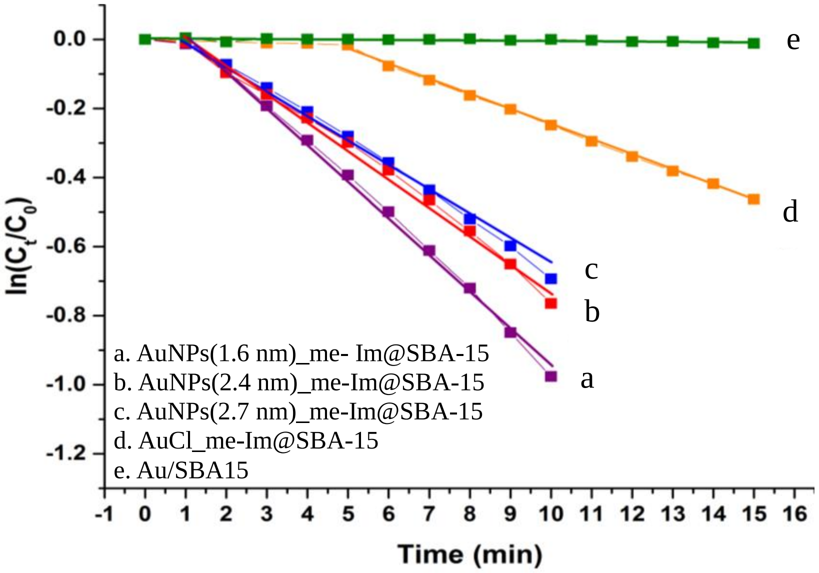

Fig. 3.3. The relationship between ln(C_t/C_0) and reaction time (t) of different prepared AuNPs catalysts on the reduction of *p*-nitrophenol.

To investigate the difference in catalytic performance of AuNPs containing immobilized ionic liquid catalysts with different size, the smallest NPs with the size of 1.6, 2.4 and 2.7 nm with the capsule-like shape were selected for the reaction. The results in Fig. 3.3 show that AuNPs(1.6 nm)_me-Im@SBA-15 gave the highest kinetic constant as compared to that of AuNPs with larger size (Table 3.1). This result suggests that the smallest NPs have higher catalytic activity compared to larger NPs. Small NPs have larger surface area to volume ratio and in this system, they could minimize pore-blocking that can be caused by large particles on porous materials, facilitating the reactant to access the active sites deeper inside porous channels, which resulted in better catalytic performance.

AuNPs prepared without IL, Au/SBA-15, showed mainly large NPs with average size of 5.6 nm (see Fig. S3.3). The formation of these large NPs showed how IL contributed to controlling the growth of NPs as discussed earlier in the previous chapter. The pore-blocking effect caused by these large NPs limits the accessibility of the reactant to reach the active sites inside pores which explains slow reaction resulting in low k_{app} value. In the case of reaction catalyzed by AuCl_me-Im@SBA-15 catalyst, the induction period occurred from t = 0–5 min suggesting that the PNP reduction cannot proceed before the complete reduction of $AuCl_2^-$ complex anions to AuNPs as shown in Fig. 3.3.

Table 3.1. The average apparent rate constant (k_{app}) of the prepared AuNPs catalysts in the reduction of PNP.*

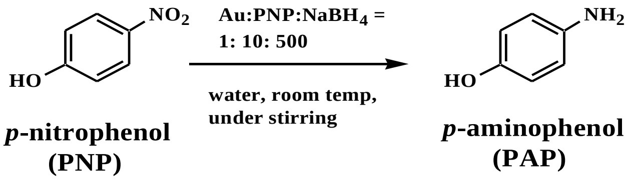

Sample	Catalyst	k_{app} x10^{-3} (s^{-1})
a.	AuNPs(1.6 nm)_me-Im@SBA-15	1.73 ± 0.07
b.	AuNPs(2.4 nm)_me-Im@SBA-15	1.50 ± 0.04
c.	AuNPs(2.7 nm)_me-Im@SBA-15	1.40 ± 0.06
d.	AuCl_me-Im@SBA-15	0.65 ± 0.05
e.	Au/SBA-15 (5.6 nm)	0.03 ± 0.00

* $Au/PNP/NaBH_4$ = 1/10/500 (0.3 mg / 0.1 mM/ 5mM)

To further confirm the active species of these catalysts in PNP reduction, a series of experiment was conducted by using SBA-15, me-Im@SBA-15, AuNPs(1.6 nm)_me-Im@SBA-15 and in the absence of any catalyst. Figure S3.4 shows plots of absorbance at 400 nm versus time for different condition. No decrease in PNP absorbance intensity at 400 nm was observed for the reaction catalyzed by SBA-15 and me-Im@SBA-15 which showed the same result as the system without any solid material. However, after the addition of AuNPs(1.6 nm)_me-Im@SBA-15 the absorbance at 400 nm dramatically decrease as a function of time. This means that the solid material SBA-15 as well as the immobilized IL on SBA-15 gave no effect in the catalytic activity without the presence of AuNPs. This also suggests that the reaction takes place on the surface of AuNPs as illustrated in Fig. 3.2.

3.3.2. Effect of NaBH$_4$ concentration

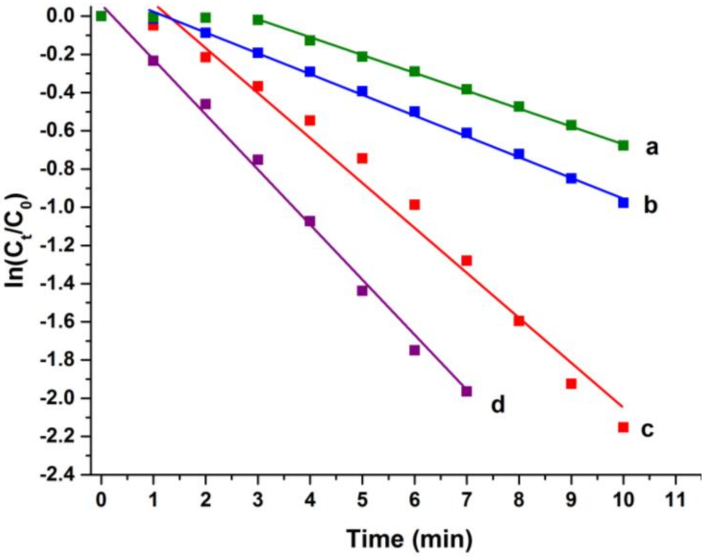

Fig. 3.4. The relationship between ln(C$_t$/C$_0$) and reaction time (t) in the effect of NaBH$_4$ concentration and catalyst loading in the reduction of *p*-nitrophenol catalyzed by AuNPs(1.6 nm)_me-Im@SBA-15.

The effects of $NaBH_4$ concentration and the catalyst loading in the reduction of PNP were also investigated. The concentration of $NaBH_4$ was varied from 5 to 10 mM while maintaining constant concentration of PNP (0.1 mM) and the amount of catalyst (0.3 mg). Figure 3.4 shows that the reaction rate increased with the increasing concentration of $NaBH_4$. The apparent rate constant increased from 1.73×10^{-3} to 4.9×10^{-3} s^{-1} by increasing the concentration of $NaBH_4$ from 5 to 10 mM. On the other hand, the reaction rate decreased with decreasing amount of catalyst. This resulted in longer induction period (3 min) and decrease in k_{app} value. The rate constant value for each condition is summarized in Table 3.2.

Table 3.2. The effect of $NaBH_4$ concentration on the apparent rate constant (k_{app}) in the reduction of PNP catalyzed by AuNPs(1.6 nm)_me-Im@SBA-15.*

Sample	PNP/$NaBH_4$	Amount of catalyst (mg)	k_{app} x10^{-3} (s^{-1})
a.	1/50	0.2	1.45 ± 0.05
b.	1/50	0.3	1.73 ± 0.07
c.	1/80	0.3	3.95 ± 0.05
d.	1/100	0.3	4.90 ± 0.0

* PNP = 0.1 mM

3.3.3. Recycle study

The catalyst with the smallest NPs, AuNPs(1.6 nm)_me-Im@SBA-15, was used to study the recyclability of the synthesized catalysts. To ensure the amount of catalyst is enough to be used for consecutive recycling processes, 1 mg of the catalyst was initially used with the molar ratio of Au:PNP:$NaBH_4$ was kept constant to 1:10:500. The concentration of PNP and $NaBH_4$ in the cell was increased into 0.33 and 16.67 mM respectively. This new composition resulted in a very fast reaction with the rate constant of 28.8 x 10^{-3} s^{-1} (Fig. S3.5). Furthermore, in order to minimize the amount of used catalyst, 0.5 mg catalyst was used instead of 1 mg with 1 min time interval monitored by UV-vis spectroscopy. Figure 3.5 and Table 3.3 show that the catalyst was reusable at least four consecutive recycle processes. The catalyst was easily to be used in the next cycle after simply being washed with distilled water for a few times.

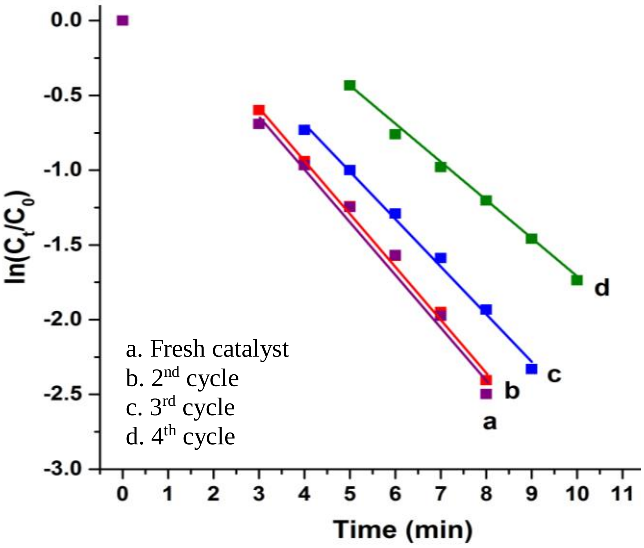

Fig. 3.5. The relationship between ln(C_t/C_0) and reaction time (t) in the reusability of the prepared AuNPs(1.6 nm)_me-Im@SBA-15 catalyst in the reduction of *p*-nitrophenol.

Since the concentration of PNP is high (0.33 mM), the extrapolation was used to determine the absorbance of PNP at t_0 (Fig. S3.6) and the rate constant was determined based on the linear relationship between ln(C_t/C_0) versus time (t). Detailed UV-vis spectra and the plot data of recycle processes can be seen in Fig. S3.7. The decrease in activity after the 2nd cycle could be due to the agglomeration process which took place during the consecutive recycle processes. Large NPs were observed together with small NPs inside porous SBA-15 of the reused catalyst as shown in Fig. S3.8, and thus increase the average AuNPs size from 1.6 to 1.9 nm. The decrease in rate constant may also be attributed to the adsorption of the product PAP on the surface of AuNPs which still remains even after the washing process, resulting in the surface blocking of the AuNPs surfaces.

Table 3.3. The rate constants of reusable AuNPs(1.6 nm)_me-Im@SBA-15 in the reduction of PNP.*

Sample	Catalyst	k_{app} x10^{-3} (s^{-1})
a.	Fresh catalyst	5.9
b.	2nd cycle	5.9
c.	3rd cycle	5.7
d.	4th cycle	4.9

* Au/PNP/$NaBH_4$ = 0.5/10/500 (0.5 mg / 0.33 mM/ 16.67 mM)

Table 3.4 compares the catalytic activity of AuNPs(1.6 nm)_me-Im@SBA-15, and the already reported ones in terms of apparent rate constant k'_{app} which is calculated from the normalization of apparent rate constant k_{app} to the amount of Au loading (mg) used in the PNP reduction. Compared with some previously reported AuNPs, the present immobilized AuNPs containing ionic liquid on SBA-15 presented better catalytic activity than those of supported AuNPs with different size and morphology on different supports.[3,6,8,11,27–29] It is noticed that the rate constant of AuNPs with 1.6 nm in size is higher than that of AuNPs with smaller NPs size.[8] Moreover, AuNPs(1.6 nm)_me-Im@SBA-15 also shows better performance than that of similar feature catalyst, SBA-15-Im$^+$-Au1.0, with bigger NPs size.[3] TOF (Turnover frequency) value is also presented in Table 3.4. TOF is defined as the moles of PNP converted divided by the moles of Au per hour, whereas the PNP conversion is calculated from the UV-Vis absorption data. Judging from the TOF values, the present catalyst gave the good performance as compared to the other reported values. The ratio of the surface Au atoms with respect to the whole Au atoms included in 1.6 nm-Au nanoparticles was calculated as 0.720 based on the mean diameter of 1.6 nm and the Au metallic atom radius 0.144 nm. With this factor we can correct TOF values considering the number of surface atoms of Au nanoparticle.

Table 3.4. Comparison of pseudo-first-order rate constant for PNP reduction by various supported gold nanoparticles.

Catalyst	AuNPs Size (nm)	Au loading (wt%)	Amount of catalyst (mg)	Mole ratio of PNP:$NaBH_4$	k_{app} (10^{-3} s^{-1})	k'_{app}* (10^{-3} $s^{-1}mg^{-1}$)	TOF** (h^{-1})	Ref.
AuNPs(1.6 nm)_ me-Im@SBA-15	1.6	2	0.3	1:50	1.73	288.3	26.32	this work
		2	1	1:50	28.8	1440	322.34	this work
Au/ZSBA-PL	4.0	0.16	1	1:100	2.33	518.75	4.86	8
SBA-15-Im^+-Au1.0	~5	1.74	20	1:50	1.06	3.05	-	3
R-Au nanocomposites	8	13.94	6	1:66.7	0.27	0.32	$9.96x10^7$ ($g^{-1}s^{-1}$)	11
Au@CeO_2	~5	0.31	10	11:464	2.16	69.7	-	27
Au-Fe_3O_4	5	19	2	1:40	10.5	27.6	-	6
Fe_3O_4@SiO_2 -Au@mSiO_2	12	2.2	3	1:400	3.3–5.8	50.45-88.3	-	28
Au/g-C_3N_{4-6}	2.6	4.35	1	1:15	8	183.68	115.7	29
AuNPs/SNTs	3-5	2.46	8	1:42	10.64	54.06	46	30
Cu/CuO-TiO_2	70	0.0024 mg Cu	0.6 x 0.6 cm^2	1:100	13.6	5666.6	115	31

* apparent rate constant per mg Au, ** calculated as the moles of PNP converted on per mole Au atom per hour.

The conversion of PNP is expressed by: $Conversion = \left(1 - \frac{At}{A0}\right) x\ 100\%$

3.4. Conclusion

In this study, the size dependency of the prepared AuNPs_me-Im@SBA-15 catalysts was investigated for *p*-nitrophenol hydrogenation reaction using $NaBH_4$. The catalyst with the smallest NPs, AuNPs(1.6 nm)_me-Im@SBA-15, exhibited the highest catalytic performance with the apparent rate constant k_{app} 1.73 x 10^{-3} s^{-1} and highly selective to convert PNP to PAP. On the other hand, Au/SBA-15 with the size of 5.6 nm which was synthesized in the absence of ionic liquid exhibited the lowest catalytic activity with the k_{app} value 0.03 x 10^{-3} s^{-1}. The activity increases as the increasing amount of catalyst and $NaBH_4$ concentration. The catalyst was reusable for four consecutive recycle processes without a significant decrease in activity with simple procedure. The size of AuNPs increased from 1.6 to 1.9 nm after the 4th cycle due to agglomeration during the successive recycle processes.

3.5. References

(1) Li, M.; Chen, G. Revisiting Catalytic Model Reaction *p*-Nitrophenol/NaBH$_4$ Using Metallic Nanoparticles Coated on Polymeric Spheres. *Nanoscale* **2013**, *5* (23), 11919.

(2) Javaid, R.; Kawasaki, S. I.; Suzuki, A.; Suzuki, T. M. Simple and Rapid Hydrogenation of *p*-Nitrophenol with Aqueous Formic Acid in Catalytic Flow Reactors. *Beilstein J. Org. Chem.* **2013**, *9*, 1156–1163.

(3) Damasceno, J. P. V.; Maroneze, C. M.; Strauss, M.; Sigoli, F. A.; Mazali, I. O. Preparation of Supported AuPd Nanoalloys Mediated by Ionic Liquid-like Functionalized SBA-15: Structural Correlations Concerning Its Catalytic Activity. *New J. Chem.* **2016**, *40* (8), 6636–6642.

(4) Rana, S.; Jonnalagadda, S. B. A Facile Synthesis of Cu–Ni Bimetallic Nanoparticle Supported Organo Functionalized Graphene Oxide as a Catalyst for Selective Hydrogenation of *p*-Nitrophenol and Cinnamaldehyde. *RSC Adv.* **2017**, *7* (5), 2869–2879.

(5) Xiao, Q.; Sarina, S.; Waclawik, E. R.; Jia, J.; Chang, J.; Riches, J. D.; Wu, H.; Zheng, Z.; Zhu, H. Alloying Gold with Copper Makes for a Highly Selective Visible-Light Photocatalyst for the Reduction of Nitroaromatics to Anilines. *ACS Catal.* **2016**, *6* (3), 1744–1753.

(6) Lin, F.; Doong, R. Bifunctional Au-Fe$_3$O$_4$ Heterostructures for Magnetically Recyclable Catalysis of Nitrophenol Reduction. *J. Phys. Chem. C* **2011**, No. 115, 6591–6598.

(7) Pozun, Z. D.; Rodenbusch, S. E.; Keller, E.; Tran, K.; Tang, W.; Stevenson, K. J.; Henkelman, G. A Systematic Investigation of *p*-Nitrophenol Reduction by Bimetallic Dendrimer Encapsulated Nanoparticles. *J. Phys. Chem. C* **2013**, *117* (15), 7598–7604.

(8) Gao, D.; Zhang, X.; Dai, X.; Qin, Y.; Duan, A.; Yu, Y.; Zhuo, H. Morphology-Selective

Synthesis of Active and Durable Gold Catalysts with High Catalytic Performance in the Reduction of 4-Nitrophenol. *Nano Res.* **2016**, *9* (10), 3099–3115.

(9) Signori, A. M.; De O. Santos, K.; Eising, R.; Albuquerque, B. L.; Giacomelli, F. C.; Domingos, J. B. Formation of Catalytic Silver Nanoparticles Supported on Branched Polyethyleneimine Derivatives. *Langmuir* **2010**, *26* (22), 17772–17779.

(10) Ma, T.; Yang, W.; Liu, S.; Zhang, H.; Liang, F. A Comparison Reduction of 4-Nitrophenol by Gold Nanospheres and Gold Nanostars. *catalysts* **2017**, No. 7, 38.

(11) Panigrahi, S.; Basu, S.; Praharaj, S.; Pande, S.; Jana, S.; Pal, A.; Ghosh, S. K.; Pal, T. Synthesis and Size-Selective Catalysis by Supported Gold Nanoparticles: Study on Heterogeneous and Homogeneous Catalytic Process. *J. Phys. Chem. C* **2007**, *111* (12), 4596–4605.

(12) Chang, Y. C.; Chen, D. H. Catalytic Reduction of 4-Nitrophenol by Magnetically Recoverable Au Nanocatalyst. *J. Hazard. Mater.* **2009**, *165* (1–3), 664–669.

(13) Chiou, J. R.; Lai, B. H.; Hsu, K. C.; Chen, D. H. One-Pot Green Synthesis of Silver/Iron Oxide Composite Nanoparticles for 4-Nitrophenol Reduction. *J. Hazard. Mater.* **2013**, *248–249* (1), 394–400.

(14) Sahiner, N.; Ozay, H.; Ozay, O.; Aktas, N. A Soft Hydrogel Reactor for Cobalt Nanoparticle Preparation and Use in the Reduction of Nitrophenols. *Appl. Catal. B Environ.* **2010**, *101* (1–2), 137–143.

(15) Guo, P.; Tang, L.; Tang, J.; Zeng, G.; Huang, B.; Dong, H.; Zhang, Y.; Zhou, Y.; Deng, Y.; Ma, L.; et al. Catalytic Reduction-Adsorption for Removal of *p*-Nitrophenol and Its Conversion *p*-Aminophenol from Water by Gold Nanoparticles Supported on Oxidized Mesoporous Carbon. *J. Colloid Interface Sci.* **2016**, *469*, 78–85.

(16) Du, Y.; Chen, H.; Chen, R.; Xu, N. Synthesis of *p*-Aminophenol from *p*-Nitrophenol over Nano-Sized Nickel Catalysts. *Appl. Catal. A Gen.* **2004**, *277* (1–2), 259–264.

(17) Rode, C. V.; Vaidya, M. J.; Chaudhari, R. V. Synthesis of *p*-Aminophenol by Catalytic Hydrogenation of Nitrobenzene. *Org. Process Res. Dev.* **1999**, *3* (6), 465–470.

(18) Corbett, J. F. An Historical Review of the Use of Dye Precursors in the Formulation of Commercial Oxidation Hair Dyes. *Dye. Pigment.* **1999**, *41* (1), 127–136.

(19) Yamamoto, H.; Yano, H.; Kouchi, H.; Obora, Y.; Arakawa, R.; Kawasaki, H. *N,N*-Dimethylformamide-Stabilized Gold Nanoclusters as a Catalyst for the Reduction of 4-Nitrophenol. *Nanoscale* **2012**, *4* (14), 4148.

(20) Bhandari, R.; Knecht, M. R. Effects of the Material Structure on the Catalytic Activity of Peptide-Templated Pd Nanomaterials. *ACS Catal.* **2011**, *1* (2), 89–98.

(21) Souza, F. D.; Fiedler, H.; Nome, F. Zwitterionic Surfactant Stabilized Palladium Nanoparticles as Catalysts in Aromatic Nitro Compound Reductions. *J. Braz. Chem. Soc.* **2016**, *27* (2), 372–381.

(22) Gu, S.; Wunder, S.; Lu, Y.; Ballau, M.; Fenger, R.; Rademann, K. Kinetic Analysis of the Catalytic Reduction of 4-Nitrophenol by Metallic Nanoparticles. *J. Phys. Chem. C* **2014**, *118*, 18618–18625.

(23) Nigra, M. M.; Ha, J.-M.; Katz, A. Identification of Site Requirements for Reduction of 4-Nitrophenol Using Gold Nanoparticle Catalysts. *Catal. Sci. Technol.* **2013**, No. 3, 2976–2983.

(24) Menumerov, E.; Hughes, R. A.; Neretina, S. Catalytic Reduction of 4-Nitrophenol: A Quantitative Assessment of the Role of Dissolved Oxygen in Determining the Induction Time. *Nano Lett.* **2016**, 7791−7797.

(25) Lu, Y.; Mei, Y.; Walker, R.; Ballauff, M.; Drechsler, M. ‘Nano-Tree’—type Spherical Polymer Brush Particles as Templates for Metallic Nanoparticles. *Polymer (Guildf).* **2006**, *47*, 4985–4995.

(26) Mei, Y.; Lu, Y.; Polzer, F.; Ballauff, M.; Drechsler, M. Catalytic Activity of Palladium Nanoparticles Encapsulated in Spherical Polyelectrolyte Brushes and Core-Shell Microgels. *Chem. Mater.* **2007**, *19* (5), 1062–1069.

(27) Zhang, J.; Chen, G.; Chaker, M.; Rosei, F.; Ma, D. Gold Nanoparticle Decorated Ceria Nanotubes with Significantly High Catalytic Activity for the Reduction of Nitrophenol and Mechanism Study. *Appl. Catal. B, Environ.* **2013**, *132–133*, 107–115.

(28) Deng, Y.; Cai, Y.; Sun, Z.; Liu, J.; Liu, C.; Wei, J.; Li, W.; Liu, C.; Wang, Y.; Zhao, D. Multifunctional Mesoporous Composite Microspheres with Well-Designed Nanostructure: A Highly Integrated Catalyst. *J. Am. Chem. Soc.* **2010**, *132* (24), 8466–8473.

(29) Fu, Y.; Huang, T.; Jia, B.; Zhu, J.; Wang, X. Reduction of Nitrophenols to Aminophenols under Concerted Catalysis by Au/g-C_3N_4 Contact System. *Appl. Catal. B Environ.* **2017**, *202*, 430–437.

(30) Zhang, Z.; Shao, C.; Zou, P.; Zhang, P.; Zhang, M.; Mu, J.; Guo, Z.; Li, X.; Wang, C.; Liu, Y. In Situ Assembly of Well-Dispersed Gold Nanoparticles on Electrospun Silica Nanotubes for Catalytic Reduction of 4-Nitrophenol. *Chem. Commun.* **2011**, *47*, 3906–3908.

(31) Jin, Z.; Liu, C.; Qi, K.; Cui, X. Photo-Reduced Cu/CuO Nanoclusters on TiO_2 Nanotube Arrays as Highly Efficient and Reusable Catalyst. *Nat. Sci. Reports* **2017**, *7* (39695), 1–9.

3.6. Supporting information

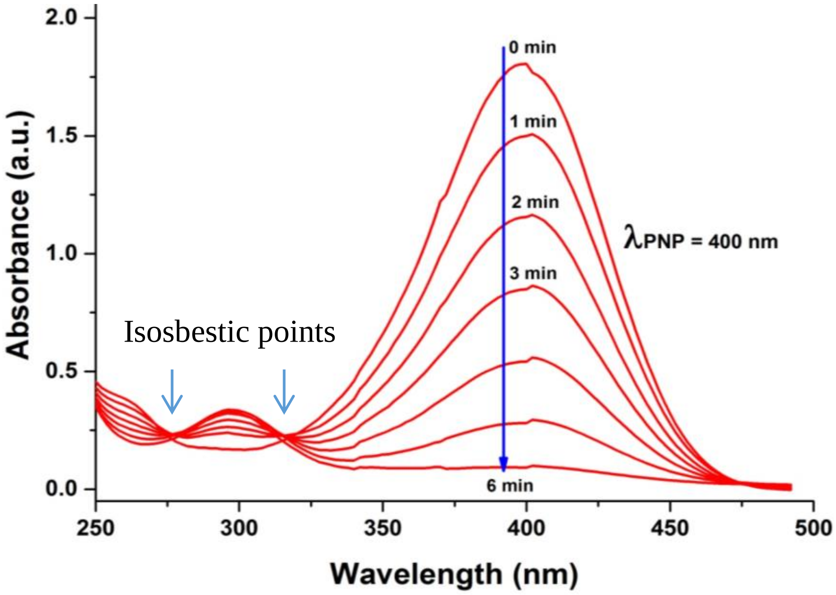

Fig. S3.1. UV-Vis absorption spectra of PNP reduction at 1 min interval catalyzed by AuNPs(1.6 nm)_me-Im@SBA-15 at 25 °C.

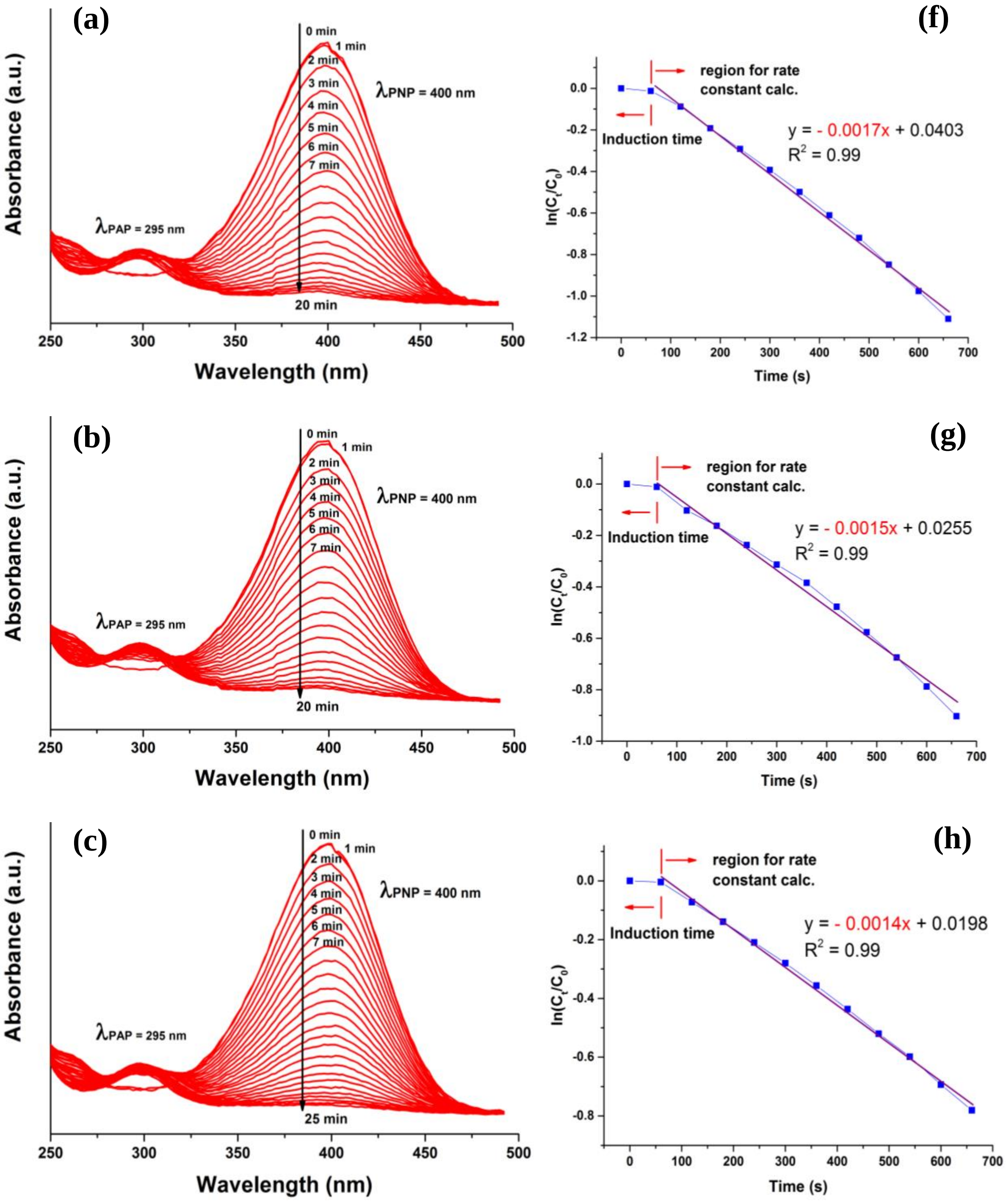

Fig. S3.2. (a-e) UV-vis absorption spectra of PNP reduction at 1 min interval catalyzed by (a) AuNPs(1.6 nm)_me-Im@SBA-15, (b) AuNPs(2.4 nm)_me-Im@SBA-15, (c) AuNPs(2.7 nm)_me-Im@SBA-15, (d) AuCl_me-Im@SBA-15, and (e) AuNPs(5.6 nm)@SBA-15; with respect to the linear relationship of ln(C_t/C_0) versus time (t) for each catalyst (f-j).

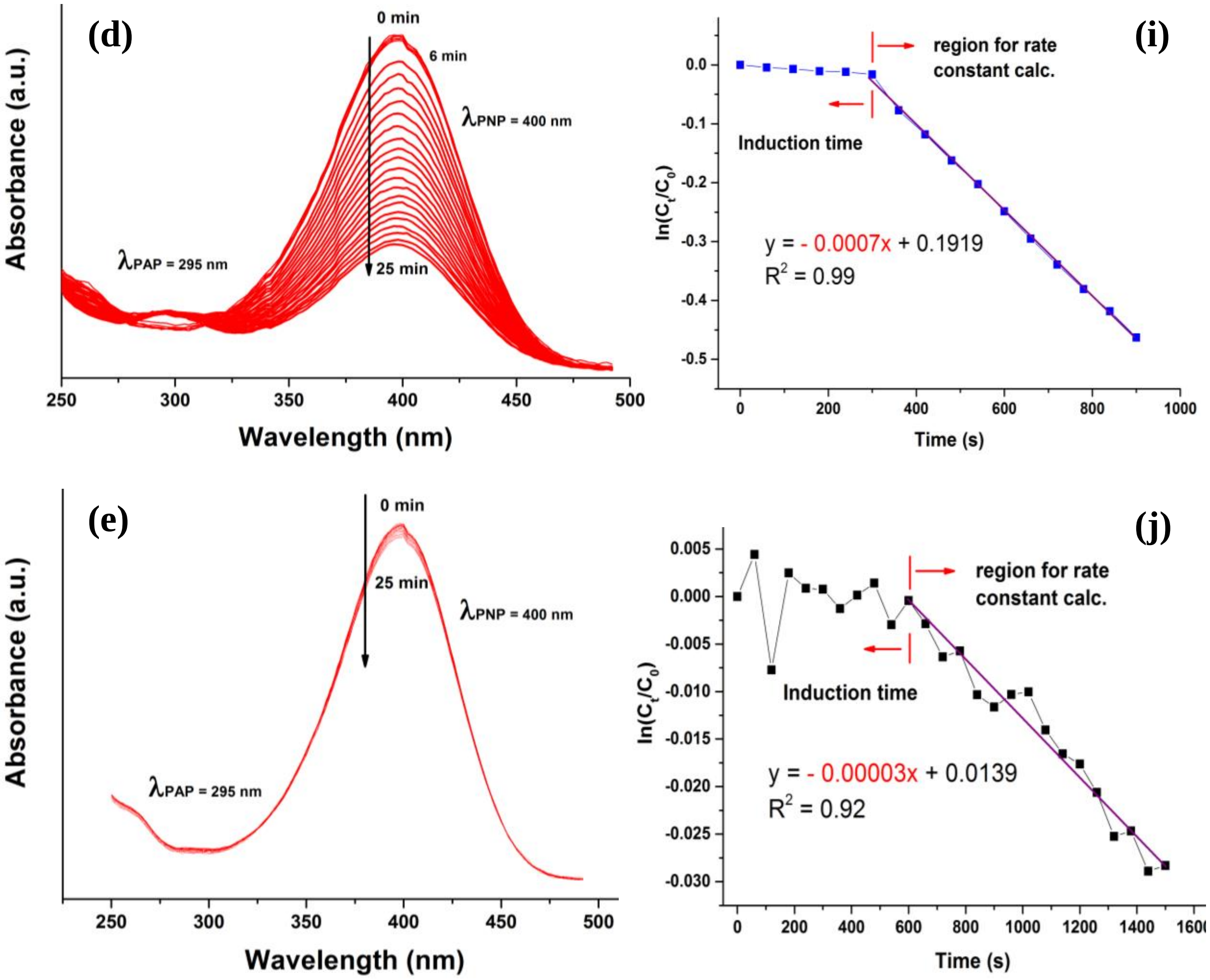

Fig. S3.2. (a-e) UV-vis absorption spectra of PNP reduction at 1 min interval catalyzed by (a) AuNPs(1.6 nm)_me-Im@SBA-15, (b) AuNPs(2.4 nm)_me-Im@SBA-15, (c) AuNPs(2.7 nm)_me-Im@SBA-15, (d) AuCl_me-Im@SBA-15, and (e) AuNPs(5.6 nm)@SBA-15; with respect to the linear relationship of ln(C_t/C_0) versus time (t) for each catalyst (f-j). (Figure S3.3 continued)

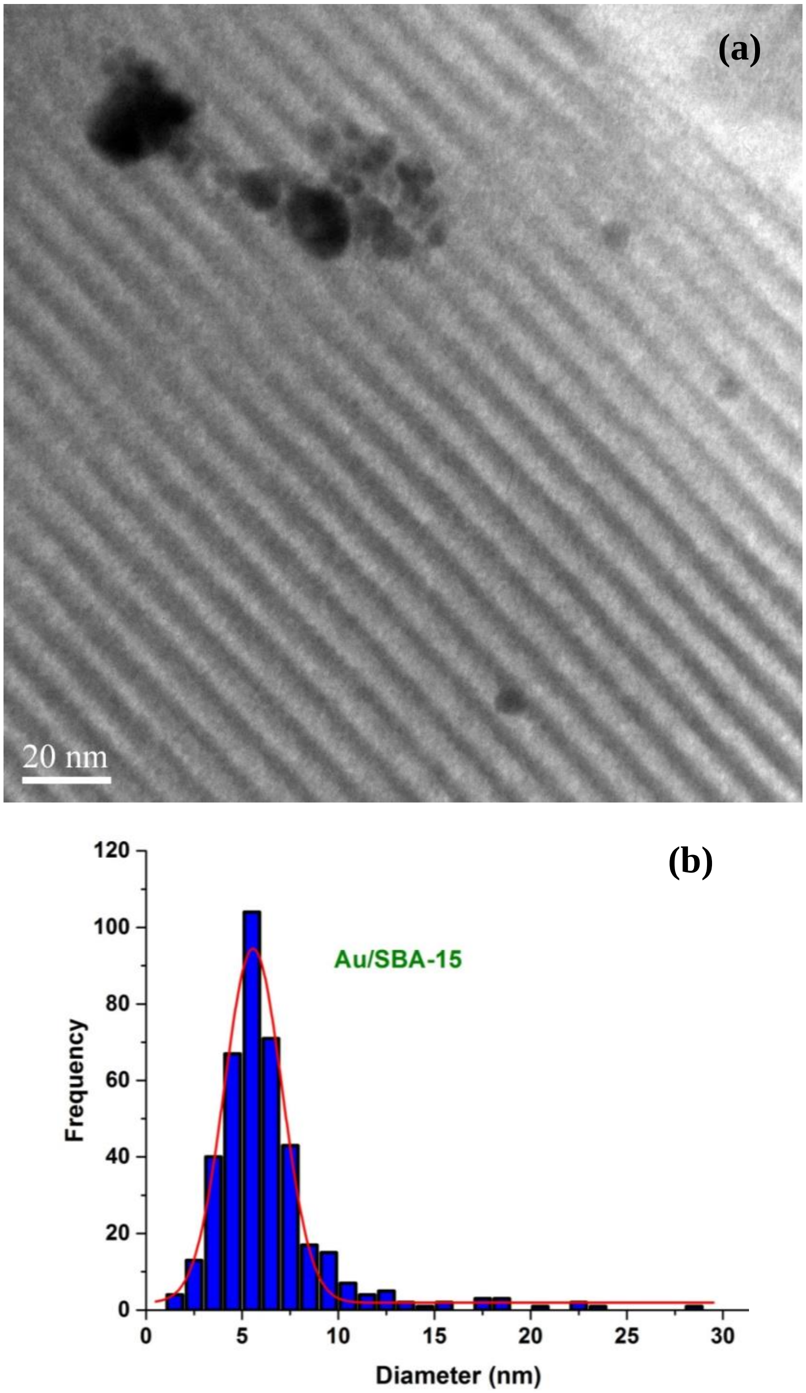

Fig. S3.3. (a) TEM image and (b) particle size distribution of Au/SBA-15.

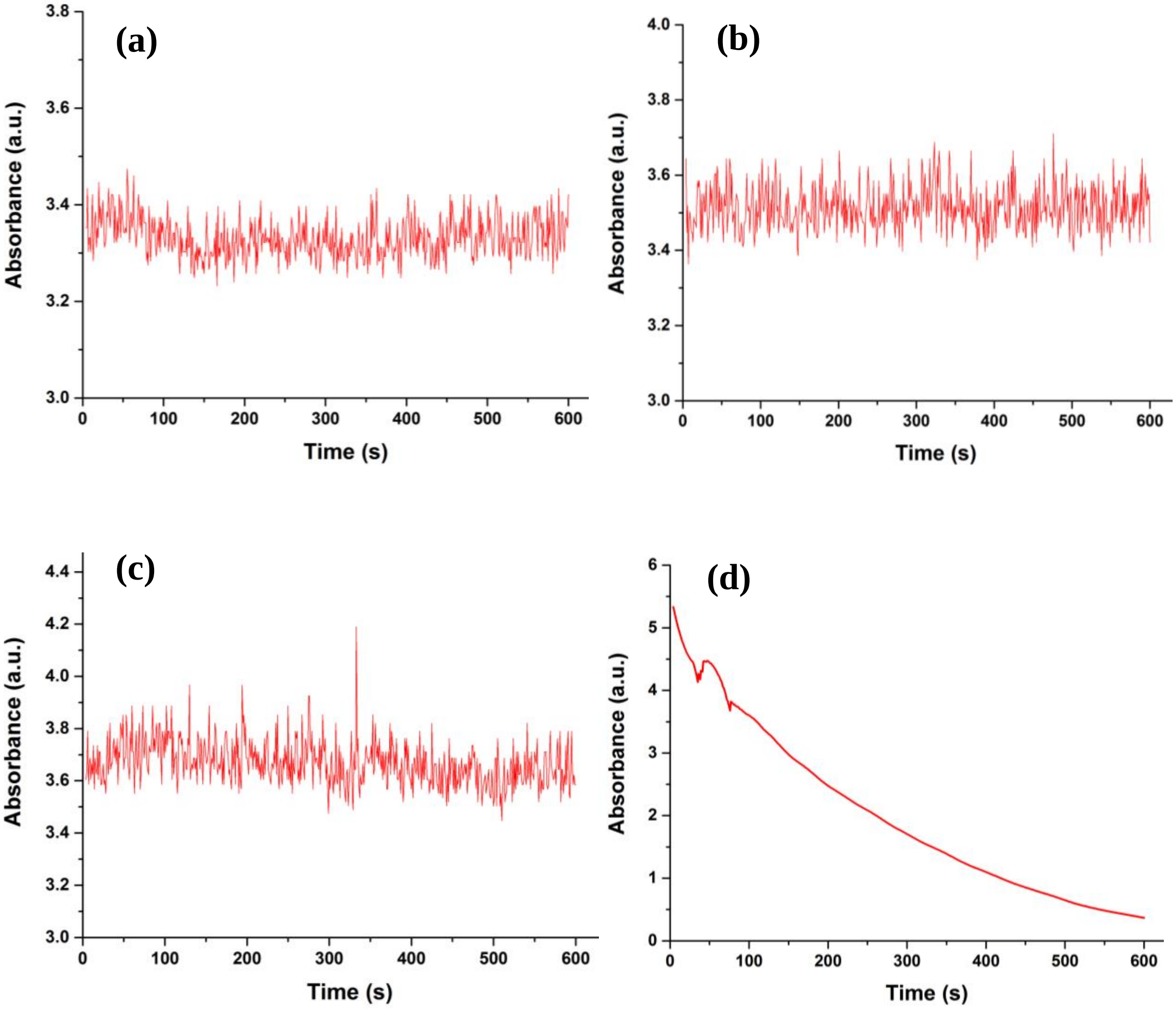

Fig. S3.4. PNP absorbance at 400 nm versus time for catalyst tests: (a) without any solid material, (b) SBA-15, (c) me-Im@SBA-15, and (d) AuNPs(1.6 nm)_me-Im@SBA-15.

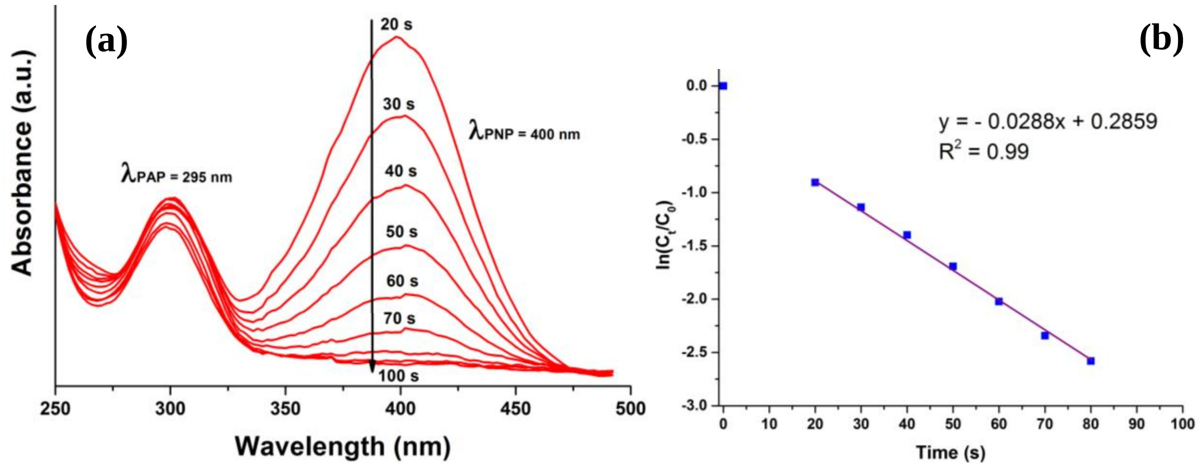

Fig. S3.5. (a) UV-vis absorption spectra of PNP reduction at 10 s interval catalyzed by 1 mg of AuNPs(1.6 nm)_me-Im@SBA-15, and (b) its linear relationship of ln(C_t/C_0) versus time (t) (concentration of PNP and $NaBH_4$ in the cell is 0.33 and 16.67 mM respectively).

The extrapolation procedure was used to determine the absorbance A_0 at t = 0 of high concentration of PNP and $NaBH_4$ in the cell (0.3 and 16.67 mM respectively). The slope was determined from the linear relationship of absorbance versus concentration of PNP. The absorbance values were obtained from five different concentration of PNP which is 0.03, 0.06, 0.08, 0.1 and 0.12 mM.

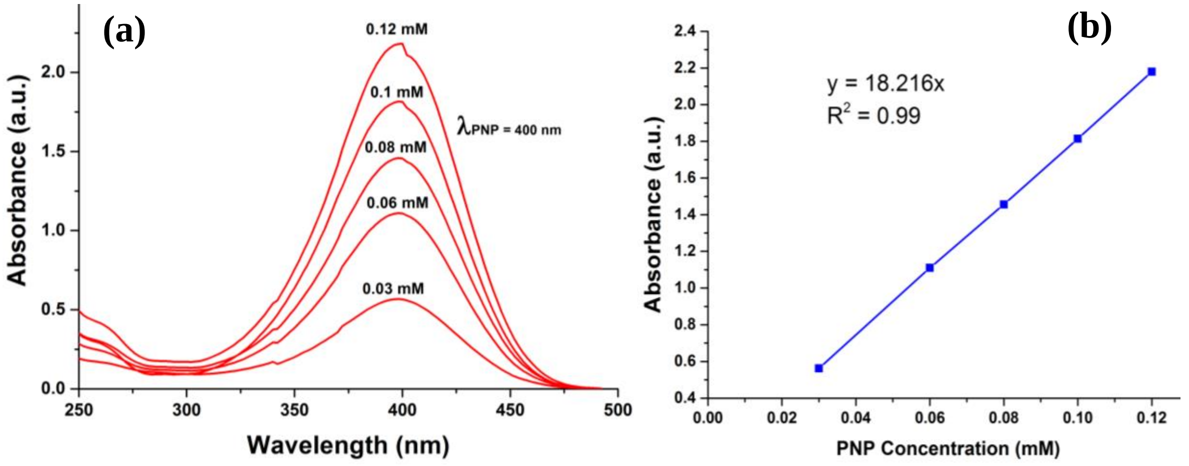

Fig. S3.6. (a) UV-vis absorption spectra of PNP with different concentration and (b) the extrapolation result from a plot of absorbance versus concentration.

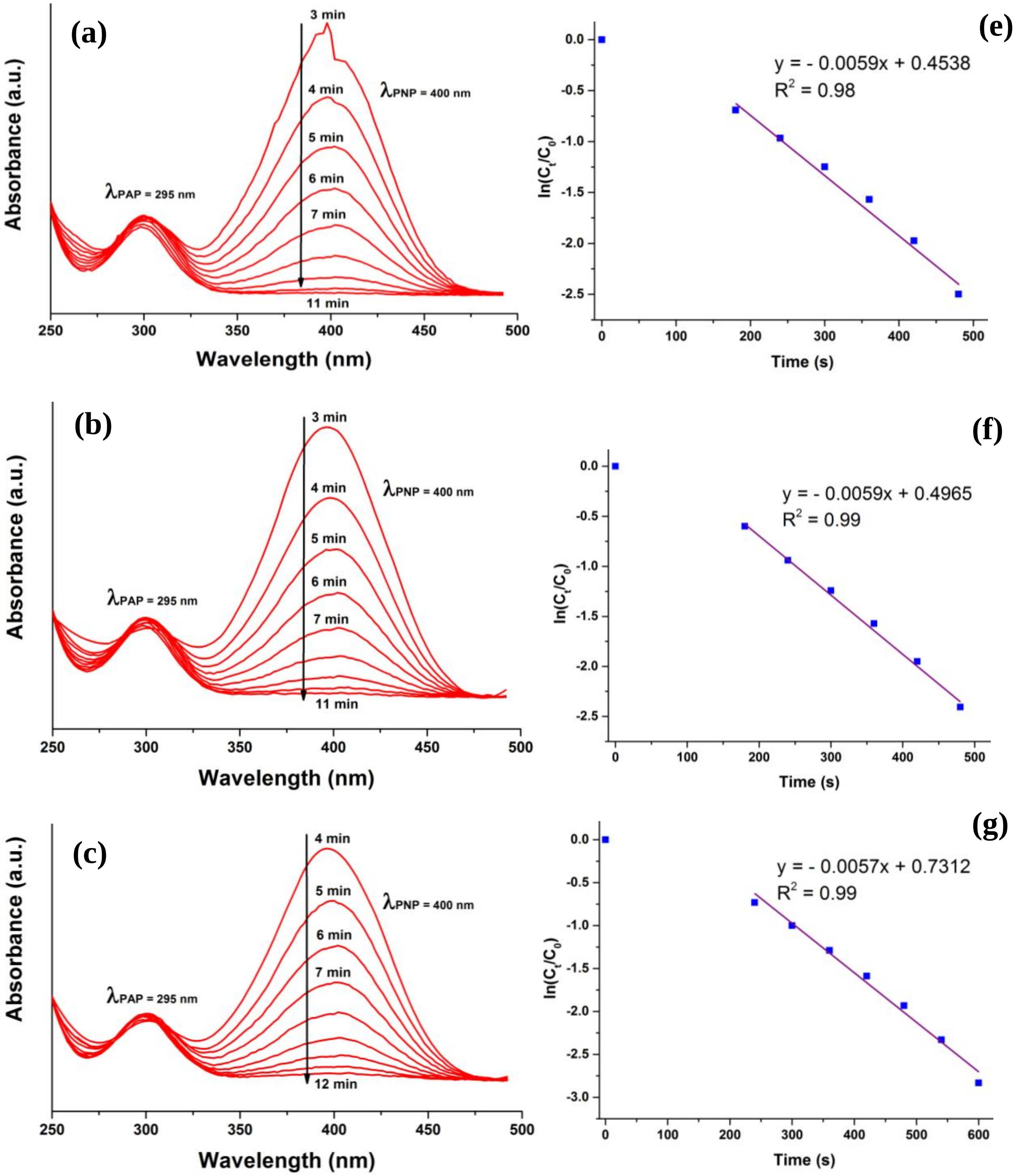

Fig. S3.7. Recyclability study of AuNPs(1.6 nm)_me-Im@SBA-15 in PNP reduction: (a-d) UV-vis spectra at 1 min interval by (a) fresh catalyst, (b) 2nd, (c) 3rd, and (d) 4th cycle; with respect to the linear relationship of $\ln(C_t/C_0)$ versus time (t) for each cycle (e-h).

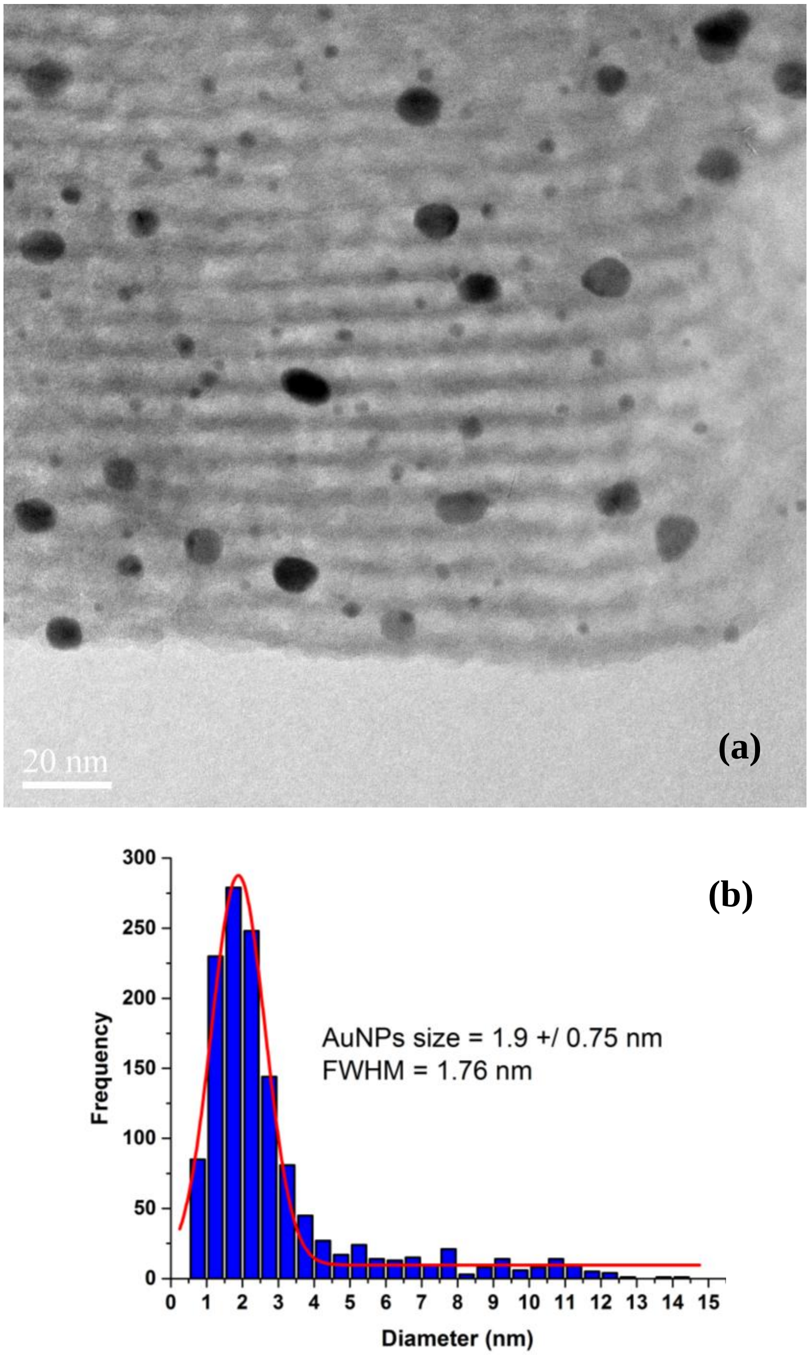

Fig. S3.8. (a) TEM image of reused AuNPs(1.6 nm)_me-Im@SBA-15 after the 4th cycle of PNP reduction and (b) size distribution histogram.

Chapter 4

Immobilization of Various Metal Nanoparticles on Ionic Liquids Functionalized SBA-15 as Active and Reusable Catalysts

Abstract

Various metal nanoparticles were successfully supported on SBA-15 in the presence of immobilized ionic liquids by the chemical reduction using $NaBH_4$ solution at fixed feed rate. In addition, palladium NPs with the immobilized imidazolium with different N-alkyl groups were prepared in order to study its effects on the particle size as well as the catalytic performance. The activity and reusability of the prepared metal nanoparticles with average size of 2–4 nm was studied for *p*-nitrophenol hydrogenation reaction. The prepared catalysts were characterized by TEM, XAFS, XPS, FTIR, XPS, solid state NMR and N_2 adsorption-desorption isotherm.

4.1. Introduction

Catalytically active nanoparticles (NPs) are unstable and tend to agglomerate and subject to sintering to minimize their surface energies under reaction conditions, especially at high reaction temperature.[1,2] The use of organic stabilizing or capping agents to stabilize NPs is the most efficient way to control the nucleation and growth of nanoparticles and protect them from sintering or further agglomeration during the catalytic reaction. These organic molecules however, often result in reduced activity of the catalysts due to the diffusion limitations and/or surface blocking of the active sites.[3,4] In the case of heterogeneous catalyst prepared from these colloidal nanoparticles, additional steps are required to eliminate the stabilizers from the surface of metal nanoparticles and immobilize onto solid support before the catalyst can be used.

On the other hand, in some cases metal NPs when dispersed on the surface of support materials showed much more active and selective compared to bulk particles.[1,5] The role of supports appears to be important since it can affect the nanoparticle stability and activity due to the interaction between the nanoparticles and support.[6–10] The use of either active or inert supports for metal NPs are both popular subjects to investigate. Mesoporous silica SBA-15 on the other hand, as an inert support offers many advantages such as uniform pore size distribution, large pore size and surface area, and easy surface modification.

Our research group reported successful immobilization of various metal ions containing ionic liquids on silica for various organic transformations, such as Kharash reaction, Suzuki cross-coupling reaction, alkoxylation, carbonylation, hydrogenation reaction, etc.[11–18] A series of metals ion-containing ILs on silica Aerosil 300 were prepared by immobilization of imidazolium ionic molecules on silanol groups of silica surfaces followed by addition of metal chloride as the metal precursor ($MnCl_2$, $FeCl_2$, $CoCl_2$, $NiCl_2$, $CuCl_2$, $PdCl_2$ and $PtCl_2$) and the local structure of metal was analyzed by EXAFS analysis.[11,13] In addition, palladium ion-containing ionic liquid on mesoporous SBA-15 was prepared as active and reusable catalyst for the synthesis of oxamate and urea by oxidative single and double carbonylation of amines, and also for polyester amide synthesis via carbonylation-polycondensation reaction.[19,20]

In 2012, Fattori and coworkers employed imidazolium-grafted on SBA-15 to immobilized AuNPs inside porous channels.[21] The AuNPs were mainly observed inside pores in highly dispersed state and found stable after thermal treatment at 973 K. More recently, Mazali *et al.* reported the preparation of supported AuPd nanoalloys on imidazolium-functionalized SBA-15 and investigated the structural correlations toward 4-nitrophenol hydrogenation reaction.[22] Small alloys between 1-5 nm with non-passivated surfaces were obtained and highly dispersed on SBA-15.

In Chapter 2, the size-controlled synthesis of AuNPs was successfully achieved on SBA-15 in the presence of immobilized ionic liquids by varying the concentration and feed rate of $NaBH_4$.[23] In this study, the synthetic approach studied in Chapter 2 was applied to support various metal NPs such as Pd, Au, Cu, Pt and Ru by reduction with 100 mM $NaBH_4$ at a fixed feed rate. The size and structural properties of metal nanoparticles before and after the reduction were studied by TEM and XAFS analysis. The activity and reusability of the prepared metal NPs was investigated for *p*-nitrophenol hydrogenation reaction at room temperature (25 °C).

4.2. Experimental

All chemicals were used as received without purification. Tetraethyl orthosilicate (TEOS, 95%) was used as silica source and was purchased from WAKO. Gold (I) chloride (AuCl, 98.5%), ruthenium (III) chloride hydrate ($RuCl_3 \cdot xH_2O$), and amphiphilic triblock copolymer poly(ethylene oxide)-poly(propylene oxide)–poly(ethylene oxide) Pluronic P123 ($EO_{20}PO_{70}EO_{20}$, M_{av} = 5800) was purchased from Sigma-Aldrich. 1-Methylimidazole ($CH_3C_3H_3N_2$), 1-butylimidazole ($C_4H_9C_3H_3N_2$), 3-trimethoxysilyl-propyl chloride ($C_6H_{15}ClO_3Si$), palladium (II) chloride ($PdCl_2$, 99.0%), platinum (II) chloride ($PtCl_2$, 98%), copper (II) chloride ($CuCl_2$, 95%), *p*-Nitrophenol ($C_6H_5NO_3$, 98.0%), sodium borohydride ($NaBH_4$, 95%), sodium hydroxide (NaOH, 96.0%), hydrochloride acid (HCl, 35.0 - 37.0%), acetone (C_3H_6O, 99.0%), dehydrated toluene (C_7H_8, 99.5%), dichloromethane (CH_2Cl_2, 99.5%), acetonitrile (C_2H_3N, 99.5%), were purchased from WAKO.

4.2.1. Synthesis of SBA-15

SBA-15 was prepared according to the procedure reported by Zhao *et al.*[24] and the detailed synthetic procedure was described in Chapter 2.

4.2.2. Preparation of ionic liquid

Immobilized ionic liquid on mesoporous silica SBA-15 were prepared using 1-methyl-3-(3-trimethoxysilylpropyl)-imidazolium chloride (MTI) or 1-butyl-3-(3-trimethoxy-silylpropyl)-imidazolium chloride (BTI). The procedure based on our group[11] was optimized in this study. In a typical reaction, the ionic liquid was prepared from 1-methyl-imidazole (or 1-butyl-imidazole) and 3-trimethoxysilylpropyl chloride, and the mixture was refluxed at 70 °C under N_2 atmosphere for 48 h. The obtained product was kept in the refrigerator under N_2 atmosphere.

4.2.3. Immobilization of metal ion-containing ionic liquid on SBA-15

In a typical synthesis, 1 g of SBA-15 was reacted with 1.3 g of MTI or 1.5 g of BTI in a separable flask with dehydrated toluene. The mixture was refluxed at 111 °C for 48 h under N_2 atmosphere. After separation and fully washed with dichloromethane, the solid product obtained after drying was denoted as me-Im@SBA-15 or bu-Im@SBA-15 [19,20].

The next step is the immobilization of metal chloride precursor (MClx, M: Au, Pd, Ru, Pt and Cu) on the functionalized SBA-15, R-Im@SBA-15 (R is me- or bu-). Only $PdCl_2$ was immobilized on both me-Im@SBA-15 and bu-Im@SBA-15 in order to study the effect of alkyl chain of ILs on the size of NPs and the catalytic performance, whereas the rest metal chlorides (AuCl, $RuCl_3$, $PtCl_2$ and $CuCl_2$) were immobilized on me-Im@SBA-15. The mixture containing MClx and R-Im@SBA-15 in 250 ml acetonitrile, was refluxed at 82 °C for 24 h under N_2 atmosphere in a separable flask. After filtration, fully washed with acetone, the solid was dried under reduced pressure. The solid powder material was denoted as MCl_me-Im@SBA-15 or MCl_bu-Im@SBA-15.

4.2.4. Syntheses of MNPs_me-Im@SBA-15

The metal reduction condition was adopted from the best condition achieved in the first study (chapter 2) with some modifications. In this procedure, the concentration of $NaBH_4$ was fixed into 100 mM in order to set the mixture at similar pH value. Centrifugation technique was also applied for better separation. In a typical reduction process, 0.1 g of MCl_R-Im@SBA-15 in 10 ml distilled water was reduced by 10 ml of 100 mM $NaBH_4$ solution under stirring using an automatic syringe pump at 0.2 ml/min feed rate. However, in order to minimize oxidation on copper nanoparticles, the feed rate of CuCl_me-Im@SBA-15 reduction was fixed at fast rate of 1.6 ml/min. The reduction was conducted at room temperature under N_2 flow. The solid was separated from the mixture by centrifugation and fully washed with distilled water. Finally, the solid product was then dried at reduced pressure overnight. The resulting materials were denoted according to their size and the type of ILs, such as PdNPs(2.4 nm)_me-Im@SBA-15 and PdNPs(3.4 nm)_bu-Im@SBA-15.

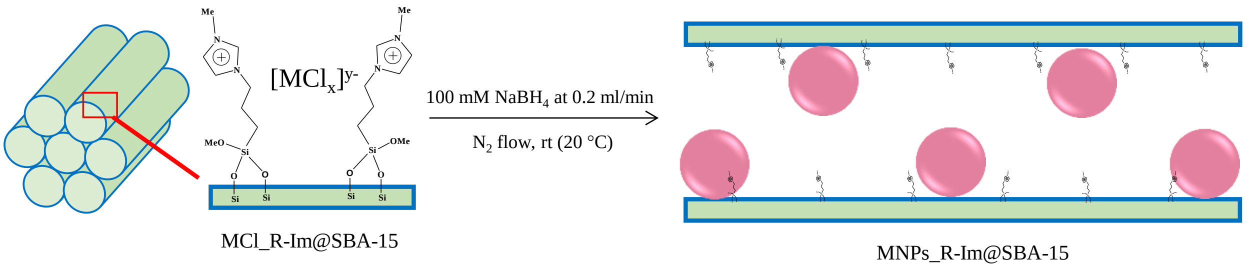

Scheme 4.1. Preparation steps for MNPs_R-Im@SBA-15.

4.2.5. Catalyst characterization

TEM images were observed on JEOL JEM-2100 operating at 200 kV, used to obtain bright field images for all catalysts, at The Institute for Solid State Physics (ISSP), The University of Tokyo. FTIR spectra of all samples in the frequency region (400-4000 cm^{-1}) were recorded at room temperature using JEOL SPX60 (KBr tablets) with a resolution of 4 cm^{-1}. Measurements of X-ray absorption fine structure (XAFS) at the Pd, Ru, and Cu *K*-edge as well as Au and Pt L_3-edge were carried out at the Photon Factory in the Institute of Materials Structure Science, High Energy Accelerator Research Organization (KEK-MSS-PF). The measurements were made in a fluorescence mode at NW10A, BL-9C and BL-12C at room temperature. The XAFS raw data were analyzed by Athena and Artemis. X-ray photoelectron spectroscopy (XPS) measurements were conducted using PHI5000 Versa Probe with a monochromatic focused (100 μm ×100 μm) Al Kα X-ray radiation (15 kV, 30 mA) and dual beam neutralization using a combination of Argon ion gun and electron irradiation. Solid-state ^{13}C and ^{29}Si CP/MAS NMR measurements were carried out using 600 MHz (JNM-ECZ600R, JEOL RESONANCE Inc.) NMR spectrometer. The N$_2$ adsorption-desorption isotherms were measured at 77 K on a Micromeritics instrument, model TriStar II 3020. The BET (Brunauer-

Emmett-Teller) and BJH (Barrett-Joyner-Halenda) methods were used to determine specific surface area and average pore diameter respectively.

4.2.6. Transfer hydrogenation of p-nitrophenol

The catalytic activities of the prepared MNPs catalysts were investigated for the catalytic hydrogenation of *p*-nitrophenol (PNP) with $NaBH_4$ in a quartz cuvette with magnetic stirrer at room temperature using UV-vis spectroscopy (Jasco V-630 BIO). Most of the catalytic procedures were the same as described in Chapter 3, however the sonication procedure differed depending on the metal. The catalyst suspension in water was sonicated for 20 min before the catalytic test. In the case of CuNPs, the catalyst suspension was added to the reaction mixture without sonication in order to avoid oxidation on CuNPs. In a typical reaction, 1 ml mixture of metal nanoparticle in water was added to 1.0 mL of aqueous PNP solution (0.3 mM), and 1.0 mL of fresh $NaBH_4$ solution (15 mM) in a quartz cuvette. The cuvette with 3 ml mixture of $M:PNP:NaBH_4 = x:10:500$ was quickly inserted in UV-vis spectrometer and the reaction progress was monitored at a certain time interval under stirring at room temperature (25 °C). The reaction was repeated for three times for each metal using fresh catalyst to obtain the more precise results.

4.3. Results and discussion

4.3.1. Transmission electron microscopy (TEM)

The size distribution of MNPs was studied by TEM observations. Figure 4.1 shows TEM images of MNPs and its size distribution histogram. The figure shows that MNPs are observed mainly inside porous SBA-15 and only sparsely located on the outer surface. Au and Pt NPs show narrow size distribution and highly dispersed NPs with the average size of 2.0 and 2.1 nm respectively. The other metals show rather broad distribution with the average size for PdNPs containing immobilized MTI and BTI (PdNPs_me-Im@SBA-15 and PdNPs_bu-Im@SBA-15), RuNPs and CuNPs were found to be 2.4, 3.4, 2.7 and 2.9 nm, respectively. Since the concentration of $NaBH_4$ was fixed to 100 mM for the reduction of all metals, it suggests that the difference in particle size probably controlled by immobilized ILs on the support.

In the case of PdNPs, the results suggest that the length of ILs has a significant effect on the size distribution of palladium NPs. Supported PdNPs on SBA-15 in the presence of immobilized MTI has smaller average size (2.4 nm) compared to that of PdNPs in the presence of immobilized BTI (3.4 nm). This suggested that short alkyl chain of IL (MTI) showed more effective to control the NPs size. This may be due to the diffusion limitation of BH_4^- which provides OH^- anions for steric stabilization of the NPs. The diffusion of BH_4^- might be more restricted in the presence of immobilized large IL which causes weaker electrostatic stabilization and as results, the NPs agglomerated and larger particles were formed. The length of ionic liquids, MTI and BTI, was calculated by DFT calculation and the figures are presented in Fig. S4.1. The length of MTI and BTI was found to be 0.85 and 1.12 nm, respectively.

In addition, because the metal content in PdNPs(3.4 nm)_bu-Im@SBA-15 is 6.7 wt% which is larger than that in PdNPs(2.4 nm)_me-Im@SBA-15 (2.4 wt%), this may also cause the formation of large NPs. The pH of a solution can be controlled by changing the ratio between the reducing agent and the metal precursor. Large metal content in PdCl_bu-Im@SBA-15 decreases the $NaBH_4/PdCl_2$ ratio which results in lower pH of mixture solution than that of PdCl_me-Im@SBA-15 with lower metal content, and this also weakens the steric stabilization. Similar results were also observed for AuNPs reduced by sodium citrate (Na_3Ct), sodium hydroxide (NaOH) and sodium borohydride ($NaBH_4$) which showed the increase in NPs size by decreasing the ratio between the reducing agent and the metal precursor.[25–27]

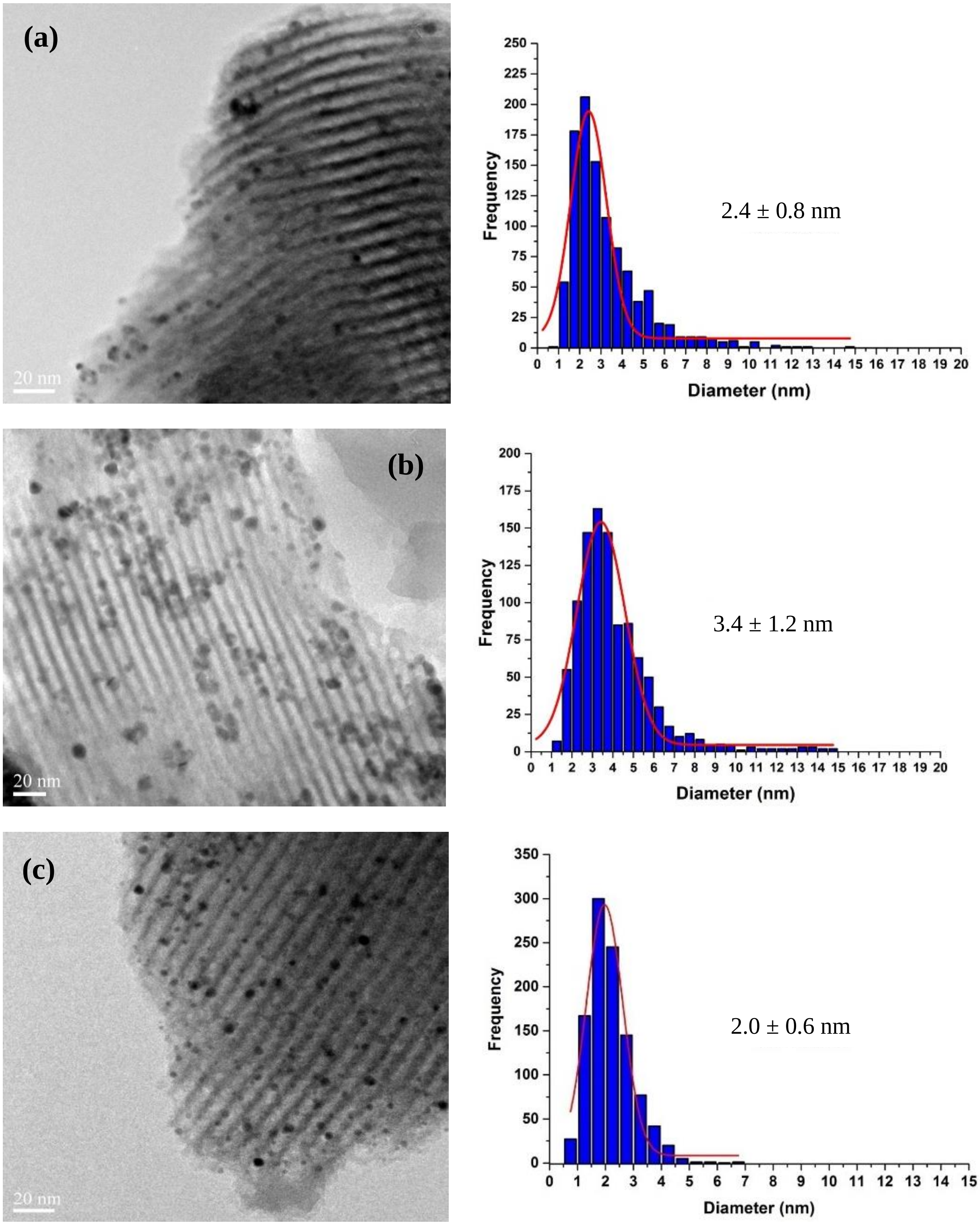

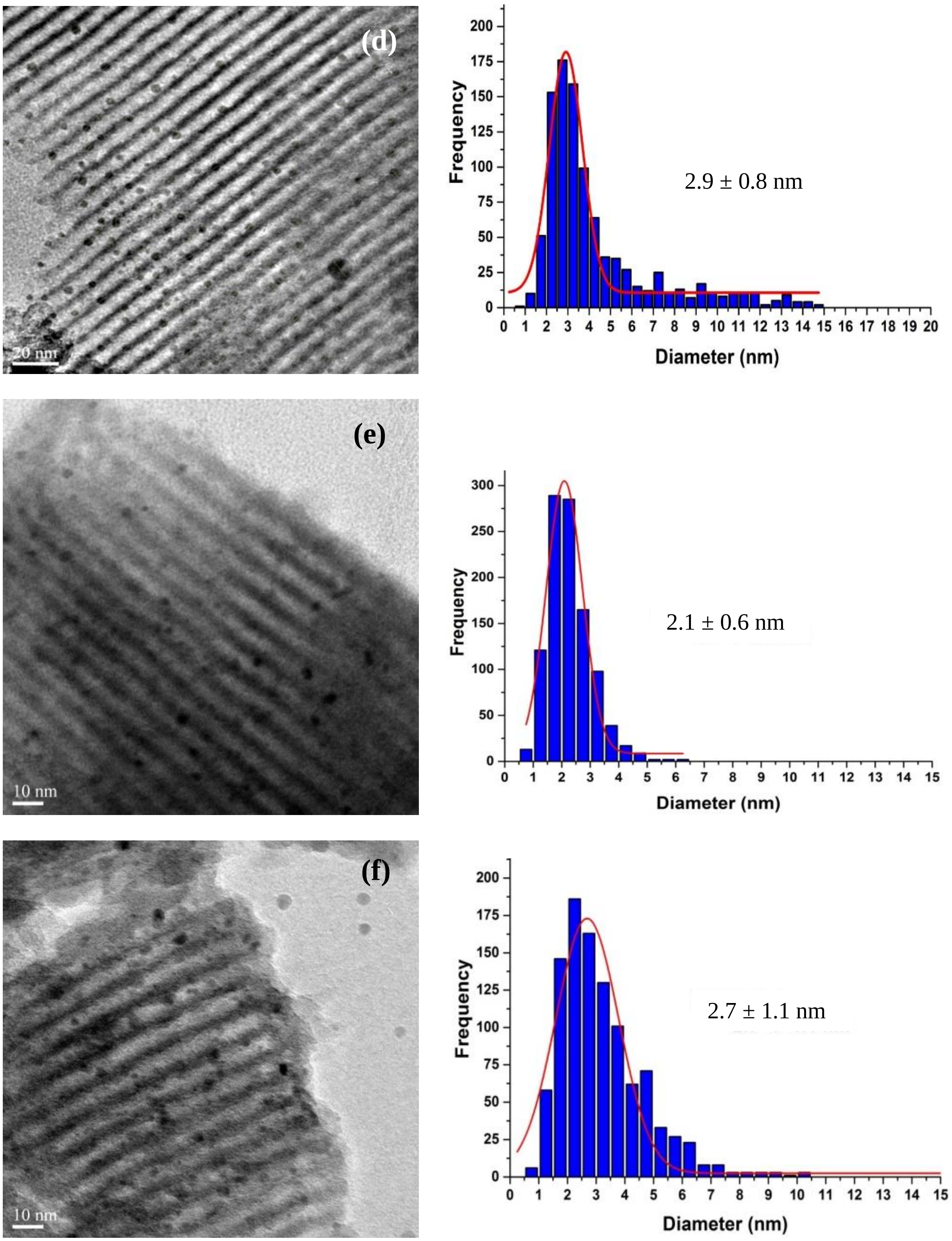

Fig. 4.1. TEM image and size distribution of (a) PdNPs(2.4 nm)_me-Im@SBA-15, (b) PdNPs (3.4 nm)_bu-Im@SBA-15, (c) AuNPs(2.0 nm)_me-Im@SBA-15, (d) CuNPs(2.9 nm)_me-Im @SBA-15, (e) PtNPs(2.1 nm)_me-Im@SBA-15, and (f) RuNPs(2.7 nm)_me-Im@SBA-15.

In the case of CuNPs, the broad size distribution seems to be due to the formation of Cu_2O which was formed during the metal reduction. In order to minimize the oxidation on Cu surface, CuNP was reduced at fast reduction rate 1.6 ml/min and it resulted in the decrease of NPs size. CuNPs synthesized at 0.2 ml/min showed broad NPs size 3.8 nm and the catalyst was easily oxidized when it was exposed to air with the color change from dark gray to dark green, attributable to the formation of $Cu(OH)_2$. The TEM image and size distribution histogram can be seen in Fig. S4.2.

The regular hexagonal pore structure of the prepared MNPs was also confirmed from the TEM images. Figure S4.3 shows the well-ordered hexagonal pore structure of AuNPs and PtNPs. Similar observations were also recorded for other metals. This result obviously shows that the SBA-15 retains its structural integrity after the formation of MNPs.

4.3.2. X-ray absorption fine structure (XAFS)

4.3.2.1. Palladium nanoparticles

Figure 4.2 shows the Pd K-edge XANES spectra for the Pd foil and the prepared Pd catalysts. Two absorption resonance appearing between ~24360 and ~24380 eV corresponds to the electronic transition that arise from the 1s to unoccupied 4p states above the Fermi level.[28–30] Compared to Pd foil spectra, both PdCl_me-Im@SBA-15 and PdCl_bu-Im@SBA-15 samples show the absence of these two peaks which characteristic for metallic Pd. It means that both samples (PdCl_me-Im@SBA-15 and PdCl_bu-Im@SBA-15) show that the Pd species is present as Pd^{2+}. On the other hand, the presence of these two characteristic Pd^0 peaks on the prepared Pd nanoparticles (PdNPs(2.4 nm)_me-Im@SBA-15 and PdNPs(3.4 nm)_bu-Im@SBA-15) suggests that the Pd^{2+} species was reduce to Pd^0 after the reduction. However, slightly different feature can be observed between the prepared PdNPs and Pd foil, such as the second peak at ~24380 eV slightly shifted to the lower energy. This suggests that Pd surface is a little oxidized which is proved by EXAFS fitting analysis.

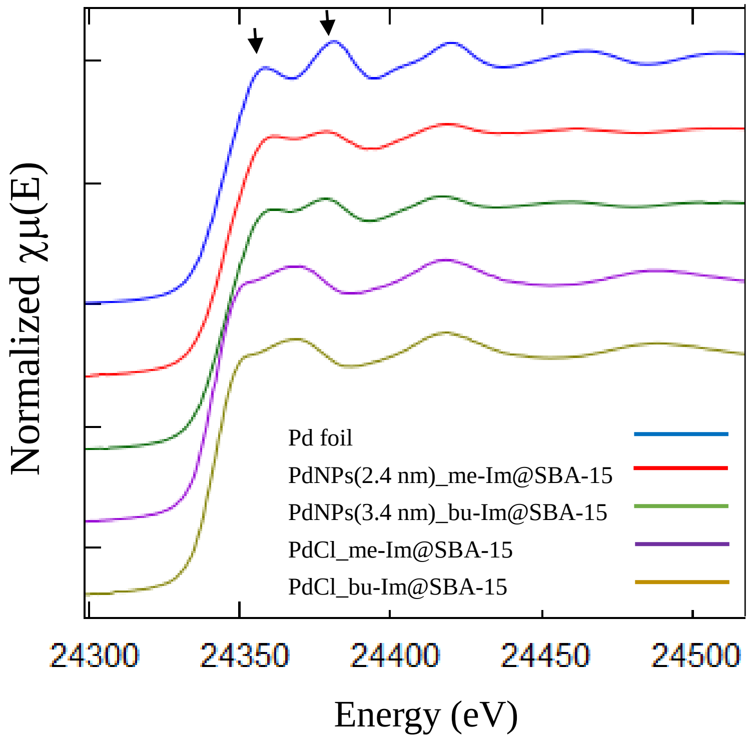

Fig. 4.2. Normalized Pd K-edge XANES spectra of Pd species in Pd foil, PdNPs(2.4 nm)_me-Im@SBA-15, PdNPs(3.4 nm)_bu-Im@SBA-15, PdCl_me-Im@SBA-15 and PdCl_bu-Im@SBA-15.

The local atomic structure of palladium was studied by EXAFS analysis. Figure 4.3 displays the Fourier-transformed EXAFS (FT-EXAFS) spectra for the prepared samples PdCl_R-Im@SBA-15 and PdNPs_R-Im@SBA-15 in comparison with the reference compounds Pd foil. The spectra of the both prepared Pd nanoparticles (PdNPs(2.4 nm)_me-Im@SBA-15 and PdNPs(3.4 nm)_bu-Im@SBA-15) and Pd foil have similar feature in *R*-space which is expected for metallic palladium (Pd^0). However, small peak was also observed for both samples which appear at the radius ~0.198 nm suggesting that some of palladium surface are covered by oxygen adatoms (see supporting information Fig. S4.4A).

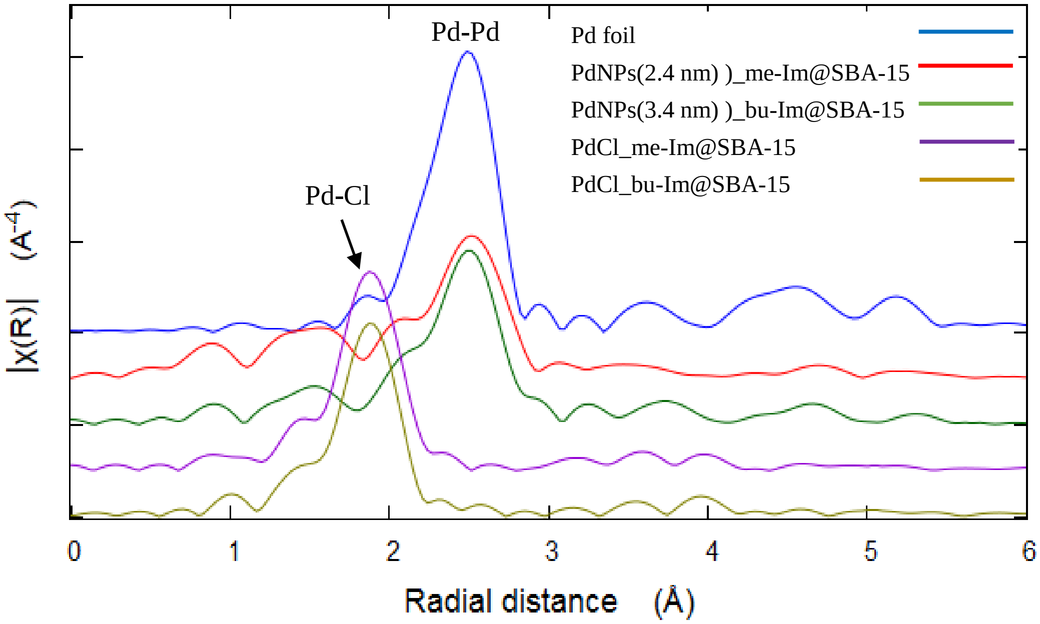

Fig. 4.3. k^3-weighted Fourier transform of Pd K-edge EXAFS for Pd foil, PdNPs(2.4 nm)_me-Im@SBA-15, PdNPs(3.4 nm)_bu-Im@SBA-15, PdCl_me-Im@SBA-15 and PdCl_bu-Im@SBA-15.

Table 4.1 summarizes the fitting results of FT-EXAFS analysis, whereas the observed and fitted data for k^3-weighted oscillation and its Fourier transform of Au L_3-edge EXAFS are presented in Fig. S4.3A. In order to examine the coordination number (CN) around Pd atom, the amplitude reduction factor S_0^2 was determined from the reference compounds, Pd foil and $[\text{Bmim}]_2[\text{PdCl}_4]$. The S_0^2 value of both PdCl_me-Im@SBA-15 and PdCl_bu-Im@SBA-15 was fixed to be 0.89 from S_0^2 value of $[\text{Bmim}]_2[\text{PdCl}_4]$ by fixing the coordination number (CN) 4 which was determined by single crystal analysis.[11,31] Neither Pd-Pd nor Pd-O bonds could be observed from the FT-EXAFS fitting result (Fig. S4.4A) before the reduction of PdCl_R-Im@SBA-15. The coordination number of Pd-Cl in both PdCl_me-Im@SBA-15 and PdCl_bu-

Im@SBA-15 were found to be 4 which means that Pd atom is coordinated by four Cl atoms at the Pd-Cl distance of ~0.231 nm by forming an anionic complex $PdCl_4^{2-}$ with square planar structure.[32]

Table 4.1. EXAFS fitting results for the prepared Pd nanoparticles.

Catalyst	**Shell**	**CN**	***R* (Å)**	**σ^2 (10^{-5} nm^2)**	**Δk (10 nm^{-1})**	**Δr (Å)**	**S_0^2**	**ΔE_0 (eV)**	**R_f (%)**
Pd foil	Pd-Pd	12.0	2.744 ± 0.002	5.8 ± 0.3	2 – 15	1.6 – 3.0	0.830±0.005	3.5 ± 0.4	0.5
PdCl_me-Im@SBA-15	Pd-Cl	4.0 ± 0.3	2.311 ± 0.005	2.6 ± 0.6	2 – 14	1.0 – 30	0.89	3.8 ± 0.6	1.6
PdCl_bu-Im@SBA-15	Pd-Cl	4.0 ± 0.3	2.311 ± 0.005	2.8 ± 0.6	3 –15	1.0 – 3.0	0.89	1.8 ± 0.6	1.8
PdNPs(2.4 nm)_me-Im@SBA-15	Pd-Pd	5.7 ± 1.9	2.757 ± 0.013	10 ± 2.1	3 –12	1.0 – 3.0	0.83	0.4 ± 2.3	2.8
	Pd-O	0.9 ± 0.6	1.973 ± 0.028	3.6 ± 6.3					
PdNPs(3.4 nm)_bu-Im@SBA-15	Pd-Pd	6.1 ± 0.8	2.768 ± 0.006	9.2 ± 0.7	3 – 14	1.0 – 3.0	0.83	-2.3 ± 1.1	1.7
	Pd-O	0.8 ± 0.5	1.977 ± 0.026	5.2 ± 5.1					

Notes: CN is the coordination number, R is the bonding distance, σ^2 is the Debye-Waller factor, Δk and Δr refer to k- and R-range, S_0^2 is the amplitude reduction factor, ΔE_0 is the energy shift on the absorption edge, and R_f is the R-factor.

On the other hand, the Pd-Pd peak was mainly observed after the formation of PdNPs for both samples, PdNPs(2.4 nm)_me-Im@SBA-15 and PdNPs(3.4 nm)_bu-Im@SBA-15, which means that $PdCl_4^{2-}$ was reduced to Pd^0 with CN was found to be 5.7 and 6.15 respectively, at the Pd-Pd distance of ~0.277 nm similar to that of Pd foil. However, small peak (Fig. 4S.4A) was also observed corresponding to Pd-O bond at the Pd-O distance of ~0.198 nm with CN 0.92 and 0.84 for PdNPs(2.4 nm)_me-Im@SBA-15 and PdNPs(3.4 nm)_bu-Im@SBA-15, respectively. This Pd-O bond is attributed to the palladium NPs surface covered with oxygen adatoms, since the Pd-Pd bond distance is characteristic for metallic Pd and not for PdO species (the Pd-Pd distances for PdO species are 0.304 and 0.342 nm).[33–35] In addition, XPS studies show that the surface chemical composition of Pd species in both PdCl_R-Im@SBA-15 samples are in the oxidized state of Pd^{2+} before transformed to Pd^0 and Cl anions were replaced to OH anions (in both PdNPs_R-Im@SBA-15 samples) after reduction with $NaBH_4$ as shown in XPS spectra for Pd 3d region and Cl 2p (Fig. 4S.5).

4.3.2.2. Gold nanoparticle

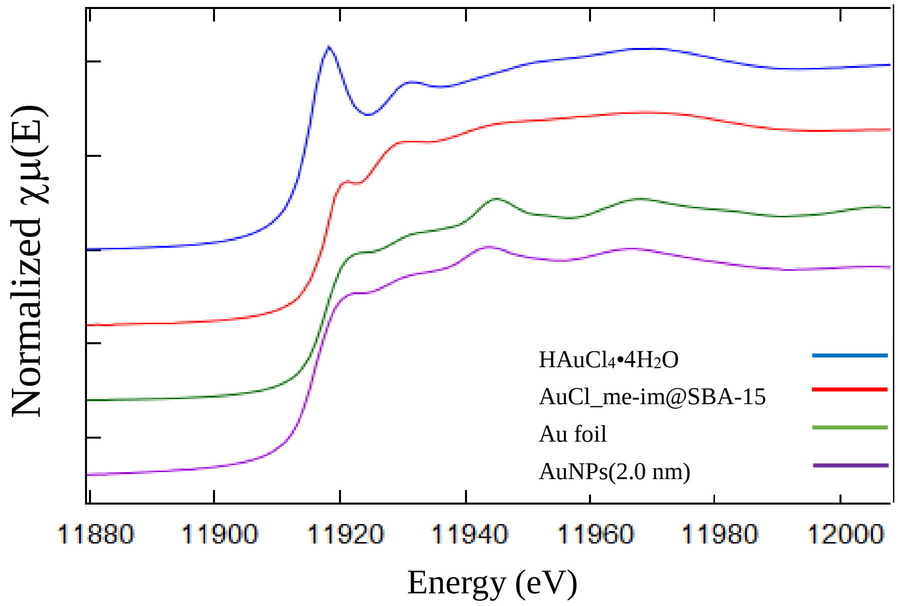

Fig. 4.4. Normalized Au L_3-edge XANES spectra of Au species in AuCl_me-Im@SBA-15, AuNPs(2.0 nm)_me-Im@SBA-15 and in both reference compounds $HAuCl_4•4H_2O$ and Au foil.

Figure 4.4 provides a comparison between the XANES spectra of the standard Au foil and $HAuCl_4•4H_2O$ with Au species of the prepared samples before and after reduction. The presence of the characteristic Au^0 peaks at ~11,944 and ~11,966 eV on AuNPs(2.0 nm)_me-

Im@SBA-15 and Au foil suggests that Au^+ species in AuCl_me-Im@SBA-15 was completely reduced to Au^0 after reduction with $NaBH_4$. In addition, the absence of white line at ~11,920 eV indicates that the 5d-orbitals are filled and therefore, no cationic Au species are expected (AuClx and AuOx species) in agreement with those of Au foil.[36–39] On the other hand, a sharp peak at ~11,918 eV observed on the reference compound $HAuCl_4 \cdot 4H_2O$ and the peak at ~11,923 eV on the AuCl_me-Im@SBA-15 sample confirmed the presence of cationic Au species Au^{3+} and Au^+ respectively as shown in Fig 2.7.[39–41] The presence of these peaks correspond to the vacant 5d-orbitals which is due to dipole transitions from $2p_{3/2}$ to the $5d_{5/2,\ 3/2}$ at the L_3 edge.[42–46] These results are in agreement with the previous study which was discussed in detail in Chapter 2.

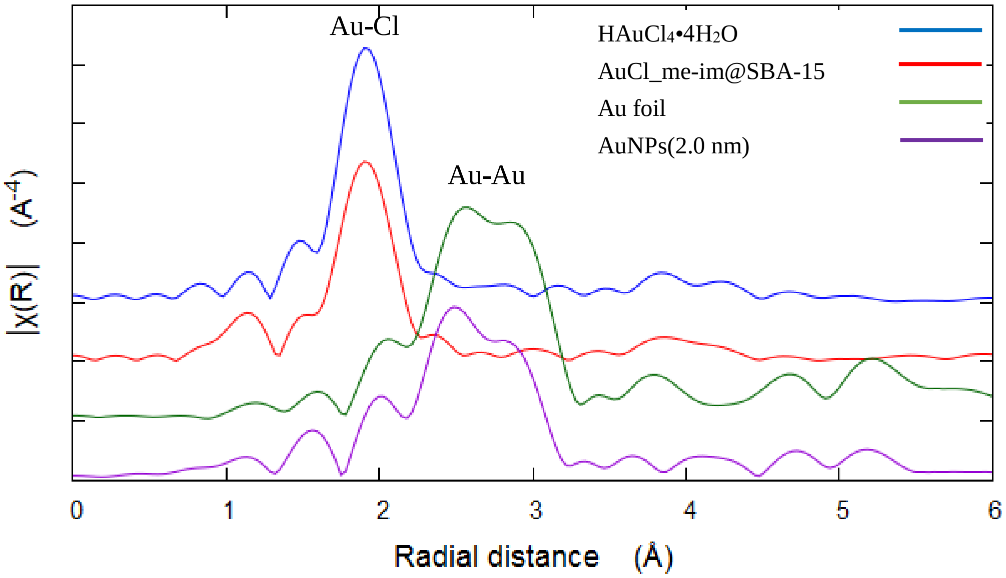

Fig. 4.5. k^3-weighted Fourier transform of Au L_3-edge EXAFS for AuCl_me-Im@SBA-15, AuNPs(2.0 nm)_me-Im@SBA-15 and both reference compounds $HAuCl_4 \cdot 4H_2O$ and Au foil.

Figure 4.5 displays the FT-EXAFS spectra for the prepared samples AuCl_me-Im@SBA-15 and AuNP(2.0 nm)_me-Im@SBA-15 in comparison with $HAuCl_4 \cdot 4H_2O$ and Au foil. The spectra of both $HAuCl_4$•$4H_2O$ and AuCl_me-Im@SBA-15 have similar features in *R*-space. The CN of AuCl_me-Im@SBA-15 was found to be 2 determined by EXAFS fitting analysis (Fig. S4.4B and Table 4.2). This means that Au atom is coordinated by two Cl atoms at the Au-Cl distance of 0.227 nm by forming an anionic complex $AuCl_2^-$ with linear structure. On the other hand, only Au-Au bond was observed after the formation of AuNP showing similar feature with the Au foil spectra. The CN of Au-Au in AuNPs(2.0 nm)_me-Im@SBA-15 was found to be 8.07 at the Au-Au distance (~0.283 nm) identical to Au foil which is ~0.285 nm. The metal species on the surface sample was also confirmed by XPS analysis which shows the formation of Au^0 from Au^+ species and the disappearance of Cl^- anion after the metal reduction (Fig S4.6).

Table 4.2. EXAFS fitting results for the prepared Au nanoparticle.

Catalyst	**Shell**	**CN**	***R* (Å)**	**σ^2 (10^{-5} nm^2)**	**Δk (10 nm^{-1})**	**Δr (Å)**	**S_0^2**	**ΔE_0 (eV)**	**R_f (%)**
$HAuCl_4 \cdot 4H_2O$	Au-Cl	4.0	2.286 ± 0.002	2.1 ± 0.2	3–14	1.3 –2.5	0.26 ± 0.01	7.7 ± 0.6	0.2
AuCl_me-Im@SBA-15	Au-Cl	1.8 ± 0.2	2.270 ± 0.006	3.1 ± 0.7	3–12	1.2 – 2.6	0.26	10.2 ± 1.3	0.4
Au foil	Au-Au	12.0	2.856 ± 0.002	7.8 ± 0.2	3–15	1.4 – 3.4	0.80 ± 0.03	2.8 ± 0.5	0.3
AuNPs(2.0 nm)_me-Im@SBA-15	Au-Au	8.0 ± 0.8	2.835 ± 0.006	10.0 ± 0.7	3–11	1.6 – 3.4	0.80	3.7 ± 0.9	0.6

Notes: CN is the coordination number, R is the bonding distance, σ^2 is the Debye-Waller factor, Δk and Δr refer to k- and R-range, S_0^2 is the amplitude reduction factor, ΔE_0 is the energy shift on the absorption edge, and R_f is the R-factor.

4.3.2.3. Copper nanoparticle

In figure 4.6, XANES spectra of the Cu species in Cu foil and in the prepared samples before (CuCl_me-Im@SBA-15) and after reduction (CuNPs(2.9 nm)_me-Im@SBA-15) are shown. The position of the first intense peak features of metallic Cu and Cu^+ are quite similar at

~8982 and ~8983 eV respectively.[47] These peaks are characteristic feature assigned to the dipole-allowed 1s to 4p transition for Cu^0 and Cu^+ species.[47–52] Both Cu foil and CuNP(2.9 nm)_me-Im@SBA-15 showed intense peak in this region which confirms the metallic Cu species on both samples. In addition to the absorption peak at the range ~8983 eV, a broad peak at ~8996 eV was also observed for the prepared CuNPs(2.9 nm)_me-Im@SBA-15 corresponding to Cu^+ species confirming the presence of Cu_2O.[53–55] On the other hand, the presence of a weak peak at ~8978 eV assigned for dipole-forbidden 1s to 3d transition and the 1s to 4p transition located at ~8987 eV characteristic for the Cu^{2+} species was observed for the prepared CuCl_me-Im@SBA-15, convincing the formation of $CuCl_4^{2-}$ in the sample.[56]

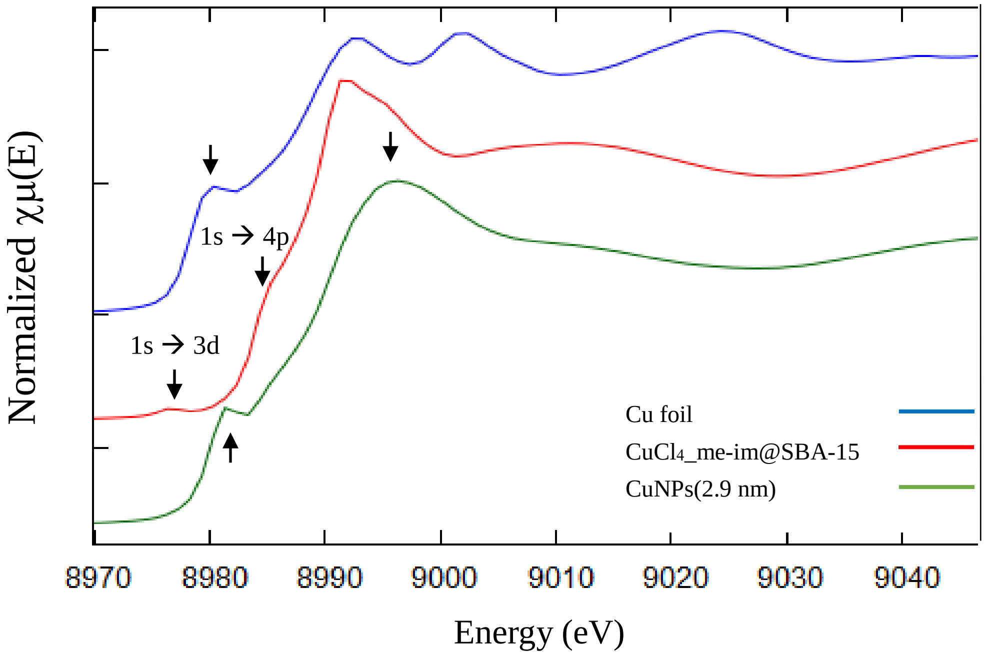

Fig. 4.6. Normalized Cu K-edge XANES spectra of Cu species in (a) Cu foil, (b) CuCl_me-Im@SBA-15, and (c) CuNPs(2.9 nm)_me-Im@SBA-15.

FT-EXAFS spectra for the prepared samples CuCl_me-Im@SBA-15 and CuNPs(2.9 nm)_me-Im@SBA-15 in comparison with Cu foil are displayed in Fig. 4.7. The spectra of

CuCl_me-Im@SBA-15 has different feature in *R*-space with that of both Cu foil and the prepared CuNPs, which is expected for the Cu-Cl bond in CuCl_me-Im@SBA-15. The CN of CuCl_me-Im@SBA-15 was found to be 4.3 determined by EXAFS fitting analysis (Fig. S4.4C and Table 4.3) by fixing the S_0^2 value to 0.83 according to the result of $[Bmim]_2[CuCl_4]$.[11,31] The Cu-Cl distance of CuCl_me-Im@SBA-15 was found at 0.225 nm which is similar to that of $[Bmim]_2[CuCl_4]$ (0.226 nm). Therefore, the Cu species in CuCl_me-Im@SBA-15 can be considered as $CuCl_4^{2-}$ with tetrahedral structure.[11,31] On the other hand, the Cu-O peak was mainly observed together with small Cu-Cu peak on CuNPs(2.9 nm)_me-Im@SBA-15 sample. It means that $CuCl_4^{2-}$ in CuCl_me-Im@SBA-15 was reduced to Cu^+ and Cu^0 by $NaBH_4$. The CN of Cu-O and Cu-Cu in CuNPs(2.9 nm)_me-Im@SBA-15 was found to be 2.5 and 0.54 at the Cu-O and Cu-Cu distance of ~0.189 and ~0.255 nm, respectively. In addition to the results obtained from XANES, the Cu species on CuNPs(2.9 nm)_me-Im@SBA-15 is mainly Cu_2O (Cu^+) and a small fraction of Cu is in a metallic state (Cu^0).

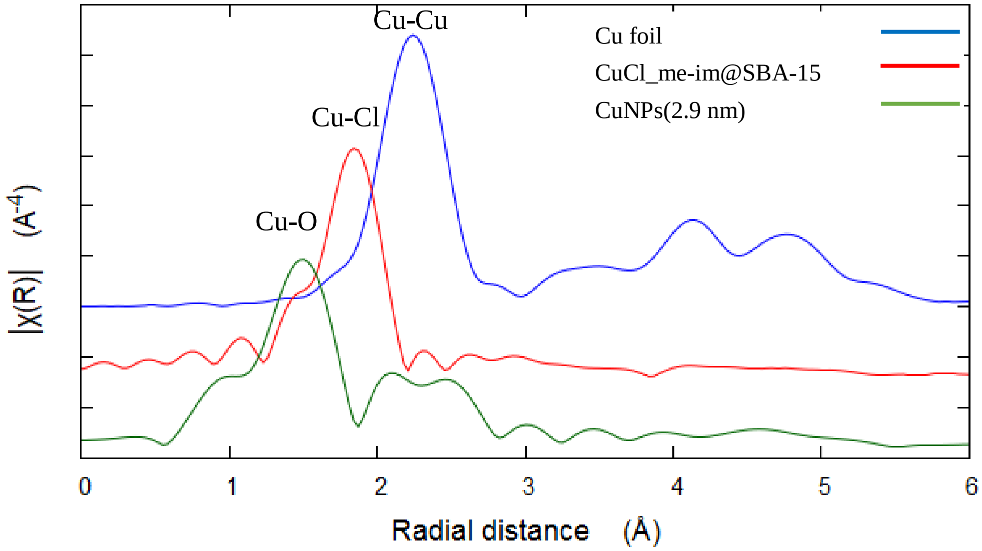

Fig. 4.7. k^3-weighted Fourier transform of Cu K-edge EXAFS for Cu foil, CuCl_me-Im@SBA-15, and CuNPs(2.9 nm)_me-Im@SBA-15.

Table 4.3. EXAFS fitting results for the prepared Cu nanoparticle.

Catalyst	**Shell**	**CN**	***R* (Å)**	**σ^2 (10^{-5} nm^2)**	**Δ*k* (10 nm^{-1})**	**Δ*r* (Å)**	**S_0^2**	**Δ*E*₀ (eV)**	***R*f (%)**
Cu foil	Cu-Cu	12.0	2.538 ± 0.006	9.0 ± 0.4	3–14	1.5 – 5.2	0.93 ± 0.50	3.4 ± 0.8	0.8
CuCl_me-Im@SBA-15	Cu-Cl	4.3 ± 0.5	2.255 ± 0.009	3.2 ± 2.2	2.5–13	1.0 – 2.2	0.83	-1.1 ± 1.4	1.0
CuNPs(3.8 nm)_me-Im@SBA-15	Cu-Cu	0.5 ± 0.4	2.554 ± 0.013	3.7 ± 4.4	2.5–11	1.0 – 2.8	0.93	7.0 ± 1.6	1.2
	Cu-O	2.5 ± 0.4	1.896 ± 0.012	6.3 ± 2.0					

Notes: CN is the coordination number, R is the bonding distance, σ^2 is the Debye-Waller factor, Δk and Δr refer to k- and R-range, S_0^2 is the amplitude reduction factor, ΔE_0 is the energy shift on the absorption edge, and R_f is the R-factor.

4.3.2.4. Platinum nanoparticle

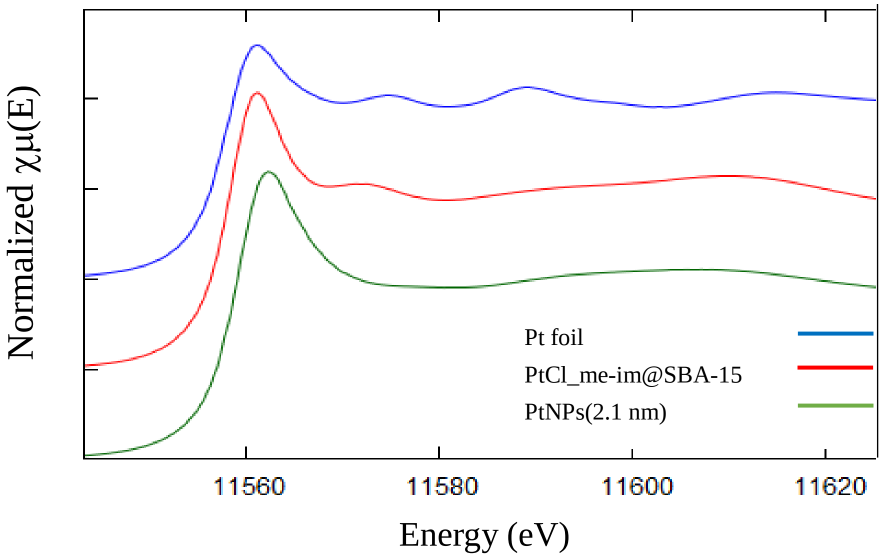

Fig. 4.8. Normalized Pt L_3-edge XANES spectra for Pt foil, PtCl_me-Im@SBA-15, and PtNPs(2.1 nm)_me-Im@SBA-15.

Normalized Pt L_3-edge XANES spectra for Pt foil, PtCl_me-Im@SBA-15, and PtNPs(2.1 nm)_me-Im@SBA-15 are shown in Fig. 4.8. The features in this region are assigned to the transition from the 2p to the 5d vacant state.[57] It is known that the lower the d orbital occupation, the more intense the white line can be observed[58] and therefore, the white line intensities in the spectra reflect the oxidation state of Pt. It can be seen that the white line intensity of the prepared PtNP is higher than that of PtCl_me-Im@SBA-15 and Pt foil shows the lower in intensity. In addition a small peak above the white line at ~11,585 eV which is present in Pt foil is not observed for the other samples. These suggest that the Pt species on both the prepared PtCl_me-Im@SBA-15 and PtNPs(2.1 nm)_me-Im@SBA-15 possess oxidation state higher than 0 or non-metallic state (positive charges). In the case of PtCl_me-Im@SBA-15, XANES spectra shows similar features with the previously reported $PtCl_6^{2-}$ for the Pt^{4+} species.[59–62] Further to confirm the oxidation state and the CN of the prepared samples, EXAFS analysis was performed to obtain more reliable results for determining the Pt species, since the Pt-Pt, Pt-Cl and Pt-O bond distances are significantly different for each sample.

FT-EXAFS spectra reveals that Pt-O species is present in the prepared PtNPs(2.1 nm)_me-Im@SBA-15 in comparison with Pt foil which are displayed in Fig. 4.9. However, a peak attributed to the Pt-Pt region was also observed which appears at the same region as Pt-Pt in Pt foil confirming the presence of metallic Pt. The CN of Pt-Pt and Pt-O in the prepared PtNPs(2.1 nm)_me-Im@SBA-15 was found to be 2.9 and 2.8 at the Pt-Pt and Pt-O bond distance of 0.270 and 0.20 nm, respectively. The Pt-Pt bond distance (0.270 nm) of PtNPs(2.1 nm)_me-Im@SBA-15 is similar to that for the metallic Pt (0.276 nm) in contrast to that of PtO_2 samples (0.3 – 0.315 nm).[58,63,64] These results suggest that the Pt species in PtNPs(2.1 nm)_me-Im@SBA-15 is metallic Pt (Pt^0) and the Pt-O coordination reflects the adsorption of oxygen adatoms on the Pt nanoparticle.

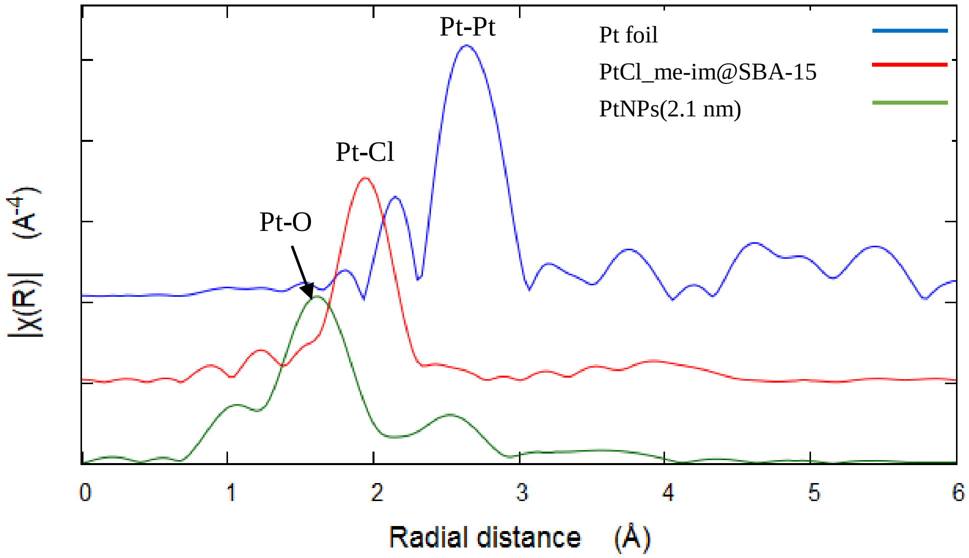

Fig. 4.9. k^3-weighted Fourier transform of Pt L_3-edge EXAFS for Pt foil, PtCl_me-Im@SBA-15, and PtNPs(2.1 nm)_me-Im@SBA-15.

The spectrum of PtCl_me-Im@SBA-15 has different features in *R*-space with that of both Pt foil and the prepared PtNP. The CN of PtCl_me-Im@SBA-15 was found to be 6.0 at the Pt-Cl distance of 0.231 nm, determined by EXAFS fitting analysis (Fig. S4.4D and Table 4.4). This means that the Pt atom is coordinated by six chloride ions ($PtCl_6^{2-}$) in octahedral geometry.[59] These results also suggest that Pt^{2+} from $PtCl_2$ precursor was oxidized to Pt^{4+} during the metal immobilization forming $PtCl_6^{2-}$ on PtCl_me-Im@SBA-15. This result was supported by XANES spectra discussed previously.

Table 4.4. EXAFS fitting results for the prepared Pt nanoparticle.

Catalyst	**Shell**	**CN**	***R* (Å)**	**σ^2 (10^{-5} nm^2)**	**Δk (10 nm^{-1})**	**Δr (Å)**	**S_0^2**	**ΔE_0 (eV)**	**R_f (%)**
Pt foil	Pt-Pt	12.0	2.765 ± 0.003	5.0 ± 0.1	3–14	1.5 – 5.2	0.90 ± 0.03	7.4 ± 0.4	0.2
PtCl_me-Im@SBA-15	Pt-Cl	6.0 ± 0.8	2.317 ± 0.007	5.8 ± 0.8	3–14	1.0 – 2.8	0.90	29.6 ± 1.8	2.7
PtNPs(2.1 nm)_me-	Pt-Pt	2.9 ± 2.5	2.703 ± 0.03	14.0 ±7.5	2.5–11.5	1.0 – 2.9	0.90	9.0 ± 2.7	2.9
Im@SBA-15	Pt-O	2.8 ± 0.5	2.016 ± 0.003	7.3 ± 2.4					

Notes: CN is the coordination number, R is the bonding distance, σ^2 is the Debye-Waller factor, Δk and Δr refer to k- and R-range, S_0^2 is the amplitude reduction factor, ΔE_0 is the energy shift on the absorption edge, and R_f is the R-factor.

4.3.2.5. Ruthenium nanoparticle

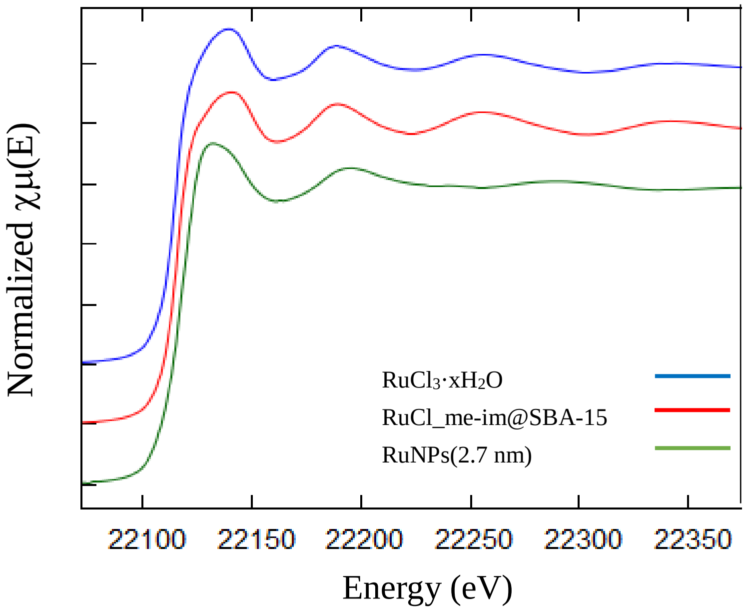

Fig. 4.10. Normalized Ru K-edge XANES spectra of Ru species in $RuCl_3{\cdot}xH_2O$, RuCl_me-Im@SBA-15, and RuNPs(2.7 nm)_me-Im@SBA-15.

The XANES spectra at the Ru K-edge of $RuCl_3 \cdot xH_2O$ as the reference, as well as the prepared RuCl_me-Im@SBA-15 and RuNPs(2.7 nm)_me-Im@SBA-15 are shown in Fig. 4.8. The edge energies for RuCl_me-Im@SBA-15 and the reference compound $RuCl_3 \cdot xH_2O$ are almost the same at ~22126 eV, suggesting a similar oxidation number (~3+) for both. On the other hand, the edge energy of RuNPs(2.7 nm)_me-Im@SBA-15 at ~22130 eV is the same as that for Ru_2O.[65–69] However, small peak corresponds to the Ru-Ru species is observed in FT-EXAFS (Fig. 4.11 and Fig. S4.4D).

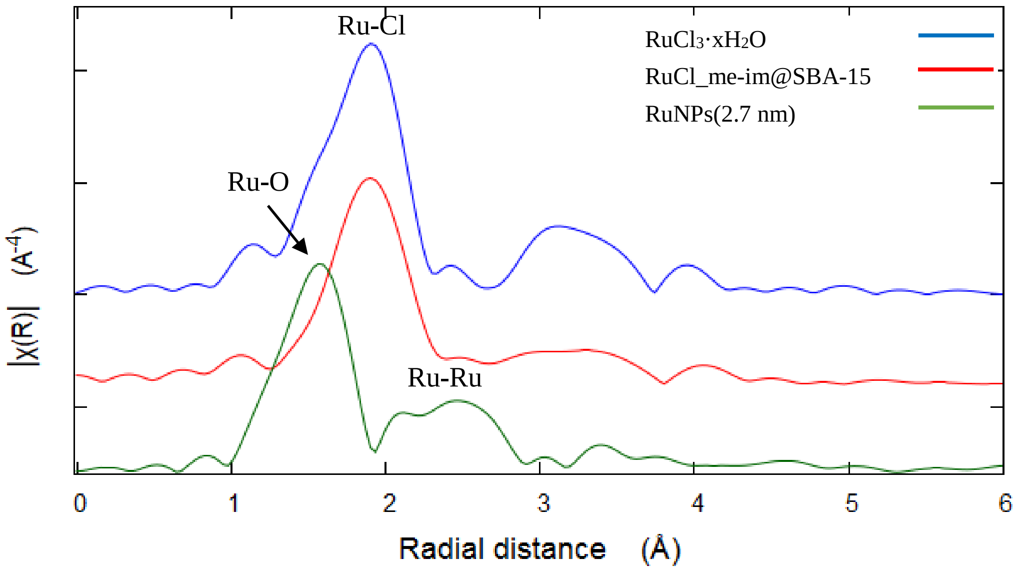

Fig. 4.11. k^3-weighted Fourier transform of Ru K-edge EXAFS for $RuCl_3 \cdot xH_2O$, RuCl_me-Im@SBA-15, and RuNPs(2.7 nm)_me-Im@SBA-15.

Small peak assigned for metallic ruthenium in Fig. 4.11 suggests the presence of Ru^0 in the prepared RuNPs(2.7 nm)_me-Im@SBA-15. The FT-EXAFS fitting results (Fig. 4S.4D and Table 4.5) show that the Ru species in the prepared RuNP consists of metallic Ru with the CN of 0.7 at the Ru-Ru distance 0.28 nm, and Ru-O species was also observed with the CN 3.35 at the Ru-O distance 0.20 nm. The fitting result was obtained by fixing the S_0^2 to 0.81 which was determined elsewhere for Ru foil.[70,71] The Ru-Ru bond distance of RuNPs(2.7 nm)_me-Im@SBA-15 is close to that for metallic Ru (0.268 – 0.27 nm) which is different from anhydrous RuO_2 or hydrate samples (0.30 – 0.35 nm).[67,72] These results suggest that the Ru species in RuNPs(2.7 nm)_me-Im@SBA-15 is metallic Ru (Ru^0) and the surface is mostly covered by oxygen adatoms. On the other hand, the spectra of RuCl_me-Im@SBA-15 has similar features in *R*-space with that of $RuCl_3 \cdot xH_2O$, which is expected for the Ru-Cl bond. The CN of Ru-Cl on RuCl_me-Im@SBA-15 was found to be 3.5 at the Ru-Cl distance of 0.236 nm. It is rather hard to conclude the exact CN of this sample due to the high error value (1.4) which may be between 3 and 4 forming $RuCl_3$ or $RuCl_4^-$ (Table 4.5).

Table 4.5. EXAFS fitting results for the prepared Ru nanoparticle.

Catalyst	**Shell**	**CN**	***R* (Å)**	**σ^2 (10^{-5} nm^2)**	**Δ*k* (10 nm^{-1})**	**Δ*r* (Å)**	**S_0^2**	**ΔE_0 (eV)**	***R_f* (%)**
$RuCl_3 \cdot xH_2O$	Ru-Cl	3.0	2.337 ± 0.026	4.2 ± 5.7	3.0 - 11	1.4 – 2.4	0.890±0.004	-3.0 ± 6.0	2.8
RuCl_me-Im@SBA-15	Ru-Cl	3.5 ± 1.4	2.362 ± 0.016	3.2 ± 2.2	2 – 14.5	1.4 – 2.2	0.89	0.3 ± 3.4	2.9
RuNPs(2.7 nm)_me-Im @SBA-15	Ru-Ru	0.7 ± 0.4	2.810 ± 0.011	3.5 ± 3.1	2 – 12	1.2 – 3.0	0.81	4.0 ± 1.3	1.2
	Ru-O	3.3 ± 0.4	2.027 ± 0.007	4.0 ± 1.2					

Notes: CN is the coordination number, R is the bonding distance, σ^2 is the Debye-Waller factor, Δk and Δr refer to k- and R-range, S_0^2 is the amplitude reduction factor, ΔE_0 is the energy shift on the absorption edge, and R_f is the R-factor.

4.3.3. Fourier transform infrared spectroscopy (FTIR)

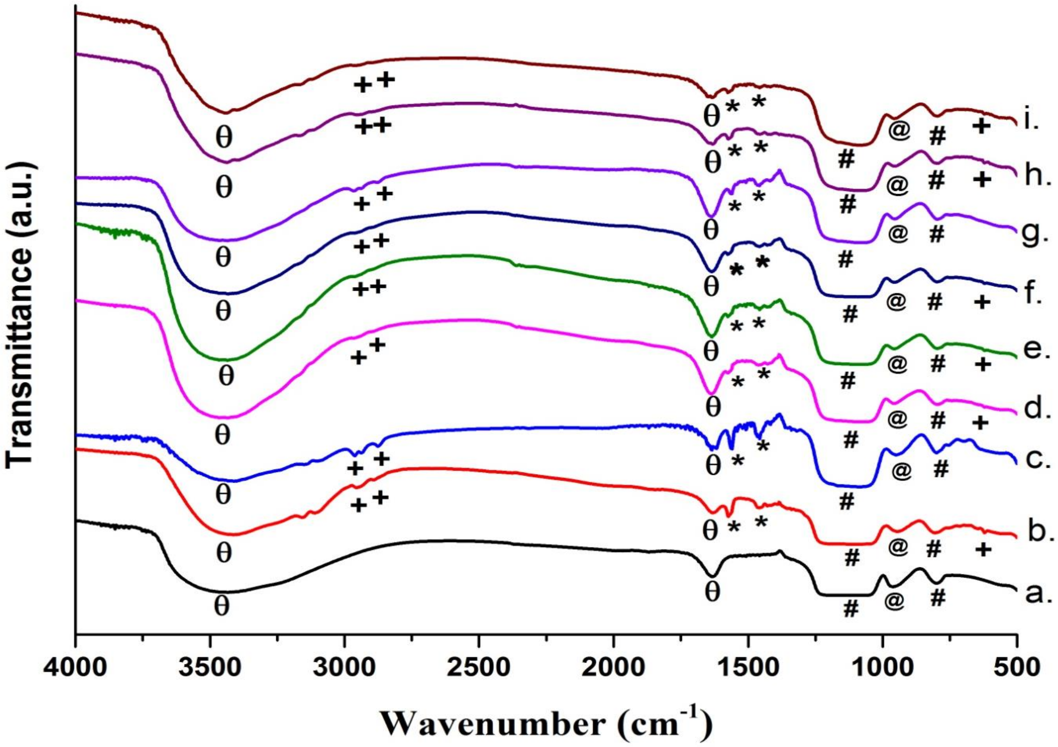

Fig. 4.12. FTIR spectra of (a) SBA-15 before immobilization, after immobilization (b) me-Im@SBA-15, (c) bu-Im@SBA-15, (d) AuNPs(2.0 nm)_me-Im@SBA-15, (e) CuNPs(2.9 nm)_ me-Im@SBA-15, (f) PdNPs(2.4 nm)_me-Im@SBA-15, (g) PdNPs(3.4 nm)_bu-Im@SBA-15, (h) PtNPs(2.1 nm)_me-Im@SBA-15, and (i) RuNPs(2.7 nm)_me-Im@SBA-15.

FTIR spectra in Fig 4.12 show the existence of ionic liquid on the surface of SBA-15 before and after the formation of metal NPs. Sharp bands at 1070, 792 cm^{-1} (#) and 950 cm^{-1} (@) assignable to the stretching and bending vibrations of condensed Si-O-Si networks, and the stretching vibrations of uncondensed Si-OH groups of the SBA-15 support were observed in all samples.[73,74] The broad bands at 3400 and 1630 cm^{-1} (θ) were attributed to the vibration of adsorbed water molecules.[74] The C-Si stretching vibrations between 1233 and 1200 cm^{-1} on the sample after immobilization of ILs cannot be resolved due to the overlapping with broad bands of Si-O-Si stretching. However, several additional bands at 3138, 3090, 2940, 616 cm^{-1} (+), and 1561 and 1453 cm^{-1} (*) for all sample after the immobilization of ILs and the metal reduction are assigned to the aliphatic C-H stretching and the ring stretching of imidazolium molecules.[73–75] These additional peaks indicate that the ILs were successfully grafted onto the siliceous SBA-15. This observation also gives evidence that the bonding strength between the IL and the surface of SBA-15 remains unchanged even after the metal reduction by 100 mM $NaBH_4$. These results are supported by ^{29}Si and ^{13}C CP/MAS NMR spectroscopy analysis.

4.3.4. Solid-state NMR spectroscopy

The confirmation of imidazolium moieties bonded to the silica framework was obtained by ^{29}Si and ^{13}C CP/MAS NMR spectroscopy of SBA-15, me-Im@SBA-15 and bu-Im@SBA-15 (Fig. 4.13 and 4.14). The ^{29}Si NMR spectra in Fig 4.13 show signals for both Q^n and T^n species. The Q^2 (two Si-atom neighbors) at -91 ppm, Q^3 (three Si-atom neighbors) at -102 ppm and Q^4 (four Si-atom neighbors) at -110 ppm signals are attributed to Si atoms (denoted as *Si) of the inorganic silica framework in germinal silanol groups $[(SiO)_2{*}Si(OH)_2]$, isolated silanol group $[(SiO)_3{*}SiOH]$, and siloxane binding without hydroxyl groups $[(SiO)_4{*}Si]$, respectively.[21,76–78] The presence of T^2 and T^3 signals in both samples after immobilization of ILs confirms the incorporation of organic group within SBA-15 (Fig. 4.13b and c). The T^2 at around -57 ppm and T^3 at -66 ppm refer to Si atoms bound to C atoms in $[R\text{-}Si{*}(OSi)_2{*}OMe]$ and $[R\text{-}Si{*}(OSi)_3]$ species respectively, where R is the organic functionalized groups.[21,77,78] The ^{13}C NMR spectra in Fig. 4.14 confirm the structure of the organic functionality of ILs. The chemical shifts obtained in ^{13}C NMR solid state spectra of both immobilized ILs on SBA-15 samples are listed in Table S4.1 and which are in agreement with previously reported literatures.[21,22,77–81]

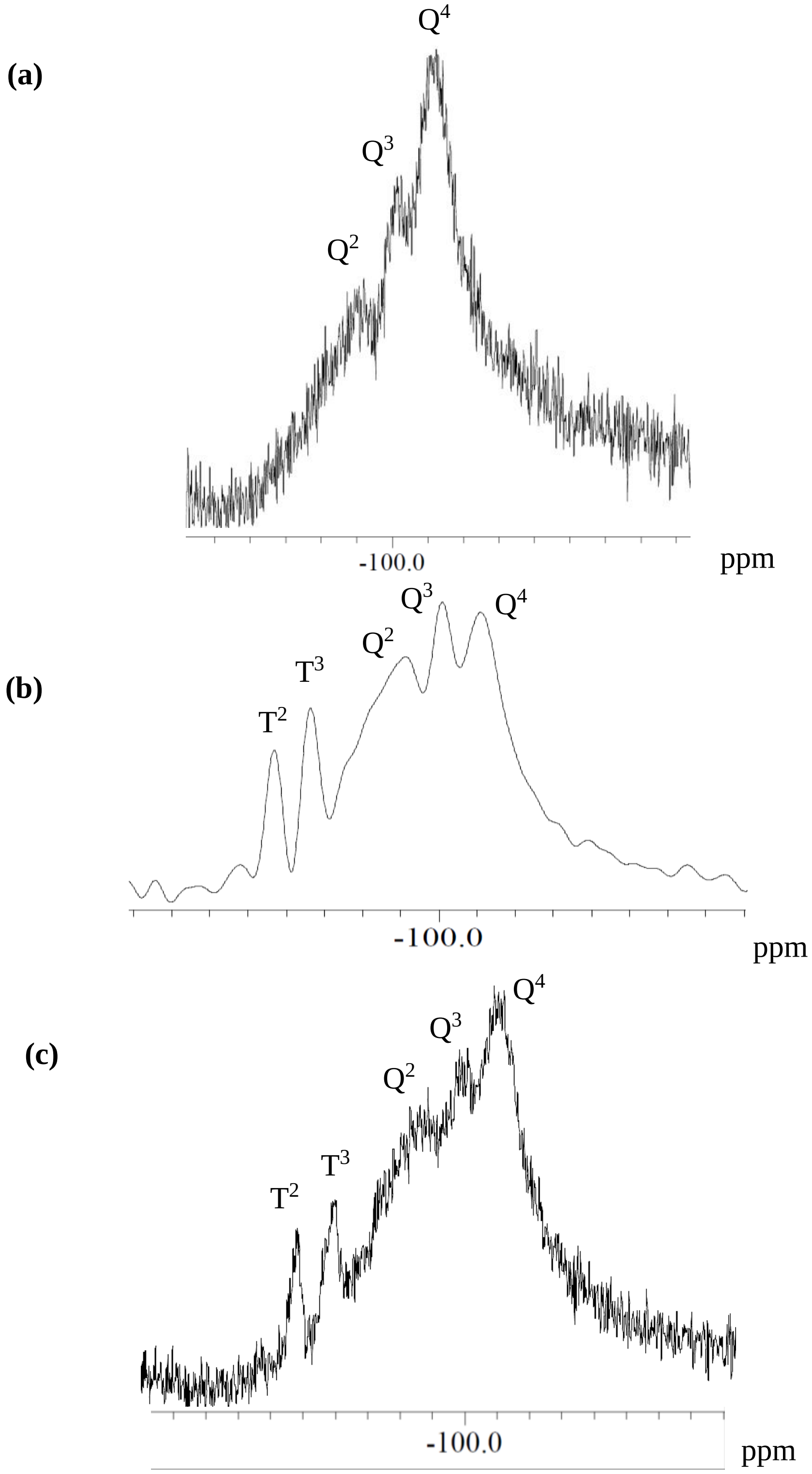

Fig. 4.13. ^{29}Si CP/MAS NMR spectra of (a) SBA-15, (b) me-Im@SBA-15, and (c) bu-Im@SBA-15.

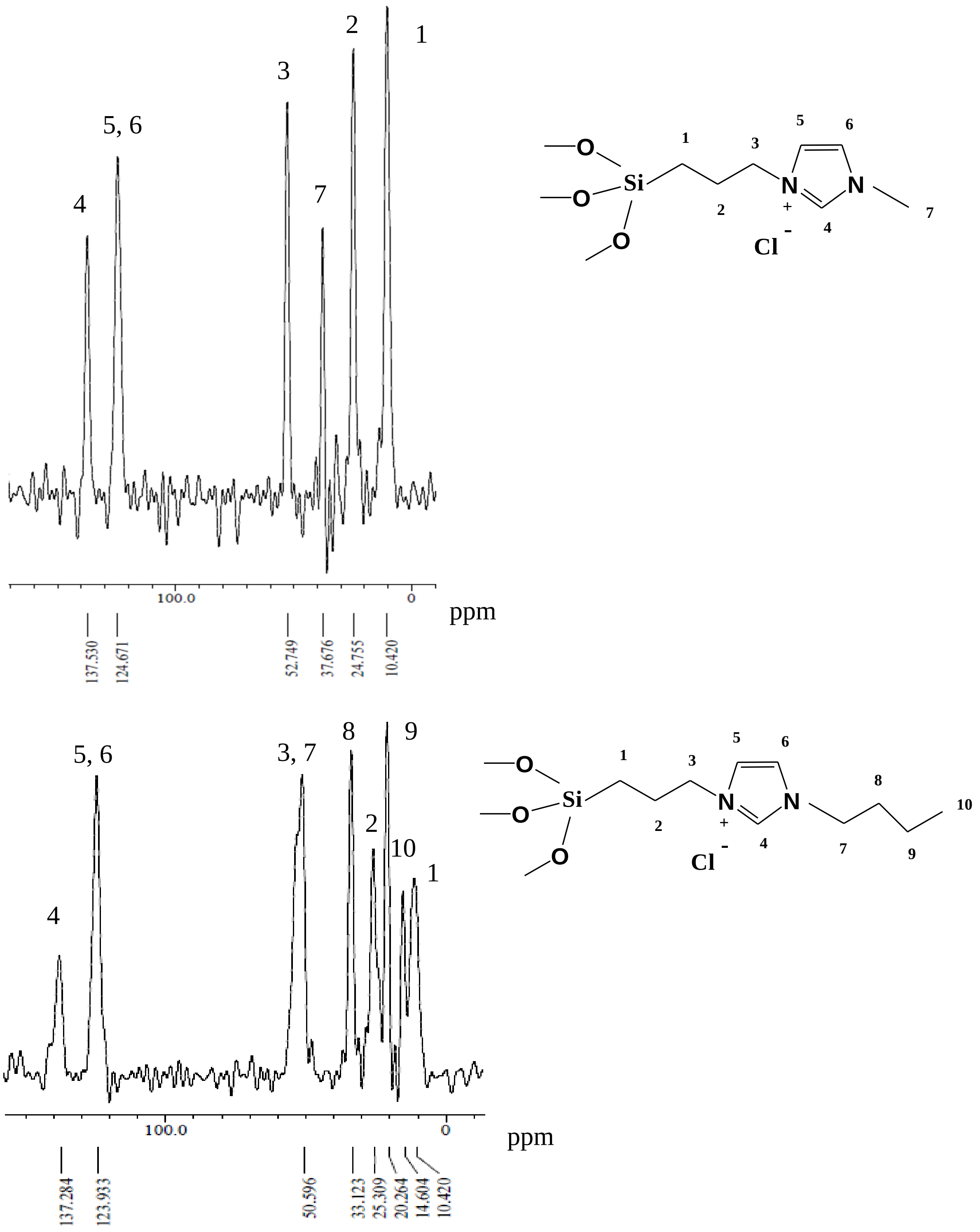

Fig. 4.14. ^{13}C CP/MAS NMR spectra of (a) me-Im@SBA-15 and (b) bu-Im@SBA-15.

The amount of immobilized ionic liquids with different alkyl length (MTI and BTI) on SBA-15 before and after metal chloride immobilization is listed in Table S4.2 as determined by the elemental analysis. The calculation was based on the N content. The amount of immobilized MTI and BTI was 0.2 and 0.14 mmol/g and after immobilization of $PdCl_2$ (0.19 and 0.13 mmol/g) no significant loss was observed. This result also confirms the strong bonding of the immobilized ILs on silica framework of SBA-15.

4.3.5. N_2 adsorption-desorption isotherms

The N_2 adsorption-desorption isotherms and pore size distributions of SBA-15 and after the immobilization of MTI and BTI are shown in Fig. 4.15. The isotherms of pure SBA-15, me-Im@SBA-15, and bu-Im@SBA-15 displayed type IV isotherm with H1 hysteresis loops, which is a characteristic of mesoporous materials. A sharp step in the P/P_0 range of 0.55–0.82 indicates the uniformity of the pore size and since the shape of the isotherms is preserved, no pore blocking or mesophase distortion is observed.[21,22,82–84] The position of capillary condensation step shifted to some extent towards lower partial pressure after ILs immobilization from 0.66–0.82 for SBA-15 to 0.55–0.7 for me-Im@SBA-15 and bu-Im@SBA-15, probably due to the changing in pore sizes because of the successful grafting of the ILs which is mainly inside porous SBA-15. This result then was supported by the decrease in pore size, surface area and pore volume, while the wall thickness increased after the immobilization as given in Table S4.3. The table presents the specific surface area (S_{BET}), the total pore volume (V_t), the average pore size calculated from BJH model (D_{BJH}) and the wall thickness, which show decrease in all parameters after the immobilization of ionic liquids on SBA-15.

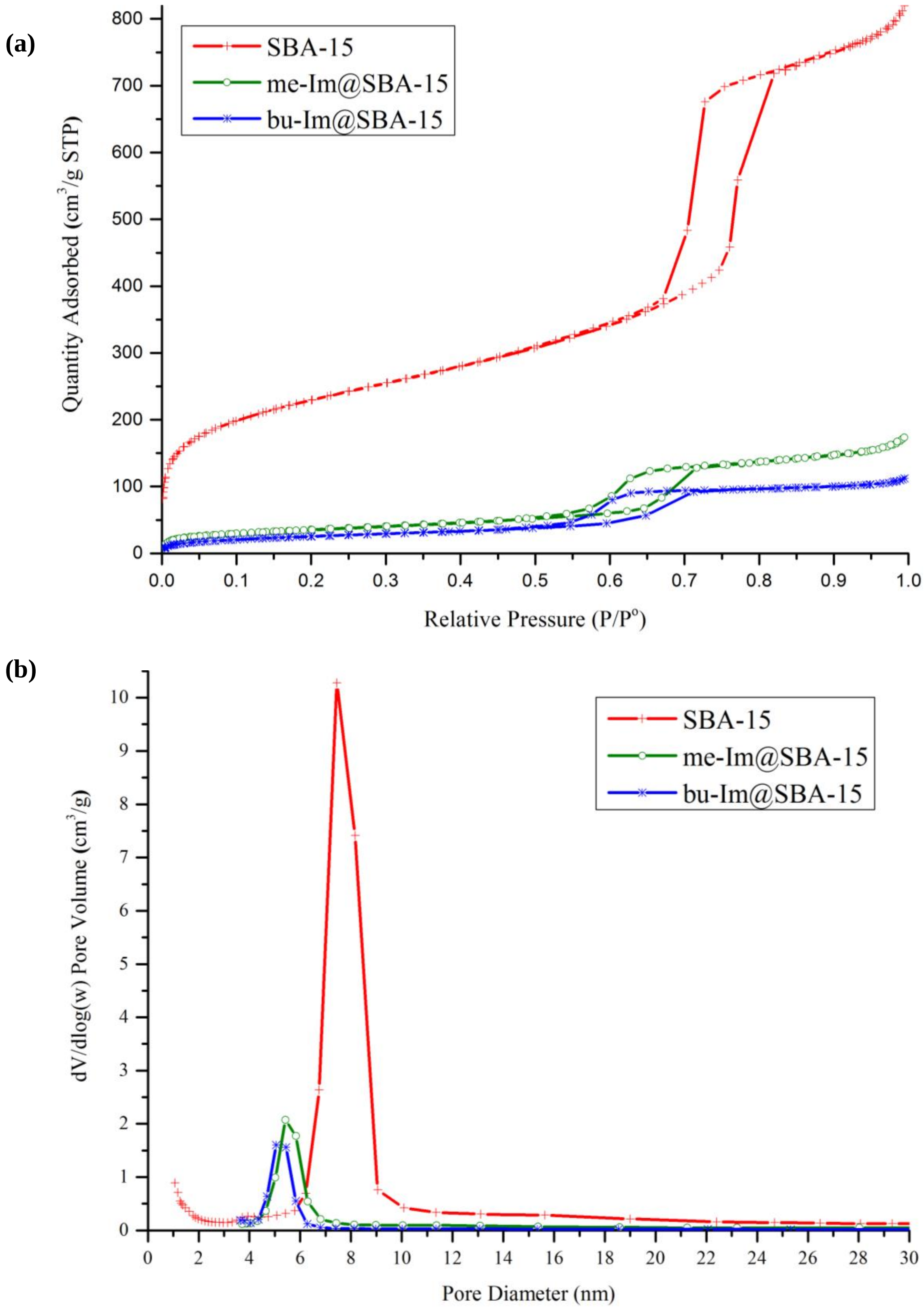

Fig. 4.15. N_2 adsorption-desorption isotherm (a) and pore size distribution (b) of SBA-15, me-Im@SBA-15 and bu-Im@SBA-15.

4.3.6. Catalytic study

The catalytic activities of the prepared MNPs catalysts were studied for *p*-nitrophenol (PNP) hydrogenation reaction with sodium borohydride in aqueous medium at room temperature. Figure S4.7 shows plots of absorbance versus wavelength and ln(C_t/C_0) versus reaction time (t) along with the R^2 value for PNP reduction catalyzed by the prepared metal nanoparticles MNPs_R-Im@SBA-15 catalysts, which show a typical spectra changed over time as the product *p*-aminophenol (PAP) was formed. The decrease in intensity of *p*-nitrophenolate band at 400 nm which represents PNP due to the addition of $NaBH_4$ followed by the increase in intensity of PAP band at 295 nm, indicate that the reaction is in progress to generate the product PAP. The reaction follows a pseudo-first order reaction with the excess $NaBH_4$ approximately by 50 times more than that of PNP (PNP: $NaBH_4$ = 1:50). The average k_{app} values and conversion efficiencies are summarized in Table 4.6.

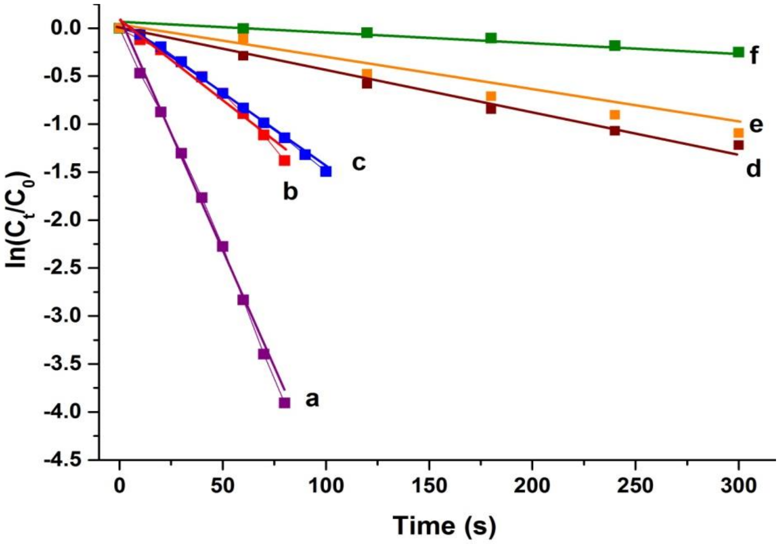

Fig. 4.16. The relationship between ln(C_t/C_0) and reaction time (t) of different prepared MNPs catalysts: (a) PdNPs(2.4 nm)_me-Im@SBA-15, (b) PdNPs(3.4 nm)_bu-Im@SBA-15, (c) AuNPs(2.0 nm)_me-Im@SBA-15, (d) PtNPs(2.1 nm)_me-Im@SBA-15, (e) RuNPs(2.7 nm)_me-Im@SBA-15 and (f) CuNPs(2.9 nm)_me-Im@SBA-15.

Figure 4.16 shows that PdNPs(2.4 nm)_me-Im@SBA-15 gave the best catalytic performance with 100% conversion efficiency on PNP hydrogenation reaction compared to other MNPs. After being normalized by the number of surface metal atoms, AuNPs(2.0 nm)_me-Im@SBA-15 showed better catalytic performance compared to that of PdNPs(3.4 nm)_bu-Im@SBA-15, followed by PtNPs(2.1 nm)_me-Im@SBA-15, RuNPs(2.7 nm)_me-Im@SBA-15 and CuNPs(2.9 nm)_me-Im@SBA-15 as shown in Table 4.6. The results show difference in catalytic performances suggesting that the activities are dependent on the particle size.

In the case of PtNPs(2.1 nm)_me-Im@SBA-15, instability of UV-Vis absorbance spectra was observed during the reaction. Therefore, reaction condition for PNP reduction was changed by increasing the concentration of $NaBH_4$ from 15 to 30 mM, which resulted in the change of PNP/$NaBH_4$ ratio from 1:50 to 1:100. This phenomenon seems to be due to the surface oxidation on Pt surface which was discussed from XAFS analysis in the previous section.

Table 4.6. Rate constants of different MNPs catalyst on PNP reduction (PNP: $NaBH_4$ = 1:50).

Sample	Catalyst	Amount of cat. (mg)	$k_{app} \times 10^{-3}$ (s^{-1})	$k_{app} \times 10^{-3}$ ($s^{-1}mmol^{-1}$)[a]	$k_{app} \times 10^{-3}$ ($s^{-1}atoms^{-1}$)[b]	Conversion efficiency (%)
a.	PdNPs(2.4 nm) (2.4wt%)	0.16	47.4 ± 0.7	113.50	1.50	100
b.	PdNPs(3.4 nm) (6.7wt%)*	0.05	15.7 ± 0.4	44.04	0.20	100
c.	AuNPs(2.0 nm) (0.8wt%)	0.50	13.4 ± 0.9	16.0	0.80	100
d.	PtNPs(2.1 nm) (4.1wt%)**	0.30	3.8 ± 0.1	1.56	0.20	85.0
e.	RuNPs(2.7 nm) (1.3wt%)	0.50	3.7 ± 0.1	5.46	0.10	89.5
f.	CuNPs(2.9 nm) (1.5wt%)	1.0	1.6 ± 0.1	1.66	0.03	90.0

a k per-mg MNPs, b k per surface metal atom in the catalyst, Metal loading was determined based on the edge jump in EXAFS analysis, k_{app} value was averaged over three experiments using fresh catalyst, %conversion was calculated after 15 min reaction but for CuNPs after 20 min, * based on XRF analysis, ** pnp/$NaBH_4$ = 1/100.

The large particle size and molecule of BTI in PdNPs(3.4 nm)_bu-Im@SBA-15 seems to be responsible for its low activity. These large particles (~3.4 nm) however, are not enough to block the pores to give the pore-blocking effect which was indicated by the absence of induction period. On the other hand, large molecule of BTI could limit the diffusion of both the reactant and product to reach and leave the active sites.

CuNPs(2.9 nm)_me-Im@SBA-15 showed the lowest activity compared to other prepared MNPs. This seems to be a consequence of large particles formation inside pores as shown by the broad size distribution from TEM image. These large particles gave the pore-blocking effect as indicated by the presence of the induction period (~3 min). The formation of Cu_2O may also be responsible for the low activity since Cu_2O may be less active than metallic Cu for this reaction.

The reusability of the all prepared metal nanoparticles was studied for at least four recycle processes (Fig. 4.17). The catalysts were reused for the next cycle after simple washing with water for three times by centrifugation. The activity of PdNPs(2.4 nm)_me-Im@SBA-15 decreased as shown by the decrease of apparent rate constant from 113.5 x 10^{-3} $s^{-1}mmol^{-1}$ at the first cycle to 56 x 10^{-3} $s^{-1}mmol^{-1}$ at the fourth cycle. Whereas the k_{app} of PdNPs(3.4 nm)_bu-Im@SBA-15 and RuNPs(2.7 nm)_me-Im@SBA-15 decreased significantly from 44 x 10^{-3} and 5.5 10^{-3} s^{-1} $mmol^{-1}$ to 0.8 x 10^{-3} and 1.3 10^{-3} $s^{-1}mmol^{-1}$, respectively. Meanwhile AuNPs(2.0 nm)_me-Im@SBA-15, CuNPs(2.9 nm)_me-Im@SBA-15 and PtNPs(2.1 nm)_me-Im@SBA-15 showed stable activity with slight decrease in activity after the fourth cycle. These results suggest that small particles of Au and Pt catalysts significantly contribute to the catalyst stability. In the case of CuNP catalyst, the results also suggest that both Cu_2O and Cu species in CuNPs(2.9 nm)_me-Im@SBA-15 are stable for the consecutive recycles processes. The apparent rate constants of the reused metal nanoparticles catalysts after being normalized by mole metal loaded in the catalyst, are summarized in Table 4.7.

The decrease in activity might be attributed to the agglomeration process due to the consecutive recycle processes which was studied for AuNPs in the previous chapter. Agglomeration process increases the average particle size leading into the decrease in catalytic performance. The decrease in rate constant might also be caused by the surface-blocking effect by the accumulation of the product PAP on the surface of MNPs even after the washing process from the previous cycle. The dramatic decreased in k_{app} of PdNPs(3.4 nm)_bu-Im@SBA-15 suggests that the large particle size and IL molecule are also responsible for the decrease in activity after the fourth cycle. Large nanoparticle which underwent agglomeration process during the consecutive recycle processes and large molecule of BTI might limit the diffusion of PNP and PAP to reach and leave the active sites of PdNPs during the reaction. In the case of RuNPs(2.7 nm)_me-Im@SBA-15, the decrease in activity seems to be a consequence of the formation of large particles and surface oxidation on Ru nanoparticles which was observed by XAFS analysis.

Table 4.7. The rate constants (k_{app}) of all recycle metal nanoparticles MNPs_R-Im@SBA-15 in the reduction of PNP (PNP: $NaBH_4$ = 1:50).

Number of cycle	PdNPs(2.4 nm) (10^{-3} $s^{-1}mmol^{-1}$)	PdNPs(3.4 nm) (10^{-3} $s^{-1}mmol^{-1}$)	AuNPs(2.0 nm) (10^{-3} $s^{-1}mmol^{-1}$)	CuNPs(2.9 nm) (10^{-3} $s^{-1}mmol^{-1}$)	RuNPs(2.7 nm) (10^{-3} $s^{-1}mmol^{-1}$)	PtNPs(2.1 nm)* (10^{-3} $s^{-1}mmol^{-1}$)
Fresh	113.5	44.0	16.0	1.6	5.5	1.6
2nd	76.0	10.1	15.6	1.4	2.7	1.3
3rd	65.0	2.2	15.4	1.3	2.2	1.4
4th	56.0	0.8	15.0	1.1	1.3	1.3

*pnp/$NaBH_4$ = 1/100.

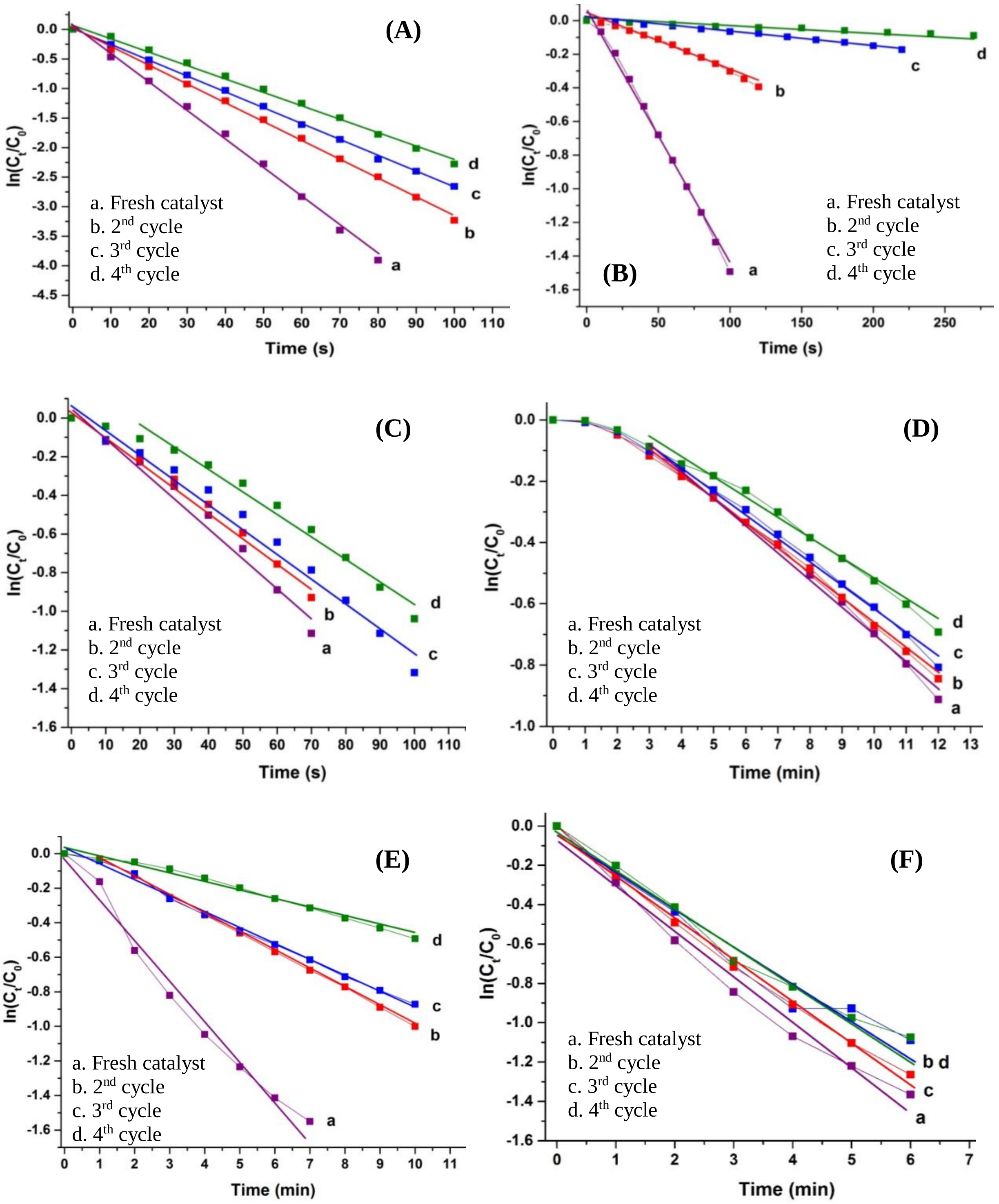

Fig. 4.17. The recyclability of (A) PdNPs(2.4 nm)_me-Im@SBA-15, (B) PdNPs(3.4 nm)_bu-Im@SBA-15, (C) AuNPs(2.0 nm)_me-Im@SBA-15, (D) CuNPs(2.9 nm)_me-Im@SBA-15, (E) and RuNPs(2.7 nm)_me-Im@SBA-15, and (F) PtNPs(2.1 nm)_me-Im@SBA-15.

Table 4.8 compares the catalytic activity of all the prepared catalysts MNPs_R-Im@SBA-15 and the reported ones in the terms of rate constant in the reduction of PNP. The prepared PdNPs and AuNPs catalysts showed better activities than that of similar feature catalysts, SBA-15-Im$^+$-Au1.0 and SBA-15-Im$^+$-Pd1.0.[22] Moreover, the present catalysts presented better catalytic performances than that of supported and unsupported metal nanoparticles with different size and morphologies, as well as that of bimetallic and trimetallic nanoparticles.[22,85–92] These results suggest that the prepared immobilized metal nanoparticles on SBA-15 in the presence of ionic liquids are highly active and reusable without a need for removing the imidazolium molecules of the ionic liquids in order to have active particles.

Table 4.8. Comparison of pseudo-first-order rate constant for PNP reduction by various supported metal nanoparticles.

Catalyst	Amount of catalyst (mg)	Mole ratio (PNP:$NaBH_4$)	k_{app} x 10^{-3} (s^{-1})	k_{app} x 10^{-3} ($s^{-1}mmol^{-1}$)^a	Conversion efficiency (%)	Ref.
PdNPs(2.4 nm) (2.4wt%)	0.16	1:50	47.4 ± 0.7	113.50	100	This work
PdNPs(3.4 nm) (6.7wt%)	0.05	1:50	15.7 ± 0.4	44.04	99.0	This work
AuNPs(2.0 nm) (0.8wt%)	0.50	1:50	13.4 ± 0.9	16.0	98.0	This work
PtNPs(2.1 nm) (4.1wt%)	0.30	1:100	3.8 ± 0.1	1.56	85.0	This work
RuNPs(2.7 nm) (1.3wt%)	0.50	1:50	3.7 ± 0.1	5.46	89.5	This work
CuNPs(2.9 nm) (1.5wt%)	1.0	1:50	1.6 ± 0.1	1.66	90.0	This work
SBA-15-Im+-Au1.0	20.0	1:50	1.1	0.015	-	[10]
SBA-15-Im+-Pd1.0	(1–5 nm)		11.8	1.72	-	
Pd-PEDOT-PSS (1-9 nm)	40 µl aliquot	Excess $NaBH_4$	65.8	7.73	-	[56]
Au/g-C_3N_{4-6} (2.6 nm)	1.0	1:15	8.0	0.93	100	[57]
Au@Pd@RuNPs (110 nm)	0.5 pM	1:100	24.2	-	-	[58]
G5-RuDEN (1.4 nm)	2.5 µM	1:50	0.6	-	-	[59]
PtNBs (60-100 nm)	0.025	1:333	2.1	-	-	[60]
PtNCs (20 nm)	100 µL	1:2000	0.6	-	-	
Fe_3O_4/graphene/Pt	2 mg/ml (2–3 nm)	1:324	20.5	-	90.0	[61]
Fe_3O_4/graphene/PdPt			36.8	-	90.0	
In situ Cu_2O-Cu-CuO (50-100 nm)	1.0	1:50	15.6	0.25	-	[62]
In situ Cu (5.6 nm)	3.0	1:166	0.4	0.002	-	[63]

a *k* per-mmol metal loaded in the catalyst.

The conversion of PNP is expressed by:

$$Conversion = \left(1 - \frac{At}{A0}\right) x\ 100\%$$

4.4. Conclusion

In this study, various supported metal nanoparticles catalysts with the average size of 2–4 nm prepared from immobilized metal chloride on ILs functionalized SBA-15 were successfully synthesized. The ILs were successfully immobilized and the bonding strength between the ILs and the surface of SBA-15 remains unchanged after the formation of MNPs. In the case PdNPs, short immobilized IL (MTI) showed more effective to stabilize the NPs than larger IL (BTI). XAFS analysis revealed that the metal atom was coordinated by chloride atoms forming metal chloride complex anion before being reduced to metal or metal oxide nanoparticles. Only AuNP was completely reduced to Au^0 without any surface oxidation on the Au surface, whereas the other metals (Pd, Pt and Ru) were partially oxidized due to the adsorption of oxygen adatoms. The prepared CuNPs was found consisting of two different species which are metallic Cu and Cu_2O. All the prepared metal NPs were active and reusable for *p*-nitrophenol hydrogenation reaction. The order of rate constant for fresh catalyst is Pd(2.4 nm) > Pd(3.4 nm) > Au > Ru > Pt > Cu. The prepared AuNPs, CuNPs and PtNPs were found most stable in the recycle process. The activity and stability of the prepared nanoparticles depend on the size of nanoparticle, metal species of the nanoparticles, and the catalyst morphology.

4.5. References

(1) Campbell, C. T.; Parker, S. C.; Starr, D. E. The Effect of Size-Dependent Nanoparticle Energetics on Catalyst Sintering. *Science* **2002**, *298* (5594), 811–814.

(2) Cao, A.; Lu, R.; Veser, G. Stabilizing Metal Nanoparticles for Heterogeneous Catalysis. *Phys. Chem. Chem. Phys.* **2010**, *12* (41), 13499.

(3) Kim, C.; Lee, H. Change in the Catalytic Reactivity of Pt Nanocubes in the Presence of Different Surface-Capping Agents. *Catal. Commun.* **2009**, *10* (9), 1305–1309.

(4) Park, J. Y.; Aliaga, C.; Renzas, J. R.; Lee, H.; Somorjai, G. A. The Role of Organic Capping Layers of Platinum Nanoparticles in Catalytic Activity of CO Oxidation. *Catal. Lett.* **2009**, *129* (1–2), 1–6.

(5) Cao, A.; Veser, G. Exceptional High-Temperature Stability through Distillation-like Self-Stabilization in Bimetallic Nanoparticles. *Nat. Mater.* **2010**, *9* (1), 75–81.

(6) Deeba, M.; Farrauto, R. J.; Lui, Y. K. Stabilization of Platinum on Silica Promoted with Lanthanum Oxide and Zirconium Oxide. *Appl. Catal. A, Gen.* **1995**, *124* (2), 339–344.

(7) Wang, C. M.; Fan, K. N.; Liu, Z. P. Insight into the Synergetic Effect in Ternary Gold-Based Catalysts: Ultrastability and High Activity of Au on Alumina Modified Titania. *J. Phys. Chem. C* **2007**, *111* (36), 13539–13546.

(8) Shinjoh, H.; Hatanaka, M.; Nagai, Y.; Tanabe, T.; Takahashi, N.; Yoshida, T.; Miyake, Y. Suppression of Noble Metal Sintering Based on the Support Anchoring Effect and Its Application in Automotive Three-Way Catalysis. *Top. Catal.* **2009**, *52* (13–20), 1967–1971.

(9) Nagai, Y.; Hirabayashi, T.; Dohmae, K.; Takagi, N.; Minami, T.; Shinjoh, H.; Matsumoto, S. Sintering Inhibition Mechanism of Platinum Supported on Ceria-Based Oxide and Pt-

Oxide-Support Interaction. *J. Catal.* **2006**, *242* (1), 103–109.

(10) Beck, A.; Horváth, A.; Stefler, G.; Katona, R.; Geszti, O.; Tolnai, G.; Liotta, L. F.; Guczi, L. Formation and Structure of Au/TiO_2 and Au/CeO_2 Nanostructures in Mesoporous SBA-15. *Catal. Today* **2008**, *139* (3), 180–187.

(11) Sasaki, T.; Zhong, C.; Tada, M.; Iwasawa, Y. Immobilized Metal Ion-Containing Ionic Liquids: Preparation, Structure and Catalytic Performance in Kharasch Addition Reaction. *Chem. Commun.* **2005**, 2506–2508.

(12) Zhong, C.; Sasaki, T.; Tada, M.; Iwasawa, Y. Ni Ion-Containing Ionic Liquid Salt and Ni Ion-Containing Immobilized Ionic Liquid on Silica: Application to Suzuki Cross-Coupling Reactions between Chloroarenes and Arylboronic Acids. *J. Catal.* **2006**, *242* (2), 357–364.

(13) Sasaki, T.; Tada, M.; Zhong, C.; Kume, T.; Iwasawa, Y. Immobilized Metal Ion-Containing Ionic Liquids: Preparation, Structure and Catalytic Performances in Kharasch Addition Reaction and Suzuki Cross-Coupling Reactions. *J. Mol. Catal. A Chem.* **2008**, *279* (2), 200–209.

(14) Khedkar, M. V; Sasaki, T.; Bhanage, B. M. Efficient, Recyclable and Phosphine-Free Carbonylative Suzuki Coupling Reaction Using Immobilized Palladium Ion-Containing Ionic Liquid: Synthesis of Aryl Ketones and Heteroaryl Ketones. *RSC Adv.* **2013**, *3* (21), 7791–7797.

(15) Patil, N. M.; Sasaki, T.; Bhanage, B. M. Chemoselective Transfer Hydrogenation of Alpha, Beta-Unsaturated Carbonyls Using Palladium Immobilized Ionic Liquid Catalyst. *Catal. Lett.* **2014**, *144* (11), 1803–1809.

(16) Khedkar, M. V.; Shinde, A. R.; Sasaki, T.; Bhanage, B. M. Immobilized Palladium Metal Containing Ionic Liquid Catalyzed One Step Synthesis of Isoindole-1,3-Diones by

Carbonylative Cyclization Reaction. *J. Mol. Catal. A Chem.* **2014**, *385*, 91–97.

(17) Patil, N. M.; Sasaki, T.; Bhanage, B. M. Immobilized Iron Metal-Containing Ionic Liquid-Catalyzed Chemoselective Transfer Hydrogenation of Nitroarenes into Anilines. *ACS Sustain. Chem. Eng.* **2016**, *4* (2), 429–436.

(18) Patil, N. M.; Sasaki, T.; Bhanage, B. M. Immobilized Ruthenium Metal-Containing Ionic Liquid-Catalyzed Dehydrogenation of Dimethylamine Borane Complex for the Reduction of Olefins and Nitroarenes. *RSC Adv.* **2016**, *6* (57), 52347–52352.

(19) Gadge, S. T.; Kusumawati, E. N.; Harada, K.; Sasaki, T.; Nishio-Hamane, D.; Bhanage, B. M. Synthesis of Oxamate and Urea by Oxidative Single and Double Carbonylation of Amines Using Immobilized Palladium Metal-Containing Ionic Liquid@SBA-15. *J. Mol. Catal. A Chem.* **2015**, *400*, 170–178.

(20) Satapathy, A.; Gadge, S. T.; Kusumawati, E. N.; Harada, K.; Sasaki, T.; Nishio-Hamane, D.; Bhanage, B. M. Synthesis of Polyester Amide by Carbonylation-Polycondensation Reaction Using Immobilized Palladium Metal Containing Ionic Liquid on SBA-15 as a Phosphine-Free Catalytic System. *Catal. Lett.* **2015**, *145* (3), 824–833.

(21) Fattori, N.; Maroneze, C. M.; Da Costa, L. P.; Strauss, M.; Sigoli, F. A.; Mazali, I. O.; Gushikem, Y. Ion-Exchange Properties of Imidazolium-Grafted SBA-15 toward $AuCl_4^-$ Anions and Their Conversion into Supported Gold Nanoparticles. *Langmuir* **2012**, *28* (27), 10281–10288.

(22) Damasceno, J. P. V.; Maroneze, C. M.; Strauss, M.; Sigoli, F. A.; Mazali, I. O. Preparation of Supported AuPd Nanoalloys Mediated by Ionic Liquid-like Functionalized SBA-15: Structural Correlations Concerning Its Catalytic Activity. *New J. Chem.* **2016**, *40* (8), 6636–6642.

(23) Kusumawati, E. N.; Nishio-Hamane, D.; Sasaki, T. Size-Controllable Gold Nanoparticles Prepared from Immobilized Gold-Containing Ionic Liquids on SBA-15. *Catal. Today* **2017**.

(24) Zhao, D.; Feng, J.; Huo, Q.; Melosh, N.; Fredrickson, G. H.; Chmelka, B. F.; Stucky, G. D. Triblock Copolymer Syntheses of Mesoporous Silica with Periodic 50 to 300 Angstrom Pores. *Science* **1998**, *279* (5350), 548–552.

(25) Frens, G. Controlled Nucleation for the Regulation of the Particle Size in Monodisperse Gold Suspensions. *Nat. Phys. Sci.* **1973**, *241* (105), 20–22.

(26) Ji, X.; Song, X.; Li, J.; Bai, Y.; Yang, W. Size Control of Gold Nanocrystals in Citrate Reduction : The Third Role of Citrate. *J. Am. Chem. Soc.* **2007**, *129* (45), 1957–1962.

(27) Shervani, Z.; Yamamoto, Y. Carbohydrate-Directed Synthesis of Silver and Gold Nanoparticles: Effect of the Structure of Carbohydrates and Reducing Agents on the Size and Morphology of the Composites. *Carbohydr. Res.* **2011**, *346* (5), 651–658.

(28) Koningsberger, D. C.; Prins, R. X-Ray Absorption: Principles, Applications, Techniques of EXAFS, SEXAFS, and XANES. **1988**.

(29) Chen, C. H.; Sarma, L. S.; Chen, J. M.; Shih, S. C.; Wang, G. R.; Liu, D. G.; Tang, M. T.; Lee, J. F.; Hwang, B. J. Architecture of Pd-Au Bimetallic Nanoparticles in Sodium Bis(2-Ethylhexyl)Sulfosuccinate Reverse Micelles as Investigated by X-Ray Absorption Spectroscopy. *ACS Nano* **2007**, *1* (2), 114–125.

(30) Fahmy, K.; Merroun, M.; Pollmann, K.; Raff, J.; Savchuk, O.; Hennig, C.; Selenska-Pobell, S. Secondary Structure and Pd(II) Coordination in S-Layer Proteins from Bacillus Sphaericus Studied by Infrared and X-Ray Absorption Spectroscopy. *Biophys. J.* **2006**, *91* (3), 996–1007.

(31) Zhong, C.; Sasaki, T.; Jimbo-Kobayashi, A.; Fujiwara, E.; Kobayashi, A.; Tada, M.; Iwasawa, Y. Syntheses, Structures, and Properties of a Series of Metal Ion-Containing Dialkylimidazolium Ionic Liquids. *Bull. Chem. Soc. Jpn.* **2007**, *80* (12), 2365–2374.

(32) Dullius, J. E. L.; Suarez, P. A. Z.; Einloft, S.; De Souza, R. F.; Dupont, J.; Fischer, J.; De Cian, A. Selective Catalytic Hydrodimerization of 1,3-Butadiene by Palladium Compounds Dissolved in Ionic Liquids. *Organometallics* **1998**, *17* (5), 815–819.

(33) Okumura, K.; Amano, J.; Niwa, M. Studies on the Formation and Structure of Highly Dispersed PdO Interacted with Brønsted Acid Sites on Zeolite by EXAFS. *Chem. Lett.* **1999**, *28* (9), 997–998.

(34) Okumura, K.; Niwa, M. Regulation of the Dispersion of PdO through the Interaction with Acid Sites of Zeolite Studied by Extended X-Ray Absorption Fine Structure. *J. Phys. Chem. B* **2000**, *104* (41), 9670–9675.

(35) Okumura, K.; Amano, J.; Yasunobu, N.; Niwa, M. X-Ray Absorption Fine Structure Study of the Formation of the Highly Dispersed PdO over ZSM-5 and the Structural Change of Pd Induced by Adsorption of NO. *J. Phys. Chem. B* **2000**, *104* (5), 1050–1057.

(36) Tanaka, T.; Ohyama, J.; Teramura, K.; Hitomi, Y. Formation Mechanism of Metal Nanoparticles Studied by XAFS Spectroscopy and Effective Synthesis of Small Metal Nanoparticles. *Catal. Today* **2012**, *183* (1), 108–118.

(37) Nishimura, S.; Dao, A. T. N.; Mott, D.; Ebitani, K.; Maenosono, S. X-Ray Absorption Near-Edge Structure and X-Ray Photoelectron Spectroscopy Studies of Interfacial Charge Transfer in Gold–Silver–Gold Double-Shell Nanoparticles. *J. Phys. Chem. C* **2012**, *116* (7), 4511–4516.

(38) Ma, J.; Zou, Y.; Jiang, Z.; Huang, W.; Li, J.; Wu, G.; Huang, Y.; Xu, H. An in Situ XAFS

Study—the Formation Mechanism of Gold Nanoparticles from X-Ray-Irradiated Ionic Liquid. *Phys. Chem. Chem. Phys.* **2013**, *15* (28), 11904.

(39) He, Y. X.; Fu, H. Y.; Li, C.; Ji, X.; Ge, X. W.; Zou, Y.; Jiang, Z.; Xu, H. J.; Wu, G. Z. Property Variation of Ionic Liquid [Bmim][AuCl$_4$] Immobilized on Carboxylated Polystyrene Submicrospheres with a Small Surface Area. *Chinese Sci. Bull.* **2013**, *58* (24), 2950–2955.

(40) Song, Z.; Kenney, J. P. L.; Fein, J. B.; Bunker, B. A. An X-Ray Absorption Fine Structure Study of Au Adsorbed onto the Non-Metabolizing Cells of Two Soil Bacterial Species. *Geochim. Cosmochim. Acta* **2012**, *86*, 103–117.

(41) Chang, S.-Y.; Uehara, A.; Booth, S. G.; Ignatyev, K.; Mosselmans, J. F. W.; Dryfe, R. A. W.; Schroeder, S. L. M. Structure and Bonding in Au(I) Chloride Species: A Critical Examination of X-Ray Absorption Spectroscopy (XAS) Data. *RSC Adv.* **2015**, *5* (9), 6912–6918.

(42) Zhang, P.; Sham, T. K. X-Ray Studies of the Structure and Electronic Behavior of Alkanethiolate-Capped Gold Nanoparticles: The Interplay of Size and Surface Effects. *Phys. Rev. Lett.* **2003**, *90* (24), 4.

(43) Benfield, R. E.; Grandjean, D.; Kröll, M.; Pugin, R.; Sawitowski, T.; Schmid, G. Structure and Bonding of Gold Metal Clusters, Colloids, and Nanowires Studied by EXAFS, XANES, and WAXS. *J. Phys. Chem. B* **2001**, *105* (10), 1961–1970.

(44) Mansour, A. N.; Cook, J. W.; Sayers, D. E. Quantitative Technique for the Determination of the Number of Unoccupied D-Electron States in a Platinum Catalyst Using the L$_{2,3}$ X-Ray Absorption Edge Spectra. *J. Phys. Chem.* **1984**, *88* (11), 2330–2334.

(45) Mattheis, L. F.; Dietz, R. E. Relativistic Tight-Binding Calculation of Core-Valence

Transitions in Pt and Au. *Phys. Rev.* **1980**, *22* (4), 1663–1676.

(46) Zhang, P.; Sham, T. K. Tuning the Electronic Behavior of Au Nanoparticles with Capping Molecules. *Appl. Phys. Lett.* **2002**, *81* (4), 736–738.

(47) Kau, L.-S.; Hodgson, K. O.; Solomon, E. I. X-Ray Absorption Edge and EXAFS Study of the Copper Sites in Zinc Oxide Methanol Synthesis Catalysts. *J. Am. Chem. Soc.* **1989**, *111* (18), 7103–7109.

(48) Kunquan, L.; Jun, W. Extended X-Ray-Absorption Fine Structure of a System of Mixed Phases. *Phys. Rev. B* **1987**, *35* (9), 4497–4499.

(49) Kau, L. shan; Spira-solomon, D. J.; Spira-solomon-penner-hahn, J. E.; Hodgson, K. O.; Solomon, E. I. X-Ray Absorption Edge Determination of the Oxidation State and Coordination Number of Copper: Application to the Type 3 Site in Rhus Vernicifera Laccase and Its Reaction with Oxygen. *J. Am. Chem. Soc.* **1987**, *109* (21), 6433–6442.

(50) Gruenert, W.; Hayes, N. W.; Joyner, R. W.; Shpiro, E. S.; Siddiqui, M. R. H.; Baeva, G. N. Structure, Chemistry, and Activity of Cu-ZSM-5 Catalysts for the Selective Reduction of NOx in the Presence of Oxygen. *J. Phys. Chem.* **1994**, *98* (42), 10832–10846.

(51) Kuroda, Y.; Yoshikawa, Y.; Konno, S. I.; Hamano, H.; Maeda, H.; Kumashiro, R.; Nagao, M. Specific Feature of Copper Ion-Exchanged Mordenite for Dinitrogen Adsorption at Room Temperature. *J. Phys. Chem.* **1995**, *99* (26), 10621–10628.

(52) Beutel, T.; Sárkány, J.; Lei, G. D.; Yan, J. Y.; Sachtler, W. M. H. Redox Chemistry of Cu/ZSM-5. *J. Phys. Chem.* **1996**, *100* (2), 845–851.

(53) Drake, I. J.; Fujdala, K. L.; Baxamusa, S.; Bell, A. T.; Tilley, T. D. Effects of Precursor Composition on the Local Structure of Cu Dispersed on Mesoporous Silica: A Detailed X-Ray Absorption Spectroscopy Study. *J. Phys. Chem. B* **2004**, *108* (48), 18421–18434.

(54) Magadzu, T.; Yang, J. H.; Henao, J. D.; Kung, M. C.; Kung, H. H.; Scurrell, M. S. Low-Temperature Water-Gas Shift Reaction over Au Supported on Anatase in the Presence of Copper: EXAFS/XANES Analysis of Gold-Copper Ion Mixtures on TiO_2. *J. Phys. Chem. C* **2017**, *121* (16), 8812–8823.

(55) Nian, J. N.; Chen, S. A.; Tsai, C. C.; Teng, H. Structural Feature and Catalytic Performance of Cu Species Distributed over TiO_2 Nanotubes. *J. Phys. Chem. B* **2006**, *110* (51), 25817–25824.

(56) Li, G.; Camaioni, D. M.; Amonette, J. E.; Zhang, Z. C.; Johnson, T. J.; Fulton, J. L. $[CuCl_n]^{2-n}$ Ion-Pair Species in 1-Ethyl-3-Methylimidazolium Chloride Ionic Liquid-Water Mixtures: Ultraviolet-Visible, X-Ray Absorption Fine Structure, and Density Functional Theory Characterization. *J. Phys. Chem. B* **2010**, *114* (39), 12614–12622.

(57) Kaito, T.; Tanaka, H.; Mitsumoto, H.; Sugawara, S.; Shinohara, K.; Ariga, H.; Uehara, H.; Takakusagi, S.; Asakura, K. In Situ X-Ray Absorption Fine Structure Analysis of PtCo, PtCu, and PtNi Alloy Electrocatalysts: The Correlation of Enhanced Oxygen Reduction Reaction Activity and Structure. *J. Phys. Chem. C* **2016**, *120* (21), 11519–11527.

(58) Lin, L. W.; Kou, Y.; Zou, M.; Yan, Z. An Amorphous Approach to the Structure of a Pt-Fe/γ-Al_2O_3 Catalyst Characterized by XAFS. *Phys. Chem. Chem. Phys.* **2001**, *3* (9), 1789–1794.

(59) Chen, S.; Wu, Y.; Tao, S.; Cui, P.; Chu, W.; Chen, X.; Wu, Z. An X-Ray Absorption Spectroscopic Investigation of the Geometry of Pt(IV) in H_2PtCl_6 ammonia Solution. *J. Mol. Struct.* **2013**, *1041*, 39–43.

(60) Tromp, M.; Slagt, M. Q.; Klein Gebbink, R. J. M.; Van Koten, G.; Ramaker, D. E.; Koningsberger, D. C. Atomic XAFS as a Probe of Electron Transfer within

Organometallic Complexes: Data Analysis and Theoretical Calculations. *Phys. Chem. Chem. Phys.* **2004**, *6* (18), 4397–4406.

(61) Chen, X.; Chu, W.; Wang, L.; Wu, Z. Geometry of Pt(IV) in H_2PtCl_6 aqueous Solution: An X-Ray Absorption Spectroscopic Investigation. *J. Mol. Struct.* **2009**, *920* (1–3), 40–44.

(62) Ankudinov, A. L.; Rehr, J. J.; Bare, S. R. Hybridization Peaks in Pt-Cl XANES. *Chem. Phys. Lett.* **2000**, *316* (5–6), 495–500.

(63) Kuznetsova, L. I.; Kuznetsova, N. I.; Koshcheev, S. V; Rogov, V. A.; Zaikovskii, V. I.; Novgorodov, B. N.; Detusheva, L. G.; Likholobov, V. A.; Kochubey, D. I. Interaction of Platinum and Molybdophosphoric Heteropoly Acid under Conditions of Catalyst Preparation for Benzene Oxidation to Phenol with an O_2-H_2 Gas Mixture. *Kinet. Catal.* **2006**, *47* (5), 704–714.

(64) Qiao, B.; Wang, A.; Yang, X.; Allard, L. F.; Jiang, Z.; Cui, Y.; Liu, J.; Li, J.; Zhang, T. Single-Atom Catalysis of CO Oxidation Using Pt_1/FeO_x. *Nat. Chem.* **2011**, *3* (8), 634–641.

(65) Chakroune, N.; Viau, G.; Ammar, S.; Poul, L.; Veautier, D.; Chehimi, M. M.; Mangeney, C.; Villain, F.; Fievet, F. Acetate- and Thiol-Capped Monodisperse Ruthenium Nanoparticles: XPS, XAS, and HRTEM Studies. *Langmuir* **2005**, *21* (15), 6788–6796.

(66) Haas, S.; Zehl, G.; Dorbandt, I.; Manke, I.; Bogdanoff, P.; Fiechter, S.; Hoell, A. Direct Accessing the Nanostructure of Carbon Supported Ru - Se Based Catalysts By. *J. Phys. Chem. C* **2010**, *114* (51), 22375–22384.

(67) Altwasser, S.; Gläser, R.; Lo, A. S.; Liu, P. H.; Chao, K. J.; Weitkamp, J. Incorporation of RuO_2 nanoparticles into MFI-Type Zeolites. *Microporous Mesoporous Mater.* **2006**, *89* (1–3), 109–122.

(68) Yang, Y.; Yang, F.; Sun, C. J.; Zhao, H.; Hao, S.; Brown, D. E.; Zhang, J.; Ren, Y. Ru-Fe

Alloy Mediated α-Fe_2O_3 particles on Mesoporous Carbon Nanofibers as Electrode Materials with Superior Capacitive Performance. *RSC Adv.* **2017**, *7* (12), 6818–6826.

(69) Yang, Y.; Sun, C. J.; Brown, D. E.; Zhang, L.; Yang, F.; Zhao, H.; Wang, Y.; Ma, X.; Zhang, X.; Ren, Y. A Smart Strategy to Fabricate Ru Nanoparticle Inserted Porous Carbon Nanofibers as Highly Efficient Levulinic Acid Hydrogenation Catalysts. *Green Chem.* **2016**, *18* (12), 3558–3566.

(70) Nashner, M. S.; Frenkel, A. I.; Adler, D. L.; Shapley, J. R.; Nuzzo, R. G. Structural Characterization of Carbon Supported Platinum-Ruthenium Nanoparticles from the Molecular Cluster Precursor $PtRu_5(CO)_{16}$. *J. Am. Chem. Soc.* **1997**, *119* (14), 7760–7771.

(71) Czekaj, I.; Pin, S.; Wambach, J. Ru/Active Carbon Catalyst: Improved Spectroscopic Data Analysis by Density Functional Theory. *J. Phys. Chem. C* **2013**, *117* (50), 26588–26597.

(72) Alayoglu, S.; Zavalij, P.; Eichhorn, B.; Wang, Q.; Frenkel, A. I.; Chupas, P. Structural and Architectural Evaluation of Bimetallic Nanoparticles: A Case Study of Pt-Ru Core-Shell and Alloy Nanoparticles. *ACS Nano* **2009**, *3* (10), 3127–3137.

(73) Udayakumar, S.; Raman, V.; Shim, H.; Park, D. Cycloaddition of Carbon Dioxide for Commercially-Imperative Cyclic Carbonates Using Ionic Liquid-Functionalized Porous Amorphous Silica. *Appl. Catal. A Gen.* **2009**, *368*, 97–104.

(74) Xu, J.; Wu, H.; Ma, C.; Xue, B.; Li, Y.; Cao, Y. Ionic Liquid Immobilized on Mesocellular Silica Foam as an Efficient Heterogeneous Catalyst for the Synthesis of Dimethyl Carbonate via Transesterification. *Appl. Catal. A, Gen.* **2013**, *464–465*, 357–363.

(75) Zhang, W.; Wang, H.; Han, J.; Song, Z. Multifunctional Mesoporous Materials with Acid-Base Frameworks and Ordered Channels Filled with Ionic Liquid: Synthesis, Characterization and Catalytic Performance of Ti-Zr-SBA-15-IL. *Appl. Surf. Sci.* **2012**,

258 (16), 6158–6168.

(76) Sutra, P.; Fajula, F.; Brunel, D.; Lentz, P.; Daelen, G.; Nagy, J. B. ^{29}Si and ^{13}C MAS-NMR Characterization of Surface Modification of Micelle-Templated Silicas during the Grafting of Organic Moieties and End-Capping. *Colloids Surfaces A Physicochem. Eng. Asp.* **1999**, *158* (1–2), 21–27.

(77) Han, P.; Zhang, H.; Qiu, X.; Ji, X.; Gao, L. Palladium within Ionic Liquid Functionalized Mesoporous Silica SBA-15 and Its Catalytic Application in Room-Temperature Suzuki Coupling Reaction. *J. Mol. Catal. A Chem.* **2008**, *295* (1–2), 57–67.

(78) Luza, L.; Gual, A.; Eberhardt, D.; Teixeira, S. R.; Chiaro, S. S. X.; Dupont, J. “Imprinting” Catalytically Active Pd Nanoparticles onto Ionic-Liquid-Modified Al_2O_3 Supports. *ChemCatChem* **2013**, *5* (8), 2471–2478.

(79) Xu, R.; Shi, X.; Zhang, W.; Xu, Y.; Tian, Z.; Lu, X.; Han, X.; Bao, X. Cooperative Structure-Directing Effect in the Synthesis of Aluminophosphate Molecular Sieves in Ionic Liquids. *Phys. Chem. Chem. Phys.* **2010**, *12* (10), 2443.

(80) Zhao, Z.; Zhang, W.; Xu, R.; Han, X.; Tian, Z.; Bao, X. Ionothermal Synthesis Process for Aluminophosphate Molecular Sieves in the Mixed Water/Ionic Liquid System. *Dalt. Trans.* **2012**, *41* (3), 990–994.

(81) Pei, R.; Wei, Y.; Li, K.; Wen, G.; Xu, R.; Xu, Y.; Wang, L.; Ma, H.; Wang, B.; Tian, Z.; et al. Mixed Template Effect Adjusted by Amine Concentration in Ionothermal Synthesis of Molecular Sieves. *Dalt. Trans.* **2010**, *39* (6), 1441–1443.

(82) Ma, C. Y.; Dou, B. J.; Li, J. J.; Cheng, J.; Hu, Q.; Hao, Z. P.; Qiao, S. Z. Catalytic Oxidation of Benzyl Alcohol on Au or Au-Pd Nanoparticles Confined in Mesoporous Silica. *Appl. Catal. B Environ.* **2009**, *92* (1–2), 202–208.

(83) Ajaikumar, S.; Golets, M.; Larsson, W.; Shchukarev, A.; Kordas, K.; Leino, A. R.; Mikkola, J. P. Effective Dispersion of Au and Au-M (M = Co, Ni, Cu and Zn) Bimetallic Nanoparticles over TiO_2 Grafted SBA-15: Their Catalytic Activity on Dehydroisomerization of α-Pinene. *Micropor. Mesopor. Mater.* **2013**, *173*, 99–111.

(84) Petkov, N.; Stock, N.; Bein, T. Gold Electroless Reduction in Nanosized Channels of Thiol-Modified SBA-15 Material. *J. Phys. Chem. B* **2005**, *109* (21), 10737–10743.

(85) Harish, S.; Mathiyarasu, J.; Phani, K. L. N.; Yegnaraman, V. Synthesis of Conducting Polymer Supported Pd Nanoparticles in Aqueous Medium and Catalytic Activity Towards 4-Nitrophenol Reduction. *Catal. Letters* **2009**, *128* (1–2), 197–202.

(86) Fu, Y.; Huang, T.; Jia, B.; Zhu, J.; Wang, X. Reduction of Nitrophenols to Aminophenols under Concerted Catalysis by Au/g-C_3N_4 Contact System. *Appl. Catal. B Environ.* **2017**, *202*, 430–437.

(87) Sahoo, A.; Tripathy, S. K.; Dehury, N.; Patra, S. A Porous Trimetallic Au@Pd@Ru Nanoparticle System: Synthesis, Characterisation and Efficient Dye Degradation and Removal. *J. Mater. Chem. A* **2015**, *3* (38), 19376–19383.

(88) Antonels, N. C.; Meijboom, R. Preparation of Well-Defined Dendrimer Encapsulated Ruthenium Nanoparticles and Their Evaluation in the Reduction of 4-Nitrophenol According to the Langmuir-Hinshelwood Approach. *Langmuir* **2013**, *29* (44), 13433–13442.

(89) Kalekar, A. M.; Sharma, K. K. K.; Lehoux, A.; Audonnet, F.; Remita, H.; Saha, A.; Sharma, G. K. Investigation into the Catalytic Activity of Porous Platinum Nanostructures. *Langmuir* **2013**, *29* (36), 11431–11439.

(90) Li, X.; Wang, X.; Song, S.; Liu, D.; Zhang, H. Selectively Deposited Noble Metal

Nanoparticles on Fe_3O_4/Graphene Composites: Stable, Recyclable, and Magnetically Separable Catalysts. *Chem. - A Eur. J.* **2012**, *18* (24), 7601–7607.

(91) Sasmal, A. K.; Dutta, S.; Pal, T. A Ternary Cu_2O-Cu-CuO Nanocomposite: A Catalyst with Intriguing Activity. *Dalt. Trans.* **2016**, *45* (7), 3139–3150.

(92) Deka, P.; Deka, R. C.; Bharali, P. In Situ Generated Copper Nanoparticle Catalyzed Reduction of 4-Nitrophenol. *New J. Chem.* **2014**, *38* (4), 1789–1793.

4.6. Supporting information

Table S4.1. ^{13}C chemical shifts for 1-methyl-3-(3-trimethoxysilylpropyl)-imidazolium chloride (MTI) or 1-buthyl-3-(3-trimethoxy-silylpropyl)-imidazolium chloride (BTI) (ppm).

Sample	C1	C2	C3	C4	C5	C6	C7	C8	C9	C10
MTI	10.4	24.7	52.7	137.5	124.6	124.6	37.7	-	-	-
BTI	10.4	25.3	50.6	137.3	124.0	124.0	50.6	33.1	20.3	14.6

Table S4.2. The amount of ionic liquids (ILs) on the catalysts before and after $PdCl_2$ immobilization.

Sample	% C	% H	% N	ILs (mmol/g)	ILs x 10^{-25} (mol/nm^2)	ILs (molecules/ 10 nm^2)
me-Im@SBA-15	16.81	3.97	5.59	0.20	2.4	1.5
bu-Im@SBA-15	20.07	4.25	4.64	0.14	1.7	1.1
PdCl_me-Im@SBA-15	16.14	3.35	5.34	0.19	2.3	1.4
PdCl_bu-Im@SBA-15	19.02	3.65	4.34	0.13	1.6	1.0

Table S4.3. N_2-adsorption data of SBA-15 and after ionic liquids immobilization.

Sample	S_{BET} (m^2/g)	Vt (cm^3/g)	D_{BJH} (nm)	a_0 (Å)	Wall thickness (nm)
SBA-15	828.1	1.27	7.7	117.6	4.0
me-Im@SBA-15	128.9	0.29	5.6	119.6	6.3
bu-Im@SBA-15	95.8	0.17	5.2	118.9	6.7

a_0 is unit cell determined by XRD analysis.

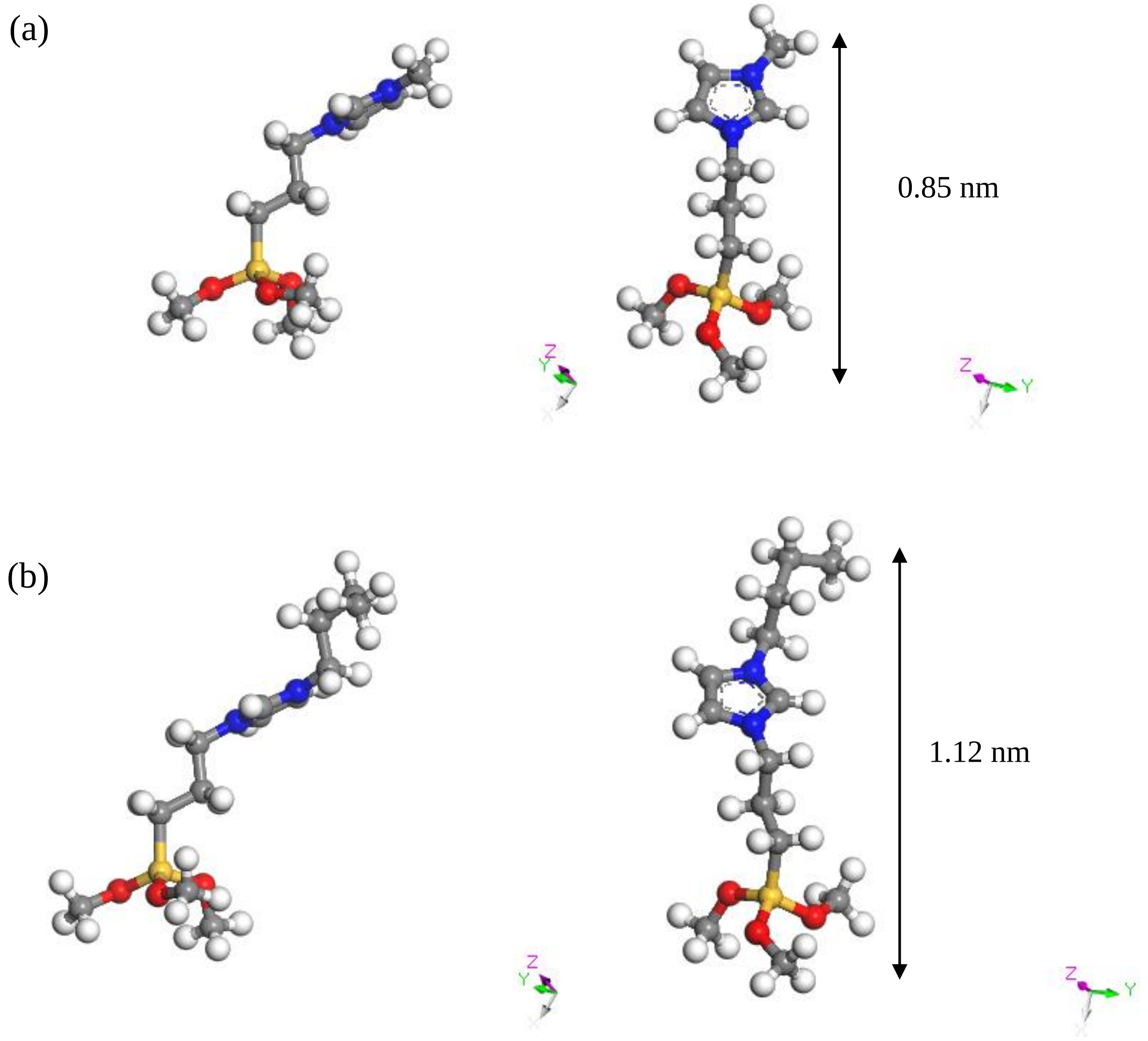

Fig. S4.1. Density Functional Theory (DFT) molecular modelling for the length calculation of (a) MTI and (b) BTI ionic liquids.

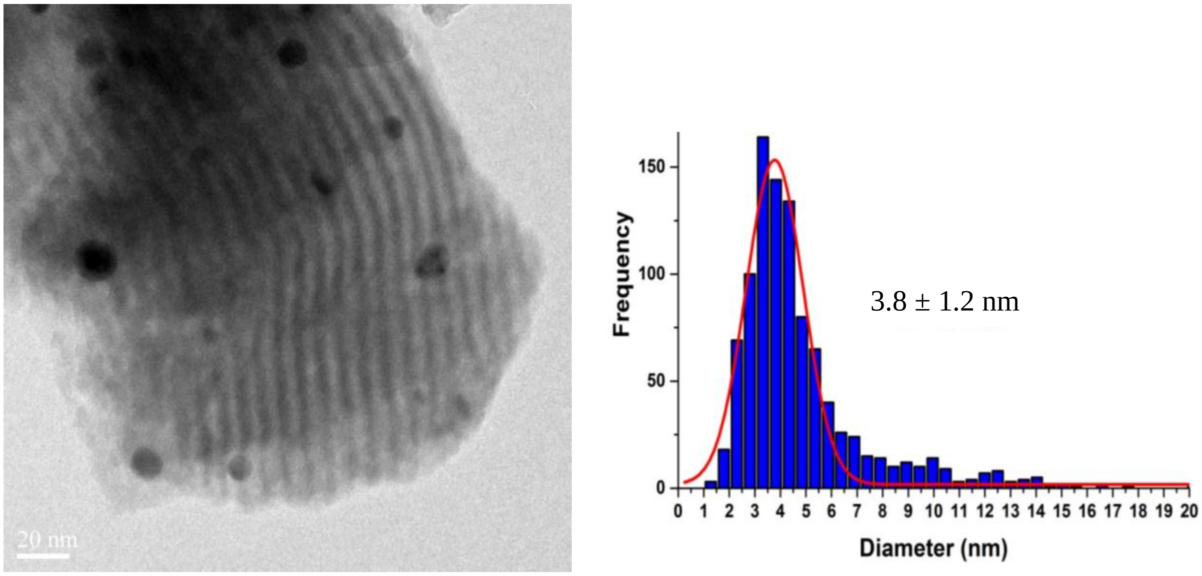

Fig. S4.2. TEM image and size distribution of CuNP(3.8 nm)_me-Im@SBA-15 which was reduce by 100 mM at 0.2 ml/min.

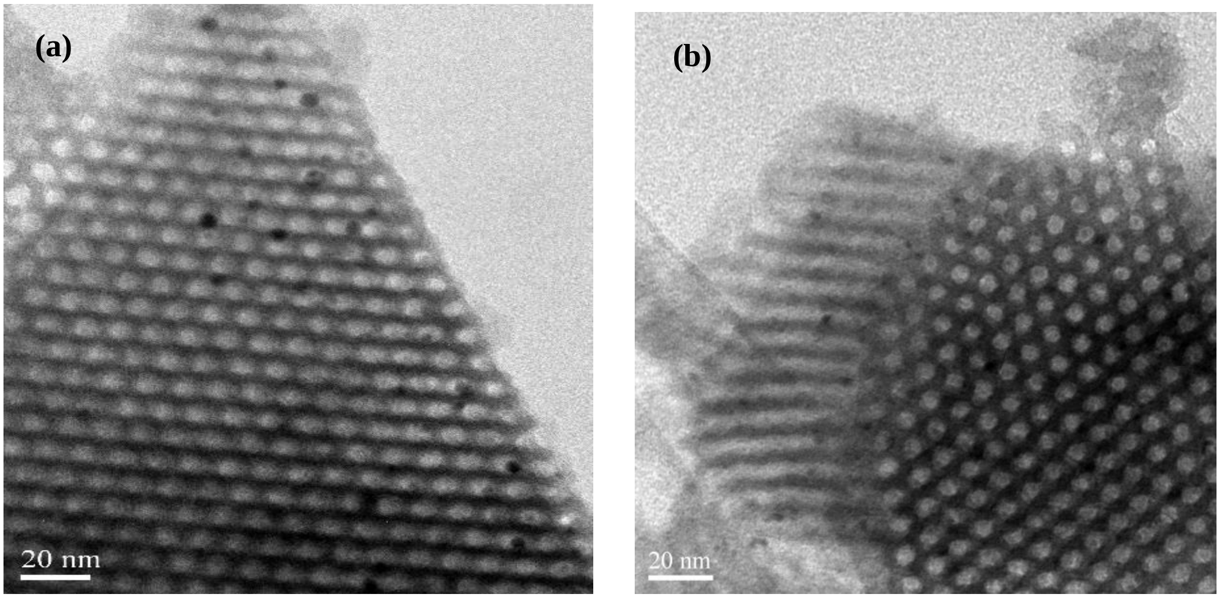

Fig. S4.3. TEM images of well-ordered hexagonal pore structure of (a) AuNP(2.0 nm)_me-Im@SBA-15 and (b) PtNP(2.1 nm)_me-Im@SBA-15.

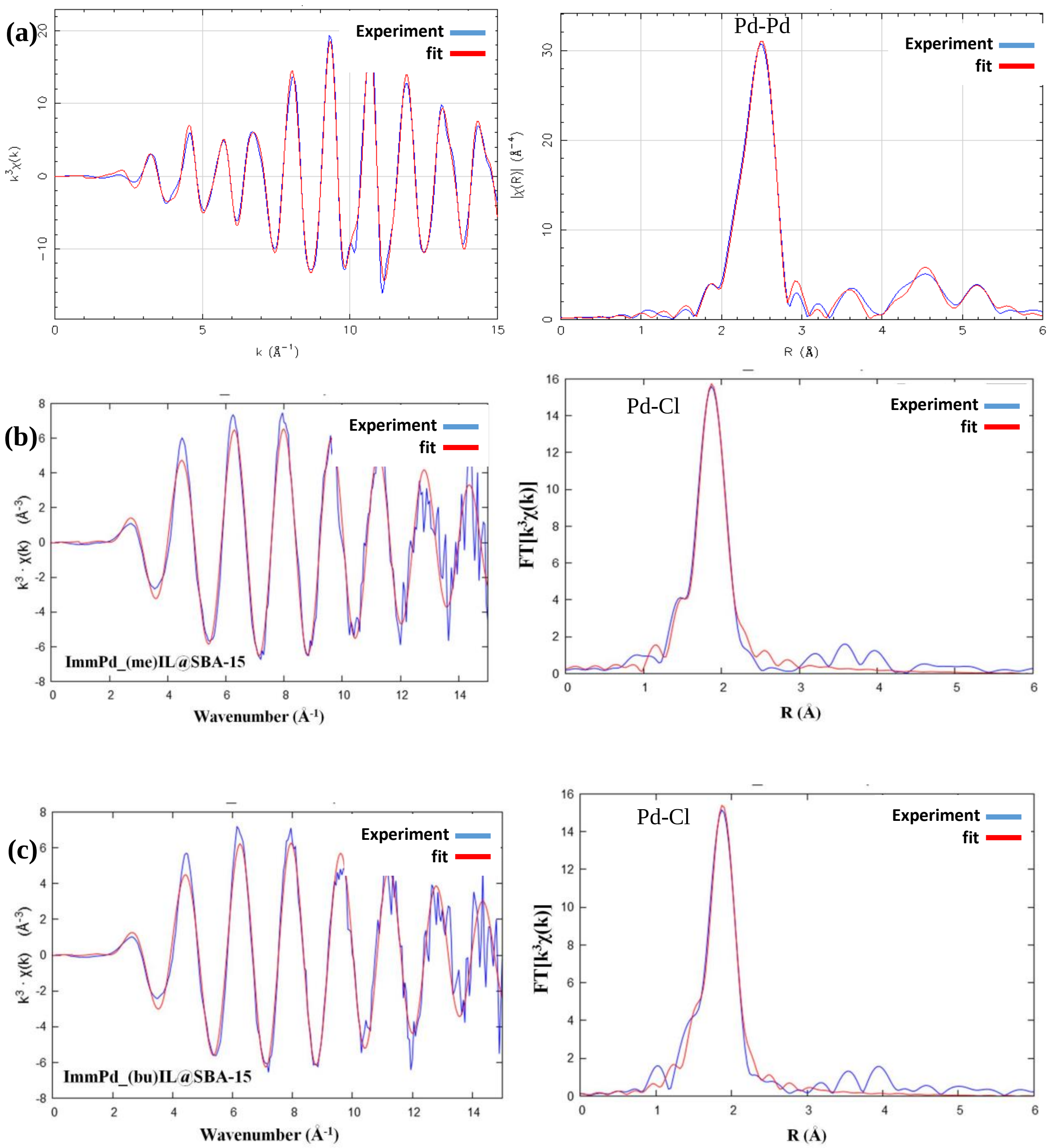

Fig. S4.4A. Observed and fitted data for k^3-weighted oscillation and its Fourier transform of Pd K-edge EXAFS for the reference compounds (a) Pd foil, and the prepared (b) PdCl_me-Im@SBA-15, (c) PdCl_bu-Im@SBA-15, (d) PdNPs(2.4 nm)_me-Im@SBA-15, and (e) PdNPs(3.4 nm)_bu-Im@SBA-15.

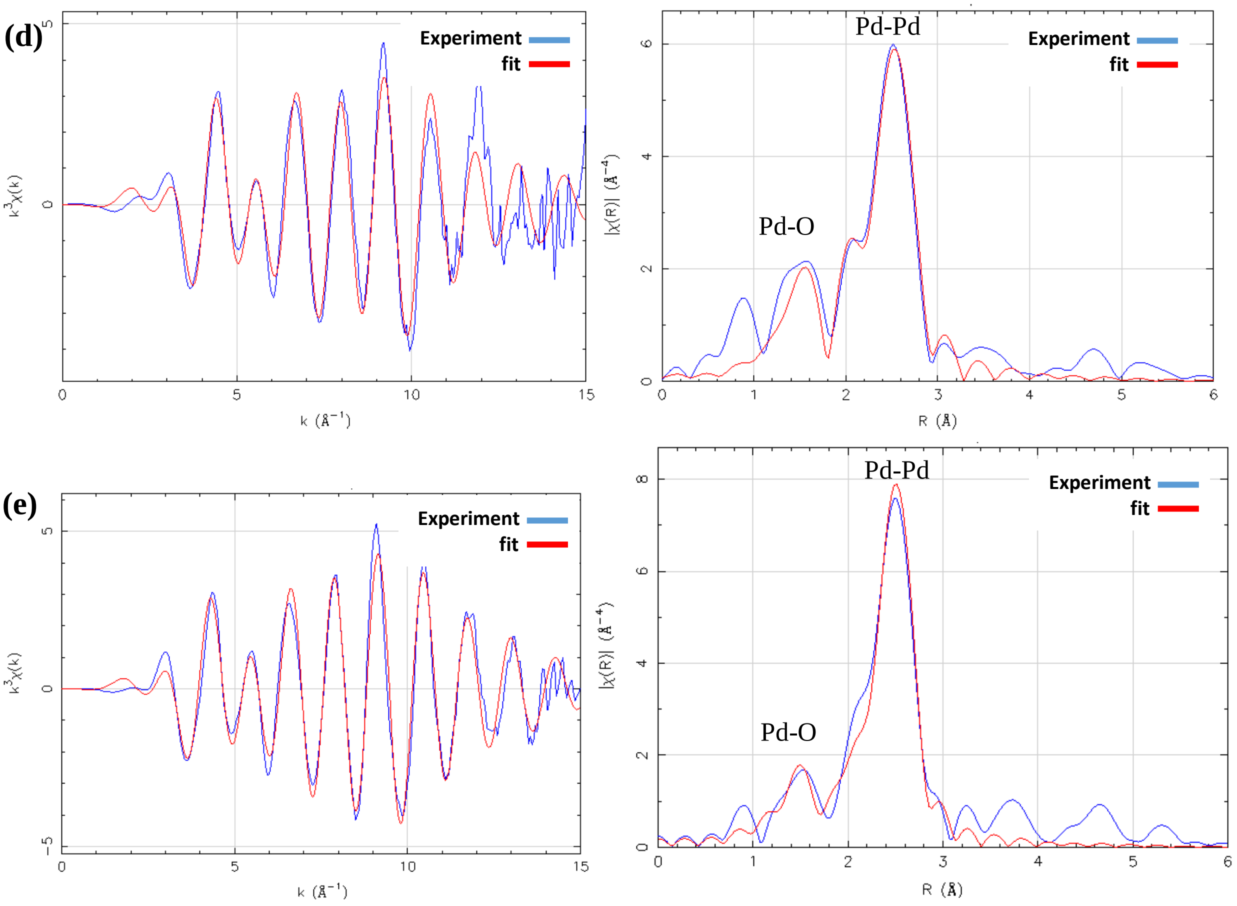

Fig. S4.4A. Figure S4.4A continued.

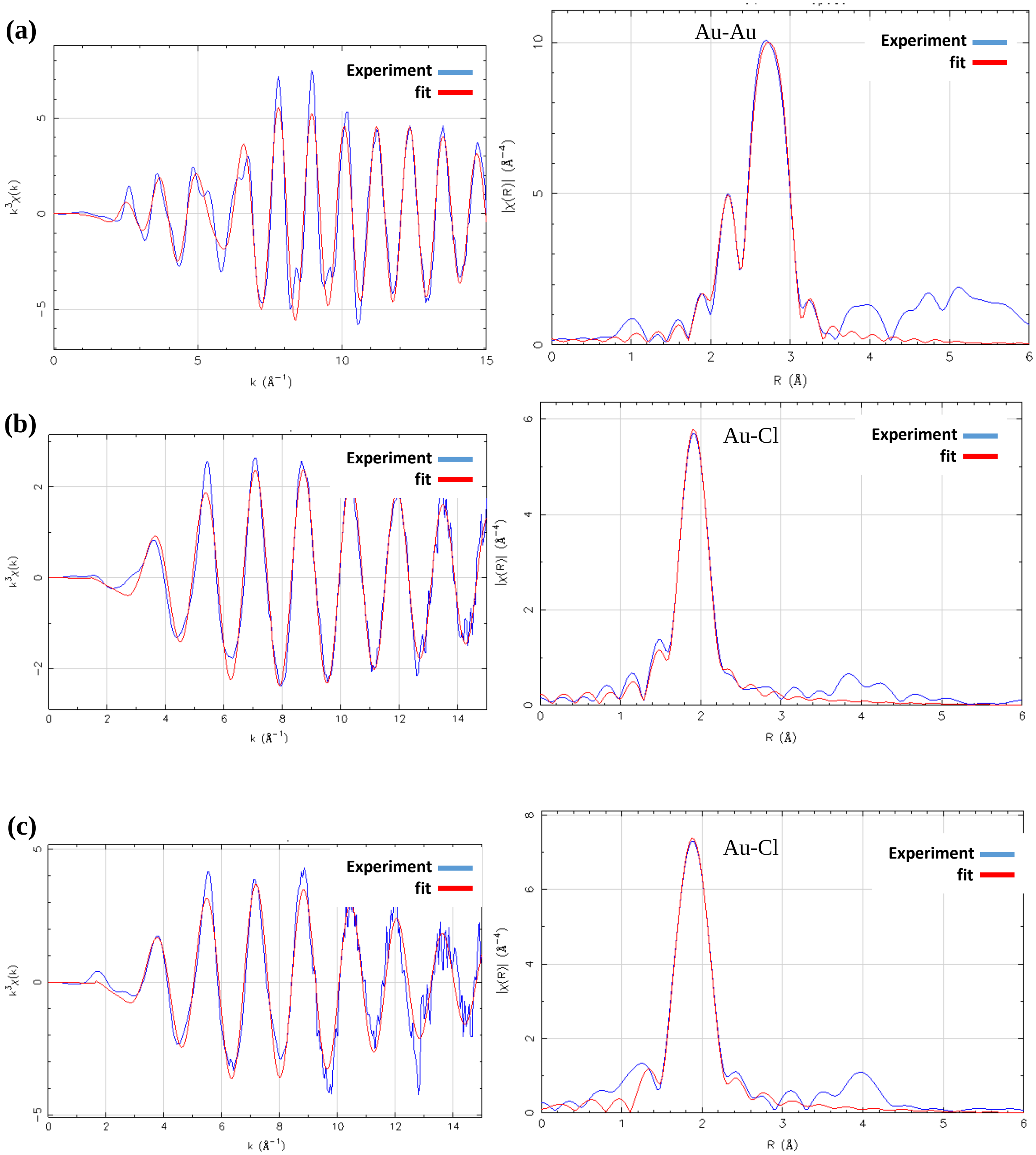

Fig. S4.4B. Observed and fitted data for k^3-weighted oscillation and its Fourier transform of Au L_3-edge EXAFS for the reference compounds (a) Au foil and (b) $HAuCl_4$•$4H_2O$, and the prepared sample (c) AuCl_me-Im@SBA-15 and (d) AuNPs(2.0 nm)_me-Im@SBA-15.

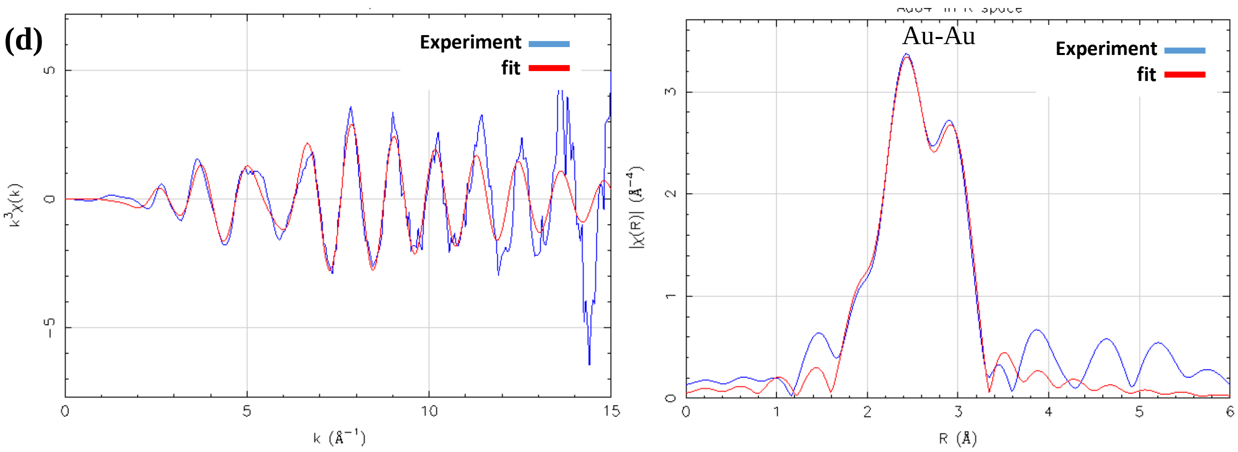

Fig. S4.4B. Figure S4.4B continued.

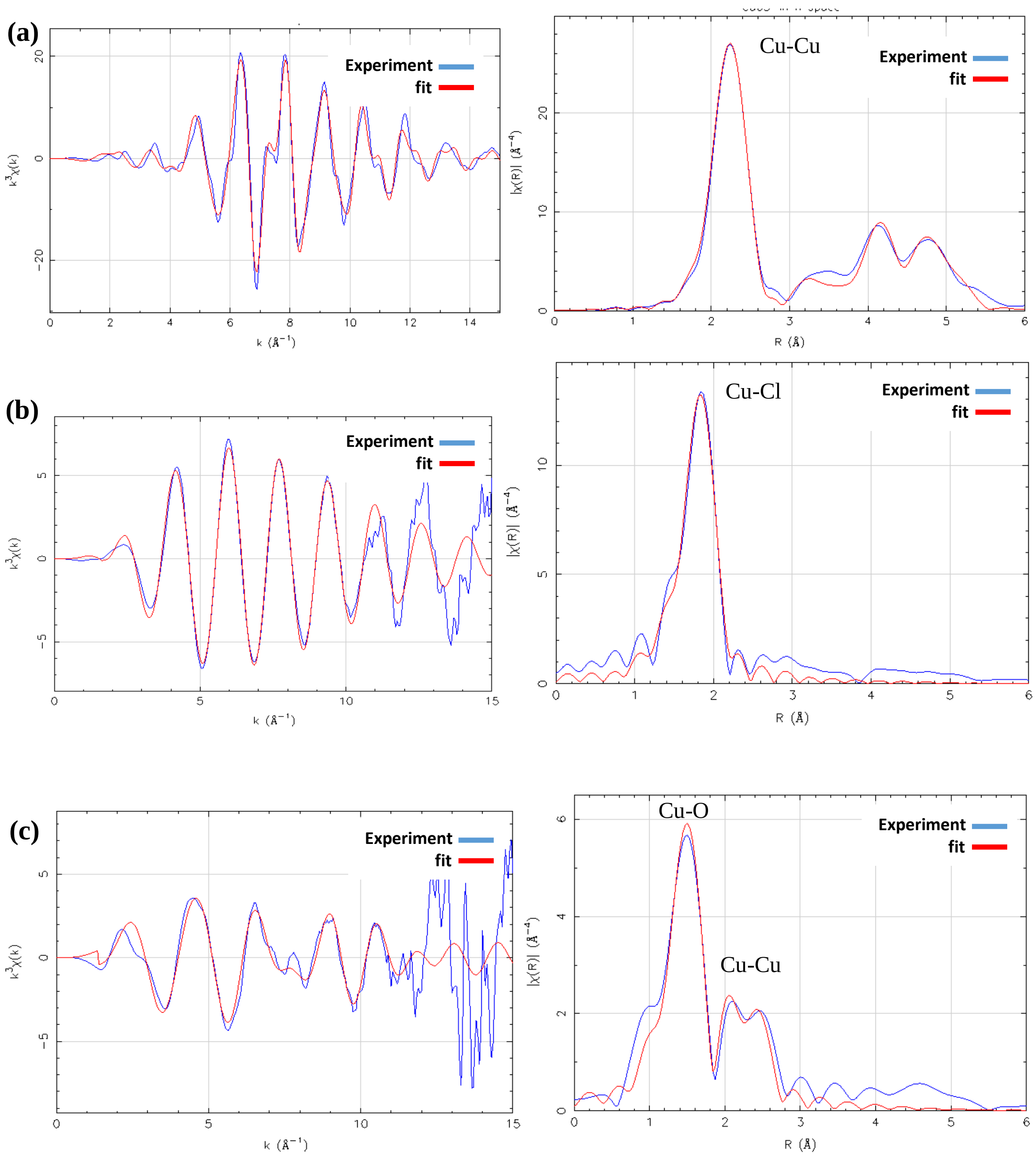

Fig. S4.4C. Observed and fitted data for k^3-weighted oscillation and its Fourier transform of Cu K-edge EXAFS for the reference compounds (a) Cu foil and the prepared sample (b) CuCl_me-Im@SBA-15 and (c) CuNPs(2.9 nm)_me-Im@SBA-15.

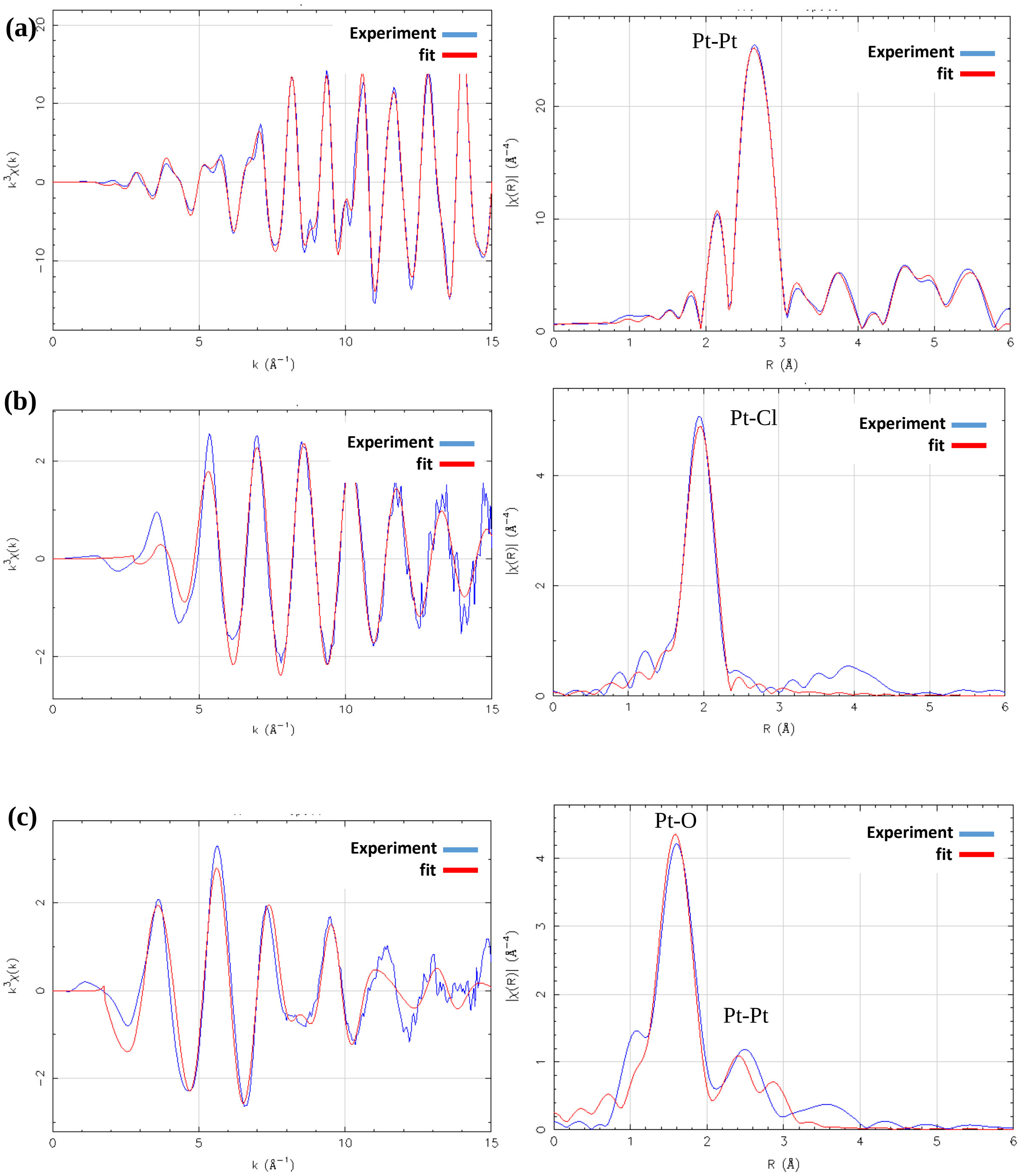

Fig. S4.4D. Observed and fitted data for k^3-weighted oscillation and its Fourier transform of Pt L_3-edge EXAFS for the reference compounds (a) Pt foil and the prepared sample (b) PtCl_me-Im@SBA-15 and (c) PtNPs(2.1 nm)_me-Im@SBA-15.

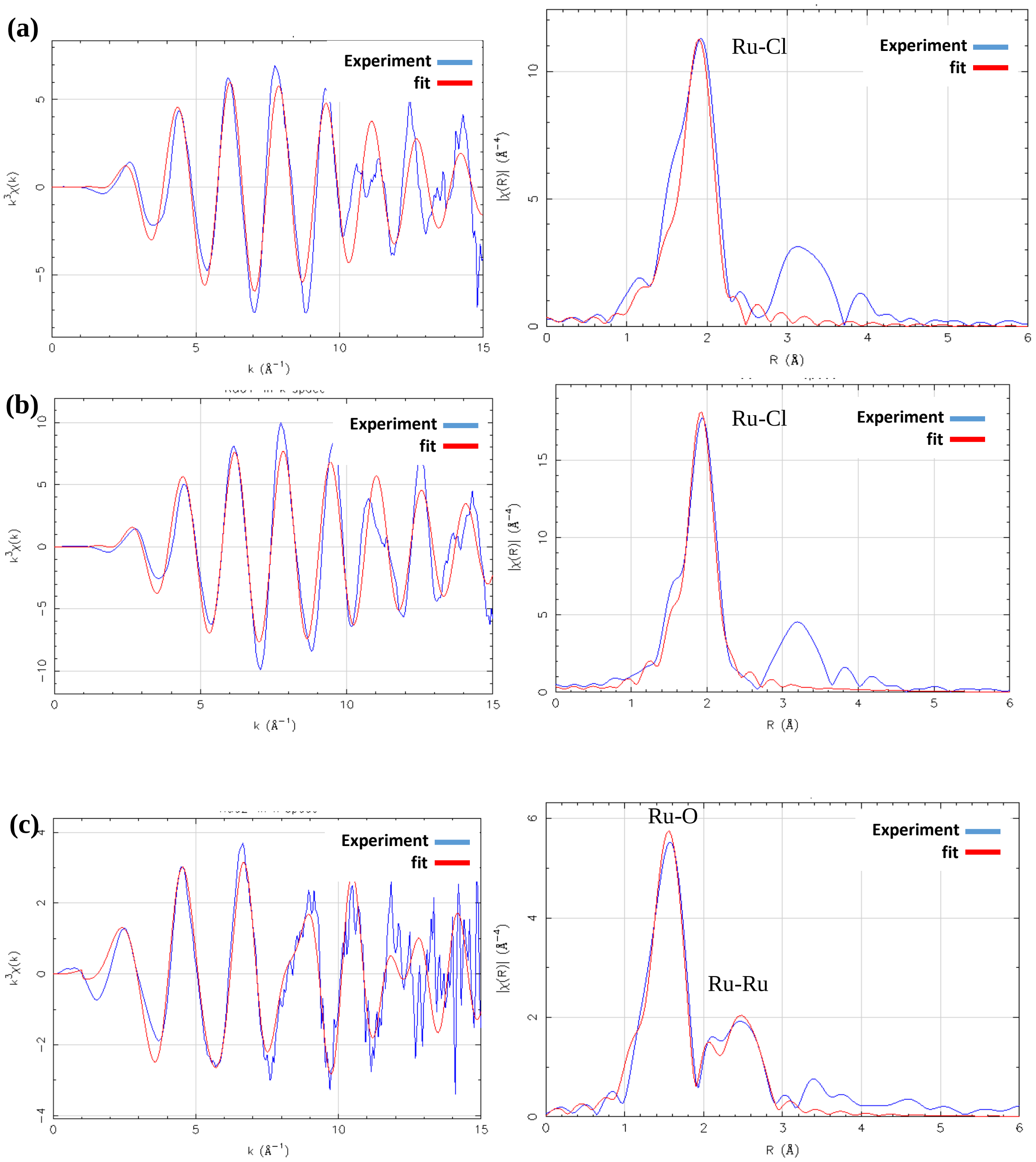

Fig. S4.4E. Observed and fitted data for k^3-weighted oscillation and its Fourier transform of Cu K-edge EXAFS for the reference compounds (a) $RuCl_3 \cdot xH_2O$ and the prepared sample (b) RuCl_me-Im@SBA-15 and (c) RuNPs(2.7 nm)_me-Im@SBA-15.

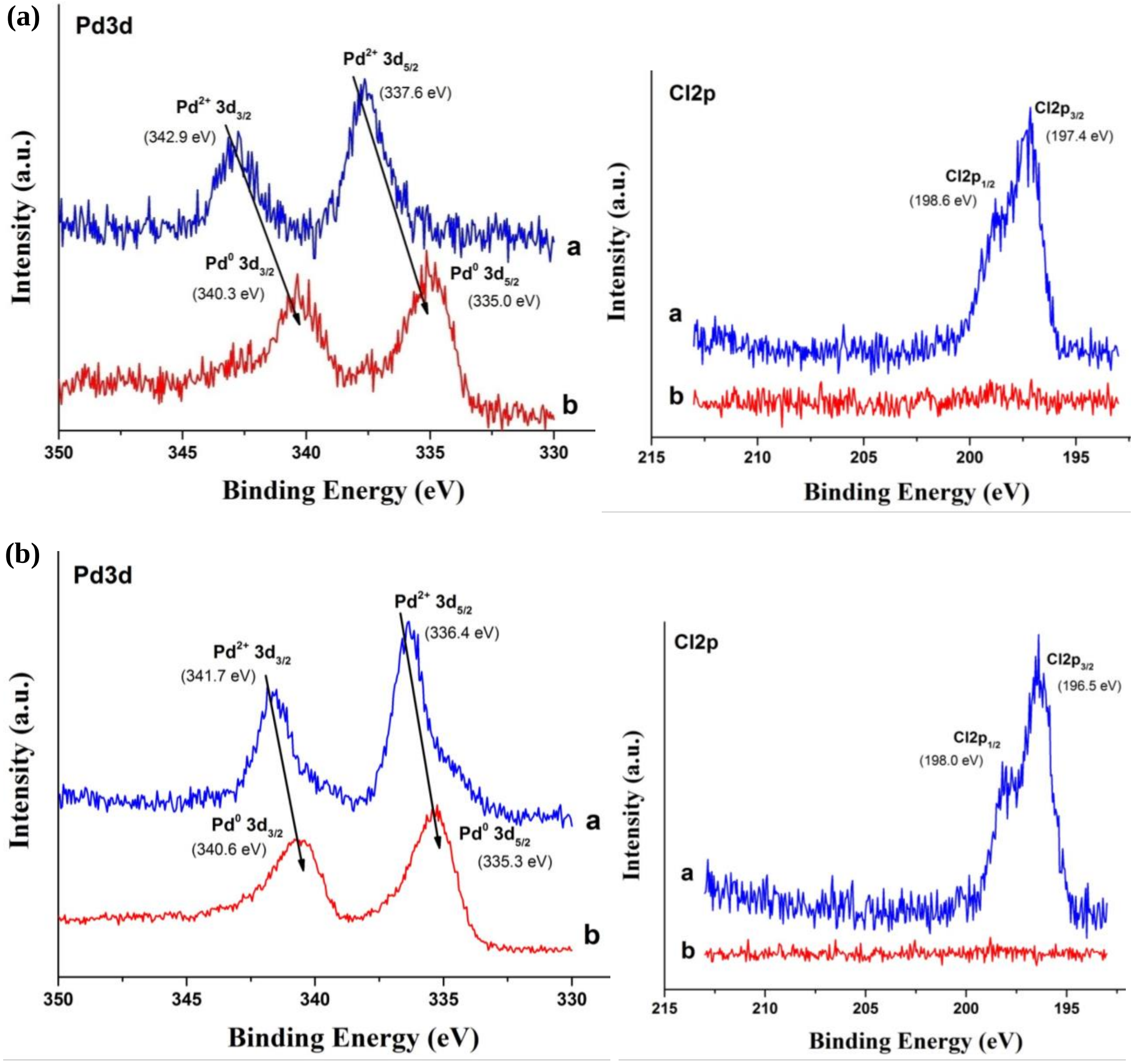

Fig. S4.5. XPS spectra of Pd 3d and Cl 2p regions of (a) PdNPs(2.4 nm) _me-Im@SBA-15 and (b) PdNPs(3.4 nm)_me-Im@SBA-15 before and after the metal reduction.

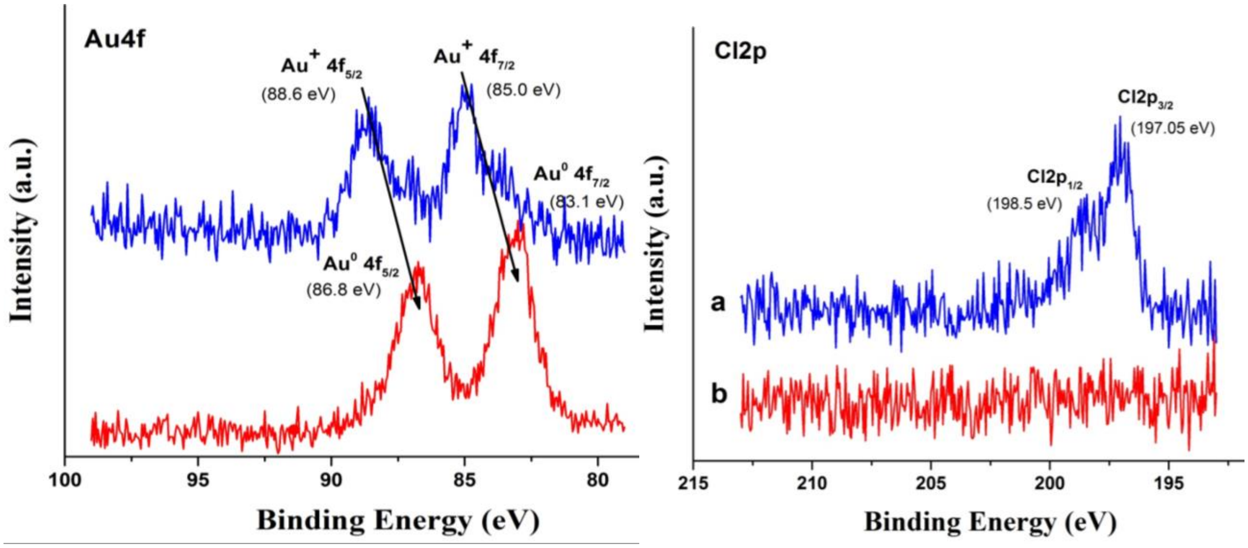

Fig. S4.6. XPS spectra of Au 4f and Cl 2p regions of AuNPs(2.0 nm) _me-Im@SBA-15 before and after the metal reduction.

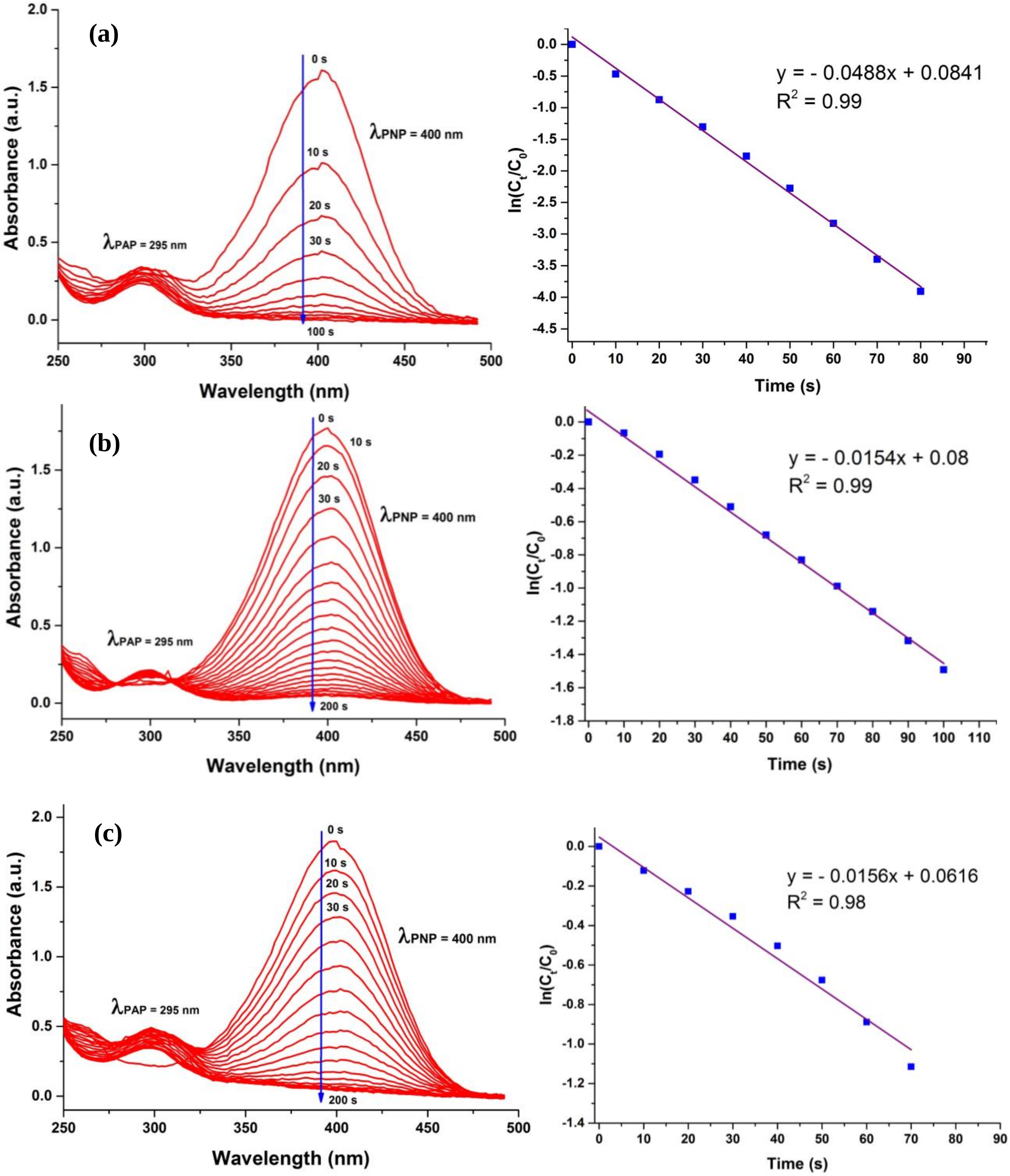

Fig. S4.7. UV-Vis spectra and ln(C_t/C_0) versus reaction time (t) along with the R^2 value for PNP reduction catalyzed by (a) PdNPs(2.4 nm)_me-Im@SBA-15, (b) PdNPs(3.4 nm)_bu-Im@SBA-15, (c) AuNPs(2.0 nm)_me-Im@SBA-15, (d) PtNPs(2.1 nm)_me-Im@SBA-15, (e) RuNPs(2.7 nm)_me-Im@SBA-15 and (f) CuNPs(2.9 nm)_me-Im@SBA-15.

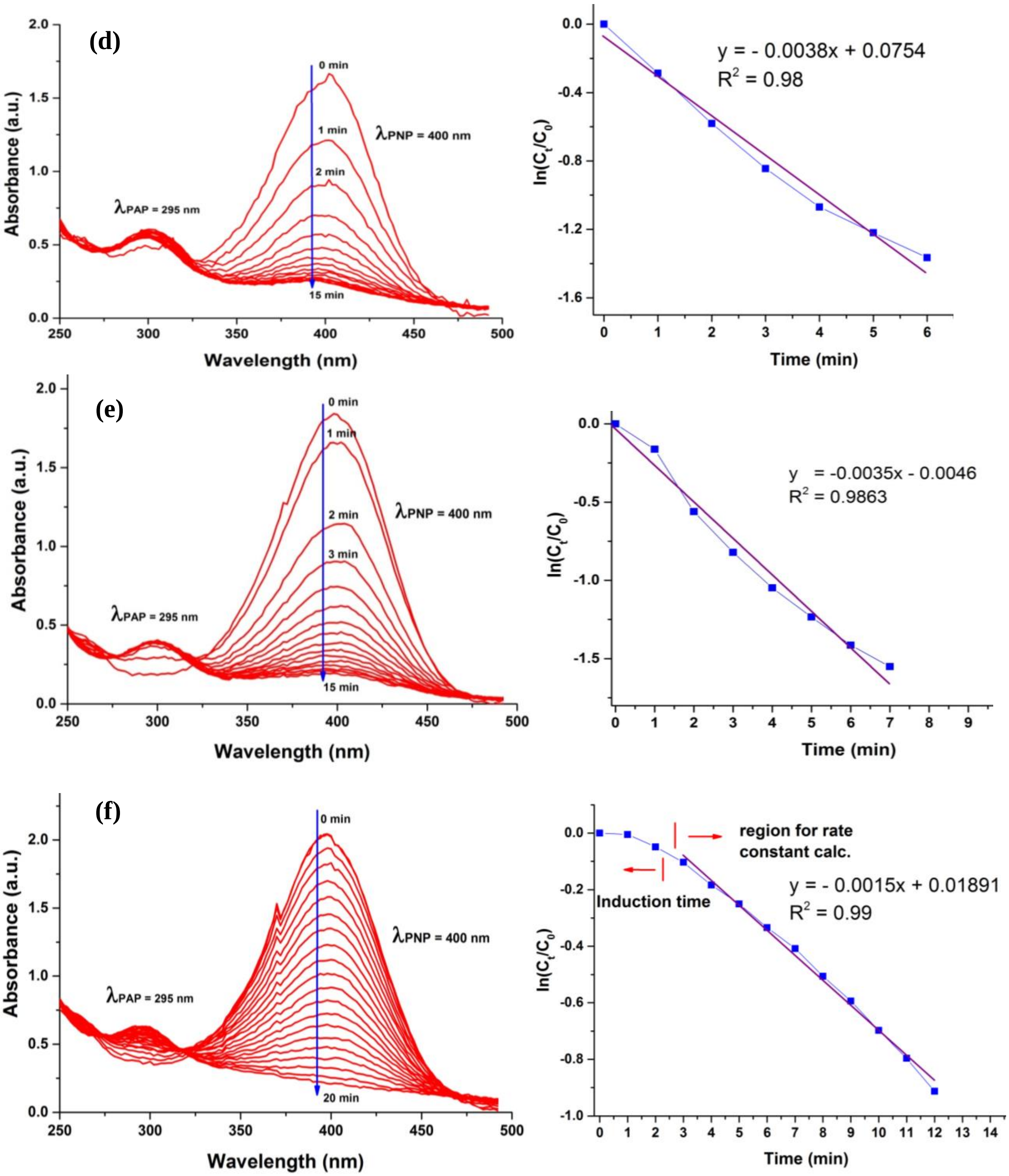

Fig. S4.7. Figure S4.10 continued.

Chapter 5

Room Temperature Suzuki-Miyaura Coupling Reaction Catalyzed by Palladium Nanoparticle

Abstract

Immobilized palladium nanoparticle on ionic liquid functionalized SBA-15 (PdNPs(2.4 nm)_me-Im@SBA-15) has been investigated as ligand-free catalyst for Suzuki-Miyaura cross-coupling reaction at room temperature. The catalyst was found active for the coupling reaction between aryl halides and phenylboronic acid in aqueous solution under air. The catalyst was reusable at least for four recycle processes without significant loss in activity with simple procedure.

5.1. Introduction

The most powerful methods for the synthesis of biaryls and related compounds which are the structural components of numerous industrial products, chemicals, pharmaceuticals and polymers, is the Suzuki-Miyaura cross-coupling reaction that was introduced by Akira Suzuki in 1979.[1,2] Since then, numerous publications have been reported involving the coupling of organoboron reagents and organic halides in the presence of metal catalysts. Most of these transformations are catalyzed by palladium nanoparticles (Pd^0) or palladium (Pd^{2+}) complex under certain reaction conditions. The use of phosphine-based ligands are generally required as the activators and stabilizers for active palladium species to achieve high performances in homogeneous and heterogeneous systems.[3–9] Since most of phosphine-based ligands are sensitive to air, various non-phosphine ligands have been developed such as *N*-heterocyclic carbenes and amine-based ligands, which also give high reaction rates.[10–12] These ligands play an important role owing to their electronic structure and binding to the palladium metal, and hence influence both the oxidative and reductive elimination steps.[13–21]

Because most of reactions require ligands which are mostly soluble in organic solvents, tremendous amounts of organic waste are produced, and removal of these ligands along with the metal from the reaction media, become a major concern for industrial application in a large scale.[22,23] Moreover, the catalyst loading, solvent, and nature of base are very important factors for the successful cross-coupling reaction and only few catalytic systems at room temperature have been reported. Therefore efforts have been focused on the development of new methods with ligand-free and the use of green solvent at room temperature. Significant progresses have been made, such as by using palladium nanoparticles, heterogeneous catalyst, and water-soluble ligands.[11,24–31]

In order to design an efficient heterogeneous catalyst, the preparation of support with essential functionalization should be taken into proper consideration to obtain the well dispersed and stable supported palladium species. In this case, mesoporous silica SBA-15 have become one of the most promising support due to the high physico-chemical stability, long-range homogeneity texture and modifiable surface chemistry.[32] Palladium (II) complexes immobilized on functionalized SBA-15 were reported to have high activity in Suzuki-Miyaura coupling reaction, however palladium nanoparticles (Pd^0) species was found to be the actual catalytic species for the reaction.[24,33–36] Han *et al.* have modified SBA-15 with immobilized ionic liquid as support for $PdCl_4^{2-}$ salt and the catalyst was active for Suzuki-Miyaura coupling reaction between *p*-bromoanisole and phenylboronic acid at room temperature in aqueous solution.[33] The active species Pd^0 was generated during the reaction and was stabilized by the ionic liquid on the support.

Supported palladium nanoparticle on ionic liquid functionalized SBA-15 and silica were prepared and investigated for coupling reaction between aryl bromides and phenylboronic acid at room temperature by M. Gruttadauria and coworker.[37] The prepared palladium nanoparticle on silica (SiO_2-Pd) showed higher activity than that of palladium on SBA-15 (SBA-15-Pd). However, in some cases palladium nanoparticle coordinated with the immobilized ligand on SBA-15 catalysts were found highly active and efficient for wide range coupling reaction between aryl halides and phenylboronic acid at 40 – 50 °C in aqueous solution.[24,25,31]

In the present work, PdNPs(2.4 nm)_me-Im@SBA-15 prepared in the previous chapter, was investigated as a ligand-free catalyst for Suzuki-Miyaura cross coupling reaction. The catalyst was active at room temperature in aqueous solution without a need of any stabilizer.

5.2. Experimental

5.2.1. Synthesis of PdNPs(2.4 nm)_me-Im@SBA-15

Palladium nanoparticle catalyst, PdNPs(2.4 nm)_me-Im@SBA-15, was prepared according to synthetic procedure described in Chapter 4. The preparation steps are illustrated in scheme 5.1.

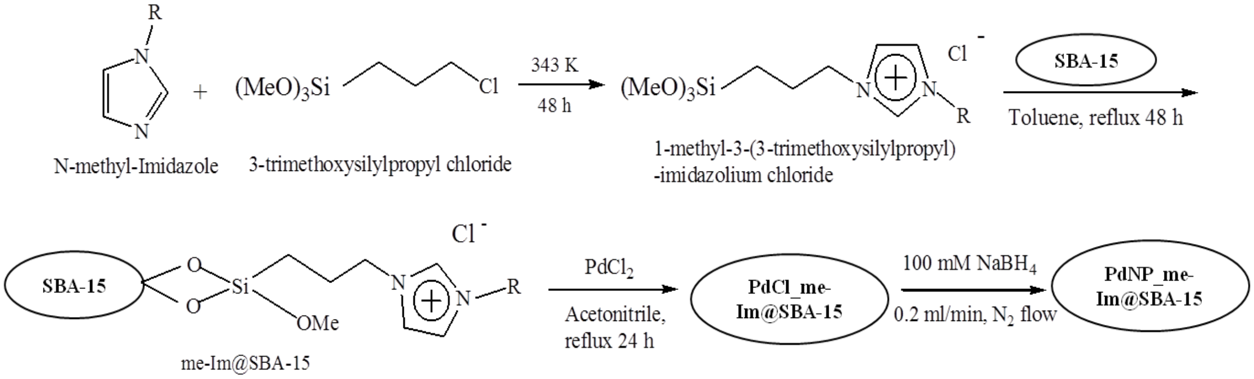

Scheme 5.1. Preparation steps for PdNPs(2.4 nm)_me-Im@SBA-15.

4.2.2. Suzuki-Miyaura coupling reaction

The general procedure for Suzuki-Miyaura coupling reaction is described as follows: an appropriate amount of PdNPs(2.4 nm)_me-Im@SBA-15 catalyst (0.3 mol%) was added to a mixture of aryl halide (1 mmol), phenylboronic acid (1.1 mmol), K_2CO_3 (2 mmol) in 5 mL solvent. The reaction mixture was stirred at room temperature under air and the reaction was monitored by GC. Small amount of the mixture was taken and after centrifugation, the filtrate was diluted with ethanol before subjected to GC. Diglyme (diethylene glycol dimethyl ether) was used as the internal standard to measure the yield. The products were confirmed by comparing the retention time with those of authentic samples. After completion, the reaction mixture was easily recovered by filtration. The catalyst was reused after washing with ethanol and water for three times.

5.3. Results and discussion

5.3.1. Optimization of reaction conditions

The reaction conditions were optimized for coupling reaction between iodobenzene and phenylboronic acid. The reaction parameters such as solvent, base and the amount of catalyst were examined to obtain the maximum yield. The results are summarized in Table 5.1. Both polar and nonpolar solvents such as water and toluene gave low yield when tested at room temperature. Other solvents such as 1,4-dioxane, MeOH, EtOH, and iPrOH also afforded low yields. When the reaction was performed in aqueous solution such as EtOH/H_2O and MeOH/H_2O the yield was improved to ~90% and among the bases screened, the use of K_2CO_3 was found to give the best result with 93% yield (entry 7). Moreover, when the amount of catalyst was increased to 0.3 mol%, the yield was also increased to 97% within 2 h of reaction time in EtOH/H_2O (1:1) solvent (entry 14). The reaction condition optimized in this study was applied to the reaction between other aryl halides and phenylboronic acid.

Table 5.1. Optimization of reaction conditions on Suzuki-Miyaura coupling reaction between iodobenzene and phenylboronic acid catalyzed by PdNPs(2.4 nm)_me-Im@SBA-15 at room temperature[a].

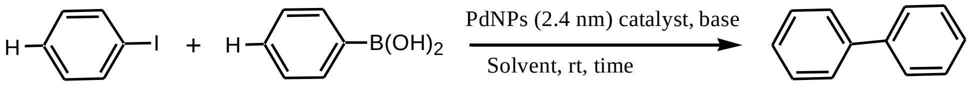

iodobenzene phenylboronic acid biphenyl

Entry	Solvent	Base	Catalyst (mol%)	t (h)	Yield (%)[b]
Effect of solvent					
1	Toluene	K_2CO_3	0.1	6	7
2	1,4-dioxane	K_2CO_3	0.1	6	1
3	H_2O	K_2CO_3	0.1	0.5	3
4	MeOH	K_2CO_3	0.1	6	40
5	EtOH	K_2CO_3	0.1	6	50
6	MeOH/H_2O (2:1)	K_2CO_3	0.1	7	88
7	EtOH/H_2O (2:1)	K_2CO_3	0.1	6 (24)	93 (95)
8	EtOH/H_2O (1:1)	K_2CO_3	0.1	6 (24)	90 (96)
9	iPrOH/H_2O (2:1)	K_2CO_3	0.1	6	20
Effect of base					
10	EtOH/H_2O (2:1)	Cs_2CO_3	0.1	6	79
11	EtOH/H_2O (2:1)	Na_2CO_3	0.1	6	55
12	EtOH/H_2O (2:1)	Na_3PO_4	0.1	6	54
Effect of catalyst amount					
13	EtOH/H_2O (2:1)	K_2CO_3	0.3	2	77
14	EtOH/H_2O (1:1)	K_2CO_3	0.3	2 (3)	97 (99)
15[c]	EtOH/H_2O (1:1)	K_2CO_3	0.1	1 (2)	92 (94)

a Reaction condition: iodobnezene (1 mmol), phenylboronic acid (1.1 mmol), base (2 mmol), solvent (5 ml), in air.
b non-isolated yield by GC with digyme as the internal standard, c the reaction was performed at 40 °C.

5.3.2. Suzuki-Miyaura coupling reaction between aryl halide and phenylboronic acid

Table 5.2. PdNPs(2.4 nm)_me-Im@SBA-15 catalyzed room temperature Suzuki-Miyaura coupling reaction of aryl halides and phenylboronic acid in aqueous solution[a].

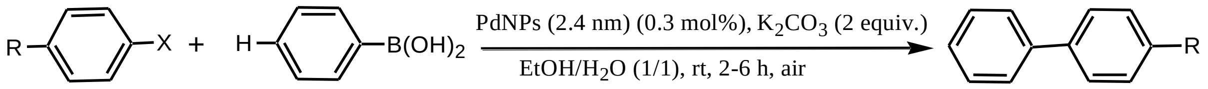

Entry	Aryl halide	Product	T (°C)	t (h)	Yield (%)[b]
1	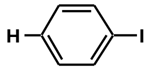	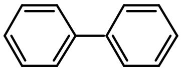	rt	2 (3)	97 (99)
2	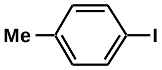	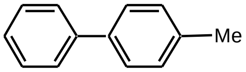	rt	6	77
3	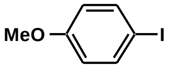	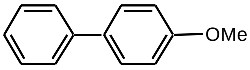	rt	3	80
4	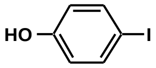	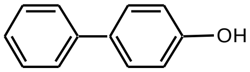	rt	3	70
5	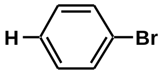	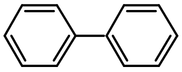	rt	4 (6)	93 (99)
6	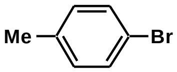	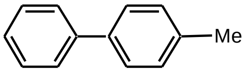	rt	4	58
			45	4	83
7	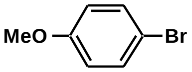	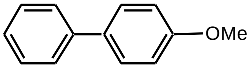	rt	4	55
			45	4	70
8	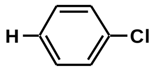	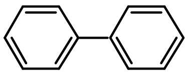	rt (80)	6	~6

a Reaction condition: iodobnezene (1 mmol), phenylboronic acid (1.1 mmol), base (2 mmol), solvent (5 ml), in air.

b non-isolated yield by GC with digyme as the internal standard.

Room Temperature Suzuki-Miyaura Coupling Reaction by PdNPs(2.4 nm)

Table 5.2 summarize the results of Suzuki-Miyaura coupling reaction between aryl halides and phenylboronic acid catalyzed by PdNPs(2.4 nm)_me-Im@SBA-15 mostly at room temperature within 2–6 h. The prepared catalyst was found active for the coupling reaction between bromobenzene and phenylboronic acid, giving 99% yield after 6 h reaction (entry 5). The presence of electron donating group on aryl halides was also examined with fair to good yields and improved at higher reaction temperature (45 °C). Moreover, the catalyst can be reused at least four times with the yield remaining 82% at the fourth cycle for the reaction between iodobenzene and phenylboronic acid at room temperature for 2 h (Table 5.3). The decreased in activity of the catalyst may be due to the secondary agglomeration of PdNPs during the recycle processes and the weight loss of catalyst during the separation and washing procedure before being used in the next cycle. In addition, to study the limitation scope of the reaction conditions, the coupling reaction of chlorobenzene with phenylboronic acid was investigated, however only a trace amount of biphenyl as the product was obtained (Table 5.2, entry 9). These results showed that the coupling reaction decreased in the order I > Br > Cl as the halide group due to the decrease in bond energy Ar-I < Ar-Br < Ar-Cl.[38]

Table 5.3. PdNPs(2.4 nm)_me-Im@SBA-15 catalyzed room temperature Suzuki-Miyaura coupling reaction of aryl halides and phenylboronic acid in aqueous solution[a].

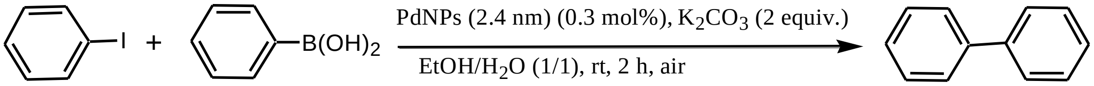

Run	1st	2nd	3rd	4th
Yield (%)	97	95	89	82
TOF (h^{-1})	162	158	148	137

TOF = mol of product per mol Pd per time (h^{-1})

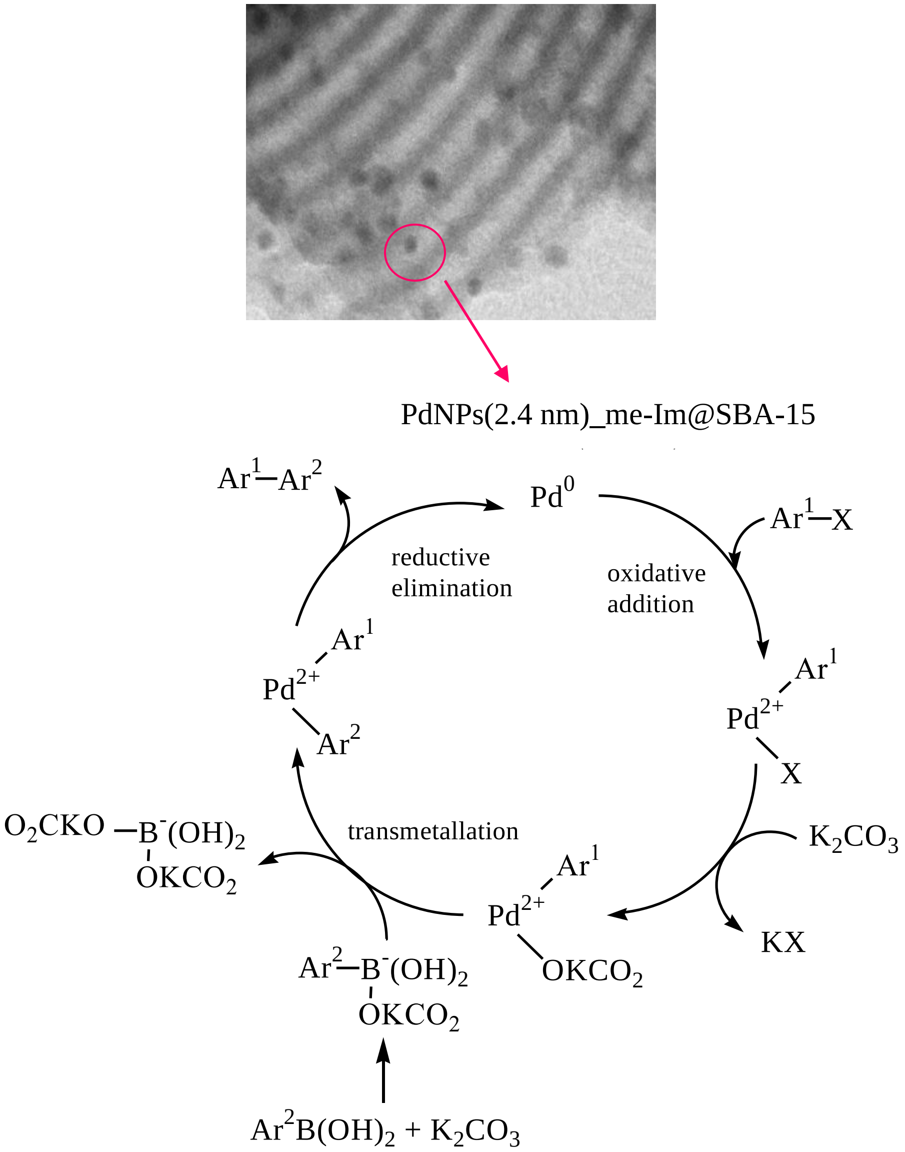

Scheme 2.2. Possible mechanism of Suzuki-Miyaura coupling reaction between aryl halide and phenylboronic acid over PdNPs(2.4 nm)_me-Im@SBA-15.

The reaction mechanism of this study was not achieved. However, based on the results obtained and the mechanistic study reported for palladium-catalyzed cross-coupling reaction so far, the possible mechanism of Suzuki-Miyaura coupling reaction of aryl halide and phenylboronic acid over PdNPs(2.4 nm)_me-Im@SBA-15 can be described as Scheme 2.2.[35,39,40] The reaction mechanism on PdNPs(2.4 nm)_me-Im@SBA-15 consists of three main stages: the oxidative addition of aryl halide, transmetalation, and reductive elimination to produce biaryl, in which the catalytic cycle is occurred on the surface of Pd nanoparticle.

In comparison to similar morphologies of supported palladium catalysts on Suzuki-Miyaura coupling reaction between iodobenzene and phenylboronic acid reported in the literature, the present catalyst has advantages in terms of room temperature reaction (TOF = 160 h^{-1} versus 133,[31] 56,[24] and 16 h^{-1} [25]), arylboronic acid loading and greener solvent (1.1 equiv. in EtOH/H_2O versus 1.5 equiv. in DMF[34]), and low catalyst loading (TOF = 160 h^{-1} (0.3 mol%) versus 50 h^{-1} (2 mol%)[41]). In comparison to non-porous support, in term of ligand-free room temperature coupling reaction between *p*-bromoanisole and phenylboronic acid (TOF = 46 h^{-1} versus 1.4[42] and 47 h^{-1} [37]) and coupling between bromobenzene and phenylboronic acid (TOF = 77.5 versus 48 h^{-1} [37]), and compared to unsupported Pd catalyst, in term of temperature reaction between iodobenzene and phenylboronic acid (TOF = 160 (25 °C) versus 143 h^{-1} (28 °C)[43]) the present catalyst shows superior performance.

5.4. Conclusion

In conclusion, the prepared PdNPs(2.4 nm) _me-Im@SBA-15 catalyst was found active for Suzuki-Miyaura coupling reaction between aryl halides (Ar-I and Ar-Br) and phenylboronic acid at room temperature without a need of additional ligand or stabilizer. The catalyst gave fair to good yield (99%) in environmentally benign reaction condition (in aqueous solvent under air at room temperature). The catalyst can be reused at least four times which reflects good reusability of the prepared catalyst.

5.5. References

(1) Miyaura, N.; Yamada, K.; Suzuki, A. A New Stereospecific Cross-Coupling by the Palladium-Catalyzed Reaction of 1-Alkenylboranes with 1-Alkenyl or 1-Alkynyl Halides. *Tetrahedron Lett.* **1979**, *20* (36), 3437–3440.

(2) Suzuki, A. Cross-Coupling Reactions via Organoboranes. *J. Organomet. Chem.* **2002**, *653* (1–2), 83–90.

(3) Ge, J.; Jiang, J.; Yuan, C.; Zhang, C.; Liu, M. Palladium Nanoparticles Stabilized by Phosphine Ligand for Aqueous Phase Room Temperature Suzuki-Miyaura Coupling. *Tetrahedron Lett.* **2017**, *58* (12), 1142–1145.

(4) Chen, T.; Mao, F.; Qi, Z.; Li, Y.; Chen, R.; Wang, Y.; Huang, J. Immobilized Palladium Nanoparticles within Polymers as Active Catalysts for Suzuki–Miyaura Reaction. *RSC Adv.* **2016**, *6*, 16899–16903.

(5) Tamura, M.; Fujihara, H. Chiral Bisphosphine BINAP-Stabilized Gold and Palladium Nanoparticles with Small Size and Their Palladium Nanoparticle-Catalyzed Asymmetric Reaction. *J. Am. Chem. Soc.* **2003**, *125* (51), 15742–15743.

(6) Mori, K.; Kondo, Y.; Yamashita, H. Synthesis and Characterization of FePd Magnetic Nanoparticles Modified with Chiral BINAP Ligand as a Recoverable Catalyst Vehicle for the Asymmetric Coupling Reaction. *Phys. Chem. Chem. Phys.* **2009**, *11* (39), 8949–8954.

(7) Sawai, K.; Tatumi, R.; Nakahodo, T.; Fujihara, H. Asymmetric Suzuki-Miyaura Coupling Reactions Catalyzed by Chiral Palladium Nanoparticles at Room Temperature. *Angew. Chemie - Int. Ed.* **2008**, *47* (36), 6917–6919.

(8) Wu, L.; Li, B. L.; Huang, Y. Y.; Zhou, H. F.; He, Y. M.; Fan, Q. H. Phosphine Dendrimer-Stabilized Palladium Nanoparticles, a Highly Active and Recyclable Catalyst for the

Suzuki-Miyaura Reaction and Hydrogenation. *Org. Lett.* **2006**, *8* (16), 3605–3608.

(9) Handa, S.; Wang, Y.; Gallou, F.; Lipshutz, B. H. Sustainable Fe-ppm Pd Nanoparticle Catalysis of Suzuki-Miyaura Cross-Couplings in Water. *Science* **2015**, *349* (6252), 1087–1091.

(10) Fortman, G. C.; Nolan, S. P. N-Heterocyclic Carbene (NHC) Ligands and Palladium in Homogeneous Cross-Coupling Catalysis: A Perfect Union. *Chem. Soc. Rev.* **2011**, *40* (10), 5151–5169.

(11) Das, P.; Sarmah, C.; Tairai, A.; Bora, U. Highly Efficient Amine-Based Catalytic System for Room Temperature Suzuki-Miyaura Reactions of Aryl Halides with Arylboronic Acids. *Appl. Organomet. Chem.* **2011**, *25* (4), 283–288.

(12) Chahen, L.; Therrien, B.; Süss-Fink, G. Square-Planar Diacetatopalladium Complexes with Trans-Configured Secondary Amine Ligands That Avoid Orthometalation: Ligand Synthesis, Coordination, Molecular Structure and Catalytic Potential for Suzuki Cross-Coupling Reactions. *Eur. J. Inorg. Chem.* **2007**, No. 32, 5045–5051.

(13) Carrow, B. P.; Hartwig, J. F. Distinguishing between Pathways for Transmetalation in Suzuki-Miyaura Reactions. *J. Am. Chem. Soc.* **2011**, *133* (7), 2116–2119.

(14) Butters, M.; Harvey, J. N.; Jover, J.; Lennox, A. J. J.; Lloyd-Jones, G. C.; Murray, P. M. Aryl Trifluoroborates in Suzuki-Miyaura Coupling: The Roles of Endogenous Aryl Boronic Acid and Fluoride. *Angew. Chem. Int. Ed.* **2010**, *49* (30), 5156–5160.

(15) Amatore, C.; Jutand, A.; Le Duc, G. Kinetic Data for the Transmetalation/Reductive Elimination in Palladium-Catalyzed Suzuki-Miyaura Reactions: Unexpected Triple Role of Hydroxide Ions Used as Base. *Chem. Eur. J.* **2011**, *17* (8), 2492–2503.

(16) Hicks, J. D.; Hyde, A. M.; Cuezva, A. M.; Buchwald, S. L. Pd-Catalyzed N-Arylation of

Secondary Acyclic Amides: Catalyst Development, Scope, and Computational Study. *J. Am. Chem. Soc.* **2009**, *131* (46), 16720–16734.

(17) Fu, G. C. The Development of Versatile Methods for Palladium-Catalyzed Coupling Reactions of Aryl Electrophiles through the Use of P(*t*-Bu)$_3$ and PCy$_3$ as Ligands. *Acc. Chem. Res.* **2008**, *41* (11), 1555–1564.

(18) Fleckenstein, C. A.; Plenio, H. Sterically Demanding Trialkylphosphines for Palladium-Catalyzed Cross Coupling Reactions—alternatives to PtBu$_3$. *Chem. Soc. Rev.* **2010**, *39* (2), 694–711.

(19) Marion, N.; Nolan, S. P. Well-Defined N-Heterocyclic Carbenes-Palladium(II) Precatalysts for Cross-Coupling Reactions. *Acc. Chem. Res.* **2008**, *41* (11), 1440–1449.

(20) Littke, A. F.; Fu, G. C. Palladium-Catalyzed Coupling Reactions of Aryl Chlorides. *Angew. Chem. Int. Ed.* **2002**, *41* (22), 4176–4211.

(21) Lundgren, R. J.; Stradiotto, M. Addressing Challenges in Palladium-Catalyzed Cross-Coupling Reactions Through Ligand Design. *Chem. Eur. J.* **2012**, *18* (32), 9758–9769.

(22) Beletskaya, I. P.; Cheprakov, A. V. Heck Reaction as a Sharpening Stone of Palladium Catalysis. *Chem. Rev.* **2000**, *100* (8), 3009–3066.

(23) Hussain, I.; Capricho, J.; Yawer, M. A. Synthesis of Biaryls via Ligand-Free Suzuki–Miyaura Cross-Coupling Reactions: A Review of Homogeneous and Heterogeneous Catalytic Developments. *Adv. Synth. Catal.* **2016**, *358* (21), 3320–3349.

(24) Veisi, H.; Hamelian, M.; Hemmati, S. Palladium Anchored to SBA-15 Functionalized with Melamine-Pyridine Groups as a Novel and Efficient Heterogeneous Nanocatalyst for Suzuki-Miyaura Coupling Reactions. *J. Mol. Catal. A Chem.* **2014**, *395*, 25–33.

(25) Veisi, H.; Amini Manesh, A.; Eivazi, N.; Faraji, A. R. Palladium Nanoparticles Supported

on 1,3-Dicyclohexylguanidine Functionalized Mesoporous Silica SBA-15 as Highly Active and Reusable Catalyst for the Suzuki–Miyaura Cross-Coupling Reaction. *RSC Adv.* **2015**, *5* (26), 20098–20107.

(26) Sarmah, G.; Bora, U. Simple Aminobenzoic Acid Promoted Palladium Catalyzed Room Temperature Suzuki-Miyaura Cross-Coupling Reaction in Aqueous Media. *Tetrahedron Lett.* **2015**, *56* (22), 2906–2909.

(27) Zhang, G.; Wang, P.; Wei, X. Palladium Supported on Functionalized Mesoporous Silica as an Efficient Catalyst for Suzuki-Miyaura Coupling Reaction. *Catal. Letters* **2013**, *143* (11), 1188–1194.

(28) Wang, P.; Zhang, G.; Liu, L.; Jiao, H.; Deng, X.; Zheng, X. Palladium Supported on Mesoporous Silica via an In-Situ Method as an Efficient Catalyst for Suzuki-Miyaura Coupling Reactions. *Mater. Res. Bull.* **2014**, *59*, 365–369.

(29) Sahu, D.; Silva, A. R.; Das, P. Facile Synthesis of Palladium Nanoparticles Supported on Silica: An Efficient Phosphine-Free Heterogeneous Catalyst for Suzuki Coupling in Aqueous Media. *Catal. Commun.* **2016**, *86*, 32–35.

(30) Kalvet, I.; Magnin, G.; Schoenebeck, F. Rapid Room-Temperature, Chemoselective Csp^2−Csp^2 Coupling of Poly(Pseudo)Halogenated Arenes Enabled by Palladium(I) Catalysis in Air. *Angew. Chem. Int. Ed.* **2017**, *56* (6), 1581–1585.

(31) Ghorbani-Vaghei, R.; Hemmati, S.; Veisi, H. Pd Immobilized on Amidoxime-Functionalized Mesoporous SBA-15: A Novel and Highly Active Heterogeneous Catalyst for Suzuki-Miyaura Coupling Reactions. *J. Mol. Catal. A Chem.* **2014**, *393*, 240–247.

(32) Molnár, Á. Efficient, Selective, and Recyclable Palladium Catalysts in Carbon-Carbon Coupling Reactions. *Chem. Rev.* **2011**, *111* (3), 2251–2320.

(33) Han, P.; Zhang, H.; Qiu, X.; Ji, X.; Gao, L. Palladium within Ionic Liquid Functionalized Mesoporous Silica SBA-15 and Its Catalytic Application in Room-Temperature Suzuki Coupling Reaction. *J. Mol. Catal. A Chem.* **2008**, *295* (1–2), 57–67.

(34) Pathak, A.; Singh, A. P. Synthesis and Characterization of D-2PA-Pd(II)@SBA-15 Catalyst via "Click Chemistry": Highly Active Catalyst for Suzuki Coupling Reactions. *J. Porous Mater.* **2017**, *24* (2), 327–340.

(35) Yu, J.; Shen, A.; Cao, Y.; Lu, G. Preparation of Pd-Diimine@SBA-15 and Its Catalytic Performance for the Suzuki Coupling Reaction. *Catalysts* **2016**, *6* (12), 181.

(36) Rajabi, F.; Fayyaza, F.; Bandyopadhyay, R.; Ivars-barcelo, F.; R. Puente-Santiago, A.; Luque, R. Cytosine Palladium Hybrid Complex Immobilized on SBA-15 as Efficient Heterogeneous Catalyst for the Aqueous Suzuki-Miyaura Coupling. *Chem. Sel.* **2018**, *3*, 6102–6106.

(37) Gruttadauria, M.; Liotta, L. F.; Salvo, A. M. P.; Giacalone, F.; La Parola, V.; Aprile, C.; Noto, R. Multi-Layered, Covalently Supported Ionic Liquid Phase (Mlc-SILP) as Highly Cross-Linked Support for Recyclable Palladium Catalysts for the Suzuki Reaction in Aqueous Medium. *Adv. Synth. Catal.* **2011**, *353* (11–12), 2119–2130.

(38) Ncube, P.; Hlabathe, T.; Meijboom, R. Palladium Nanoparticles Supported on Mesoporous Silica as Efficient and Recyclable Heterogenous Nanocatalysts for the Suzuki C–C Coupling Reaction. *J. Clust. Sci.* **2015**, *26* (5), 1873–1888.

(39) Hajighorbani, M.; Hekmati, M. Pd Nanoparticles Deposited on Isoniazid Grafted Multi Walled Carbon Nanotubes: Synthesis, Characterization and Application for Suzuki Reaction in Aqueous Media. *RSC Adv.* **2016**, *6* (92), 88916–88924.

(40) Balanta, A.; Godard, C.; Claver, C. Pd Nanoparticles for C-C Coupling Reactions. *Chem.*

Soc. Rev. **2011**, *40* (10), 4973–4985.

(41) Zhong, L.; Chokkalingam, A.; Cha, W. S.; Lakhi, K. S.; Su, X.; Lawrence, G.; Vinu, A. Pd Nanoparticles Embedded in Mesoporous Carbon: A Highly Efficient Catalyst for Suzuki-Miyaura Reaction. *Catal. Today* **2015**, *243*, 195–198.

(42) Maegawa, T.; Kitamura, Y.; Sako, S.; Udzu, T.; Sakurai, A.; Tanaka, A.; Kobayashi, Y.; Endo, K.; Bora, U.; Kurita, T.; et al. Heterogeneous Pd/C-Catalyzed Ligand-Free, Room-Temperature Suzuki-Miyaura Coupling Reactions in Aqueous Media. *Chem. Eur. J.* **2007**, *13* (20), 5937–5943.

(43) Deraedt, C.; Salmon, L.; Astruc, D. "Click" Dendrimer-Stabilized Palladium Nanoparticles as a Green Catalyst down to Parts per Million for Efficient C-C Cross-Coupling Reactions and Reduction of 4-Nitrophenol. *Adv. Synth. Catal.* **2014**, *356* (11–12), 2525–2538.

Chapter 6

Conclusions and Outlook

In this thesis, I developed heterogeneous catalysts based on supported metal nanoparticles prepared from immobilized metal chloride on mesoporous silica SBA-15 in the presence of immobilized ionic liquid, studied their morphology and structural properties, and investigated their catalytic performance and reusability. The synthetic method for size-controlled nanoparticles was developed to obtain small and uniform size distribution inside porous channels, as well as to minimize the pore-blocking effect in order to improve the catalytic performance of the prepared catalysts. This thesis contains mainly three aims; a) development of supported metal nanoparticles with controllable size on mesoporous silica SBA-15, b) studying the properties of the prepared catalysts, and c) investigation of their activity and reusability in organic transformation.

In **Chapter 2**, size-controlled gold nanoparticles prepared from immobilized gold chloride on ionic liquid functionalized SBA-15 was successfully synthesized by varying the concentration and feed rate of $NaBH_4$. Au NPs with the size of 1.6 nm was obtained by fixing the feed rate at 0.2 ml/min, whereas larger and capsule-like NPs were observed at slow feed rate of 0.04 ml/min reduced by 4 mM $NaBH_4$. Au NPs size decreased as the concentration of $NaBH_4$ increased suggesting that the excess OH^- facilitates the electrostatic stabilization by providing the protective layer on NPs surface. Particle size distribution and shape strongly depend on the interaction forces between the monomers, either small (Cl^- and OH^-) or large (imidazolium cation) molecules, as well as the reduction and growth rates which directly affect the agglomeration process.

In **Chapter 3**, the size-dependence of gold nanoparticles activity was investigated for *p*-nitrophenol hydrogenation reaction. Various prepared AuNPs catalysts with different size and morphology were examined and the catalyst with the smallest size, AuNPs(1.6 nm)_ me-

Im@SBA-15, showed the best performance with the highest apparent rate constant (k_{app}) to convert *p*-nitrophenol to *p*-aminophenol. Meanwhile, Au/SBA-15 with the size of 5.6 nm which was synthesized in the absence of ionic liquid exhibited the lowest activity with the lowest k_{app} value. The catalyst was reusable at least for four cycles with slight decrease in k_{app} value due to the agglomeration during the successive recycle processes.

In **Chapter 4**, various metal (Pd, Au, Cu, Ru and Pt) nanoparticles catalysts with the average size of 2 – 4 nm were prepared according to the synthetic approach developed in Chapter 2. The use of immobilized ionic liquids with different alkyl groups for Pd nanoparticles suggested that shorter alkyl substitutional group could control the particle size more efficiently than the longer one. Characterization of catalyst revealed that immobilized metal chloride on SBA-15 formed metal chloride complex anion in which it was stabilized by immobilized imidazolium cation on SBA-15. Some parts of metal nanoparticles surfaces are covered by oxygen adatoms which later strongly affect the catalyst performance. The activity and stability of the prepared MNPs depend on the particle size, metal species of the nanoparticles and the catalyst morphology.

In **Chapter 5**, the catalytic activity of the prepared palladium nanoparticle, PdNPs(2.4 nm)_me-Im@SBA-15, was investigated for Suzuki-Miyaura cross-coupling reaction between aryl halides and phenylboronic acid at room temperature. The catalyst was found active and reusable giving fair to good yield for the coupling reaction between phenylboronic acid and aryl halides Ar-I and Ar-Br at room temperature without additional ligand or stabilizer.

Throughout **Chapter 2** and **3**, controlling the nanoparticles size on porous material is required to design active and efficient heterogeneous catalyst, since the nanoparticle size affects strongly the catalytic performance of the catalyst. Thus, the development of synthetic method is essential to control the nanoparticle growth and understand the growth mechanism of nanoparticles on solid support especially on porous materials. Therefore, through the synthetic strategies studied in this thesis hopefully will be one of the methods considered for the synthesis of metal nanoparticle with controlled size on solid support. Throughout **Chapter 4** and **5**, a comprehensive understanding of structural properties of various metal nanoparticles with regards to their effect on the catalytic performances was studied. Such study is essentially necessary to achieve optimal control of the reaction performances and obtain the best results. By modifying the structure and morphology of the catalyst, the efficient and more environmentally benign reaction system can be achieved. In addition, the catalysts prepared in this work offer many advantages to be used as active and reusable catalyst for variety of organic transformation.

Finally, I believe that this work could contribute to the synthetic method for controlling the nanoparticle size on porous material, and trigger further work on the development of heterogeneous catalyst based on supported metal nanoparticles. Further, I hope this thesis will inspire other scientists to the continuous development of supported metal nanoparticles on ionic liquid functionalized SBA-15 for heterogeneous catalysis.

Acknowledgments

Three years of my PhD studies was supported by the Ministry of Education, Culture, Sports, Science and Technology (MEXT) Japan, that I otherwise would not have been able to pursue my studies here. This work was performed using facilities (TEM and XRD) of the Institute of Solid State Physics, the University of Tokyo. XPS measurements were conducted in Research Hub for Advanced Nano Characterization, the University of Tokyo, supported by MEXT Japan. The XAFS measurements were performed at KEK-IMSS-PF with the approval of the Photon Factory Adivisory Committee (projects 2015G712 and 2017G190).

I would like to express my gratitude to my supervisor, Prof. Takehiko Sasaki for giving me the opportunities to learn many things and work in such motivating environment. His guidance in introducing me into the world of nanoparticles and catalysis, also especially for his daily patient assistance enable me to finish this challenging study. I would like to thank Prof. Koichiro Saiki for his inputs and suggestions to improve my thesis, and Dr. Seiji Obata for his assistances and helps in solving my problems. I would like to thank Dr. Daisuke Nishio-Hamane for his assistance in teaching me how to operate TEM which is mainly used for this study. I would also like to thank Ohnuki-san and Jimbo-san for their great help in assisting me how to operate the laboratory instruments. A general thanks to all the Surface and Artificial Materials Chemistry Laboratory members for their supports and valuable suggestions during the lab seminars and also for the many entertaining and joyful days.

Special thanks to my labmates, Harada, Itako, Kawano, Ambar, Yuuki, Saito and Chang, who have been supportive in many ways. A hundred thanks to my stepmothers, Windy Iriana and Suhaila, also my stepfather Helbert, for their punches to keep me awake back into the reality

(haha). My good mom, mbak Dian, who helped and gave me foods not to share. A gigantic thanks to all the Munyingers for their physical and emotional supports, and those many happy memories keeping us stay on the track. I will definitely miss you guys. And finally, I would like to express my entire gratitude to my family, who were always my best supporters through my whole life, especially my father. His tremendous support and faith in me were the driving forces behind everything I did.